Rational design of next-generation filovirus vaccines through glycoprotein stabilization, nanoparticle display, and glycan modification

Yi-Zong Lee[1#], Yi-Nan Zhang[1#], Maddy L. Newby[2], Garrett Ward[1], Keegan Braz Gomes[3], Sarah Auclair[1], Connor DesRoberts[1], Joel D. Allen[2], Andrew B. Ward[1], Robyn L. Stanfield[1], Linling He[1], Max Crispin[2], Ian A. Wilson[1,4], and Jiang Zhu[1,5]*

[1]Department of Integrative Structural and Computational Biology, The Scripps Research Institute, La Jolla, CA 92037, USA

[2]School of Biological Sciences, Highfield Campus, University of Southampton, Southampton, SO17 1BJ, UK

[3]Uvax Bio, LLC, Newark, DE 19702, USA

[4]Skaggs Institute for Chemical Biology, The Scripps Research Institute, La Jolla, CA 92037, USA

[5]Department of Immunology and Microbiology, The Scripps Research Institute, La Jolla, CA 92037, USA

[#] These authors contributed equally to this work

* Corresponding author

JZ: Phone (858) 784-8157; Email: jiang@scripps.edu

ABSTRACT (200 WORD LIMIT)

Filoviruses pose a significant threat to human health due to frequent outbreaks and high mortality. Although two vector-based vaccines are available for Ebola virus, a broadly protective filovirus vaccine remains elusive. Here, we evaluate a general strategy for stabilizing glycoprotein (GP) structures from Ebola, Sudan, and Bundibugyo orthoebolaviruses and Ravn orthomarburgvirus. A 3.2 Å crystal structure provides atomic-level details of the redesigned Ebola virus GP, while cryo-electron microscopy reveals how a pan-orthoebolavirus neutralizing antibody targets a conserved site on the stabilized Sudan virus GP (3.13 Å resolution), along with a low-resolution model of antibody-bound Ravn virus GP. A self-assembling protein nanoparticle (SApNP), I3-01v9, is redesigned at the N terminus to enable optimal surface display of filovirus GP trimers. Following detailed in vitro characterization, we examine the lymph node dynamics of Sudan virus GP and GP-presenting SApNPs in mice. Compared with the soluble trimer, SApNPs exhibit ~112-fold longer retention in lymph node follicles, up to 28-fold greater presentation on follicular dendritic cell dendrites, and up to 3-fold stronger germinal center reactions. Functional antibody responses induced by filovirus GP trimers and SApNPs bearing wild-type and modified glycans are assessed in mice. This study provides a foundation for next-generation filovirus vaccine development.

ONE-SENTENCE SUMMARY

Filovirus glycoproteins and nanoparticles were rationally designed and characterized in vitro and in vivo to aid filovirus vaccine development.

41 **INTRODUCTION**

42 The first documented case of human filovirus infection occurred in 1967 in Marburg and Frankfurt,
43 Germany, when laboratory workers were infected with Marburg virus (MARV) by non-human
44 primates (NHPs) imported from Africa (*1*). The largest filovirus outbreak on record was caused
45 by Ebola virus (EBOV), first identified in 1976 in Zaire, Central Africa (*2, 3*). The 2013–2016
46 EBOV epidemic resulted in approximately 28,600 cases and 11,325 deaths (*4*). Both MARV and
47 EBOV cause viral hemorrhagic fever (VHF) in humans, with case fatality rates of up to 90% (*5,*
48 *6*). Filoviruses are classified into nine genera, of which *Orthoebolavirus* and *Orthomarburgvirus*
49 are the most clinically relevant *(7-9)*. *Orthoebolavirus* includes pathogenic species such as EBOV,
50 Bundibugyo virus (BDBV), and Sudan virus (SUDV), as well as other species that are either non-
51 pathogenic or rarely infect humans. *Orthomarburgvirus* comprises a single species containing two
52 members: MARV and Ravn virus (RAVV). The single-stranded, negative-sense RNA genome of
53 filoviruses encodes structural proteins, including nucleoprotein, virion proteins, glycoprotein
54 (GP), and RNA polymerase. As a class I viral fusion protein (*10-13*), GP functions as a trimer of
55 heterodimers, mediating host cell attachment, membrane fusion, and viral entry (*14*). GP is
56 recognized by the host immune system during natural infection (*15-17*) and represents the primary
57 target for the development of prophylactic vaccines and antibody therapeutics (*18-21*).

58 Substantial progress has been made in filovirus research (*22*). First, our understanding of
59 filovirus pathogenesis and infection mechanisms has advanced considerably (*23-25*). Niemann-
60 Pick C1 (NPC1) was identified as the endosomal receptor for filovirus entry, indicating that NPC1
61 inhibitors may have antiviral potential (*26-28*). Second, neutralizing antibodies (NAbs) have been
62 established as effective therapeutics for treating filovirus infections (*29-32*). Compared to the
63 monoclonal antibody (mAb) cocktail ZMapp (*33*), which initially showed promise (*34*), REGN-

64 EB3 (a three-mAb cocktail (*35*)) and mAb114 (*36*) demonstrated superior efficacy against EBOV
65 in a randomized controlled trial (*37*). The 2013–2016 EBOV outbreak led to sustained efforts to
66 identify anti-filovirus antibodies (*38*). Panels of mAbs were isolated from human survivors and
67 immunized animals, revealing multiple sites of vulnerability on GP (*16, 17, 36, 39-54*). At the
68 peak of this effort, the Viral Hemorrhagic Fever Immunotherapeutic Consortium analyzed 171
69 mAbs targeting diverse epitopes on GP, including the base, glycan cap, fusion loop, GP1/core,
70 GP1/head, GP1/2 interface, heptad repeat 2 (HR2), and mucin-like domain (MLD) (*55*). Third, X-
71 ray crystallography and cryo-electron microscopy (cryo-EM) have determined atomic structures
72 of filovirus GP bound to NPC1 (*28*), small-molecule ligands (*56-58*), and mAbs (*16, 39, 40, 42,*
73 *43, 47, 49-52, 59, 60*). Notably, negative-stain EM (nsEM) remains an effective tool for validating
74 GP conformation and mapping mAb epitopes (*17, 41, 46-48, 53-55*). These structural insights have
75 advanced our understanding of filovirus neutralization and supported the development of antibody
76 therapeutics and vaccines (*18, 61, 62*). Fourth, two viral vector-based EBOV vaccines have been
77 approved for human use. ERVEBO (*63*) is a single-dose vaccine based on recombinant vesicular
78 stomatitis virus (rVSV) expressing EBOV GP, whereas Zabdeno/Mvabea (*64*) delivers two doses
79 – an Adenovirus 26 (Ad26) vector encoding EBOV GP followed by a modified Vaccinia Ankara
80 (MVA) vector expressing multiple filovirus GPs. Additional EBOV vaccines using DNA (*65*) and
81 viral vectors (*66-71*) have been tested in humans. Recent efforts have expanded to mRNA, protein
82 subunit, and nanoparticle (NP) platforms (*72-75*).

83 Despite this progress, critical innovations are still needed to advance next-generation
84 filovirus vaccines (*76*). Although correlates of protection remain undefined (*77*), in-depth B cell
85 analysis revealed diverse yet convergent polyclonal NAb responses in a Phase 1 trial of the rVSV-
86 ZEBOV vaccine (*78*). A follow-up study elucidated how NAbs from multiple individuals used the

87 same germline genes to target the receptor-binding site (RBS) on GP (*79*), reinforcing the central
88 role of GP as the primary vaccine antigen. Over the past decade, antibody-guided, structure-based
89 antigen design has transformed vaccine development for important targets such as HIV-1 (*80-83*)
90 and respiratory syncytial virus (RSV) (*84*). Rational design strategies have been applied to stabilize
91 the HIV-1 envelope (Env) (*85-87*), the RSV fusion (F) protein (*88-91*), and, more recently, the
92 SARS-CoV-2 spike (*92, 93*) in their prefusion conformations. Many of these constructs have
93 progressed from preclinical testing to human trials (*94, 95*), with multiple COVID-19 vaccines
94 (*96, 97*) and three RSV vaccines now approved for human use (*98*). By contrast, only two studies
95 have reported rationally stabilized filovirus GP designs, both with limited in vivo evaluation (*99,*
96 *100*). Most recently, Xu et al. proposed an immunofocusing approach by engineering additional
97 N-linked glycans onto GP (*74*). Notably, nearly all current filovirus vaccine candidates (*101*) rely
98 on wild-type GP, which contains a highly variable MLD that shields conserved NAb epitopes and
99 facilitates immune evasion (*102, 103*). A mucin-deleted GP (GPΔmuc) could, in principle, elicit
100 NAbs more effectively than wild-type GP, but it has yet to be evaluated in humans. In addition to
101 antigen format, the choice of delivery platform may also influence vaccine-induced immunity.
102 Although viral vectors remain prominent, as reflected in the licensure of two EBOV vaccines,
103 mRNA platforms represent a compelling alternative given their success during the COVID-19
104 pandemic (*104, 105*). In the realm of protein-based vaccines, NPs have emerged as a promising
105 platform due to their virus-like size, multivalent surface display, and ability to elicit strong and
106 durable NAb responses (*106-111*). Although two EBOV GP-presenting NP vaccines have recently
107 been reported (*74, 100*), neither has been evaluated in animal challenge models. Finally, glycan
108 modification may be a key strategy for optimizing filovirus vaccine antigens. Glycan trimming has
109 improved NAb responses in vaccine candidates targeting influenza hemagglutinin (HA), SARS-

110 CoV-2 spike, and HIV-1 Env (*112-115*). Whether this approach applies to filovirus GP, which is
111 covered with up to 17 surface glycans per protomer, remains to be determined.

112 In our previous study, we stabilized EBOV GP with mutations in the $HR1_C$ bend and HR2
113 stalk and displayed one of two lead designs, termed GPΔmuc-WL^2P^2, on self-assembling protein
114 nanoparticles (SApNPs) as EBOV vaccine candidates (*100*). Here, we first extended the GPΔmuc-
115 WL^2P^2 and WL^2P^4 construct designs from EBOV to SUDV and BDBV and determined a crystal
116 structure of EBOV GPΔmuc-WL^2P^4 at 3.2 Å resolution. We also obtained a 3.13 Å cryo-EM
117 reconstruction of SUDV GPΔmuc-WL^2P^4 bound to the CA45 Fab (*47*). The nearly identical
118 backbones of SUDV and EBOV GPΔmuc-WL^2P^4 demonstrate a broadly applicable strategy for
119 stabilizing orthoebolavirus GPs. We next displayed EBOV, SUDV, and BDBV GPΔmuc-WL^2P^4
120 trimers on SApNPs derived from E2p and I3-01v9, the latter of which was computationally
121 redesigned at the N terminus. A similar design approach was applied to RAVV GP, resulting in a
122 promising trimer construct termed GPΔmuc-P^2CT. We then examined the lymph node delivery
123 and immunological responses of SUDV GPΔmuc-WL^2P^4 trimer and SApNPs at the tissue, cellular,
124 and subcellular levels in a mouse model. Compared to soluble trimers, 60-meric SApNPs exhibited
125 prolonged retention and sustained presentation on follicular dendritic cell (FDC) dendrites, along
126 with more robust and durable germinal center (GC) reactions in lymph node follicles. Finally, we
127 immunized mice with a panel of filovirus GP vaccines to assess antibody responses. While the
128 EBOV and SUDV GPΔmuc-WL^2P^4 trimer and SApNP vaccines elicited serum neutralization
129 limited to orthoebolaviruses, the RAVV GPΔmuc-P^2CT trimer induced detectable cross-genus
130 NAb responses. Both multivalent display and glycan modification influenced the immunogenicity
131 of GP-based filovirus vaccines. Although no universal glycan modification strategy may apply to
132 all viral GPs, enriching the GP glycan shield with oligomannose-type glycans improved filovirus

133 vaccine-induced NAb responses in mice. Together, these findings provide a foundation for
134 developing broadly effective vaccines to combat future filovirus outbreaks.

135 **RESULTS**

136 **A universal design strategy for orthoebolavirus GP stabilization**

137 GPs within the *Orthoebolavirus* genus share a high degree of sequence and structural similarity
138 (*59, 116*). These viral GPs consist of conserved functional domains, including GP1, MLD, internal
139 fusion loop (IFL), and GP2, which contains heptad repeat 1 (HR1), heptad repeat 2 (HR2), and the
140 transmembrane domain (TMD). Previously, we stabilized EBOV GPΔmuc by introducing a T577P
141 (P^2) or L579P (P^4) mutation in the $HR1_C$ bend, a W615L mutation in the neck region of the HR2
142 stalk, and a C-terminal extension in HR2 (D632–D637) (*100*) (**Fig. 1a**). A foldon trimerization
143 motif was appended to the C terminus of HR2. These modifications enhanced the structural and
144 thermal stability of EBOV GPΔmuc trimers compared with wild-type GP.

145 Here, we applied the same design principles to SUDV and BDBV GPs and characterized
146 two constructs, GPΔmuc-WL^2P^2 and GPΔmuc-WL^2P^4, across all three orthoebolaviruses (**Fig.**
147 **S1a**). Following our previous protocol (*100*), all six GPΔmuc constructs were transiently expressed
148 in HEK293F cells and purified using two methods. In addition to immobilized nickel affinity
149 chromatography, pan-orthoebolavirus NAbs ADI-15878 (*117*) and CA45 (*118*), expressed in
150 immunoglobulin G (IgG) form in ExpiCHO cells, were used to prepare immunoaffinity
151 chromatography (IAC) columns. The IAC method was established in our prior study, where
152 mAb100 and mAb114 (*36*) columns were used to purify EBOV GP trimers and SApNPs (*100*).
153 The IAC- or nickel-purified orthoebolavirus GP samples were then characterized by size-exclusion
154 chromatography (SEC) on a Superdex 200 column following ADI-15878 (**Fig. 1b)** and CA45 (**Fig.**
155 **S1b**) purification. All SEC profiles displayed an aggregation peak around 8.0 ml and a consistent

156 trimer peak at ~11.0 ml, with minimal evidence of dimer or monomer species. Compared to IAC,
157 nickel purification resulted in higher aggregation for EBOV and SUDV GPs (**Fig. S1b**). Of the
158 two broadly neutralizing antibodies (bNAbs) tested, ADI-15878 captured orthoebolavirus GPs
159 more efficiently than CA45, as indicated by stronger ultraviolet absorbance at 280 nm (UV_{280}) in
160 the elution fractions (**Fig. 1b** and **S1b**). These results support the use of ADI-15878 as a universal
161 affinity ligand for tag-free purification of orthoebolavirus GP immunogens. Blue native
162 polyacrylamide gel electrophoresis (BN-PAGE) confirmed that SEC fractions eluting at ~11 ml
163 corresponded to GPΔmuc trimers, with bands consistent with theoretical molecular weights (**Fig.
164 1c**). Thermostability was assessed by differential scanning calorimetry (DSC). For EBOV, the
165 GPΔmuc-WL^2P^2 trimer showed two melting temperatures at 60.9 ºC (T_{m1}) and 67.7 ºC (T_{m2}),
166 whereas GPΔmuc-WL^2P^4 had a single, broadened melting peak at 64.4 ºC (**Fig. 1d**), consistent
167 with our previous findings (*100*). In contrast, all four SUDV and BDBV GPΔmuc trimers
168 generated similar DSC curves with a single denaturing state and tightly clustered T_m values (62.9–
169 63.6 ºC). Among the three orthoebolaviruses, SUDV GPΔmuc exhibited the highest onset
170 temperatures (T_{onset}, 54.8 ºC and 56.0 ºC), followed by EBOV and BDBV GP constructs (50.1–
171 54.2 ºC). Based on these biochemical and biophysical profiles, GPΔmuc-WL^2P^4 was selected as
172 the lead design candidate for pan-orthoebolavirus GP stabilization.

173 The HIV-1 Env spike employs a glycan shield as a primary defense mechanism to evade
174 host NAb responses (*113*). Similarly, orthoebolavirus GPs contain a glycan cap that shields the
175 receptor binding site (RBS) (*100*), along with a heavily glycosylated MLD, which is removed in
176 GPΔmuc constructs. These glycans play a critical role in both immune evasion and modulating
177 antibody interactions with GP. To generate site-specific glycosylation profiles, the purified EBOV,
178 SUDV, and BDBV GPΔmuc-WL^2P^4 proteins were digested with trypsin, chymotrypsin, and α-

179 lytic protease to produce glycopeptides, each containing a single N-linked glycan site. Site-specific
180 composition and occupancy were analyzed by liquid chromatography-mass spectrometry (LC-
181 MS), as previously described (*113*). All glycosylation sites on the three orthoebolavirus GPΔmuc-
182 WL^2P^4 proteins predominantly carried complex-type glycans, except at positions N563 and N257,
183 where mixed glycan forms were detected. At N563, ~30% of glycans were oligomannose-type for
184 EBOV, compared to ~60% for both SUDV and BDBV. At N257, ~15% oligomannose-type
185 glycans were observed for EBOV (**Fig. 1e** and **Fig. S1c**). Due to technical limitations, glycan
186 compositions could not be assessed accurately at all sites.

187 Negative-stain EM (nsEM) was used to characterize orthoebolavirus GPΔmuc-WL^2P^4
188 structures, either alone or bound to bNAb ADI-15878 (**Fig. S1d**). For EBOV and BDBV, crystal
189 structures of wild-type GPΔmuc in complex with ADI-15878 (Protein Data Bank [PDB] IDs: 7JPH
190 (*100*), 6EA7, and 6EA5 (*116*)) were fitted into three-dimensional (3D) EM reconstructions. For
191 SUDV, the GPΔmuc and ADI-15878 structures from two separate complexes (PDB IDs: 3S88 (*59*)
192 and 6DZM (*117*)) were fitted individually (**Fig. 1f** and **Figs. S1e-g**). Overall, the low-resolution
193 nsEM models of three orthoebolavirus GPΔmuc trimers displayed a three-lobed chalice shape
194 consistent with the native-like structure, although the HR2 stalk was unresolved. The ADI-15878-
195 bound nsEM models were highly similar across all three species, revealing an epitope that spans
196 two GP protomers and overlaps the conserved regions of the IFL and HR1 in GP2 (*48, 117*).

197 The antigenicity of six stabilized orthoebolavirus GPΔmuc trimers was assessed using four
198 pan-orthoebolavirus bNAbs – CA45 (*47*), ADI-15878, ADI-15946 (*119*), and BDBV-289 (*52*) –
199 alongside MR78, a MARV-specific NAb (*40*). In enzyme-linked immunosorbent assays (ELISA),
200 the proline mutation in HR1c (P^2 or P^4) had no effect on antibody binding (**Fig. 1g** and **Fig. S1h**).
201 Among the four bNAbs, ADI-15946 and BDBV-289 showed the lowest binding affinity for SUDV

202 GPΔmuc trimers, 2.5- to 6-fold weaker than those for EBOV and BDBV GPΔmuc trimers, as
203 indicated by the half-maximal effective concentration (EC_{50}) values. The NHP-derived bNAb
204 CA45 exhibited 1.5- to 2.5-fold stronger binding to EBOV GPΔmuc than to its SUDV and BDBV
205 counterparts. As expected, the negative control MR78 showed no detectable binding to any of the
206 GPΔmuc trimers from the *Orthoebolavirus* genus. These findings were confirmed by biolayer
207 interferometry (BLI) (**Fig. 1h** and **Fig. S1i**). Among the six orthoebolavirus antigens tested, CA45
208 bound most strongly to EBOV GPΔmuc, whereas ADI-15946 and BDBV-289 interacted least
209 favorably with SUDV GPΔmuc. Consistent with ELISA, BLI revealed negligible or no binding
210 between orthoebolavirus GPΔmuc trimers and MARV-specific NAb MR78.

211 **Structural characterization of rationally designed orthoebolavirus GPΔmuc trimers**

212 Previously, we determined the crystal structure of EBOV GPΔmuc-WL^2P^2 (*100*). Here, we sought
213 to obtain atomic details for the more stable EBOV GPΔmuc-WL^2P^4. To this end, EBOV GPΔmuc-
214 WL^2P^4 was transiently expressed in HEK293S cells and purified by IAC (mAb100) and SEC, as
215 previously described (*100*) (**Fig. S2a**). Crystallization under conditions similar to those used for
216 GPΔmuc-WL^2P^2 resulted in comparable packing in the P321 space group (**Table S1**). The final
217 structure was resolved at 3.2 Å. Each asymmetric unit contained one GP protomer, with the glycan
218 cap atop GP1 and the belt-forming IFL of GP2 clearly visible in the electron density (**Fig. 2a**).
219 Three GP1-GP2 heterodimers assembled into a chalice-shaped trimer in the crystal lattice, with
220 the GP2 subunits forming a base that cradles the outward-facing GP1 lobes (**Fig. S2b**). Four N-
221 linked glycans (N228, N257, N563, and N618) were identified in the structure. The most complete
222 carbohydrate chain was observed at N563 (with $Man_4GlcNAc_2$ density), part of the ADI-15878
223 epitope in HR1a (*116*), whereas only a single *N*-acetylglucosamine (GlcNAc) was visible at the
224 other three sites. The backbone of GPΔmuc-WL^2P^4 closely resembled that of GPΔmuc-WL^2P^2,

225 with a global Cα root-mean-square deviation (RMSD) of 0.48 Å across 243 aligned Cα atoms and
226 a local Cα-RMSD of 0.68 Å for the HR1c bend following protomer superposition (**Fig. 2a** and
227 **Fig. S2c**). In GPΔmuc-WL^2P^4, the amine group of the K95 side chain formed hydrogen bonds with
228 the backbone carbonyls of L573 and T576 (~3.0 Å) – interactions absent in GPΔmuc-WL^2P^2.
229 These interprotomer hydrogen bonds at the trimer center likely contributed to the enhanced
230 thermostability of GPΔmuc-WL^2P^4. Similar interactions were observed in the EBOV GPΔmuc-
231 WL^2 structure (PDB ID: 7JPI), where K95 formed hydrogen bonds with L573 and T576 at 2.7 and
232 2.9 Å, respectively. This structural analysis is consistent with the DSC data, in which EBOV
233 GPΔmuc-WL^2P^4 exhibited a single denaturation transition with a T_m of 64.4°C (*100*).

234 Cryo-EM plays an important role in understanding how viral GPs interact with antibodies
235 (*120-122*). Several cryo-EM models have been reported for EBOV and BDBV GPs (*43, 52, 117*),
236 but only two crystal structures (*59, 123*) and no cryo-EM models are currently available for SUDV
237 GP. Here, we determined a cryo-EM structure of SUDV GPΔmuc-WL^2P^4 in complex with the
238 CA45 Fab. SUDV GP was transiently expressed in HEK293F cells and purified using an ADI-
239 15878 IAC column, prior to complexation with CA45 Fab and SEC on a Superose 6 16/600 GL
240 column (**Fig. S2d**). The complex fraction at ~72 ml was imaged on a Krios G4 transmission
241 electron microscope (TEM), with data processed in CryoSPARC (*124*) (**Fig. S2e**). A resolution of
242 3.13 Å with an EMRinger score of 2.60 (*125*) was obtained for the final reconstruction, in which
243 the SUDV GPΔmuc-WL2P4 trimer flanked by three CA45 Fabs was well resolved in the density
244 map (**Fig. 2b**). Three regions – GP1 (A187-L218), GP2 (E522-N525), and C-terminal stalk (P612-
245 N637) – were excluded from the final model due to limited local resolution (**Fig. S2f**). The glycan
246 cap and GP2 stalk became partially visible when the density threshold was lowered beyond 4.0 Å
247 (**Fig. S2e**). Crystal structures of EBOV GPΔmuc-WL^2P^2 (PDB ID: 7JPH) (*100*) and CA45 variable

248 domains (PDB ID: 6EAY) (*118*) were used as starting models for EM fitting, followed by manual
249 refinement. The final SUDV GPΔmuc-WL^{2}P^4 model, lacking the glycan cap and GP2 stalk, was
250 superimposed onto the EBOV GPΔmuc-WL^{2}P^4 crystal structure, yielding a Cα-RMSD of 0.66 Å
251 for 154 matching Cα atoms (**Fig. S2g**, left). The three HR1$_C$ bends of SUDV GPΔmuc-WL^{2}P^4
252 were also superimposed onto those of EBOV GPΔmuc-WL^{2}P^4 from this study and BDBV
253 GPΔmuc (PDB ID: 7KFE) (*52*), with Cα-RMSDs of 0.34 and 0.53 Å for the 24 aligned Cα atoms,
254 respectively (**Fig. 2c**, right). Compared with the crystal structure of the EBOV GPΔmuc/CA45
255 complex (PDB ID: 6EAY) (*118*), cryo-EM revealed a highly similar antibody epitope in the SUDV
256 GPΔmuc-WL^{2}P^4/CA45 complex, with a Cα-RMSD of 0.69 Å for 147 aligned Cα atoms after
257 superposition of a single GP/CA45 component from each complex (**Fig. S2g**, right). Specifically,
258 the CA45-GP2 interface was stabilized by a backbone hydrogen bond between CA45 HC-Y32 and
259 GP2-E545 (~3.0 Å), a side chain hydrogen bond between the CA45 HC-Y33 carboxyl group and
260 the GP2-H516 imidazole ring (~3.4 Å), and additional hydrogen bonds involving the CA45 LC-
261 Y49 and LC-N53 side chains with the GP2-N550 backbone (~3.3 Å and ~3.8 Å, respectively), as
262 well as the CA45 LC-S56 backbone with the GP2-N514 side chain (~2.9 Å) (**Fig. 2c**). Although
263 interpretation of these interactions may be limited by the cryo-EM resolution, similar contacts were
264 observed in the 3.7 Å-resolution crystal structure of the EBOV GPΔmuc/CA45 complex (PDB ID:
265 6EAY) (**Fig. S2h**) (*118*), including those between CA45 HC-Y32 and GP2-E545 (~3.2 Å), CA45
266 HC-D101 and GP2-H549 (~3.9 Å), and the same CA45 LC-GP2 residue pairs with nearly identical
267 distances. Snapshots of the cryo-EM density at the GP-CA45 interface were inspected fragment
268 by fragment for anisotropy, demonstrating that the modeled side chain contacts are supported by
269 well-defined density (**Fig. S2i and S2j**). Furthermore, we compared our SUDV GPΔmuc-
270 WL^{2}P^4/CA45 complex with previously reported cryo-EM models of EBOV GPΔmuc bound to

271 ADI-15878 (PDB ID: 6DZL and EMD-8935 (*117*)) (**Fig. S2k**), rEBOV-515 and rEBOV-442
272 (PDB ID: 7M8L and EMD-23719 (*126*)) (**Fig. S2l**), and rEBOV-520 and rEBOV-548 (PDB ID:
273 6PCI and EMD-20301 (*50*)) (**Fig. S2m**), demonstrating comparable model quality.

274 **Rational design and characterization of orthoebolavirus GPΔmuc-presenting nanoparticles**

275 In our previous EBOV study, a 10GS linker was used to connect GPΔmuc to the N-termini of I3-
276 01v9, which formed a triangle of 55.0 Å (*100*). This SApNP exhibited variability in yield, purity,
277 and stability, suggesting that further optimization might be necessary (*100*). In a more recent study,
278 we redesigned the I3-01v9 SApNP to display monomeric antigens (*127*). The resulting I3-01v9a
279 scaffold featured a smaller triangle of 43.9 Å between the N-termini (**Fig. 3a**, left). Here, using I3-
280 01v9a as a template, we aimed to improve the design of an I3-01v9 scaffold optimized for surface
281 display of filovirus GP trimers, which contain a narrow stalk. After removing the first 4 amino
282 acids (aa) of I3-01v9a, we fused a 9-aa helix to the truncated I3-01v9a *N*-terminal helix via a 4-aa
283 turn. The resulting model was computationally optimized – first in structure and then in sequence
284 – to generate two I3-01v9 variants, termed I3-01v9b and I3-01v9c (**Fig. S3a**), in which the N-
285 termini form a triangle of 12.9 Å (**Fig. 3a**, right). The trimeric forms of I3-01v9b/c, termed I3-
286 01v9b/c-T, were generated by interrupting the particle-forming interface based on the structure of
287 the aldolase (PDB ID: 1VLW), from which I3-01 was derived. Two "scaffolded" EBOV GP
288 constructs, termed GPΔmuc-WL^{2}P^4-I3-01v9b-T and GPΔmuc-WL^{2}P^4-I3-01v9c-T, were designed
289 to test whether the I3-01v9b/c N-termini could accommodate the GP2 stalk (**Fig. S3b**). Both
290 constructs were transiently expressed in HEK293S cells, purified using a mAb100 column, and
291 analyzed by SEC (**Fig. S3c**). The trimer fractions were validated by BN-PAGE (**Fig. S3d**) prior to
292 nsEM analysis, which yielded two-dimensional (2D) classes consistent with native-like GPΔmuc-
293 WL^{2}P^4 trimers anchored to I3-01v9b/c-T (**Figs. S3e** and **S3f**). The GP2 stalk, although not visible

294 by EM, was likely well-formed, as the GPΔmuc trimer displayed the classic chalice shape (**Fig.**
295 **3b** and **Fig. S3g**). Computational modeling suggested that EBOV GPΔmuc-WL^{2}P^4-I3-01v9b
296 would form a particle with a diameter of 49.1 nm, measured at GP1-T269 (**Fig. 3c**).

297 Six SApNP constructs – displaying EBOV, SUDV, and BDBV GPΔmuc-WL^{2}P^4 trimers
298 on the E2p and I3-01v9b scaffolds (**Fig. S3h**) – were transiently expressed in ExpiCHO cells and
299 purified by IAC using an ADI-15878 column, followed by SEC on a Superose 6 increase 10/300
300 GL SEC column. All constructs exhibited a peak at ~8.7 ml, corresponding to assembled protein
301 particles (**Fig. 3d**). For EBOV and BDBV, higher yields were observed for the E2p SApNPs,
302 whereas for SUDV, 3-01v9b produced a more prominent particle peak in the SEC profile. The
303 structural integrity of these SApNPs was validated by nsEM (**Fig. 3e**). Most micrographs showed
304 well-formed protein particles displaying arrays of GP trimers on the outer surface. Particle size
305 distributions were analyzed in solution by dynamic light scattering (DLS) (**Fig. 3f**). For EBOV
306 SApNPs, E2p and I3-01v9b exhibited sizes of 55.7 nm and 84.0 nm, respectively (**Fig. 3f**). The
307 unusually large DLS size for I3-01v9b may reflect SApNP aggregation, although this form was
308 rarely observed by EM. For SUDV and BDBV SApNPs, particle sizes ranged from 61.1 to 71.9
309 nm and from 51.3 to 53.8 nm, respectively. This variation may be attributed to the intrinsic
310 structural flexibility of the glycan cap that likely affects the hydrodynamic radius measured by
311 DLS. Site-specific glycosylation profiles were generated for SUDV GPΔmuc-presenting SApNPs
312 (**Fig. 3g** and **Fig. S3i**). An increase in oligomannose-type glycans was observed on SApNPs
313 compared to soluble trimers. At site N563, both the soluble GPΔmuc trimer and SApNPs presented
314 predominantly oligomannose-type glycans (**Fig. 3g**).

315 The antigenicity of orthoebolavirus GPΔmuc-WL^{2}P^4-presenting SApNPs was assessed
316 against the same antibody panel. In ELISA, SApNPs exhibited broadly similar antibody-binding

317 patterns to the corresponding soluble trimers (**Fig. 3h** and **Fig. S3j**). For example, SUDV SApNPs
318 bound less favorably to ADI-15946 and BDBV-289 than EBOV and BDBV SApNPs, with 5.0- to
319 16.8-fold higher EC_{50} values. Between the two NP scaffolds, E2p outperformed I3-01v9b, showing
320 1.4- to 1.9-fold lower EC_{50} values for both bNAbs. A similar trend was observed in SUDV SApNP
321 binding to CA45, with a 2.5-fold difference in EC_{50} between the two NP platforms. Interestingly,
322 the opposite pattern was seen for EBOV and BDBV SApNPs, where I3-01v9b bound more tightly
323 than E2p. BLI revealed a somewhat different antigenic profile (**Fig. 3i** and **Fig. S3k**). Most notably,
324 SUDV and BDBV SApNPs exhibited stronger binding signals to ADI-15878 and ADI-15946 than
325 EBOV SApNPs, whereas SUDV SApNPs showed the weakest binding to BDBV-289 among the
326 three orthoebolaviruses. For each GP antigen, binding signals to individual bNAbs were generally
327 similar between E2p and I3-01v9b, except in the cases of SUDV SApNPs with CA45 and BDBV
328 SApNPs with CA45 and BDBV-289, where scaffold-dependent differences were apparent.

329 In this study, we displayed the stabilized GPΔmuc-WL^2P^4 trimer on two SApNP scaffolds,
330 E2p and the newly designed I3-01v9b, for three representative orthoebolaviruses. SEC, nsEM, and
331 DLS were used to assess particle properties, which were largely comparable to those of our
332 previously reported HIV-1 Env trimer-presenting SApNPs (*113*). However, site-specific glycan
333 analysis and antigenic profiling revealed distinct features unique to the SApNP platform, including
334 an increased proportion of oligomannose-type glycans.

335 **In vitro effect of glycan modification on orthoebolavirus GPΔmuc trimers and SApNPs**

336 Previously, we investigated the effect of glycan modification on rationally designed HIV-1 Env
337 trimer and SApNP vaccines (*113*). Supplementing ExpiCHO cultures with kifunensine (Kif) – a
338 class I α-mannosidase inhibitor that blocks ER glycan processing and leads to accumulation of
339 high mannose – did not affect NAb responses. In contrast, glycan trimming with endoglycosidase

340 H (Endo H) significantly enhanced NAb elicitation, as reflected by a higher vaccine responder rate
341 (*113*). The benefit of glycan trimming has also been reported for influenza HA and SARS-CoV-2
342 spike vaccines (*112, 114*). These findings highlight the importance of examining how glycan
343 modification may affect filovirus vaccines in vivo. However, the glycan-modified filovirus GP
344 immunogens first needed to be generated and characterized in vitro.

345 Here, we adopted a similar strategy (*113*) to produce orthoebolavirus GPΔmuc trimers
346 carrying either oligomannose-only glycans or a single layer of mono-*N*-acetylglucosamine (mono-
347 GlcNAc) glycans. EBOV and SUDV GPΔmuc-WL^{2}P^4 were transiently expressed in HEK293F
348 cells in the presence of Kif, which yielded oligomannose-only glycans, and were purified using an
349 ADI-15878 column followed by SEC. The SEC profiles showed a trimer peak at ~10.7 ml, similar
350 to wild-type trimers (**Fig. 4a**). SEC-purified, Kif-treated GPΔmuc (e.g., 1 mg) was then treated
351 with Endo H (termed Kif/Endo H) to reduce the glycan shield to mono-GlcNAc stumps, with the
352 enzyme subsequently removed by SEC. The resulting profiles showed a trimer peak at ~11.1 ml
353 and an Endo H peak at ~13.9 ml (**Fig. 4a**). Sodium dodecyl sulfate (SDS)-PAGE and BN-PAGE
354 confirmed that Kif/Endo H-treated GPΔmuc had a lower molecular weight than both wild-type
355 and Kif-treated GPΔmuc (**Fig. S4a**). DSC revealed a differential effect of glycan modification on
356 GPΔmuc thermostability (**Fig. 4b**). The Kif-treated EBOV GPΔmuc-WL^{2}P^4 trimer exhibited two
357 denaturation states, with T_{m1} at 58.2 ºC and T_{m2} at 64.3 ºC. Endo H treatment further reduced T_{m1}
358 and T_{m2} by 5.2 ºC and 2.6 ºC, respectively. In contrast, the Kif-treated SUDV GPΔmuc-WL^{2}P^4
359 trimer remained thermostable, displaying the same T_m (63.6 ºC) as the wild-type trimer, with T_{onset}
360 measured at 54.7 ºC. Endo H treatment slightly reduced the T_m to 62.6 ºC and lowered the T_{onset} to
361 48.9 ºC. Antigenicity was assessed using the same antibody panel. In the ELISA (**Fig. 4c and Fig.
362 S4b**), Endo H treatment enhanced trimer binding to CA45, ADI-15878, and ADI-15946, which

363 recognize a quaternary epitope near the trimer base with few glycan contacts, but reduced binding
364 to BDBV-289, which targets the glycan cap and relies on glycans at N238 and N268. However,
365 the EC_{50} differences were small (1.5- to 1.9-fold) and not specific to either orthoebolavirus. In the
366 BLI analysis, glycan-modified trimers generated slightly higher binding signals than wild-type
367 trimers (**Fig. 4d** and **Fig. S4c**). Overall, glycan modification had only a modest impact on the
368 biochemical, biophysical, and antigenic properties of stabilized orthoebolavirus GPΔmuc trimers,
369 except for thermostability in the EBOV constructs.

370 We next characterized glycan-modified GPΔmuc-WL^2P^4-presenting SApNPs. For SUDV,
371 both E2p and I3-01v9 SApNPs were included in this analysis, whereas for EBOV, only the E2p
372 scaffold was tested due to the low yield of I3-01v9b SApNPs. Notably, an N655D mutation was
373 introduced to eliminate an N-glycan site at the base of the SUDV GP2 stalk that may interfere with
374 SApNP assembly. This design variant, termed SUDV GPΔmuc-WL^2P^4-PD, will be used hereafter
375 (**Fig. S4d**). EBOV and SUDV SApNPs were transiently expressed in ExpiCHO cells with Kif and
376 purified by IAC (ADI-15878) followed by SEC. SEC-purified, Kif-treated SApNP was trimmed
377 with Endo H and further purified by SEC. The resulting SEC profiles showed a main peak at ~8.5-
378 9.0 ml corresponding to SApNPs, and following Endo H treatment, an additional peak at ~16.8 ml
379 corresponding to the enzyme (**Fig. 4e**). The structural integrity of glycan-modified EBOV and
380 SUDV GPΔmuc-presenting SApNPs was validated by nsEM (**Fig. 4e**). SDS-PAGE confirmed that
381 Kif/Endo H-treated SApNPs had a lower molecular weight than Kif-treated SApNPs (**Fig. S4e**).
382 Because of the low yield of EBOV SApNPs, only SUDV SApNPs were subjected to glycan
383 profiling and antigenic characterization. Site-specific glycan profiles confirmed that all complex
384 glycans in SUDV GPΔmuc were replaced by oligomannose-type glycans in the Kif-treated
385 material (**Fig. 4f** and **Fig. S4f**). As expected, the N655 glycan was absent in the N655D mutant

386 construct. In the ELISA (**Fig. 4g** and **Fig. S4g**), the antigenic profiles of SApNPs appeared to be
387 largely consistent with those of the trimers, though a greater difference in EC_{50} values between Kif
388 and Kif/Endo H-treated samples (1.0- to 7.9-fold) was observed for CA45, ADI-15878, and ADI-
389 15946. In the BLI analysis, all pan-orthoebolavirus bNAbs showed increased binding signals to
390 Kif/Endo H-treated SApNPs, which displayed only a single layer of mono-GlcNAc stumps on the
391 GPΔmuc trimer (**Fig. 4h** and **Fig. S4h**). In summary, these results suggest that glycan trimming
392 enhances antibody access to conserved GP epitopes on the SApNP surface.

393 **Rational design of a prefusion-stabilized RAVV GPΔmuc trimer**

394 RAVV is one of the two known members of the *Orthomarburgvirus* genus in the filovirus family
395 (*40, 49*). Similar to orthoebolavirus GPs, RAVV GP contains GP1 with a heavily glycosylated
396 MLD and GP2 (**Fig. 5a**). Here, we applied a similar strategy to stabilize the prefusion RAVV GP
397 trimer, using a mucin-deleted construct (ΔN257-T425), termed GPΔmuc. Additional mutations –
398 T578P (P^2) or E580P (P^4) in the HR1c bend, and E631F/Q632V at the C terminus (termed CT) –
399 were also evaluated. The five RAVV GP constructs tested were: (1) GPΔTM (truncation at residue
400 637), (2) GPΔmuc, (3) GPΔmuc-P^2, (4) GPΔmuc-P^4, and (5) GPΔmuc-P^2CT, each containing a
401 C-terminal foldon motif and His_6 tag (**Fig. S5a**). All constructs were expressed in ExpiCHO cells
402 and purified using a nickel column followed by SEC. Both GPΔTM and GPΔmuc yielded low
403 expression levels with multiple GP species, including aggregates (~9-10 ml), trimers (~10.5 ml),
404 dimers (~13.6 ml), and monomers (~14.7 ml) (**Fig. 5b**). The P^2 mutation substantially improved
405 the SEC profiles of GPΔmuc constructs, producing a predominant trimer peak at ~10.5 ml, along
406 with visible dimer and monomer peaks. In contrast, the P^4 mutation resulted in significant
407 aggregation, indicated by a peak at ~8.6 ml (**Fig. S5b**). The GPΔmuc-P^2CT construct demonstrated
408 an optimal SEC profile, comparable in yield to GPΔmuc-P^2 but with reduced dimer and monomer

409 content. When MARV NAbs MR78 and MR191 (*49*) were used in IAC purification, they failed to
410 capture GPΔmuc-P^2 and GPΔmuc-P^2CT (**Fig. S5c**). Nevertheless, distinct trimer bands were
411 observed by SDS-PAGE after nickel/SEC purification (**Fig. 5c** and **Fig. S5d**). In DSC, GPΔmuc-
412 P^2 exhibited two melting transitions at 51.0 ºC and 60.0 ºC, while GPΔmuc-P^2CT displayed three
413 transitions at 54.5 ºC, 58.3 ºC, and 66.6 ºC (**Fig. 5d**). Although CT appeared to enhance trimer
414 thermostability, this double mutation introduced an additional unfolding intermediate.

415 The lead design, RAVV GPΔmuc-P^2CT, was complexed with MR78 for nsEM analysis
416 (**Fig. 5e** and **Fig. S5e**). We hypothesized that if the nsEM model, despite its low resolution,
417 matched the crystal structure (PDB ID: 5UQY) (*40*), it would validate our design and confirm
418 presentation of a conserved NAb epitope. Indeed, 2D class averages revealed well-formed RAVV
419 GPΔmuc/MR78 complexes, with the crystal structure fitting well into the nsEM density map (**Fig.
420 5e**, left). Notably, our model also aligned closely with a previously reported nsEM reconstruction
421 of the same complex (*42*) (**Fig. 5e**, right). Site-specific glycan analysis revealed distinct patterns
422 relative to orthoebolavirus GPs (**Fig. 5f** and **Fig. S5f**). Specifically, N-glycan sites N94, N171,
423 N219, and N564 carried primarily oligomannose-type glycans. In contrast, sites N190, N202, and
424 N487 presented either oligomannose- or complex-type glycans, while N475 and N619 were mostly
425 occupied by complex-type glycans. In ELISA (**Fig. 5g** and **Fig. S5g**), RAVV GPΔmuc-P^2 and
426 GPΔmuc-P^2CT trimers bound to MR78 and MR191 with similar EC_{50} values, consistent with the
427 BLI data (**Fig. 5h** and **Fig. S5h**). RAVV GPΔmuc-P^2CT was subsequently displayed on E2p and
428 I3-01v9b SApNPs and analyzed by nsEM following ExpiCHO expression and IAC purification
429 (**Fig. S5i**). However, well-formed protein particles were not observed in the micrographs. Taken
430 together, these findings support the use of RAVV GPΔmuc-P^2CT as a native-like, prefusion-

431 stabilized GP construct for orthomarburgvirus vaccine development, although further optimization
432 is needed for multivalent display on SApNPs.

433 **Distribution and retention of SUDV GPΔmuc trimers and SApNPs in lymph nodes**

434 In our previous studies, we observed a positive correlation between the thermostability of a viral
435 antigen (i.e., T_m) displayed on E2p or I3-01v9 SApNPs and the retention time of the resulting
436 SApNP vaccine antigens in lymph node follicles (*113, 127, 128*). Given the comparable T_m values
437 (~63-66 °C) of SUDV GPΔmuc and HIV-1 Env trimers, we anticipated that SUDV GPΔmuc-
438 presenting SApNPs would exhibit similar in vivo behavior. Following our previously established
439 protocol (*113, 127, 128*), we immunized mice with SUDV GPΔmuc-WL^2P^4 trimer and SApNPs
440 (including both E2p and I3-01v9b) to investigate their interaction with cellular components in
441 lymph nodes and analyze vaccine-induced immunological responses.

442 To induce a robust humoral response, vaccine antigens must be transported through the
443 lymphatic system, accumulate in lymph node follicles, and effectively engage B cell receptors
444 (BCRs) to stimulate B cell activation (*129-132*). We first examined the distribution of E2p and I3-
445 01v9b SApNPs in lymph nodes. SApNPs were administered intradermally to mice via footpads (4
446 footpads, 10 μg/footpad). The brachial and popliteal sentinel lymph nodes were isolated from both
447 sides of the body of the mouse 12 h after a single-dose injection for immunohistological studies.
448 Four NAbs – ADI-15878 (*116*), ADI-15946 (*119*), CA45 (*118*), and mAb100 (*133*) – were used
449 to stain lymph node sections for antigen detection (**Fig. S6a**). Overall, the immunostaining images
450 from CA45 exhibited the best signal-to-noise ratio. Based on these data, CA45 was selected to
451 study the distribution and trafficking of SUDV GPΔmuc vaccines in lymph nodes. Consistent with
452 our previous studies of SARS-CoV-2 spike (*128*), HIV-1 Env (*113*), and influenza M2ex3 (*127*)

453 SApNPs, SUDV GPΔmuc-presenting E2p and I3-01v9b SApNPs accumulated in the centers of
454 lymph node follicles (**Figs. 6a** and **6b**, images on the left; schematics on the right).

455 We next assessed the trafficking and retention patterns of SUDV GPΔmuc-WL^{2}P^4 trimer
456 and SApNPs in lymph node follicles over a period of 8 weeks following a single-dose injection (4
457 footpads, 10 μg/footpad) (**Fig. 6c**). Histological images showed that all SUDV immunogens were
458 transported into lymph nodes and accumulated in the subcapsular sinus within 2 h (**Fig. 6c**). While
459 the soluble trimer was transported into lymph node follicles within 2 h and completely cleared by
460 48 h, both E2p and I3-01v9b SApNPs appeared in follicles at 2 h, reached peak accumulation at
461 48 h, and were retained in follicles over the entire 8-week period (**Fig. 6c**). Next, the CA45-stained
462 area was quantified in a time-dependent manner, revealing a ~112-fold longer retention for E2p
463 and I3-01v9b SApNPs compared with the soluble trimer (**Figs. 6c** and **6d**). The area under the
464 curve (AUC) indicated that the exposure of SUDV GPΔmuc presented on the SApNP surface was
465 14-28 times higher than the same antigen in soluble trimer form (**Fig. 6e**). At 48 h, the two large
466 SApNPs displaying 20 GPΔmuc trimers also showed 19-33 times greater accumulation compared
467 with the soluble GPΔmuc trimer (**Fig. 6f**). These findings are consistent with our previous studies
468 (*113, 127, 128*), in which individual antigens were cleared from follicles within 48 h, whereas
469 large antigen-presenting SApNPs exhibited prolonged follicular retention lasting 2-8 weeks.
470 Notably, the retention time of SUDV GPΔmuc SApNPs fell within the same range as HIV-1 Env
471 and influenza M2ex3 SApNPs, all of which had T_m values of 62-66°C. Together, these data support
472 the conclusion that stabilized antigens with high thermostability (T_m > 62°C) result in prolonged
473 SApNP retention in lymph node follicles for at least 8 weeks.

474 FDCs are resident stromal cells that form a network structure in lymph node follicles and
475 play an essential role in antigen retention and presentation to stimulate B cell responses (*129-131,*

476 *134*). FDC networks retain soluble antigens, immune complexes, viruses, and bacteria on their
477 surfaces and dendrites to initiate and maintain GC responses (*135-137*). Our previous studies
478 demonstrated that FDC networks are the primary follicular components responsible for retaining
479 SARS-CoV-2 spike, HIV-1 Env, and influenza M2ex3 SApNPs (*113, 127, 128*). To test whether
480 this was also true for SUDV GPΔmuc SApNPs, we isolated sentinel lymph nodes at the peak of
481 antigen accumulation (48 h), as well as a series of timepoints (2 h to 8 weeks) after intradermal
482 injection (**Fig. 6g** and **Figs. S6b-g**). Lymph node sections were stained with the NAb CA45 (white)
483 (*118*) for SUDV GPΔmuc, anti-CD21 antibodies (green) for FDCs, and anti-CD169 antibodies
484 (red) for subcapsular sinus macrophages. To confirm the identity of FDC networks, co-staining
485 was performed using the more specific FDC marker, anti-FDC-M1. Immunofluorescence imaging
486 showed that SApNPs colocalized with FDC networks labeled by both CD21 and FDC-M1 at 48 h
487 post-injection (**Fig. 6g** and **Fig. S6h**), supporting the conclusion that FDC networks mediate the
488 accumulation and retention of SUDV GPΔmuc-presenting SApNP vaccines.

489 **Interaction of SUDV GPΔmuc SApNPs with FDCs and phagocytic cells in lymph nodes**

490 FDC networks form a reservoir in lymph node follicles for antigen sequestration, alignment, and
491 presentation to effectively crosslink BCRs, activate naive B cells, and stimulate GC reactions (*129-*
492 *131, 138*). Our previous TEM analysis showed that FDC networks retained SARS-CoV-2 spike
493 and HIV-1 Env SApNPs on their surfaces and dendrites through interactions with complement
494 protein 3 (C3) and complement receptor 2 (CR2) (*113, 128*). Here, we visualized the interface
495 between FDC dendrites and B cells to understand how FDC networks present SUDV GPΔmuc
496 SApNPs adjuvanted with aluminum phosphate (AP) to engage B cells. To this end, we injected
497 adjuvanted E2p and I3-01v9b SApNPs into the mouse hind footpads (2 footpads, 50 μg/footpad).
498 Fresh popliteal sentinel lymph nodes were isolated 2, 12, and 48 h after a single injection. The

499 lymph node tissues were sectioned and processed for TEM analysis. TEM images revealed the
500 expected, characteristic morphology of long FDC dendrites interacting with B cells in lymph node
501 follicles (**Figs. 7a-c**). Intact SApNPs (round-shaped granules, yellow arrows) were aligned on FDC
502 dendrites and B cell surfaces at all timepoints, and AP particles did not appear to colocalize with
503 SApNPs (**Figs. 7a-c** and **Fig. S7a-f**). These findings demonstrate FDC networks collect and
504 present vaccine antigens (i.e., SUDV GPΔmuc SApNPs) and use their long dendrites to maximize
505 interactions between antigens and BCRs. At the later timepoints (12 and 48 h), SUDV GPΔmuc
506 SApNPs were also found within endolysosomes of B cells (**Figs. S7c** and **e**).

507 Phagocytic cell populations, such as macrophages and dendritic cells, take up and process
508 vaccine antigens to facilitate adaptive immune responses (*132, 139, 140*). These innate immune
509 cells, located in the subcapsular sinus and medullary sinus of lymph nodes, can capture vaccine
510 antigens, transport them to migrating B cells, and eventually deposit them on FDCs through a
511 complement-dependent transport mechanism (*130, 131, 141-145*). In this study, we assessed the
512 interaction between phagocytic cells and AP-adjuvanted SApNPs. SUDV GPΔmuc SApNPs, both
513 E2p and I3-01v9b, were found either on the surface or within endolysosomes of phagocytic cells
514 (**Figs. 7d** and **e** and **Figs. S7g-l**), consistent with our previous findings for SARS-CoV-2 spike and
515 HIV-1 Env SApNPs (*113, 128*). AP particles tended to aggregate in the extracellular matrix (ECM)
516 2 h after injection (**Fig. 7f** and **Fig. S7m**). Both I3-01v9b SApNPs and AP particles were also
517 observed inside endolysosomes of phagocytic cells at all timepoints (**Fig. 7g** and **Figs. S7n-p**).
518 Overall, E2p and I3-01v9b SApNPs exhibited similar patterns of interaction with FDC networks,
519 B cells, and phagocytic cells. FDC networks retained SApNPs on their dendrites and presented
520 native antigens to B cells in lymph node follicles. A substantial amount of SApNPs was also
521 processed inside endolysosomes of phagocytic cells in the presence of AP adjuvant.

522 **Assessment of GC reactions induced by SUDV GPΔmuc trimers and SApNPs in lymph nodes**

523 In lymph node follicles, GCs are the sites where B cell somatic hypermutation, selection, affinity
524 maturation, and class switching occur (*135, 146, 147*). GC reactions lead to the formation of
525 immune memory and the development of NAb responses following vaccination (*129, 132*). As the
526 essential components supporting GC initiation and maintenance, FDC networks and T follicular
527 helper (T_{fh}) cells present vaccine antigens and stimulate B cells, respectively (*148-150*). Here, we
528 hypothesized that SUDV GPΔmuc SApNPs, due to prolonged retention by FDC networks, would
529 induce more robust and long-lived GC reactions in lymph node follicles compared with the soluble
530 trimers. We first characterized GC reactions induced by I3-01v9b SApNPs after a single-dose
531 injection (4 footpads, 10 μg/footpad). As previously described (*113, 127, 128*), vaccine-induced
532 GC B cells ($GL7^+$, red) and T_{fh} cells ($CD4^+$ $Bcl6^+$, co-labeled with cyan and red) in lymph nodes
533 were assessed by immunohistological analysis. Robust GCs were formed and attached to FDC
534 networks ($CD21^+$, green), with well-organized dark zone (DZ) and light zone (LZ) compartments
535 in B cell follicles (B220+, blue) (**Fig. 8a**, left). T_{fh} cells were observed in the LZ of GCs, sustaining
536 B cell affinity maturation (**Fig. 8a**, right). We then applied this immunohistological assessment to
537 the SUDV GPΔmuc trimer and SApNPs (E2p and I3-01v9b) at 2, 5, and 8 weeks after a single-
538 dose injection (**Fig. 8b** and **Figs. S8a-c**), and at 2 and 5 weeks after the boost (**Fig. 8c** and **Figs.**
539 **S8d** and **e**). GC reactions were quantified using two metrics: GC/FDC ratio (the frequency of GCs
540 associated with FDC networks) and size of GCs (area occupied in follicles) as previously described
541 (*113, 127, 128*). All three SUDV GPΔmuc immunogens induced robust GCs, with the I3-01v9b
542 SApNP group showing the largest GCs at 2 weeks after a single-dose vaccination (**Fig. 8b** and **Fig.**
543 **S8a**). While the GC/FDC ratio decreased significantly over 8 weeks following a single trimer dose,
544 both SApNPs supported long-lived GCs with high GC/FDC ratios (e.g., > 50%) lasting for 8 weeks

545 (**Fig. 8b**). GC sizes declined over time in both trimer and SApNP groups (**Figs. 8b** and **d**). After
546 boosting, all vaccine groups showed restored GC formation, and the GC/FDC ratio in the GPΔmuc
547 trimer group remained comparable (all > 75%) to those in the two SApNP groups (**Fig. 8c**). Overall,
548 the two SApNPs generated larger GCs than the soluble trimer, 1.3 to 2.5 times larger after the
549 prime (**Figs. 8b** and **d**) and 1.4 to 1.8 times larger after the boost (**Figs. 8c** and **e**).

550 Next, we assessed GC reactions using flow cytometry. We intradermally immunized mice
551 with three vaccines, and sentinel lymph nodes were isolated at 2, 5, and 8 weeks after a single-
552 dose injection (**Fig. 8f** and **Fig. S9**) and 2 and 5 weeks after the boost (**Fig. 8g**) (four footpads, 10
553 μg/injection). Fresh lymph node tissues were disaggregated into a single-cell suspensions and
554 stained with an antibody cocktail. GC reactions were quantified based on the percentage and
555 number of GC B and T_{fh} cells (**Fig. S9**). The I3-01v9b SApNP group yielded the highest percentage
556 and number of GC B cells at 2 weeks post-prime (**Fig. 8f**), consistent with the immunohistological
557 findings. Among all vaccine groups, GC B cells declined over time, whereas T_{fh} cell levels
558 remained stable over the 8-week period. A boost enhanced both the frequency and number of GC
559 B and T_{fh} cells (**Fig. 8g**). Notably, GC B and T_{fh} cells induced by I3-01v9b SApNP persisted at
560 relatively high levels over 8 weeks post-boost. Compared with the soluble trimer, the E2p and I3-
561 01v9b SApNPs elicited 1.8/2.4-3.3 times more GC B cells, and 1.5-1.8/2.4-3.2 times more T_{fh}
562 cells, at 8 weeks after the single-dose/boost injection, respectively (**Figs. 8f** and **g**). In summary,
563 the two SUDV GPΔmuc SApNPs generated more robust and long-lived GC reactions than the
564 soluble GPΔmuc trimer, leading to more potent and durable humoral immune responses.

565 **Antibody responses induced by rationally designed filovirus GPΔmuc vaccines in mice**

566 We assessed the immunogenicity of rationally designed filovirus GPΔmuc constructs, including
567 trimers and SApNPs (E2p and I3-01v9b), in mice (**Fig. 9a**). The filovirus antigen (10 μg) was

568 adjuvanted with aluminum hydroxide (AH) and a Toll-like receptor 9 (TLR9) agonist, CpG ODN
569 1826. Mice were immunized intraperitoneally at weeks 0, 3, 9, and 15 with 6-week intervals
570 between the second and third doses and between the third and fourth doses. Serum was collected
571 two weeks after each dose for serological analysis. EBOV vaccine-induced binding antibody (bAb)
572 responses were measured by ELISA using an EBOV GPΔmuc-WL^{2}P^4(1TD0) antigen (**Fig. 9b** and
573 **Figs. S10a**, **b**). The use of 1TD0, rather than foldon, as the trimerization motif in the coating
574 antigen enabled the detection of GPΔmuc-specific bAb responses. Overall, the EBOV GPΔmuc
575 E2p SApNP elicited the highest bAb titers at all four timepoints, with EC_{50} values 8.2- and 5.3-
576 fold higher than those of the soluble trimer at weeks 2 and 5, respectively. All vaccine groups
577 reached plateau EC_{50} titers by week 11, after three immunizations. The EBOV GPΔmuc I3-01v9b
578 SApNP achieved an EC_{50} titer of 182,253 at week 11, identical to its E2p counterpart and 2.5-fold
579 higher than that elicited by the soluble trimer. Week-17 sera (after four doses) were tested against
580 a SUDV GPΔmuc-WL^{2}P^4(1TD0) antigen (**Fig. 9c** and **Fig. S10c**). The EBOV GPΔmuc E2p
581 SApNP again elicited the highest EC_{50} titer (32,585), 3.5-fold higher than that of the soluble trimer.
582 Cross-reactive bAb responses were also evaluated against a RAVV GPΔmuc-P^{2}CT(1TD0) antigen
583 (**Fig. 9d** and **Fig. S10d**). Both E2p and I3-01v9b SApNP groups showed significantly higher serum
584 binding signals, indicated by absorbance at 450 nm (A450), compared with the soluble trimer
585 group. NAb responses were evaluated using a filovirus pseudoparticle (pp) neutralization assay
586 (*36*), with 50% inhibitory dilution (ID_{50}) values calculated for comparison. Week-2 sera served as
587 negative controls for longitudinal analysis. None of the EBOV GPΔmuc vaccines elicited NAb
588 responses at week 2, but ID_{50} titers were detected at weeks 5, 11, and 17, increasing steadily against
589 EBOV-Makona pseudovirus (**Fig. 9e** and **Figs. S10e** and **f**). Consistent with the bAb results,
590 EBOV GPΔmuc E2p SApNP produced the highest NAb titers at all timepoints, although no

591 statistical significance was observed across groups. Week-17 sera were also evaluated against the
592 SUDV-Gulu pseudovirus (**Fig. 9f** and **Fig. S10g**). The EBOV GPΔmuc E2p SApNP yielded the
593 highest ID_{50} titer (761) among all groups. Notably, the EBOV GPΔmuc trimer group elicited the
594 highest ID_{50} titer (2,759) at week 17 against a BDBV-Uganda pseudovirus, 4.5- and 4.9-fold higher
595 than those elicited by the E2p and I3-01v9b SApNPs, respectively (**Fig. 9g** and **Fig. S10h**). Thus,
596 while soluble trimers can achieve high NAb titers, they may require more doses than SApNPs.

597 We assessed SUDV vaccine-induced serum bAb responses by ELISA against a SUDV
598 GPΔmuc-WL^2P^4(1TD0) antigen (**Fig. 9h** and **Figs. S10i**, **j**). Consistent with the bAb responses
599 elicited by EBOV vaccines, SUDV GPΔmuc E2p SApNP generated the highest EC_{50} titers of 871,
600 82,910, and 307,187 at weeks 2, 5 and 11, respectively, 12.4-, 4.5-, and 5.7-fold higher than those
601 induced by the soluble trimer. EC_{50} titers in both E2p and I3-01v9 SApNP groups plateaued after
602 three doses by week 11, whereas the soluble trimer group reached a peak of 102,959 after four
603 doses at week 17, which remained slightly lower than the titers induced by SApNPs. These results
604 correlated well with the GC reactions generated by SUDV GPΔmuc trimer and SApNPs (**Fig. 8**).
605 Week-17 sera were then evaluated against an EBOV GPΔmuc-WL^2P^4(1TD0) antigen (**Fig. 9i** and
606 **Fig. S10k**). The SUDV GPΔmuc E2p and I3-01v9b SApNPs elicited EC_{50} titers of 27,290 and
607 25,446, respectively, which were 2.6- and 2.4-fold higher than that of the soluble GPΔmuc trimer.
608 Cross-reactive bAb responses were further tested using week-17 sera against a RAVV GPΔmuc-
609 P^2CT(1TD0) antigen (**Fig. 9j** and **Fig. S10l**). Both E2p and I3-01v9b SApNP groups exhibited
610 significantly higher serum binding signals (A_{450}) compared with the soluble trimer group. Next,
611 we evaluated SUDV GPΔmuc vaccine-induced autologous NAb responses using a SUDV-Gulu
612 pseudovirus assay. Week-2 sera were used as a negative control for the longitudinal analysis. At
613 this timepoint, none of the vaccines elicited detectable NAb responses, except for one mouse in

614 the E2p group. ID_{50} titers became detectable at week 5, plateaued at week 11 (after three doses),
615 and remained stable through week 17 (**Fig. 9k** and **Figs. S10m**, **n**). Overall, the SUDV GPΔmuc
616 trimer and SApNP vaccines generated comparable ID_{50} titers (1,329-4,628) at each timepoint after
617 two doses. Finally, week-17 sera were assessed for cross-neutralizing activity against EBOV-
618 Makona (**Fig. 9l** and **Fig. S10o**) and BDBV-Uganda (**Fig. 9m** and **Fig. S10p**) pseudoviruses. No
619 statistically significant differences in cross-NAb responses were observed between the SUDV
620 trimer and SApNP groups, as measured by ID_{50} titers.

621 Lastly, we assessed RAVV GPΔmuc trimer-induced serum bAb responses in ELISA using
622 a RAVV GPΔmuc-P^2CT(1TD0) antigen (**Fig. 9n** and **Fig. S10q**). Similar to EBOV and SUDV
623 GPΔmuc trimers, RAVV GPΔmuc trimer generated a strong bAb response after two doses, with
624 the peak EC_{50} titer of 36,2215 at week 5. Cross-reactive bAb responses were evaluated using week-
625 17 sera against two orthoebolavirus antigens: EBOV GPΔmuc-WL^2P^4(1TD0) (**Fig. 9o** and **Fig.**
626 **S10r**) and SUDV GPΔmuc-WL^2P^4(1TD0) (**Fig. 9p** and **Fig. S10s**). Low bAb titers, indicated by
627 A_{450} values, were observed for SUDV GPΔmuc in most mice. Vaccine-induced NAb responses
628 were evaluated against pseudotyped MARV-Angola and orthoebolaviruses using purified IgG and
629 week-17 sera, respectively (**Fig. 9q** and **Figs. S10t**, **u**). Notably, IgG purification was required to
630 eliminate nonspecific serum background in the MARV pseudovirus assay (**Fig. S10t**, left), and
631 neutralization potency was measured by the 50% inhibitory concentration (IC_{50}). The RAVV
632 GPΔmuc trimer group yielded IC_{50} values of 30.9-148.4 μg/ml, with a geometric mean of 70.2
633 μg/ml, when IgG was tested against MARV-Angola (**Fig.9q**, left). RAVV GPΔmuc trimer-induced
634 sera were then assessed against EBOV-Makona, SUDV-Gulu, and BDBV-Uganda pseudoviruses
635 (**Fig. 9q**, right). Interestingly, cross-genus neutralization activity was demonstrated by detectable
636 ID_{50} titers, although confirmation by IgG-based assays will be needed.

637 **Antibody responses induced by glycan-modified filovirus GPΔmuc vaccines in mice**

638 We characterized the immunogenicity of filovirus GPΔmuc vaccines bearing oligomannose-rich
639 (Kif) and trimmed (Kif/Endo H) glycans in mice (**Fig. 10a**). The same immunization protocol used
640 in our previous vaccine studies (*100, 113, 151, 152*) was applied here, which differed from the
641 longer-interval (6-week) regimen used for wild-type GPΔmuc vaccines (**Fig. 9a**). Mice were
642 immunized intraperitoneally at weeks 0, 3, 6, and 9, with 3-week intervals between doses. Each
643 injection contained 10 μg of glycan-modified antigen formulated with 100 μl of CpG/AH adjuvant,
644 resulting in a final volume of 200 μl. Serum was collected two weeks after each vaccination to
645 enable longitudinal comparison of bAb and NAb responses.

646 We first measured serum bAb responses induced by glycan-modified EBOV GPΔmuc
647 trimers by ELISA using an EBOV GPΔmuc-WL^{2}P^4(1TD0) antigen (**Fig. 10b** and **Figs. S11a, b**).
648 Among the three groups, the glycan-trimmed trimer elicited the lowest EC_{50} titers at all timepoints,
649 while the Kif-treated trimer generated the highest EC_{50} titers, 212 and 42,360 at weeks 2 and 5,
650 respectively. In terms of EC_{50} titers, the Kif-treated group was 2.2- and 6.2-fold higher at week 2,
651 and 1.2- and 2.1-fold higher at week 5, compared with the wild-type and glycan-trimmed groups,
652 respectively. All trimer groups reached peak EC_{50} titers after three doses. Following a similar trend,
653 the Kif-treated EBOV GPΔmuc E2p SApNP group showed the highest bAb titers at all three
654 timepoints (**Fig. 10c** and **Figs. S11a**, **b**). Responses appeared to plateau at week 5, with the Kif-
655 treated E2p SApNP yielding an EC_{50} titer of 300,502, 1.5- and 3.2-fold higher than its wild-type
656 and glycan-trimmed counterparts, respectively. Wild-type and Kif-treated EBOV GPΔmuc I3-
657 01v9 SApNPs induced comparable bAb responses, both reaching peak EC_{50} titers after three doses
658 (**Fig. 10d** and **Figs. S11a, b**). We next evaluated NAb responses induced by glycan-modified
659 EBOV GPΔmuc vaccines against EBOV-Makona. Overall, the Kif-treated vaccines were the most

660 immunogenic, while the glycan-trimmed vaccines elicited the lowest NAb titers at all three
661 timepoints (**Fig. 10e-g** and **Figs. S11c, d**). Specifically, the Kif-treated EBOV GPΔmuc trimer
662 yielded an ID_{50} titer of 449 at week 5, 1.5- and 1.9-fold higher than its wild-type and glycan-
663 trimmed counterparts, respectively (**Fig. 10e**). The Kif-treated EBOV GPΔmuc E2p SApNP
664 elicited an ID_{50} titer of 1,459 at week 5, 2.3- and 4.1-fold higher than those of the wild-type and
665 glycan-trimmed groups, respectively (**Fig. 10f**). A similar pattern was observed in the I3-01v9b
666 SApNP groups (**Fig. 10g**). These results demonstrated the beneficial effect of an oligomannose-
667 rich glycan shield on bAb and NAb responses induced by EBOV GPΔmuc vaccines, in marked
668 contrast to the glycan effects observed in our recent HIV-1 Env vaccine study (*113*).

669 We then used a SUDV GPΔmuc-WL^2P^4(1TD0) antigen in ELISA to assess serum bAb
670 responses induced by glycan-modified SUDV GPΔmuc trimers (**Fig. 10h** and **Figs. S11e, f**). At
671 all three timepoints, the Kif-treated SUDV GPΔmuc trimer elicited the highest bAb titers, whereas
672 the glycan-trimmed trimer elicited the lowest, consistent with results observed for EBOV.
673 Regardless of glycan modification, all vaccine groups reached peak EC_{50} titers after three doses.
674 The Kif-treated SUDV GPΔmuc trimer yielded EC_{50} titers of 425 and 150,326 at weeks 2 and 5,
675 respectively. In terms of EC_{50} titers, this trimer achieved 6.1- and 13.3-fold increases at week 2,
676 and 8.2- and 27.6-fold increases at week 5, compared with the wild-type and glycan-trimmed
677 counterparts, respectively. Similarly, for both SUDV GPΔmuc E2p and I3-01v9b SApNPs, the
678 Kif-treated groups showed the highest bAb responses at weeks 2 and 5 (**Figs. 10i, j** and **Figs. S11e,**
679 **f**). For both SApNPs, Kif treatment led to plateaued EC_{50} titers after two doses (week 5), whereas
680 the wild-type and glycan-trimmed groups required three doses to reach their EC_{50} titers at week 8.
681 The Kif-treated SUDV GPΔmuc E2p and I3-01v9b SApNPs elicited EC_{50} titers of 329,358 and
682 271,692 at week 5, respectively, 2.1- and 6.9-fold higher than their wild-type counterparts and 2.3-

683 and 5.7-fold higher than their glycan-trimmed counterparts, respectively. We then evaluated NAb
684 responses induced by glycan-modified SUDV GPΔmuc vaccines against SUDV-Gulu. All three
685 SUDV GPΔmuc trimer groups reached peak ID_{50} titers after three doses (**Fig. 10k** and **Figs. S11g,**
686 **h**). The Kif-treated SUDV GPΔmuc trimer group showed the highest ID_{50} titer of 3,652 at week 5,
687 2.7- and 2.2-fold higher than those of the wild-type and glycan-trimmed groups, respectively (**Fig.**
688 **10k**). While all three E2p SApNPs exhibited comparable ID_{50} titers (**Fig. 10l**), the Kif-treated I3-
689 01v9 SApNP elicited the highest ID_{50} titer of 4,041 at week 8, 2.9- and 3.2-fold higher than its
690 wild-type and glycan-trimmed counterparts, respectively (**Fig. 10m**). Therefore, oligomannose
691 enrichment conferred a similar advantage to SUDV as to EBOV vaccines (**Figs. 10e–g**).

692 We assessed serum bAb responses induced by the wild-type and glycan-trimmed RAVV
693 GPΔmuc trimers by ELISA using a wild-type RAVV GPΔmuc-P^2CT(1TD0) antigen (**Fig. 10n** and
694 **Figs. S11i**, **j**). The wild-type group reached a peak EC_{50} titer of 362,215 after two doses, whereas
695 the glycan-trimmed group required three doses to plateau at 446,121. Overall, no significant
696 differences were observed between the two groups at any timepoint. We also compared NAb
697 responses by testing purified IgG against pseudotyped MARV-Angola and orthoebolaviruses (**Fig.**
698 **10o** and **Fig. S10k**). Against MARV-Angola, both groups yielded similar IC_{50} values, ranging
699 from 25.9 to 191.6 μg/ml. Cross-orthoebolavirus neutralization was evaluated using mouse IgG
700 against EBOV-Makona, SUDV-Gulu, and BDBV-Uganda. The wild-type trimer induced stronger
701 cross-genus activity than its glycan-trimmed counterpart, although the longer dosing interval may
702 have contributed to this difference. Neither group showed nonspecific IgG neutralization against
703 lymphocytic choriomeningitis virus pseudoparticles (LCMV-pps), included as a negative control.
704 These findings were largely consistent with serum neutralization data (**Fig. 9q**).

705 **Sex-dependent antibody responses induced by stabilized SUDV GPΔmuc trimers**

706 We studied the impact of sex on NAb responses induced by wild-type and Kif-treated SUDV
707 GPΔmuc trimers. Briefly, mice were injected at weeks 0, 3, 6, and 9 via intradermal injection into
708 four footpads, with 3-week intervals between doses (**Fig. S12a**). Each administered dose consisted
709 of 80 µl of antigen/AH adjuvant mix containing 10 µg of trimer antigen and 40 µl of adjuvant.
710 Serum samples collected at week 11, after four injections, were assessed against SUDV Gulu
711 pseudovirus. For the wild-type SUDV GPΔmuc trimer, a significant sex-specific difference was
712 observed: the ID_{50} titer in female mice (607) was 2.3-fold higher than in male mice (**Fig. S12b**).
713 For the Kif-treated SUDV GPΔmuc trimer, female mice developed a slightly higher ID_{50} titer (593)
714 than males, although the difference was not statistically significant (**Fig. S12c**). In both vaccine
715 groups, female mice mounted greater NAb responses than males. This result is consistent with our
716 previous study on RSV F trimer vaccines (*153*) and with broader consensus that females tend to
717 generate stronger humoral immune responses than males following vaccination (*154, 155*).

718 Our detailed analysis of vaccine-induced antibody responses underscores the critical role
719 of multivalent display and glycan modification in enhancing filovirus vaccine immunogenicity.
720 Overall, Kif-treated GPΔmuc SApNPs elicited the strongest bAb and NAb responses. However,
721 due to differences in immunization protocols (e.g., dosing intervals), additional in vivo studies are
722 needed to confirm these results. Another key observation is the induction of cross-orthoebolavirus
723 NAbs by the RAVV GPΔmuc-P^2CT trimer, detected at both serum and IgG levels (**Fig. 9q**, right;
724 **Fig. 10o**). This finding suggests that this GP possesses intrinsic immunogenic potential, warranting
725 further validation in animal models, and could be incorporated into a pan-filovirus vaccine. Finally,
726 sex is an important variable in evaluating filovirus vaccine responses.

727 **DISCUSSION**

728 Filoviruses are a major cause of lethal VHF in humans and NHPs (*5, 6*). The viral GP mediates
729 host cell entry by facilitating attachment and membrane fusion (*14*). Structural studies of filovirus
730 GPs bound to NAbs from human survivors have shown that GP harbors neutralizing epitopes and
731 is the primary target for vaccine development (*18-21*). Two vector-based EBOV vaccines, rVSV-
732 ZEBOV (ERVEBO) (*63*) and a two-dose regimen (Zabdeno + Mvabea) (*64*), were approved by
733 the U.S. FDA and the European Commission in 2019 and 2020, respectively. However, no licensed
734 vaccines are available to prevent VHF caused by other filoviruses. Over the past decade, structure-
735 based rational design has emerged as a powerful approach to accelerate vaccine development (*84,*
736 *85, 87, 88*). Like other class I viral fusion proteins, filovirus GP is metastable (*99, 100*), and
737 vaccines expressing wild-type GP may not elicit optimal immune responses. Two recent studies
738 identified molecular features contributing to GP metastability and stabilized the GPΔmuc trimer
739 in a native-like prefusion conformation (*99, 100*). While native-like GP trimers have remained the
740 focus of filovirus vaccine design, engineered protein NPs have emerged as a promising platform
741 to enhance antigen presentation and immunogenicity (*74, 100*). In parallel, glycan trimming has
742 been shown to improve NAb responses to vaccines targeting influenza, HIV-1, and SARS-CoV-2
743 (*112-114*), suggesting a broadly applicable strategy for viral GP-based immunogens. However, the
744 combined effects of GP stabilization, NP display, and glycan modification have not been evaluated
745 systematically across diverse filoviruses in the context of rational vaccine design.

746 We previously reported that the HR2 stalk and HR1c bend in GP2 contribute to EBOV GP
747 metastability, and that a W615L mutation combined with a C-terminal extension (targeting HR2),
748 along with a proline substitution at T577 or L579 (targeting HR1c), yielded a stable GPΔmuc
749 trimer with high yield and homogeneity in mammalian cells (*100*). In this study, we extended this
750 rational GP design strategy to SUDV and BDBV of the *Orthoebolavirus* genus and to RAVV of

751 the *Orthomarburgvirus* genus to support vaccine development against future filovirus outbreaks –
752 a priority of the U.S. Biomedical Advanced Research and Development Authority (BARDA) (*76,*
753 *156, 157*). Although the same GP2 elements (HR1c and HR2 stalk) appear to drive metastability
754 across both filovirus genera, the stabilization strategies differ. For EBOV, SUDV, and BDBV,
755 comparative analysis of GPΔmuc-WL^{2}P^2 and -WL^{2}P^4 constructs revealed that the P^4 mutation
756 conferred a more favorable thermostability profile, while trimer yield, purity, and antigenicity
757 remained comparable between P^2 and P^4. The crystal structure of EBOV GPΔmuc-WL^{2}P^4 revealed
758 a stabilizing interprotomer hydrogen bond (R130-A575), while the cryo-EM structure of SUDV
759 GPΔmuc-WL^{2}P^4 resolved atomic details of the GP-CA45 interface, together confirming GPΔmuc-
760 WL^{2}P^4 as a broadly applicable design for stabilizing orthoebolavirus GP in a native-like prefusion
761 conformation. In contrast, for RAVV, the P^2 (T578P) construct yielded substantially more trimer
762 than the P^4 (E580P) variant. A double mutation at the base of the HR2 stalk (E631F/Q632V)
763 further improved trimer stability, resulting in the GPΔmuc-P^{2}CT design. Notably, the W615L
764 mutation used to stabilize orthoebolavirus GPs was originally derived from MARV (*100*), whereas
765 the E631F/Q632V mutation used here to stabilize RAVV GP was introduced from EBOV. This
766 reciprocal exchange suggests that filoviruses may have evolved distinct mechanisms for regulating
767 GP metastability, via a widened neck in orthoebolaviruses or a charged tail in orthomarburgviruses,
768 within the HR2 stalk. These findings suggest that triggers of metastability may also reside in the
769 stalk regions of other class I viral fusion proteins, such as RSV F and SARS-CoV-2 spike.

770 We previously focused our design efforts on the NP interior, incorporating an inner shell
771 of locking domains (LDs) and a core of helper T-cell epitopes (*100*). The resulting multilayered
772 E2p and I3-01v9 SApNPs were used to present antigens from EBOV, SARS-CoV-2, HIV-1, and
773 influenza (*100, 113, 127, 151, 158*). We also observed that EBOV GP and RSV F (*100, 153*), both

774 containing a C-terminal coiled-coil stalk, dissociated into monomers in the absence of a C-terminal
775 trimerization motif. This suggests that SApNPs with small, rigid anchoring sites may be better
776 suited for displaying trimeric antigens with extended stalks. Compared with E2p, which features a
777 compact triangular anchoring site (~9 Å) on the NP surface (*159*), I3-01v9 presents a wider spacing
778 of 50.5 Å between N-termini (*160*), which may destabilize filovirus GPs when displayed on the
779 NP surface. To address this, we redesigned I3-01v9 using a previously developed I3-01v9a variant
780 (*127*) as a template. An N-terminal helix was modeled and packed against the protein core in silico,
781 yielding I3-01v9b and I3-01v9c. When the I3-01v9b/c-T variants were used as scaffolds to present
782 EBOV GPΔmuc-WL^2P^4, the resulting constructs showed native-like GP trimer structures by EM.
783 Notably, while all three orthoebolavirus GPΔmuc-WL^2P^4 trimers were successfully displayed on
784 E2p and I3-01v9b SApNPs, a similar attempt with RAVV GPΔmuc-P^2CT resulted in low yield
785 and aggregation. It is plausible that specific regions within RAVV GP may interact with the NP
786 backbone and cause misfolding. Nonetheless, our findings suggest that I3-01v9b/c can be used to
787 display filovirus GPs, as well as other class I viral GPs such as RSV F and SARS-CoV-2 spike,
788 with improved trimer stability. Glycan modification adds another dimension to rational vaccine
789 design (*113*), but its biochemical, biophysical, structural, and antigenic effects must be carefully
790 assessed. Although glycan-trimmed GPΔmuc trimers exhibited lower thermostability (T_m) than
791 both wild-type and Kif-treated forms, glycan trimming enhanced NAb epitope recognition in both
792 trimer and SApNP formats, consistent with our previous HIV-1 study (*113*).

793 In recent studies, we established a vaccine strategy that integrates detailed mechanistic
794 analysis to characterize the in vivo behavior of immunogens and provide insights into vaccine-
795 induced NAb responses (*113, 127, 128*). In the analysis of SUDV GPΔmuc vaccines, multivalent
796 display on SApNPs enhanced GP interactions with FDC networks, B cells, and phagocytic cells

797 in lymph nodes. The size and intrinsic thermostability of SApNPs contributed to prolonged vaccine
798 retention and sustained antigen presentation in lymph node follicles (over 8 weeks), resulting in
799 more robust and durable GC reactions compared with the soluble GPΔmuc trimer. Nearly identical
800 trafficking and retention patterns were observed for SApNPs presenting SUDV GPΔmuc, HIV-1
801 Env (*113*), and influenza M2e×3 (*127*), despite their distinct glycan profiles. These results support
802 our previous conclusion that glycans are not a major determinant of follicular localization for NP
803 vaccines in lymph nodes (*113*). Collectively, these findings suggest that NP size and antigen
804 thermostability are key factors influencing the lymph node behavior of protein NPs (*113, 127,*
805 *128*). Mouse immunization studies further elucidated antibody responses to diverse filovirus
806 vaccines. Overall, longitudinal analysis revealed that NAb responses closely tracked with bAb
807 responses. Among wild-type vaccines, E2p SApNPs presenting EBOV and SUDV GPΔmuc
808 elicited the highest EC_{50} and ID_{50} titers at most timepoints, consistent with the strong GC reactions
809 observed in lymph nodes. The two glycan modification strategies, however, yielded unexpected
810 results. Glycan-trimmed trimers and SApNPs consistently elicited the lowest EC_{50} and ID_{50} titers,
811 while oligomannose-rich immunogens – produced in the presence of kifunensine (Kif) – induced
812 the strongest bAb and NAb responses at most timepoints. This pattern contrasts with findings from
813 the previous studies of influenza HA, SARS-CoV-2 spike, and HIV-1 Env vaccines, where glycan
814 trimming enhanced the breadth and potency of NAb responses (*112-115*). Although the reasons
815 for these differences remain unclear, our results suggest that there may not be a single glycan
816 modification strategy applicable to all viral GP vaccines.

817 Our future research will follow several directions. First, antibodies induced by GPΔmuc
818 trimers and SApNPs, with or without glycan modification, will be isolated for structural epitope
819 mapping. This will help determine how SApNP display enhances NAb function, as demonstrated

820 for SARS-CoV-2 (*128*), how cross-NAbs recognize diverse GPs, and how glycan modification
821 influences epitope targeting. Such analyses may explain why improved epitope exposure following
822 glycan trimming did not translate into stronger NAb responses in vivo. Second, alternative glycan
823 modification strategies will be explored. While it is unclear whether oligomannose enrichment
824 improves NAb elicitation for other viral GPs, various approaches that alter glycan profiles can be
825 tested using filovirus vaccine constructs. Non-mammalian systems, such as fungal (*161, 162*) and
826 insect (*163*) cell lines, may provide simpler oligomannose-type glycans and reduce the need for
827 chemical modification. Third, pan-filovirus vaccine strategies merit further investigation. EBOV
828 and SUDV GPΔmuc SApNPs elicited cross-orthoebolavirus NAbs, and combining these with an
829 optimized SApNP presenting RAVV GPΔmuc-P^2CT trimers may, in principle, induce a cross-
830 genus, pan-filovirus bNAb response. Finally, filovirus challenge studies in mice and guinea pigs
831 will be essential to evaluate protection and support advancement to NHP models.

832 **METHODS**

833 **Construct design, expression, and purification of filovirus GP immunogens**

834 For orthoebolaviruses, the amino acid sequences of EBOV GP (Mayinga strain, GenBank
835 Accession: NP_066246) with a T42A substitution, SUDV GP (Gulu strain, GenBank Accession:
836 AAU43887), and BDBV GP (R4386L strain, GenBank Accession: AYI50307) were used to
837 design GPΔmuc trimers (**Fig. S1a**) and SApNPs (**Fig. S3h**). Notably, an N637D mutation was
838 later introduced to the SUDV GPΔmuc-WL^2P^4 construct to eliminate a potential N-linked
839 glycosylation site at N637 due to the enzymatic site "AS" between the GP and SApNP backbone.
840 For orthomarburgviruses, the amino acid sequence of RAVV GP (Ravn-87 strain, GenBank
841 Accession: ABE27071) was used to design GPΔTM and various GPΔmuc trimers (**Fig. S5a**).

842 Rationally designed EBOV, SUDV, and BDBV GPΔmuc trimers were transiently
843 expressed in HEK293F cells as previously described (*100*). Briefly, HEK293F cells were thawed
844 and suspended in FreeStyle 293 Expression Medium (Life Technologies, Carlsbad, CA) and
845 placed in a shaker incubator at 37°C, 135 rotations per minute (rpm), with 8% CO_2. When the cells
846 reached a density of 2.0×10^6/ml, they were diluted to a concentration of 1.0×10^6/ml in 1 L of
847 FreeStyle 293 Expression Medium for transfection using a polyethyleneimine (PEI) (Polysciences)
848 transfection protocol. In brief, 900 µg of plasmid DNA in 25 ml of Opti-MEM transfection medium
849 (Life Technologies) was mixed with 5 ml of PEI-MAX (1.0 mg/ml) in 25 ml of Opti-MEM and
850 incubated for 30 min at room temperature. Cells were then transfected with the DNA–PEI-MAX
851 mixture and incubated in a shaker incubator at 37°C, 135 rpm, with 8% CO_2. Kifunensine (10
852 mg/L, Tocris Bioscience) was added at the time of transfection to inhibit α-mannosidase I and
853 promote oligomannose-type glycosylation. Five days later, the supernatants containing the target
854 protein were harvested, clarified by centrifugation at 1,126 × g for 22 min, and filtered through a
855 0.45 µm membrane (Thermo Scientific). Orthoebolavirus GP was purified with an ADI-15878
856 IAC column, except for EBOV GPΔmuc-WL^2P^4 used in X-ray crystallography and EBOV
857 GPΔmuc-WL^2P^4-I3-01v9b/c-T used in nsEM, which were purified with an mAb100 IAC column.
858 Orthoebolavirus GPs were eluted three times with 5 ml of 0.2 M glycine (pH 2.2), neutralized with
859 0.5 ml of 2 M Tris base (pH 9.0), and buffer-exchanged into phosphate-buffered saline (PBS; pH
860 7.2). IAC-purified orthoebolavirus GPs were further purified by SEC using a Superdex 200
861 Increase 10/300 GL column (Cytiva).

862 RAVV GPΔmuc trimers and all orthoebolavirus GPΔmuc-presenting SApNPs were
863 produced in ExpiCHO cells (Thermo Fisher). Briefly, ExpiCHO cells were thawed and incubated
864 in ExpiCHO Expression Medium (Thermo Fisher) in a shaker incubator at 37°C, 135 rpm, with

865 8% CO_2. When cell density reached 10×10^6/ml, ExpiCHO Expression Medium was added to
866 adjust the cell density to 6×10^6/ml for transfection. ExpiFectamine CHO–plasmid DNA
867 complexes were prepared for 100-ml transfections according to the manufacturer's instructions.
868 Kifunensine (10 mg/L) was added at the time of ExpiCHO transfection to inhibit α-mannosidase
869 I. For these constructs, 100 µg of plasmid and 320 µl of ExpiFectamine CHO reagent were mixed
870 in 7.7 ml of cold OptiPRO™ medium (Thermo Fisher). Following the first feed on day 1, cells
871 were cultured in a shaker incubator at 33°C, 115 rpm, with 8% CO_2 using the Max Titer protocol,
872 with an additional feed on day 5 (Thermo Fisher). Culture supernatants were harvested 13–14 days
873 post-transfection, clarified by centrifugation at 3724 × g for 25 min, and filtered through a 0.45 µm
874 membrane (Thermo Fisher). RAVV GPΔmuc trimers were purified using Ni Sepharose excel resin
875 (Nickel, Cytiva), eluted twice with 15 ml of 0.5 M imidazole, and buffer-exchanged into Tris-
876 buffered saline (TBS; pH 7.2). Orthoebolavirus GPΔmuc-presenting SApNPs were purified using
877 an ADI-15878 IAC column, eluted three times with 5 ml of 0.2 M glycine (pH 2.2), neutralized
878 with 0.5 ml of 2 M Tris base (pH 9.0), and buffer-exchanged into PBS (pH 7.2). Final polishing
879 was performed by SEC using a Superdex 200 Increase 10/300 GL column (Cytiva) for nickel-
880 purified RAVV GPΔmuc trimers and a Superose 6 Increase 10/300 GL column (Cytiva) for IAC-
881 purified orthoebolavirus GPΔmuc-presenting SApNPs. Selected SEC fractions were pooled,
882 aliquoted, and stored in liquid nitrogen or at -80 ºC until use.

883 **Expression and purification of neutralizing antibodies (NAbs)**

884 Antibodies in the IgG form were transiently expressed in ExpiCHO cells (Thermo Fisher). At 12–
885 14 days post-transfection, cells were centrifuged at 3,724 × *g* for 25 min, and the supernatants were
886 filtered through a 0.45-µm membrane (Millipore). IgGs were purified using protein A affinity resin
887 (Cytiva) and eluted with 0.3 M citric acid (pH 3.0). The eluate was immediately titrated to neutral

888 pH (7.0) by adding 2 M Tris base (pH 9.0). IgGs were then concentrated and buffer-exchanged
889 into PBS using Amicon 10 kDa filters (Millipore). Concentrations were determined by UV_{280}
890 absorption using theoretical extinction coefficients.

891 **Glycan trimming by Endo H treatment and enzyme removal**

892 The protocol for Endo H treatment and removal was described in our previous study (*113*). Briefly,
893 surface glycans of filovirus GPΔmuc trimers and SApNPs were trimmed using endoglycosidase H
894 (Endo Hf), a fusion of Endo H and MBP (NEB, catalog no. P0703L). In each reaction, 1 mg of
895 antigen was mixed with 200 µl of 10× GlycoBuffer 3, 250 µl of Endo Hf, and H_2O (if necessary)
896 to a final volume of 2 ml. The mixture was incubated at room temperature (25°C) for 5 h to allow
897 enzymatic processing of the GP glycans. After incubation, the reaction mixtures were purified by
898 SEC using a Superdex 200 Increase 10/300 GL column (for trimers) or a Superose 6 Increase
899 10/300 GL column (for SApNPs) to remove the MBP-tagged enzyme. Notably, glycan trimming
900 by Endo H requires expression of filovirus GPΔmuc immunogens in the presence of kifunensine.
901 In our previous study (*113*), amylose resin (NEB, catalog no. E8021S) was used to remove residual
902 Endo Hf from SEC-purified HIV-1 Env trimers and SApNPs. In the present study, this additional
903 step of Endo Hf removal was omitted to preserve vaccine antigens for animal studies. SEC-purified
904 fractions were pooled, aliquoted, and stored in liquid nitrogen or at -80 ºC until use.

905 **SDS-PAGE and BN-PAGE**

906 Filovirus GPΔmuc trimers and SApNPs were analyzed by sodium dodecyl sulfate-polyacrylamide
907 gel electrophoresis (SDS-PAGE) and blue native-polyacrylamide gel electrophoresis (BN-PAGE).
908 Proteins were mixed with loading dye and loaded onto a 10% Tris-Glycine Gel (Bio-Rad) or a 4-
909 12% Bis-Tris NativePAGE gel (Life Technologies). For SDS-PAGE under reducing conditions,
910 proteins were mixed with 6× Laemmli SDS sample buffer (Thermo Scientific) and boiled for 5 min

911 at 100 °C. SDS-PAGE gels were run at 250 V for 25 min using SDS running buffer (Bio-Rad) and
912 stained with InstantBlue (Abcam). For BN-PAGE, proteins were mixed with 4× native dye and
913 loaded onto a BN-PAGE gel. The gel was run at 150 V for 2–2.5 h with NativePAGE running
914 buffer (Life Technologies), following the manufacturer's instructions. BN-PAGE gels were
915 stained with Coomassie Brilliant Blue R-250 (Bio-Rad) and destained using a solution of 6%
916 ethanol and 3% glacial acetic acid.

917 **Differential scanning calorimetry (DSC)**

918 The melting temperature (T_m) and other thermal parameters of filovirus GPΔmuc trimers purified
919 by an IAC or nickel column followed by SEC were measured using a MicroCal PEAQ-DSC Man
920 instrument (Malvern). Briefly, purified proteins in PBS buffer were diluted to 0.5-5 μM. Melting
921 was assessed at a scan rate of 60 °C/h from 20 °C to 100 °C. Data processing, including buffer
922 correction, normalization, and baseline subtraction, was conducted using MicroCal PEAQ-DSC
923 software. Gaussian fitting was carried out using GraphPad Prism version 10.3.1.

924 **Site-specific glycan analysis**

925 To generate site-specific glycan profiles, 100 μg aliquots of each antigen were denatured for 1 h
926 in 50 mM Tris/HCl (pH 8.0) containing 6 M urea and 5 mM dithiothreitol (DTT). The denatured
927 antigens were reduced and alkylated by adding 20 mM iodoacetamide (IAA) and incubating for 1
928 h in the dark, followed by 1h of incubation with 20 mM DTT to eliminate residual IAA. Alkylated
929 samples were buffer-exchanged into 50 mM Tris/HCl (pH 8.0) using Vivaspin columns (10 kDa
930 cutoff). Three aliquots were then digested separately overnight with trypsin (Mass Spectrometry
931 Grade, Promega), chymotrypsin (Mass Spectrometry Grade, Promega), or alpha lytic protease
932 (Sigma Aldrich) at a ratio of 1:30 (w/w). The next day, peptides were dried and extracted using an
933 Oasis HLB μElution Plate (Waters).

934 Peptides were dried again, resuspended in 0.1% formic acid, and analyzed by nanoLC-
935 electrospray ionization MS using an Ultimate 3000 HPLC (Thermo Fisher Scientific) system
936 coupled to an Orbitrap Eclipse mass spectrometer (Thermo Fisher Scientific). Stepped higher-
937 energy collisional dissociation (HCD) fragmentation was applied. Peptides were separated using
938 an EasySpray PepMap RSLC C18 column (75 µm × 75 cm). A trapping column (PepMap 100 C18
939 3µM 75µM × 2cm) was used in line with liquid chromatography (LC) prior to separation with the
940 analytical column. The LC conditions were as follows: 280-minute linear gradient consisting of 4-
941 32% acetonitrile in 0.1% formic acid over 260 minutes followed by 20 minutes of alternating 76%
942 acetonitrile in 0.1% formic acid and 4% ACN in 0.1% formic acid, used to ensure all the sample
943 had eluted from the column. The flow rate was set to 300 nl/min. The spray voltage was set to 2.7
944 kV and the temperature of the heated capillary was set to 40 °C. The ion transfer tube temperature
945 was set to 275 °C. The scan range was 375−1500 m/z. The stepped HCD collision energies were
946 set to 15%, 25%, and 45% and the MS2 for each energy was combined. Precursor and fragment
947 detection were performed using an Orbitrap at a resolution of MS^1 = 120,000 and MS^2 = 30,000.
948 The AGC target for MS1 was set to standard and injection time set to auto which involves the
949 system setting the two parameters to maximize sensitivity while maintaining cycle time. Full LC
950 and MS methodology can be extracted from the appropriate Raw file using XCalibur FreeStyle
951 software or upon request.

952 Glycopeptide fragmentation data were extracted from the raw file using Byos 4.6 (Protein
953 Metrics). The glycopeptide fragmentation data were evaluated manually for each glycopeptide;
954 the peptide was scored as true-positive when the correct b and y fragment ions were observed
955 along with oxonium ions corresponding to the glycan identified. The MS data was searched using
956 the Protein Metrics 38 insect N-glycan library. The relative amounts of each glycan at each site as

957 well as the unoccupied proportion were determined by comparing the extracted chromatographic
958 areas for different glycotypes with an identical peptide sequence. All charge states for a single
959 glycopeptide were summed. The precursor mass tolerance was set at 4 ppm and 10 ppm for
960 fragments. A 1% false discovery rate (FDR) was applied. The relative amounts of each glycan at
961 each site as well as the unoccupied proportion were determined by comparing the extracted ion
962 chromatographic areas for different glycopeptides with an identical peptide sequence. Glycans
963 were categorized according to the composition detected.

964 HexNAc(2)Hex(9−3) was classified as M9 to M3. Any of these structures containing a
965 fucose were categorized as fucosylated mannose (FM). Complex-type glycans were classified
966 according to the number of HexNAc subunits and the presence or absence of fucose. Core glycans
967 refer to truncated structures smaller than M3. As this fragmentation method does not provide
968 linkage information, compositional isomers are grouped.

969 **Biolayer interferometry**

970 Antigenic profiles of filovirus GPΔmuc trimers and SApNPs were measured on an Octet RED96
971 (FortéBio, Pall Life Sciences) against a panel of antibodies, including five pan-orthoebolavirus
972 NAbs and two MARV NAbs, all in the IgG form. All assays were performed with agitation set to
973 1000 rpm in FortéBio 1× kinetic buffer. The final volume for all solutions was 200 µl per well.
974 Experiments were conducted at 30 °C in solid black 96-well plates (Greiner Bio-One). For all
975 antigens, 5 µg/ml antibody in 1× kinetic buffer was loaded onto the surface of anti-human IgG
976 Quantitation (AHQ) Biosensors for 300 s. Next, a 2-fold concentration gradient of antigen, starting
977 at 500 nM for trimers and 10 nM for SApNPs, was used in a 6-point dilution series. A 60-s
978 biosensor baseline step was applied before measuring association of antigen in solution with
979 antibody-loaded biosensors for 200 s. Dissociation of the interaction was monitored for 300 s. The

980 correction of baseline drift was performed by subtracting the mean value of shifts recorded for a
981 sensor loaded with antibody but not incubated with antigen, and for a sensor without antibody but
982 incubated with antigen. Octet data were processed using FortéBio's data acquisition software
983 (version 8.1). Peak response signals at the highest antigen concentration were summarized in a
984 matrix and color-coded for comparison across constructs. Experimental data for each antigen-
985 antibody pair were fitted to a 1:1 binding model, and the three best-fitting datasets were grouped
986 to calculate K_{on} and K_D values. Antibody-antigen binding curves were plotted using GraphPad
987 Prism version 10.3.1.

988 **Enzyme-linked immunosorbent assay (ELISA)**

989 Costar 96-well, high-binding, flat-bottom, half-area plates (Corning) were coated with 50 µl of
990 PBS containing 0.1 µg of the appropriate filovirus GPΔmuc trimer or SApNP antigen. Plates were
991 incubated overnight at 4 °C and then washed five times with PBST wash buffer (PBS containing
992 and 0.05% (v/v) Tween 20). Each well was then blocked for 1 h at room temperature with 150 µl
993 of blocking buffer consisting of 4% (w/v) blotting-grade blocker (Bio-Rad) in PBS. Plates were
994 washed again five times with PBST wash buffer. To evaluate antibody binding to the coating
995 antigens, antibodies were diluted in blocking buffer to a maximum concentration of 10 µg/ml,
996 followed by a 10-fold dilution series. For each antibody dilution, a total volume of 50 µl was added
997 to the appropriate wells. For serum sample analysis, mouse sera were diluted 1:40 in blocking
998 buffer and subjected to a 10-fold dilution series. For each sample dilution, 50 µl of each dilution
999 was added to the wells. Plates were incubated for 1 h at room temperature and then washed five
1000 times with PBST wash buffer. For secondary antibody binding, a 1:5000 dilution of goat anti-
1001 human IgG antibody (Jackson ImmunoResearch Laboratories) or, for mouse sample analysis, a
1002 1:3000 dilution of horseradish peroxidase (HRP)-conjugated goat anti-mouse IgG antibody

1003 (Jackson ImmunoResearch Laboratories) was prepared in PBST wash buffer. Then, 50 µl of the
1004 diluted secondary antibody was added to each well. Plates were incubated for 1 h at room
1005 temperature and then washed six times with PBST wash buffer. Finally, wells were developed
1006 with 50 µl of 3,3',5,5'-tetramethylbenzidine (Life Sciences) for 3-5 min before the reaction was
1007 stopped with 50 µl of 2 N sulfuric acid. Plates were immediately read on a BioTek Synergy plate
1008 reader at a wavelength of 450 nm. EC_{50} values were calculated from full curves using GraphPad
1009 Prism version 10.3.1. For samples with OD_{450} values below 0.5, EC_{50} values were set to 10 µg/ml
1010 in **Figs. 1g**, **3h**, **4c**, and **4h** to facilitate EC_{50} plotting and comparison.

1011 **Protein crystallization and data collection**

1012 EBOV GPΔmuc-WL^2P^4 was transiently expressed in HEK293S cells using the same protocol as
1013 for HEK293F cells, followed by IAC and SEC purification. The mAb100/SEC-purified EBOV
1014 GPΔmuc-WL^2P^4 trimer protein at 9.3 mg/ml was subjected to crystallization by sitting-drop vapor
1015 diffusion using an automated CrystalMation robotic system (Rigaku) at 20 °C at The Scripps
1016 Research Institute (*164*). The reservoir solution consisted of 12% PEG-6000 (*v/v*) and 0.1 M
1017 sodium citrate-citric acid (pH 4.51). Diffraction-quality crystals were obtained after 2 weeks of
1018 incubation at 20°C. Crystals were cryoprotected in well solution containing 25% (*v/v*) ethylene
1019 glycol, mounted on a nylon loop, and flash-cooled in liquid nitrogen. Diffraction data were
1020 collected at beamline 12-1 of the Stanford Synchrotron Radiation Lightsource (SSRL) and
1021 processed with HKL-2000 (*165*). The data were indexed in space group P321.

1022 **Structure determination and refinement**

1023 The crystal structure of EBOV GPΔmuc-WL^2P^4 was determined by molecular replacement using
1024 Phaser-MR in Phenix (version 1.19.2-4158), with the coordinates of the previously reported EBOV
1025 GPΔmuc-WL^2P^2 structure (PDB ID: 7JPH) (*100*) as the search model. Polypeptide chains were

1026 manually adjusted into electron density using Coot (*166*), refined with *phenix.refine* (*167*), and
1027 validated using the wwPDB Validation System (*168*). Carbohydrates were further validated using
1028 Privateer in CCP4i (*169*), both before and after refinement. Final data processing and refinement
1029 statistics are described in **Table S1**. All images for crystal structures shown in the figures were
1030 generated using PyMOL version 2.3.4. Notably, due to weak electron density, structural models
1031 were not built for residues K633-D637 in the GP2 stalk region of EBOV GPΔmuc-WL^{2}P^4, nor for
1032 the C-terminal foldon trimerization motif. These omissions result in apparent gaps in crystal
1033 packing when visualizing the GP structure within the electron density map.

1034 **Negative-stain electron microscopy (nsEM)**

1035 The nsEM analysis of filovirus GPΔmuc trimers, their antibody-bound complexes, and GPΔmuc-
1036 presenting SApNPs, was performed by the Core Microscopy Facility at The Scripps Research
1037 Institute. Briefly, samples were prepared at concentrations of 0.008 and 0.01 mg/ml, respectively.
1038 Carbon-coated copper grids (400 mesh) were glow-discharged, and 8 µl of each sample was
1039 adsorbed for 2 min. Excess samples were removed, and grids were negatively stained with 2%
1040 uranyl formate for 2 min. Excess stain was wicked away, and the grids were allowed to air-dry.
1041 Trimer samples were analyzed at 120 kV with a Talos L120C transmission electron microscope
1042 (Thermo Fisher), and images were acquired using a CETA 16 M CMOS camera under 73,000×
1043 magnification at a resolution of 1.93 Å/pixel and a defocus range of 0.5-2 µm. For SApNP samples,
1044 the images were collected under 52,000× magnification. The resulting pixel size at the specimen
1045 plane was 2.05 Å, and the defocus was set to −1.50 µm. Computational analysis of the images was
1046 performed using the high-performance computing core facility at The Scripps Research Institute.
1047 nsEM images were converted to MRC format using EMAN2 (*170*) and further processed with
1048 CryoSPARC version 4.3.0 (*124*). Micrographs were contrast-transfer function (CTF)-corrected by

1049 patch CTF estimation. Particles were selected using a blob/template picker and later extracted with
1050 a box size of 130 pixels for 2D classification, with 50 and 230 Å used as the minimum and
1051 maximum particle sizes for blob picking. 3D models were generated by *ab initio* reconstruction
1052 and optimized using heterogeneous and homogeneous refinement procedures. All nsEM and fitted
1053 structure images were generated using UCSF Chimera (*171*) and ChimeraX (*172-174*).

1054 **Cryo-electron microscopy (cryo-EM) for SUDV GP-CA45 complexes**

1055 The SUDV GPΔmuc-WL^{2}P^4 construct was expressed in HEK293F cells and purified using an
1056 ADI-15878 column. The eluate was mixed with CA45 Fab at a 1:1.5 molar ratio. The mixture was
1057 further purified using a Superose 6 Increase 10/300 GL column, and complex fractions were
1058 pooled. Cryo-EM grid preparation and data collection were performed at the UC San Diego Cryo-
1059 EM Facility. Vitrification was carried out using a Vitrobot Mark IV (FEI) equilibrated to 4 ºC and
1060 100% humidity. Quantifoil Cu 1.2/1.3 300 grids were plasma cleaned using a Solarus II (Gatan)
1061 with a mixture of Ar/O_2 for 10 s. Following plasma cleaning, the grid was blotted on one side with
1062 3.5 µl of the SUDV GPΔmuc-WL^{2}P^4/CA45 Fab complex at a concentration of 0.55 mg/ml for 4 s,
1063 and frozen in liquid ethane. The frozen grids were stored in liquid nitrogen until imaging. Cryo-
1064 EM data were collected on a Titan Krios G4 (Thermo Fisher) operated at 200 keV, equipped with
1065 a Falcon 4 camera and a Selectris-X energy filter (Thermo Fisher). Automated data collection was
1066 performed using Smart EPU software (Thermo Fisher). Images were acquired under 130,000×
1067 magnification, corresponding to a pixel size of 0.89 Å, with a defocus range of -1 to -2.5 µm. All
1068 datasets were processed using CryoSPARC version 3.3. Movie frames were aligned using Patch
1069 Motion Correction, and CTF estimation was performed with Patch CTF Estimation (**Fig. S2d**).
1070 Initial particle picking was done with Blob Picker with the particle size set to 100-350 Å, and
1071 particles were extracted using a box size of 360 pixels. After 2D classification, selected particle

1072 classes were used as input for Template Picking and re-extracted with a box size of 360 pixels.
1073 After multiple rounds of 2D classification, 249,139 particles were selected for 3D reconstruction.
1074 Three starting reference models were generated using Ab-Initio Reconstruction and used for
1075 Heterogeneous Refinement. Particles in the largest cluster (163,924 particles) were refined using
1076 Homogeneous Refinement with a focusing mask and C3 symmetry. The refined model was further
1077 subjected to 3D Classification, resulting in 10 models. The class associated with the most complete
1078 model (41,233 particles) was subjected to another round of Ab-Initio Reconstruction. This
1079 intermediate model was further optimized using Non-uniform Refinement and Local Refinement,
1080 both using 163,924 particles and a focusing mask. The final GSFSC resolution was 3.13 Å, and
1081 the final structural model was built using the crystal structures of EBOV GPΔmuc-WL^{2}P^2 (PDB
1082 ID: 7JPH) (*100*) and EBOV GPΔmuc-bound CA45 Fab (PDB ID: 6EAY) (*118*) as templates. The
1083 structures were fitted into the density map using ChimeraX (*172-174*), followed by real-space
1084 refinement in Phenix (*167*), manual model correction in Coot (*166*), and a final round of real-space
1085 refinement in Phenix (*167*). Statistics for the cryo-EM reconstruction and model refinement are
1086 provided in **Table S2**. The coordinates and 3D density map have been deposited in Protein Data
1087 Bank (PDB) and Electron Microscopy Data Bank (EMDB), respectively.

1088 **Rational design of trimer-presenting I3-01v9b/c SApNP scaffolds**

1089 We previously redesigned the I3-01v9 scaffold for optimal display of monomeric antigens (*127*).
1090 In the resulting I3-01v9a SApNP, the *N*-terminal helix was extended such that its first residue was
1091 positioned just above the NP surface. Here, we further redesigned I3-01v9a to optimize NP display
1092 of trimeric antigens with a long coiled-coil stalk (**Fig. S3**). First, the 11-aa *N*-terminal helix in I3-
1093 01v9a was truncated to 7 aa. Then, a 13-aa helix-turn fragment (9-aa helix + 4-aa turn, all alanine)
1094 was fused to this truncated N-terminus. The newly added 9-residue helix was designed to pack

1095 within the groove formed by two helices in the I3-01 core. This 9-residue helix was derived from
1096 the structure of a human transcription factor (PDB ID: 6G6L). To accommodate this new helix,
1097 four mutations were introduced into the I3-01 core helices to remove steric clashes. The helix-turn
1098 backbone was first relaxed using iterative modular optimization (IMO) (*175*), followed by
1099 structural sampling with the CONCOORD program (*176*) to generate 1,000 slightly perturbed
1100 backbone conformations. An ensemble-based protein design protocol (*87, 152*) was then used to
1101 identify the optimal amino acid sequence for the 9-residue N-terminal helix based on Cα and Cβ-
1102 based RAPDF (*177*) scoring functions. The 4-residue turn was fixed as "GSGS" during design.
1103 The final I3-01v9b design was selected by combining the results from both scoring functions. A
1104 second design, I3-01v9c, was derived by mutating the turn sequence from "GSGS" to "GPPS" to
1105 increase rigidity. The I3-01v9b structural model was further relaxed using IMO with a minimum
1106 backbone perturbation angle. The distance between the N-termini of the I3-01v9b/c trimer model
1107 (I3-01v9b/c-T) was 43.9 Å. EBOV GPΔmuc-WL^{2}P^4-I3-01v9b/c-T constructs (**Fig. S3b**) were
1108 designed, transiently expressed in HEK293F cells, and structurally validated by nsEM.

1109 **Dynamic Light Scattering (DLS)**

1110 Particle size distributions of orthoebolavirus GPΔmuc-presenting SApNPs were measured using a
1111 Zetasizer Ultra instrument (Malvern). Briefly, ADI-15878/SEC-purified SApNPs produced from
1112 ExpiCHO cells were diluted to 0.2 mg/ml in 1× PBS, and 30 µl of each sample was added to a
1113 quartz batch cuvette (Malvern, catalog no. ZEN2112). Measurements were performed at 25 °C in
1114 backscatter mode. Data processing was carried out using the Zetasizer particle size analyzer with
1115 the Ultra instrument software. The resulting particle size distributions were plotted using GraphPad
1116 Prism version 10.3.1.

1117 **Mouse immunization and sample collection**

1118 Mouse immunization protocols were adapted from our previous studies (*113, 127, 128*). All animal
1119 experiments were conducted in accordance with the guidelines of the Association for the
1120 Assessment and Accreditation of Laboratory Animal Care (AAALAC) and approved by the
1121 Institutional Animal Care and Use Committee (IACUC) of The Scripps Research Institute. Female
1122 and male BALB/c mice, aged 6–8 weeks, were purchased from The Jackson Laboratory and
1123 housed in ventilated cages in environmentally controlled rooms at 20°C with 50% humidity, under
1124 a 12 h/12 h light-dark cycle. For mechanistic studies of vaccine transport and immune responses
1125 in lymph nodes, mice were intradermally inoculated via four footpads using a 29-gauge insulin
1126 needle under 3% isoflurane anesthesia with oxygen. The injection dose was 80 µl of antigen and
1127 AP adjuvant mix, containing 40 µg of vaccine antigen per mouse or 10 µg per footpad. In the first
1128 immunogenicity study, mice were injected via the intraperitoneal (i.p.) route at weeks 0, 3, 9, and
1129 15. A 6-week interval was maintained between the second and third, and the third and fourth doses.
1130 In the second immunogenicity study, our standard 4-dose screening regimen (*113, 127, 128, 158*)
1131 was used, with mice injected at weeks 0, 3, 6, and 9 at 3-week intervals. Each injection consisted
1132 of 200 µl of antigen/adjuvant mix containing 10 µg of vaccine antigen and 100 µl of adjuvant,
1133 including 40 µg/50 µl of CpG (oligonucleotide 1826, a TLR9 agonist from InvivoGen) adsorbed
1134 onto 50 µl of AH (InvivoGen). In the sex-dependent antibody response study, mice were injected
1135 intradermally via the footpads at weeks 0, 3, 6, and 9, with 3-week intervals between doses. Each
1136 mouse received 80 µl of an antigen/AH adjuvant mixture containing 10 µg of immunogen and 40 µl
1137 of adjuvant. Blood samples were collected 2 weeks after each injection through the retro-orbital
1138 sinus using heparinized capillary tubes. Samples were centrifuged at 12,000 rpm for 10 min to
1139 separate serum (top layer) and the rest of the whole blood layer. Upon heat inactivation at 56°C
1140 for 30 min, serum was centrifuged again at 12000 rpm for 10 min to remove precipitates. For the

1141 last timepoint, the rest of the whole blood layer was diluted with an equal volume of PBS and then
1142 overlaid on 4.5 ml of Ficoll in a 15 ml SepMate tube (STEMCELL Technologies) and centrifuged
1143 at 1,200 rpm for 10 min at 20 °C to separate peripheral blood mononuclear cells (PBMCs). Cells
1144 were washed once in PBS and then resuspended in 1 ml of ACK red blood cell lysis buffer (Lonza).
1145 After washing with PBS, PBMCs were resuspended in 1 ml of freezing media (10% dimethyl
1146 sulfoxide [DMSO]/90% fetal calf serum [FCS]). Two weeks after the last bleed, spleens were
1147 harvested and ground against a 70-µm cell strainer (BD Falcon) to release splenocytes into a cell
1148 suspension. Splenocytes were centrifuged, washed in PBS, treated with 5 ml of ACK lysing buffer
1149 (Lonza), and frozen with 3 ml of freezing media (10% DMSO/90% FCS). Serum samples from
1150 week 11 in the second study were purified using a CaptureSelect™ IgG-Fc (Multispecies) Affinity
1151 Matrix (Thermo Scientific) following the manufacturer's instructions. Purified IgG from
1152 individual mice was analyzed in filovirus-pp assays to assess vaccine-induced NAb responses.

1153 **Histology, immunostaining, and imaging for lymph node tissues**

1154 To study vaccine distribution, trafficking, retention, cellular interaction, and GC reactions in
1155 sentinel lymph nodes, SUDV GPΔmuc trimer and SApNPs (E2p and I3-01v9b) adjuvanted with
1156 AP were intradermally injected into four footpads of mice. A similar protocol was described in our
1157 previous studies (*113, 127, 128*). Briefly, each injection consisted of 80 µl of antigen/adjuvant mix
1158 containing 40 µg of filovirus antigen (10 µg/footpad; 40 µg/mouse). Mice were euthanized at time
1159 points ranging from 2 h to 8 weeks after a single-dose injection. Fresh sentinel lymph nodes were
1160 collected and embedded in frozen section compound (VWR International, catalog no. 95057-838).
1161 Sample molds were immersed in liquid nitrogen and stored at -80°C before shipping to The Centre
1162 for Phenogenomics (Toronto, Canada). Lymph node tissues were sectioned at 8 µm thickness using
1163 a cryostat (Cryostar NX70). Primary antibodies were applied to lymph node sections and incubated

1164 overnight at 4°C. After washing with TBS containing 0.1% Tween-20 (TBST), biotin- or
1165 fluorophore-conjugated secondary antibodies were added, and sections were incubated at 25 °C
1166 for 1 h. Lymph node sections were stained with NAbs ADI-15878 (*116*), ADI-15946 (*119*), CA45
1167 (*118*), or mAb100 (*133*) (1:100), followed by biotinylated goat anti-human secondary antibody
1168 (Abcam, catalog no. ab7152, 1:300), streptavidin-horseradish peroxidase (HRP) reagent
1169 (Vectastain Elite ABC-HRP Kit, Vector, catalog no. PK-6100), and ImmPACT diaminobenzidine
1170 (DAB; Vector, catalog no. SK-4105).

1171 To study the interaction between SUDV GPΔmuc immunogens with lymph node cell
1172 populations, FDCs were labeled using anti-CD21 primary antibody (Abcam, catalog no. ab75985,
1173 1:1800), followed by anti-rabbit secondary antibody conjugated with Alexa Fluor 555 (Thermo
1174 Fisher, catalog no. A21428, 1:200). FDCs were also co-stained using anti-FDC-M1 primary
1175 antibody (BD Biosciences, catalog no. 551320, 1:20), followed by anti-rat secondary antibody
1176 conjugated with Alexa Fluor 488 (Abcam, catalog no. ab150165, 1:200). Subcapsular sinus
1177 macrophages were labeled with anti-sialoadhesin (CD169) antibody (Abcam, catalog no. ab53443,
1178 1:600), followed by anti-rat secondary antibody conjugated with Alexa Fluor 488 (Abcam, catalog
1179 no. ab150165, 1:200). B cells were labeled with anti-B220 antibody (eBioscience, catalog no. 14-
1180 0452-82, 1:100), followed by anti-rat secondary antibody conjugated with Alexa Fluor 647
1181 (Thermo Fisher, catalog no. A21247, 1:200). GC responses were assessed by immunohistology.
1182 GC B cells were stained with FITC-conjugated rat anti-GL7 antibody (BioLegend, catalog no.
1183 144604, 1:250). T_{fh} cells were stained with anti-CD4 antibody (BioLegend, catalog no. 100402,
1184 1:100), followed by anti-rat secondary antibody conjugated with Alexa Fluor 488 (Abcam, catalog
1185 no. ab150165, 1:1000). GC cells were stained with Bcl6 antibody (Abcam, catalog no. ab220092,
1186 1:300), followed by anti-rabbit secondary antibody conjugated with Alexa Fluor 555 (Thermo

1187 Fisher, catalog no. A21428, 1:1000). Nuclei were stained with 4',6-diamidino-2-phenylindole
1188 (DAPI; Sigma-Aldrich, catalog no. D9542, 100 ng/ml).

1189 Stained lymph node tissues were scanned using an Olympus VS-120 slide scanner
1190 equipped with a Hamamatsu ORCA-R2 C10600 digital camera or an Akoya Vectra Polaris
1191 imaging system with a 20×/0.45NA objective. The transport of SUDV GPΔmuc trimer and SApNP
1192 immunogens, as well as the GCs they induced in lymph nodes, were quantified from bright-field
1193 and fluorescent images using ImageJ software (*178*).

1194 **Electron microscopy analysis of protein nanoparticles in lymph node tissues**

1195 To assess interactions between SUDV GPΔmuc immunogens and stromal and immune cells in
1196 lymph nodes, TEM analysis was performed by the Core Microscopy Facility at The Scripps
1197 Research Institute (TSRI). The protocol for lymph node isolation, processing, and analysis
1198 followed our previous studies (*113, 128*). To visualize AP-adjuvanted SUDV GPΔmuc SApNPs
1199 (E2p and I3-01v9b) interacting with FDCs and phagocytic cells, mice were injected with 200 µl
1200 of antigen/adjuvant mix containing 100 µg of SUDV immunogen and 100 µl of AP adjuvant,
1201 administered into two hind footpads (50 µg/footpad). Fresh popliteal lymph nodes were collected
1202 at 2, 12, and 48 h after a single-dose injection. Lymph node tissues were bisected and immersed
1203 in oxygenated fixative containing 2.5% glutaraldehyde and 4% paraformaldehyde in 0.1 M sodium
1204 cacodylate buffer (pH 7.4) overnight at 4°C. Lymph node samples were then fixed and stained
1205 with 0.5% uranyl acetate overnight at 4°C, infiltrated with LX-112 (Ladd) epoxy resin, and
1206 polymerized at 60 °C. Ultrathin tissue sections (70 nm) were cut and mounted on copper grids for
1207 imaging. TEM was performed at 80 kV using a Talos L120C transmission electron microscope
1208 (Thermo Fisher), and images were acquired with a CETA 16M CMOS camera for further analysis.

1209 **Lymph node disaggregation, cell staining, and flow cytometry**

1210 To assess vaccine-induced humoral immune responses, the frequency and number of GC B cells
1211 ($GL7^+B220^+$) and T_{fh} cells ($CD3^+CD4^+CXCR5^+PD\text{-}1^+$) were measured by flow cytometry to
1212 quantify GC reactions (**Fig. S9**). The protocol for lymph node tissue collection, processing, and
1213 analysis followed our previous studies (*113, 127, 128*). Briefly, mice were administered with 80
1214 μl of antigen/adjuvant mix containing 40 μg of vaccine immunogen (10 μg/injection, 40 μg/mouse)
1215 into four footpads. Mice were euthanized at 2, 5, and 8 weeks after a single-dose injection, or at 2
1216 and 5 weeks after the boost. Fresh sentinel lymph nodes were isolated and immediately processed
1217 by mechanical disaggregation. Lymph node tissues were then incubated in enzyme digestion
1218 solution at 37 °C for 30 min on a rotator, with the resulting cells filtered through a 70 μm cell
1219 strainer to obtain a single-cell suspension. Anti-CD16/32 antibody (BioLegend, catalog no.
1220 101302, 1:50) was added to the cell samples to block the nonspecific binding of Fc receptors and
1221 the samples were kept on ice for 30 min. Next, cells were transferred to 96-well V-shaped-bottom
1222 microplates with a cocktail of antibodies and stains, including: Zombie NIR live/dead stain
1223 (BioLegend, catalog no. 423106, 1:100), Brilliant Violet 510 anti-mouse/human CD45R/B220
1224 antibody (BioLegend, catalog no. 103247, 1:300), FITC anti-mouse CD3 antibody (BioLegend,
1225 catalog no. 100204, 1:300), Alexa Fluor 700 anti-mouse CD4 antibody (BioLegend, catalog no.
1226 100536, 1:300), PE anti-mouse/human GL7 antibody (BioLegend, catalog no. 144608, 1:500),
1227 Brilliant Violet 605 anti-mouse CD95 (Fas) antibody (BioLegend, catalog no. 152612, 1:500),
1228 Brilliant Violet 421 anti-mouse CD185 (CXCR5) antibody (BioLegend, catalog no. 145511,
1229 1:500), and PE/Cyanine7 anti-mouse CD279 (PD-1) antibody (BioLegend, catalog no. 135216,
1230 1:500). Cells were incubated with the antibody cocktail on ice for 30 min and centrifuged at 400
1231 × *g* for 10 min. They were then fixed with 1.6% paraformaldehyde (Thermo Fisher Scientific,
1232 catalog no. 28906) in Hank's Balanced Salt Solution (HBSS) on ice for 30 min, centrifuged again

1233 at 400 × *g* for 10 min, resuspended in HBSS blocking solution at 4 °C. Sample acquisition was
1234 performed on a 5-laser AZE5 flow cytometer (Yeti, Bio-Rad) with Everest software at the Core
1235 Facility of The Scripps Research Institute. Data analysis was conducted with FlowJo version 10.

1236 **Pseudovirus production and neutralization assays**

1237 A filovirus-pseudoparticle (pp) neutralization assay (*100*) was performed to assess the neutralizing
1238 activity of vaccine-induced mouse sera and purified mouse IgG. Filovirus-pps were generated by
1239 co-transfecting HEK293T cells with the envelope-deficient HIV-1 pNL4-3.lucR^{-}E^{-} plasmid (NIH
1240 AIDS Reagent Program: https://www.aidsreagent.org/) and an expression plasmid encoding the
1241 GP gene from EBOV Makona (GenBank accession no. KJ660346), SUDV Gulu (GenBank
1242 accession no. AY729654), BDBV Uganda (GenBank accession no. KR063673), or MARV
1243 Angola (GenBank accession no. DQ447653) at a 4:1 ratio using the Lipofectamine 3000
1244 transfection protocol (Thermo Fisher). After 72 h, pseudoviruses were harvested from the
1245 supernatant by centrifugation at 3,724 × *g* for 10 min, aliquoted, and stored at -80°C until use. For
1246 pseudovirus neutralization assays, mouse sera (starting dilution 1:100) or purified IgG (starting at
1247 300 µg/ml) were serially diluted 3-fold and incubated with pseudoviruses at 37°C for 1 h in white
1248 solid-bottom 96-half-well plates (Corning). Then, 0.8×10^4 Huh-7 cells were added to each well,
1249 and the plates were incubated at 37°C for 60-72 h. After incubation, the supernatant was removed,
1250 and cells were lysed. Luciferase reporter gene expression was quantified by adding Bright-Glo
1251 Luciferase substrate (Promega) according to the manufacturer's instructions. Luciferase activity
1252 (in relative light units, RLU) was measured on a BioTek microplate reader using Gen 5 software.
1253 Values from experimental wells were compared to virus-only wells, with background
1254 luminescence from a series of uninfected wells subtracted from both. Dose-response neutralization
1255 curves were fit by nonlinear regression (0-100% constraints) in GraphPad Prism version 10.3.1,

1256 from which IC_{50} and ID_{50} were calculated. The same protocols were used to produce and assay
1257 pseudoparticles displaying the envelope glycoprotein of lymphocytic choriomeningitis virus
1258 (LCMV-pps) as a negative control for IgG neutralization.

1259 **Statistical analysis**

1260 Data were collected from $n = 8$ mice per group in the immunization studies and $n = 3$-5 mice per
1261 group in the mechanistic study. All ELISA and pseudovirus neutralization assays were performed
1262 in duplicate. Different vaccine constructs and adjuvant-formulated filovirus vaccine antigens were
1263 compared using one-way analysis of variance (ANOVA), followed by Tukey's multiple
1264 comparison *post hoc* test. Two-tailed unpaired *t*-tests were used to compare two independent
1265 vaccine groups. Statistical significance is indicated in the figures as follows: ns (not significant),
1266 $*p < 0.05$, $**p < 0.01$, $***p < 0.001$, and $****p < 0.0001$. Graphs were generated and statistical
1267 analyses were performed using GraphPad Prism version 10.3.1.

1268 **ACKNOWLEDGEMENTS**

1269 The authors acknowledge the facilities of the UC San Diego cryo-EM facility, part of the
1270 Goeddel Family Technology Sandbox, and the scientific and technical assistance of Dr. Mariusz
1271 Matyszewski. We thank G. Ossetchkine, K. Duffin, M. Ganguly, and V. Bradaschia at The
1272 Centre for Phenogenomics for their expertise and technical support in immunohistology. We
1273 also thank M. Livneh, K. Spencer, and S. Henderson of the Histology and Microscopy Core
1274 Facility at The Scripps Research Institute for their technical support in immunostaining and
1275 imaging. We acknowledge K. Vanderpool, T. Fassel, and S. Henderson of the Core Microscopy
1276 Facility at The Scripps Research Institute for their expert assistance with TEM imaging. We
1277 thank A. Saluk, B. Seegers, and B. Monteverde of the Flow Cytometry Core Facility at The
1278 Scripps Research Institute for their technical support in flow cytometry. Diffraction data were

collected at beamline 12-1 of the Stanford Synchrotron Radiation Lightsource (SSRL). Use of the Stanford Synchrotron Radiation Lightsource and Stanford Linear Accelerator Center (SLAC), National Accelerator Laboratory, is supported by the U.S. Department of Energy, Office of Science, Office of Basic Energy Sciences under Contract No. DE-AC02-76SF00515. The SSRL Structural Molecular Biology Program is supported by the Department of Energy (DOE) Office of Biological and Environmental Research, and by the National Institutes of Health (NIH), National Institute of General Medical Sciences (NIGMS) (P30GM133894). The contents of this publication are solely the responsibility of the authors and do not necessarily represent the official views of NIGMS or NIH. We thank M. Arends for proofreading the manuscript. **Funding:** This work was supported by Ufovax/SFP-2018-1013 and Uvax/SFP-2020-0111 (J.Z.). **Author contributions:** Project design by Y.-Z.L., Y.-N.Z., L.H., and J.Z.; protein design by J.Z.; protein expression and purification by Y.-Z.L., G.W., C.D., and L.H.; glycan analysis by M.N., J.D.A., and M.C.; negative-stain EM and cryo-EM by Y.-Z.L., A.B.W., and J.Z.; x-ray crystallographic analysis by Y.-Z.L., R.L.S., and I.A.W; mouse immunization, lymph node isolation, immunohistology, TEM, flow cytometry, and serum ELISA by Y.-N.Z.; pseudovirus neutralization assays by G.W., K.B.G., C.D., and L.H.; manuscript written by Y.-Z.L., Y.-N.Z., M.N., K.B.G., S.A., L.H., M.C., and J.Z. All authors reviewed and provided feedback on the manuscript. **Competing interests:** Dr. Jiang Zhu is the Co-Founder and a Scientific Advisory Board member of Uvax Bio, LLC, and holds associated financial interests. All other authors declare no competing interests. **Data and material availability:** All data needed to evaluate the conclusions of this study are available in the main text and Supplementary Materials. Structural data obtained from X-ray crystallography and cryo-EM have been deposited in the Protein Data Bank (PDB, https://www.rcsb.org/) under accession codes 9N8E and 9N8F, respectively. Cryo-

EM density maps have been deposited in the Electron Microscopy Data Bank (EMDB, https://www.ebi.ac.uk/emdb/) under accession code EMD-49127. Mass spectrometry data have been deposited in the MassIVE server (https://massive.ucsd.edu) under accession code MassIVE MSV000097145. All data supporting the findings of this study are available within the article and its Supplementary Information. Source data are provided with this paper.

1307 **References**:

1308 1. W. Slenczka, in *Marburg- and Ebolaviruses: From Ecosystems to Molecules,* E.
1309 Muhlberger, L. L. Hensley, J. S. Towner, Eds. (2017), vol. 411, pp. 3-21.
1310 2. K. M. Johnson, J. V. Lange, P. A. Webb, F. A. Murphy, Isolation and partial
1311 characterisation of a new virus causing acute haemorrhagic fever in Zaire. *Lancet* **1**, 569-
1312 571 (1977).
1313 3. E. T. Bowen *et al.*, Viral haemorrhagic fever in southern Sudan and northern Zaire.
1314 Preliminary studies on the aetiological agent. *Lancet* **1**, 571-573 (1977).
1315 4. C. E. M. Coltart, B. Lindsey, I. Ghinai, A. M. Johnson, D. L. Heymann, The Ebola
1316 outbreak, 2013-2016: old lessons for new epidemics. *Philos. Trans. R. Soc. B, Biol. Sci.*
1317 **372**, 20160297 (2017).
1318 5. S. Paessler, D. H. Walker, Pathogenesis of the viral hemorrhagic fevers. *Annu. Rev.*
1319 *Pathol.* **8**, 411-440 (2013).
1320 6. A. M. Marty, P. B. Jahrling, T. W. Gelsbert, Viral hemorrhagic fevers. *Clin. Lab. Med.*
1321 **26**, 345-386 (2006).
1322 7. J. H. Kuhn *et al.*, New filovirus disease classification and nomenclature. *Nat. Rev.*
1323 *Microbiol.* **17**, 261-263 (2019).
1324 8. J. H. Kuhn *et al.*, Virus nomenclature below the species level: a standardized
1325 nomenclature for filovirus strains and variants rescued from cDNA. *Arch. Virol.* **159**,
1326 1229-1237 (2014).
1327 9. N. Biedenkopf *et al.*, Renaming of genera Ebolavirus and Marburgvirus to
1328 Orthoebolavirus and Orthomarburgvirus, respectively, and introduction of binomial
1329 species names within family Filoviridae. *Arch. Virol.* **168**, 220 (2023).
1330 10. S. C. Harrison, Viral membrane fusion. *Virol.* **479**, 498-507 (2015).
1331 11. M. Kielian, Mechanisms of virus membrane fusion proteins. *Annu. Rev. Virol.* **1**, 171-189
1332 (2014).
1333 12. J. M. White, S. E. Delos, M. Brecher, K. Schornberg, Structures and mechanisms of viral
1334 membrane fusion proteins: multiple variations on a common theme. *Crit. Rev. Biochem.*
1335 *Mol. Biol.* **43**, 189-219 (2008).
1336 13. S. C. Harrison, Viral membrane fusion. *Nat. Struct. Mol. Biol.* **15**, 690-698 (2008).
1337 14. J. E. Lee, E. O. Saphire, Ebolavirus glycoprotein structure and mechanism of entry.
1338 *Future Virol.* **4**, 621-635 (2009).
1339 15. T. R. W. Tipton *et al.*, Characterisation of the T-cell response to Ebola virus glycoprotein
1340 amongst survivors of the 2013-16 West Africa epidemic. *Nat. Commun.* **12**, 1153 (2021).
1341 16. A. I. Flyak *et al.*, Cross-reactive and potent neutralizing antibody responses in human
1342 survivors of natural ebolavirus infection. *Cell* **164**, 392-405 (2016).
1343 17. Z. A. Bornholdt *et al.*, Isolation of potent neutralizing antibodies from a survivor of the
1344 2014 Ebola virus outbreak. *Science* **351**, 1078-1083 (2016).
1345 18. X. Y. Yu, E. O. Saphire, Development and structural analysis of antibody therapeutics for
1346 filoviruses. *Pathog.* **11**, 374 (2022).
1347 19. L. B. King, B. R. West, S. L. Schendel, E. O. Saphire, The structural basis for filovirus
1348 neutralization by monoclonal antibodies. *Curr. Opin. Immunol.* **53**, 196-202 (2018).
1349 20. R. W. Cross, C. E. Mire, H. Feldmann, T. W. Geisbert, Post-exposure treatments for
1350 Ebola and Marburg virus infections. *Nat. Rev. Drug Discov.* **17**, 413-434 (2018).

1351 21. B. M. Friedrich *et al.*, Potential vaccines and post-exposure treatments for filovirus
1352 infections. *Viruses* **4**, 1619-1650 (2012).
1353 22. R. Burk *et al.*, Neglected filoviruses. *FEMS Microbiol. Rev.* **40**, 494-519 (2016).
1354 23. S. Mahanty, M. Bray, Pathogenesis of filoviral haemorrhagic fevers. *Lancet Infect. Dis.*
1355 **4**, 487-498 (2004).
1356 24. I. Messaoudi, G. K. Amarasinghe, C. F. Basler, Filovirus pathogenesis and immune
1357 evasion: insights from Ebola virus and Marburg virus. *Nat. Rev. Microbiol.* **13**, 663-676
1358 (2015).
1359 25. S. Moller-Tank, W. Maury, Ebola virus entry: a curious and complex series of events.
1360 *PLoS Pathog.* **11**, e1004731 (2015).
1361 26. M. Cote *et al.*, Small molecule inhibitors reveal Niemann-Pick C1 is essential for Ebola
1362 virus infection. *Nature* **477**, 344-348 (2011).
1363 27. I. Khan *et al.*, Tubeimosides are pan-coronavirus and filovirus inhibitors that can block
1364 their fusion protein binding to Niemann-Pick C1. *Nat. Commun.* **15**, 162 (2024).
1365 28. H. Wang *et al.*, Ebola viral glycoprotein bound to its endosomal receptor Niemann-Pick
1366 C1. *Cell* **164**, 258-268 (2016).
1367 29. A. P. Cardile, L. G. Downey, P. D. Wiseman, T. K. Warren, S. Bavari, Antiviral
1368 therapeutics for the treatment of Ebola virus infection. *Curr. Opin. Pharmacol.* **30**, 138-
1369 143 (2016).
1370 30. O. T. Mbaya, P. Mukumbayi, S. Mulangu, Review: insights on current FDA-approved
1371 monoclonal antibodies against Ebola virus infection. *Front. Immunol.* **12**, 721328 (2021).
1372 31. T. Hoenen, A. Groseth, H. Feldmann, Therapeutic strategies to target the Ebola virus life
1373 cycle. *Nat. Rev. Microbiol.* **17**, 593-606 (2019).
1374 32. Y. Gao *et al.*, Effects of therapies for Ebola virus disease: a systematic review and
1375 network meta-analysis. *Lancet Microbe* **3**, e683-e692 (2022).
1376 33. X. G. Qiu *et al.*, Reversion of advanced Ebola virus disease in nonhuman primates with
1377 ZMapp. *Nature* **514**, 47-53 (2014).
1378 34. R. T. Davey *et al.*, A randomized, controlled trial of ZMapp for Ebola virus infection. *N.*
1379 *Engl. J. Med.* **375**, 1448-1456 (2016).
1380 35. A. Markham, REGN-EB3: first approval. *Drugs* **81**, 175-178 (2021).
1381 36. D. Corti *et al.*, Protective monotherapy against lethal Ebola virus infection by a potently
1382 neutralizing antibody. *Science* **351**, 1339-1342 (2016).
1383 37. S. Mulangu *et al.*, A randomized, controlled trial of Ebola virus disease therapeutics. *N.*
1384 *Engl. J. Med.* **381**, 2293-2303 (2019).
1385 38. E. O. Saphire, M. J. Aman, Feverish quest for Ebola immunotherapy: straight or cocktail?
1386 *Trends Microbiol.* **24**, 684-686 (2016).
1387 39. C. D. Murin *et al.*, Structures of protective antibodies reveal sites of vulnerability on
1388 Ebola virus. *Proc. Natl. Acad. Sci. U. S. A.* **111**, 17182-17187 (2014).
1389 40. T. Hashiguchi *et al.*, Structural basis for Marburg virus neutralization by a cross-reactive
1390 human antibody. *Cell* **160**, 904-912 (2015).
1391 41. M. L. Fusco *et al.*, Protective mAbs and cross-reactive mAbs raised by immunization
1392 with engineered Marburg virus GPs. *PLoS Pathog.* **11**, e1005016 (2015).
1393 42. A. I. Flyak *et al.*, Mechanism of human antibody-mediated neutralization of Marburg
1394 virus. *Cell* **160**, 893-903 (2015).
1395 43. J. Pallesen *et al.*, Structures of Ebola virus GP and sGP in complex with therapeutic
1396 antibodies. *Nat. Microbiol.* **1**, 16128 (2016).

1397 44. Z. Y. Keck *et al.*, Macaque monoclonal antibodies targeting novel conserved epitopes
1398 within filovirus glycoprotein. *J. Virol.* **90**, 279-291 (2016).
1399 45. F. W. Holtsberg *et al.*, Pan-ebolavirus and pan-filovirus mouse monoclonal antibodies:
1400 protection against Ebola and Sudan viruses. *J. Virol.* **90**, 266-278 (2016).
1401 46. K. A. Howell *et al.*, Antibody treatment of Ebola and Sudan virus infection via a
1402 uniquely exposed epitope within the glycoprotein receptor-binding site. *Cell Rep.* **15**,
1403 1514-1526 (2016).
1404 47. X. L. Zhao *et al.*, Immunization-elicited broadly protective antibody reveals ebolavirus
1405 fusion loop as a site of vulnerability. *Cell* **169**, 891-904.e15 (2017).
1406 48. A. Z. Wec *et al.*, Antibodies from a human survivor define sites of vulnerability for broad
1407 protection against ebolaviruses. *Cell* **169**, 878-890 (2017).
1408 49. L. B. King *et al.*, The marburgvirus-neutralizing human monoclonal antibody MR191
1409 targets a conserved site to block virus receptor binding. *Cell Host Microbe* **23**, 101-
1410 109.e4 (2018).
1411 50. P. Gilchuk *et al.*, Analysis of a therapeutic antibody cocktail reveals determinants for
1412 cooperative and broad ebolavirus neutralization. *Immunity* **52**, 388-403.e12 (2020).
1413 51. P. Gilchuk *et al.*, Multifunctional pan-ebolavirus antibody recognizes a site of broad
1414 vulnerability on the ebolavirus glycoprotein. *Immunity* **49**, 363-374.e10 (2018).
1415 52. C. D. Murin *et al.*, Convergence of a common solution for broad ebolavirus
1416 neutralization by glycan cap-directed human antibodies. *Cell Rep.* **35**, 108984 (2021).
1417 53. A. I. Flyak *et al.*, Broadly neutralizing antibodies from human survivors target a
1418 conserved site in the Ebola virus glycoprotein HR2-MPER region. *Nat. Microbiol.* **3**,
1419 670-677 (2018).
1420 54. K. A. Howell *et al.*, Cooperativity enables non-neutralizing antibodies to neutralize
1421 ebolavirus. *Cell Rep.* **19**, 413-424 (2017).
1422 55. E. O. Saphire *et al.*, Systematic analysis of monoclonal antibodies against Ebola virus GP
1423 defines features that contribute to protection. *Cell* **174**, 938-952.e13 (2018).
1424 56. Y. G. Zhao *et al.*, Toremifene interacts with and destabilizes the Ebola virus
1425 glycoprotein. *Nature* **535**, 169-172 (2016).
1426 57. F. Shaikh *et al.*, Structure-based in silico screening identifies a potent ebolavirus inhibitor
1427 from a traditional Chinese medicine library. *J. Med. Chem.* **62**, 2928-2937 (2019).
1428 58. J. S. Ren, Y. G. Zhao, E. E. Fry, D. I. Stuart, Target identification and mode of action of
1429 four chemically divergent drugs against ebolavirus infection. *J. Med. Chem.* **61**, 724-733
1430 (2018).
1431 59. J. M. Dias *et al.*, A shared structural solution for neutralizing ebolaviruses. *Nat. Struct.*
1432 *Mol. Biol.* **18**, 1424-1427 (2011).
1433 60. J. E. Lee *et al.*, Structure of the Ebola virus glycoprotein bound to an antibody from a
1434 human survivor. *Nature* **454**, 177-182 (2008).
1435 61. C. D. Murin, P. Gilchuk, J. E. Crowe, A. B. Ward, Structural biology illuminates
1436 molecular determinants of broad ebolavirus neutralization by human antibodies for pan-
1437 ebolavirus therapeutic development. *Front. Immunol.* **12**, 808047 (2022).
1438 62. A. Hargreaves *et al.*, Filovirus neutralising antibodies: mechanisms of action and
1439 therapeutic application. *Pathog.* **10**, 1201 (2021).
1440 63. A. M. Henao-Restrepo *et al.*, Efficacy and effectiveness of an rVSV-vectored vaccine in
1441 preventing Ebola virus disease: final results from the Guinea ring vaccination, open-label,
1442 cluster-randomised trial (Ebola Ca Suffit!). *Lancet* **389**, 505-518 (2017).

1443 64. I. D. Milligan *et al.*, Safety and immunogenicity of novel adenovirus type 26- and
1444 modified vaccinia Ankara-vectored Ebola vaccines: a randomized clinical trial. *J. Am.*
1445 *Med. Assoc.* **315**, 1610-1623 (2016).
1446 65. U. N. Sarwar *et al.*, Safety and immunogenicity of DNA vaccines encoding ebolavirus
1447 and marburgvirus wild-type glycoproteins in a phase I clinical trial. *J. Infect. Dis.* **211**,
1448 549-557 (2015).
1449 66. J. E. Ledgerwood *et al.*, Chimpanzee adenovirus vector Ebola vaccine. *N. Engl. J. Med.*
1450 **376**, 928-938 (2017).
1451 67. K. Ewer *et al.*, A monovalent chimpanzee adenovirus Ebola vaccine boosted with MVA.
1452 *N. Engl. J. Med.* **374**, 1635-1646 (2016).
1453 68. F. C. Zhu *et al.*, Safety and immunogenicity of a recombinant adenovirus type-5 vector-
1454 based Ebola vaccine in healthy adults in Sierra Leone: a single-centre, randomised,
1455 double-blind, placebo-controlled, phase 2 trial. *Lancet* **389**, 621-628 (2017).
1456 69. F. C. Zhu *et al.*, Safety and immunogenicity of a novel recombinant adenovirus type-5
1457 vector-based Ebola vaccine in healthy adults in China: preliminary report of a
1458 randomised, double-blind, placebo-controlled, phase 1 trial. *Lancet* **385**, 2272-2279
1459 (2015).
1460 70. M. J. Hamer *et al.*, Safety, tolerability, and immunogenicity of the chimpanzee
1461 adenovirus type 3-vectored Marburg virus (cAd3-Marburg) vaccine in healthy adults in
1462 the USA: a first-in-human, phase 1, open-label, dose-escalation trial. *Lancet* **401**, 294-
1463 302 (2023).
1464 71. M. D. Tapia *et al.*, Safety, reactogenicity, and immunogenicity of a chimpanzee
1465 adenovirus vectored Ebola vaccine in adults in Africa: a randomised, observer-blind,
1466 placebo-controlled, phase 2 trial. *Lancet Infect. Dis.* **20**, 707-718 (2020).
1467 72. A. To *et al.*, Thermostable bivalent filovirus vaccine protects against severe and lethal
1468 Sudan ebolavirus and marburgvirus infection. *Vaccine* **42**, 598-607 (2024).
1469 73. K. B. Preston *et al.*, Single-vial filovirus glycoprotein vaccines: biophysical
1470 characteristics and immunogenicity after co-lyophilization with adjuvant. *Vaccine* **39**,
1471 5650-5657 (2021).
1472 74. D. Xu *et al.*, Design of universal Ebola virus vaccine candidates via immunofocusing.
1473 *Proc. Natl. Acad. Sci. U. S. A.* **121**, e2316960121 (2024).
1474 75. M. Meyer *et al.*, Modified mRNA-based vaccines elicit robust immune responses and
1475 protect guinea pigs from Ebola virus disease. *J. Infect. Dis.* **217**, 451-455 (2018).
1476 76. L. A. Parish, E. J. Stavale, C. R. Houchens, D. N. Wolfe, Developing vaccines to
1477 improve preparedness for filovirus outbreaks: the perspective of the USA biomedical
1478 advanced research and development authority (BARDA). *Vaccines* **11**, 1120 (2023).
1479 77. M. Meyer, D. C. Malherbe, A. Bukreyev, Can Ebola virus vaccines have universal
1480 immune correlates of protection? *Trends Microbiol.* **27**, 8-16 (2019).
1481 78. S. A. Ehrhardt *et al.*, Polyclonal and convergent antibody response to Ebola virus vaccine
1482 rVSV-ZEBOV. *Nat. Med.* **25**, 1589-1600 (2019).
1483 79. H. Cohen-Dvashi *et al.*, Structural basis for a convergent immune response against Ebola
1484 virus. *Cell Host Microbe* **27**, 418-427.e4 (2020).
1485 80. B. F. Haynes, J. R. Mascola, The quest for an antibody-based HIV vaccine. *Immunol.*
1486 *Rev.* **275**, 5-10 (2017).
1487 81. P. D. Kwong, J. R. Mascola, G. J. Nabel, Broadly neutralizing antibodies and the search
1488 for an HIV-1 vaccine: the end of the beginning. *Nat. Rev. Immunol.* **13**, 693-701 (2013).

1489 82. B. F. Haynes, G. Kelsoe, S. C. Harrison, T. B. Kepler, B-cell-lineage immunogen design
1490 in vaccine development with HIV-1 as a case study. *Nat. Biotechnol.* **30**, 423-433 (2012).
1491 83. L. M. Walker, D. R. Burton, Rational antibody-based HIV-1 vaccine design: current
1492 approaches and future directions. *Curr. Opin. Immunol.* **22**, 358-366 (2010).
1493 84. B. S. Graham, M. S. A. Gilman, J. S. McLellan, Structure-based vaccine antigen design.
1494 *Annu. Rev. Med.* **70**, 91-104 (2019).
1495 85. R. W. Sanders *et al.*, A next-generation cleaved, soluble HIV-1 Env trimer, BG505
1496 SOSIP.664 gp140, expresses multiple epitopes for broadly neutralizing but not non-
1497 neutralizing antibodies. *PLoS Pathog.* **9**, e1003618 (2013).
1498 86. S. K. Sharma *et al.*, Cleavage-independent HIV-1 Env trimers engineered as soluble
1499 native spike mimetics for vaccine design. *Cell Rep.* **11**, 539-550 (2015).
1500 87. L. Kong *et al.*, Uncleaved prefusion-optimized gp140 trimers derived from analysis of
1501 HIV-1 envelope metastability. *Nat. Commun.* **7**, 12040 (2016).
1502 88. J. S. McLellan *et al.*, Structure-based design of a fusion glycoprotein vaccine for
1503 respiratory syncytial virus. *Science* **342**, 592-598 (2013).
1504 89. M. G. Joyce *et al.*, Iterative structure-based improvement of a fusion-glycoprotein
1505 vaccine against RSV. *Nat. Struct. Mol. Biol.* **23**, 811-820 (2016).
1506 90. A. Krarup *et al.*, A highly stable prefusion RSV F vaccine derived from structural
1507 analysis of the fusion mechanism. *Nat. Commun.* **6**, 8143 (2015).
1508 91. Y. Che *et al.*, Rational design of a highly immunogenic prefusion- stabilized F
1509 glycoprotein antigen for a respiratory syncytial virus vaccine. *Sci. Transl. Med.* **15**,
1510 eade6422 (2023).
1511 92. D. Wrapp *et al.*, Cryo-EM structure of the 2019-nCoV spike in the prefusion
1512 conformation. *Science* **367**, 1260-1263 (2020).
1513 93. K. S. Corbett *et al.*, SARS-CoV-2 mRNA vaccine design enabled by prototype pathogen
1514 preparedness. *Nature* **586**, 567-571 (2020).
1515 94. K. V. Houser *et al.*, Safety and immunogenicity of an HIV-1 prefusion-stabilized
1516 envelope trimer (Trimer 4571) vaccine in healthy adults: A first-in-human open-label,
1517 randomized, dose-escalation, phase 1 clinical trial. *Eclinicalmedicine* **48**, 101477 (2022).
1518 95. G. Papazisis *et al.*, Respiratory syncytial virus vaccines: analysis of pre-marketing
1519 clinical trials for immunogenicity in the population over 50 years of age. *Vaccines* **12**,
1520 353 (2024).
1521 96. E. Y. Fang *et al.*, Advances in COVID-19 mRNA vaccine development. *Sig.*
1522 *Transduct.Target. Ther.* **7**, (2022).
1523 97. Y. N. Lamb, BNT162b2 mRNA COVID-19 vaccine: First approval. *Drugs* **81**, 495-501
1524 (2021).
1525 98. M. Melgar *et al.*, Use of respiratory syncytial virus vaccines in older adults:
1526 recommendations of the advisory committee on immunization practices - United States,
1527 2023. *Morb. Mortal. Wkly. Rep.* **72**, 793-801 (2023).
1528 99. L. Rutten *et al.*, Structure-based design of prefusion-stabilized filovirus glycoprotein
1529 trimers. *Cell Rep.* **30**, 4540-4550.e3 (2020).
1530 100. L. He *et al.*, Single-component multilayered self-assembling nanoparticles presenting
1531 rationally designed glycoprotein trimers as Ebola virus vaccines. *Nat. Commun.* **12**, 2633
1532 (2021).
1533 101. J. J. Suschak, C. S. Schmaljohn, Vaccines against Ebola virus and Marburg virus: recent
1534 advances and promising candidates. *Hum. Vaccin. Immunother.* **15**, 2359-2377 (2019).

1535 102. O. Reynard *et al.*, Ebolavirus glycoprotein GP masks both its own epitopes and the
1536 presence of cellular surface proteins. *J. Virol.* **83**, 9596-9601 (2009).
1537 103. J. R. Francica *et al.*, Steric shielding of surface epitopes and impaired immune
1538 recognition induced by the Ebola virus glycoprotein. *PLoS Pathog.* **6**, e1001098 (2010).
1539 104. N. Chaudhary, D. Weissman, K. A. Whitehead, mRNA vaccines for infectious diseases:
1540 principles, delivery and clinical translation. *Nat. Rev. Drug Discov.* **20**, 817-838 (2021).
1541 105. D. S. Khoury *et al.*, Neutralizing antibody levels are highly predictive of immune
1542 protection from symptomatic SARS-CoV-2 infection. *Nat. Med.* **27**, 1205-1211 (2021).
1543 106. B. Nguyen, N. H. Tolia, Protein-based antigen presentation platforms for nanoparticle
1544 vaccines. *NPJ Vaccines* **6**, 70 (2021).
1545 107. D. J. Irvine, B. J. Read, Shaping humoral immunity to vaccines through antigen-
1546 displaying nanoparticles. *Curr. Opin. Immunol.* **65**, 1-6 (2020).
1547 108. R. Rappuoli, D. Serruto, Self-assembling nanoparticles usher in a new era of vaccine
1548 design. *Cell* **176**, 1245-1247 (2019).
1549 109. P. J. M. Brouwer, R. W. Sanders, Presentation of HIV-1 envelope glycoprotein trimers on
1550 diverse nanoparticle platforms. *Curr. Opin. HIV AIDS* **14**, 302-308 (2019).
1551 110. M. Brinkkemper, K. Sliepen, Nanoparticle vaccines for inducing HIV-1 neutralizing
1552 antibodies. *Vaccines* **7**, 76 (2019).
1553 111. B. Asbach, R. Wagner, Particle-based delivery of the HIV envelope protein. *Curr. Opin.*
1554 *HIV AIDS* **12**, 265-271 (2017).
1555 112. H. Y. Huang *et al.*, Vaccination with SARS-CoV-2 spike protein lacking glycan shields
1556 elicits enhanced protective responses in animal models. *Sci. Transl. Med.* **14**, eabm0899
1557 (2022).
1558 113. Y.-N. Zhang *et al.*, Single-component multilayered self-assembling protein nanoparticles
1559 presenting glycan-trimmed uncleaved prefusion optimized envelope trimers as HIV-1
1560 vaccine candidates. *Nat. Commun.* **14**, 1985 (2023).
1561 114. C. C. Wang *et al.*, Glycans on influenza hemagglutinin affect receptor binding and
1562 immune response. *Proc. Natl. Acad. Sci. U. S. A.* **106**, 18137-18142 (2009).
1563 115. S. C. Wang, H. Y. Liao, J. Y. Zhang, T. J. R. Cheng, C. H. Wong, Development of a
1564 universal influenza vaccine using hemagglutinin stem protein produced from Pichia
1565 pastoris. *Virol.* **526**, 125-137 (2019).
1566 116. B. R. West *et al.*, Structural basis of pan-ebolavirus neutralization by a human antibody
1567 against a conserved, yet cryptic epitope. *mBio* **9**, e01674-18 (2018).
1568 117. C. D. Murin *et al.*, Structural basis of pan-ebolavirus neutralization by an antibody
1569 targeting the glycoprotein fusion loop. *Cell Rep.* **24**, 2723-2732 (2018).
1570 118. B. M. Janus *et al.*, Structural basis for broad neutralization of ebolaviruses by an antibody
1571 targeting the glycoprotein fusion loop. *Nat. Commun.* **9**, 3934 (2018).
1572 119. B. R. West *et al.*, Structural basis of broad ebolavirus neutralization by a human survivor
1573 antibody. *Nat. Struct. Mol. Biol.* **26**, 204-212 (2019).
1574 120. D. Lyumkis *et al.*, Cryo-EM structure of a fully glycosylated soluble cleaved HIV-1
1575 envelope trimer. *Science* **342**, 1484-1490 (2013).
1576 121. S. Bangaru *et al.*, Structural analysis of full-length SARS-CoV-2 spike protein from an
1577 advanced vaccine candidate. *Science* **370**, 1089-1094 (2020).
1578 122. H. L. Turner *et al.*, Potent anti-influenza H7 human monoclonal antibody induces
1579 separation of hemagglutinin receptor-binding head domains. *PLoS Biol.* **17**, e3000139
1580 (2019).

1581 123. S. Bale *et al.*, Structural basis for differential neutralization of ebolaviruses. *Viruses* **4**,
1582 447-470 (2012).
1583 124. A. Punjani, J. L. Rubinstein, D. J. Fleet, M. A. Brubaker, cryoSPARC: algorithms for
1584 rapid unsupervised cryo-EM structure determination. *Nat. Methods* **14**, 290-296 (2017).
1585 125. B. A. Barad *et al.*, EMRinger: side chain directed model and map validation for 3D cryo-
1586 electron microscopy. *Nat. Methods* **12**, 943-946 (2015).
1587 126. P. Gilchuk *et al.*, Pan-ebolavirus protective therapy by two multifunctional human
1588 antibodies. *Cell* **184**, 5593-5607.e18 (2021).
1589 127. K. Braz Gomes *et al.*, Single-component multilayered self-assembling protein
1590 nanoparticles displaying extracellular domains of matrix protein 2 as a pan-influenza A
1591 vaccine. *ACS Nano* **17**, 23545-23567 (2023).
1592 128. Y.-N. Zhang *et al.*, Mechanism of a COVID-19 nanoparticle vaccine candidate that elicits
1593 a broadly neutralizing antibody response to SARS-CoV-2 variants. *Sci. Adv.* **7**, eabj3107
1594 (2021).
1595 129. R. Rappuoli, Glycoconjugate vaccines: principles and mechanisms. *Sci. Transl. Med.* **10**,
1596 eaat4615 (2018).
1597 130. J. G. Cyster, B cell follicles and antigen encounters of the third kind. *Nat. Immunol.* **11**,
1598 989-996 (2010).
1599 131. B. A. Heesters, R. C. Myers, M. C. Carroll, Follicular dendritic cells: dynamic antigen
1600 libraries. *Nat. Rev. Immunol.* **14**, 495-504 (2014).
1601 132. J. G. Cyster, P. C. Wilson, Antibody modulation of B cell responses-Incorporating
1602 positive and negative feedback. *Immunity* **57**, 1466-1481 (2024).
1603 133. J. Misasi *et al.*, Structural and molecular basis for Ebola virus neutralization by protective
1604 human antibodies. *Science* **351**, 1343-1346 (2016).
1605 134. A. Martínez-Riaño *et al.*, Long-term retention of antigens in germinal centers is
1606 controlled by the spatial organization of the follicular dendritic cell network. *Nat.*
1607 *Immunol.* **24**, 1281-1294 (2023).
1608 135. G. D. Victora, M. C. Nussenzweig, Germinal centers. *Annu. Rev. Immunol.* **30**, 429-457
1609 (2012).
1610 136. C. D. Allen, J. G. Cyster, Follicular dendritic cell networks of primary follicles and
1611 germinal centers: phenotype and function. *Semin. Immunol.* **20**, 14-25 (2008).
1612 137. B. A. Heesters, C. E. van der Poel, A. Das, M. C. Carroll, Antigen presentation to B cells.
1613 *Trends Immunol.* **37**, 844-854 (2016).
1614 138. M. E. M. El Shikh, R. M. El Sayed, S. Sukumar, A. K. Szakal, J. G. Tew, Activation of B
1615 cells by antigens on follicular dendritic cells. *Trends Immunol.* **31**, 205-211 (2010).
1616 139. G. A. Roth *et al.*, Designing spatial and temporal control of vaccine responses. *Nat. Rev.*
1617 *Mater.* **7**, 174-195 (2022).
1618 140. P. Yousefpour, K. Ni, D. J. Irvine, Targeted modulation of immune cells and tissues
1619 using engineered biomaterials. *Nat. Rev. Bioeng.* **1**, 107-124 (2023).
1620 141. Y. R. Carrasco, F. D. Batista, B cells acquire particulate antigen in a macrophage-rich
1621 area at the boundary between the follicle and the subcapsular sinus of the lymph node.
1622 *Immunity* **27**, 160-171 (2007).
1623 142. T. Junt *et al.*, Subcapsular sinus macrophages in lymph nodes clear lymph-borne viruses
1624 and present them to antiviral B cells. *Nature* **450**, 110-114 (2007).

1625 143. T. G. Phan, I. Grigorova, T. Okada, J. G. Cyster, Subcapsular encounter and
1626 complement-dependent transport of immune complexes by lymph node B cells. *Nat.*
1627 *Immunol.* **8**, 992-1000 (2007).
1628 144. T. G. Phan, J. A. Green, E. E. Gray, Y. Xu, J. G. Cyster, Immune complex relay by
1629 subcapsular sinus macrophages and noncognate B cells drives antibody affinity
1630 maturation. *Nat. Immunol.* **10**, 786-793 (2009).
1631 145. S. F. Gonzalez *et al.*, Capture of influenza by medullary dendritic cells via SIGN-R1 is
1632 essential for humoral immunity in draining lymph nodes. *Nat. Immunol.* **11**, 427-434
1633 (2010).
1634 146. C. D. Allen, T. Okada, J. G. Cyster, Germinal-center organization and cellular dynamics.
1635 *Immunity* **27**, 190-202 (2007).
1636 147. J. G. Cyster, C. D. C. Allen, B cell responses: cell interaction dynamics and decisions.
1637 *Cell* **177**, 524-540 (2019).
1638 148. F. D. Batista, N. E. Harwood, The who, how and where of antigen presentation to B cells.
1639 *Nat. Rev. Immunol.* **9**, 15-27 (2009).
1640 149. Z. Shulman *et al.*, T follicular helper cell dynamics in germinal centers. *Science* **341**,
1641 673-677 (2013).
1642 150. S. Crotty, T follicular helper cell differentiation, function, and roles in disease. *Immunity*
1643 **41**, 529-542 (2014).
1644 151. L. He *et al.*, Single-component, self-assembling, protein nanoparticles presenting the
1645 receptor binding domain and stabilized spike as SARS-CoV-2 vaccine candidates. *Sci.*
1646 *Adv.* **7**, eabf1591 (2021).
1647 152. L. He *et al.*, Proof of concept for rational design of hepatitis C virus E2 core nanoparticle
1648 vaccines. *Sci. Adv.* **6**, eaaz6225 (2020).
1649 153. Y. Z. Lee *et al.*, Rational design of uncleaved prefusion-closed trimer vaccines for human
1650 respiratory syncytial virus and metapneumovirus. *Nat. Commun.* **15**, 9939 (2024).
1651 154. S. E. Dunn, W. A. Perry, S. L. Klein, Mechanisms and consequences of sex differences in
1652 immune responses. *Nat. Rev. Nephrol.* **20**, 37-55 (2024).
1653 155. S. L. Klein, K. L. Flanagan, Sex differences in immune responses. *Nat. Rev. Immunol.*
1654 **16**, 626-638 (2016).
1655 156. R. W. Cross *et al.*, An introduction to the Marburg virus vaccine consortium, MARVAC.
1656 *PLoS Pathog.* **18**, e1010805 (2022).
1657 157. D. N. Wolfe *et al.*, Selection of filovirus isolates for vaccine development programs.
1658 *Vaccines* **9**, 1045 (2021).
1659 158. Y.-N. Zhang *et al.*, A single-component multilayered self-assembling protein
1660 nanoparticle vaccine based on extracellular domains of matrix protein 2 against both
1661 influenza A and B. *Vaccines* **12**, 975 (2024).
1662 159. L. He *et al.*, Presenting native-like trimeric HIV-1 antigens with self-assembling
1663 nanoparticles. *Nat. Commun.* **7**, 12041 (2016).
1664 160. L. He *et al.*, HIV-1 vaccine design through minimizing envelope metastability. *Sci. Adv.*
1665 **4**, aau6769 (2018).
1666 161. M. Gonzalez-Hernandez *et al.*, Preclinical immunogenicity and protective efficacy of a
1667 SARS-CoV-2 RBD-based vaccine produced with the thermophilic filamentous fungal
1668 expression system Thermothelomyces heterothallica C1. *Front. Immunol.* **14**, 1204834
1669 (2023).

162. L. Lazo *et al.*, A recombinant SARS-CoV-2 receptor-binding domain expressed in an engineered fungal strain of Thermothelomyces heterothallica induces a functional immune response in mice. *Vaccine* **40**, 1162-1169 (2022).
163. J. Korn *et al.*, Baculovirus-free insect cell expression system for high yield antibody and antigen production. *Sci. Rep.* **10**, 21393 (2020).
164. M.-A. Elsliger *et al.*, The JCSG high-throughput structural biology pipeline. *Acta Crystallogr. Sect. F Struct. Biol. Cryst. Commun.* **66**, 1137-1142 (2010).
165. Z. Otwinowski, W. Minor, Processing of X-ray diffraction data collected in oscillation mode. *Methods Enzymol.* **276**, 307-326 (1997).
166. P. Emsley, B. Lohkamp, W. G. Scott, K. Cowtan, Features and development of Coot. *Acta Crystallogr. D Biol. Crystallogr.* **66**, 486-501 (2010).
167. D. Liebschner *et al.*, Macromolecular structure determination using X-rays, neutrons and electrons: recent developments in Phenix. *Acta Crystallogr. D: Struct. Biol.* **75**, 861-877 (2019).
168. H. Berman, K. Henrick, H. Nakamura, Announcing the worldwide Protein Data Bank. *Nat. Struct. Biol.* **10**, 980 (2003).
169. E. Potterton, P. Briggs, M. Turkenburg, E. Dodson, A graphical user interface to the CCP4 program suite. *Acta Crystallogr. D Biol. Crystallogr.* **59**, 1131-1137 (2003).
170. G. Tang *et al.*, EMAN2: An extensible image processing suite for electron microscopy. *J. Struct. Biol.* **157**, 38-46 (2007).
171. E. F. Pettersen *et al.*, UCSF chimera - A visualization system for exploratory research and analysis. *J. Comput. Chem.* **25**, 1605-1612 (2004).
172. E. C. Meng *et al.*, UCSF ChimeraX: Tools for structure building and analysis. *Protein Sci.* **32**, e4792 (2023).
173. E. F. Pettersen *et al.*, UCSF ChimeraX: Structure visualization for researchers, educators, and developers. *Protein Sci.* **30**, 70-82 (2021).
174. T. D. Goddard *et al.*, UCSF ChimeraX: Meeting modern challenges in visualization and analysis. *Protein Sci.* **27**, 14-25 (2018).
175. J. Zhu, L. Xie, B. Honig, Structural refinement of protein segments containing secondary structure elements: Local sampling, knowledge-based potentials, and clustering. *Proteins: Struct. Funct. Bioinf.* **65**, 463-479 (2006).
176. B. L. deGroot *et al.*, Prediction of protein conformational freedom from distance constraints. *Proteins: Struct. Funct. Genet.* **29**, 240-251 (1997).
177. R. Samudrala, J. Moult, An all-atom distance-dependent conditional probability discriminatory function for protein structure prediction. *J. Mol. Biol.* **275**, 895-916 (1998).
178. C. A. Schneider, W. S. Rasband, K. W. Eliceiri, NIH Image to ImageJ: 25 years of image analysis. *Nat. Methods* **9**, 671-675 (2012).

1709 **Figure Legends**

1710 **Fig. 1. Rational design and in vitro characterization of orthoebolavirus GP trimers.** (**a**)
1711 Schematic of GP construct design, including MLD deletion (Δmuc, residues G314–N463), a P^2
1712 (T577P) or P^4 (L579P) mutation in the HR1c bend, a W615L mutation at the neck of the HR2 stalk,
1713 and a C-terminal extension (D632–D637). IFL: internal fusion loop. (**b**) Schematic of an
1714 orthoebolavirus GP trimer bound to NAb ADI-15878 (left), and SEC profiles of six GPΔmuc
1715 constructs expressed in 500 ml HEK293F cultures and purified using an ADI-15878 IAC column
1716 (right). Aggregation (A) and trimer (T) peaks are indicated. (**c**) BN-PAGE analysis of six ADI-
1717 15878/SEC-purified GPΔmuc trimers, showing bands consistent with trimer size and molecular
1718 weight. (**d**) DSC thermograms of six ADI-15878/SEC-purified GPΔmuc trimers. Experimental
1719 data (black dots) and Gaussian fits (red lines) are shown, with key parameters labeled: melting
1720 temperature(s) (T_m, or T_{m1} and T_{m2}), onset temperature (T_{onset}), and peak half-width ($\Delta T_{1/2}$). (**e**)
1721 Site-specific glycan profiles of ADI-15878/SEC-purified EBOV, SUDV, and BDBV GPΔmuc-
1722 WL^2P^4 trimers. Glycan compositions are grouped into four types, including complex (pink), hybrid
1723 (pink striped), oligomannose (green), and unoccupied (gray). "N.D.": not determined; "N.P.": not
1724 present. (**f**) nsEM-derived 3D reconstructions of EBOV, SUDV, and BDBV GPΔmuc-WL^2P^4
1725 trimers and their complexes with NAb ADI-15878. Crystal structures of EBOV GPΔmuc-WL^2P^2
1726 (PDB ID: 7JPH) and ADI-15878 (PDB ID: 6DZN) were used in the density fitting, with GP1, GP2,
1727 and Fab shown in cyan, green, and pink, respectively. (**g**) ELISA-derived EC_{50} (μg/ml) values for
1728 the six orthoebolavirus GPΔmuc trimers binding to four pan-orthoebolavirus NAbs and the MARV
1729 NAb, MR78. If absorbance at 450 nm was <0.5 at the starting concentration (10 μg/ml), the antigen
1730 was considered a non-binder with the EC_{50} value set to 10 μg/ml. (**h**) BLI profiles for the same six
1731 GPΔmuc trimers binding to the same NAbs. Sensorgrams were collected using a six-point, 2-fold

1732 antigen dilution (starting at 600 nM) from an Octet RED96 instrument and are shown in **Fig. S1i**.
1733 Peak responses at the highest concentration are summarized in a matrix, color-coded from green
1734 (weak binding) to red (strong binding).

1735 **Fig. 2. Structural characterization of an unliganded EBOV GPΔmuc-WL^{2}P^4 trimer and a**
1736 **SUDV GPΔmuc-WL^{2}P^4 trimer bound to NAb CA45.** (**a**) Left: crystal structure of the stabilized
1737 EBOV GPΔmuc-WL^{2}P^4 trimer determined at 3.2 Å resolution, with GP1 in cyan, glycan cap in
1738 gray, IFL in pink, and GP2 in gold. Structural details could not be resolved for residues R200-
1739 P209, K294-I301, and T634-D637 (C terminus). Right: comparative analysis of the HR1c bend
1740 and its local structure for EBOV GPΔmuc constructs bearing WL^2 (PDB ID: 7JPI), WL^{2}P^2 (PDB
1741 ID: 7JPH), and WL^{2}P^4 mutations. Side chains are shown for residues forming cross-protomer
1742 interactions (L95, R130, L573, and T576). A 3.3 Å cutoff was used to define donor-acceptor
1743 distances for hydrogen bonds. (**b**) Cryo-EM 3D reconstruction of the SUDV GPΔmuc-WL^{2}P^4
1744 trimer bound to CA45 Fab at 3.13 Å resolution, with GP1 in orange, GP2 in green, CA45 heavy
1745 chain in blue, and light chain in pink. The glycan cap and HR2 stalk were not resolved and became
1746 partially visible at lower density thresholds beyond 4.0 Å (see **Fig. S2e**). (**c**) Ribbon representation
1747 of the cryo-EM-derived SUDV GPΔmuc-WL^{2}P^4/CA45 complex using the color scheme. Atomic
1748 details of the glycan cap and HR2 stalk could not be resolved due to limited local resolution. Left:
1749 atomic details of hydrogen bonds between GP and the CA45 heavy chain (top) and light chain
1750 (bottom). Right: superposition of the HR1c bend in SUDV GPΔmuc-WL^{2}P^4 with that of BDBV
1751 GPΔmuc (top, cryo-EM) and EBOV GPΔmuc-WL^{2}P^4 (bottom, crystal structure).

1752 **Fig. 3. Rational design and in vitro characterization of orthoebolavirus GP-presenting**
1753 **SApNPs.** (**a**) SApNP optimization for surface display of trimeric antigens with a narrow stalk.
1754 Twenty I3-01v9a trimers assemble into an SApNP (left), with the N-termini forming a triangle of

1755 43.9 Å (middle). Using computational design, a helical extension was added to the I3-01v9a N-
1756 terminus to pack against the protein core, reducing the triangle to 12.9 Å and yielding I3-01v9b/c
1757 (right). (**b**) nsEM analysis of EBOV GPΔmuc-WL^{2}P^4-I3-01v9b-T, in which I3-01v9b-T is a
1758 trimeric version of I3-01v9b with mutations that interrupt particle assembly. Top: representative
1759 2D class averages; Bottom: side and top views of the 3D reconstruction with fitted EBOV
1760 GPΔmuc-WL^{2}P^4 and aldolase (PDB: 1VLW) structures. (**c**) Schematic of EBOV GPΔmuc-
1761 WL2P4-presenting I3-01v9b/c SApNP. The predicted particle diameter is 49.1 nm, measured at
1762 GP1 residue T269. (**d**) SEC profiles of six orthoebolavirus GPΔmuc-WL^{2}P^4-presenting SApNPs
1763 expressed in ExpiCHO cells and purified using an ADI-15878 IAC column. Peaks corresponding
1764 to full NPs, partially assembled NPs (pNP), and trimers (T) are indicated. (**e**) Representative nsEM
1765 images of the six SEC-purified SApNPs. Scale bar: 50 nm. (**f**) Particle size distributions of the six
1766 SEC-purified SApNPs measured by DLS. Three independent measurements are shown for each
1767 construct, with hydrodynamic diameters (D_h) labeled. (**g**) Site-specific glycan profile of SUDV
1768 GPΔmuc-WL^{2}P^4-presenting E2p and I3-01v9b SApNPs. Glycan types are colored as in **Fig. 1e**.
1769 (**h**) ELISA-derived EC_{50} (μg/ml) values for six orthoebolavirus GPΔmuc-WL^{2}P^4-presenting
1770 SApNPs binding to five NAbs. Absorbance <0.5 at 10 μg/ml was used as a non-binding cutoff, as
1771 in **Fig. 1g**. (**i**) BLI profiles for the same six SApNPs binding to the same five NAbs. Sensorgrams
1772 were obtained using the same protocol as in **Fig. 1h** (see **Fig. S3k**). Peak responses at the highest
1773 concentration are summarized in a matrix as in **Fig. 1h**.

1774 **Fig. 4. Glycan modification of EBOV and SUDV GPΔmuc-WL^{2}P^4 trimers and SApNPs.** (**a**)
1775 SEC profiles of EBOV and SUDV GPΔmuc-WL^{2}P^4 constructs expressed in 500 ml HEK293F
1776 cultures and purified using an ADI-15878 IAC column. For each construct, two types of glycan
1777 modifications were performed: kifunensine (Kif) treatment and Kif plus Endo H (Kif/Endo H)

1778 treatment. HEK293F expression in the presence of Kif enriches oligomannose-type glycans, and
1779 subsequent Endo H treatment yields GlcNAc stumps. The SEC peak at 14.7 ml corresponds to
1780 Endo H. (**b**) DSC thermograms of ADI-15878/SEC-purified EBOV and SUDV GPΔmuc-WL^{2}P^4
1781 trimers after glycan modification. Experimental data and Gaussian fits are shown as black dots and
1782 red lines, respectively. Melting temperatures (T_m or T_{m1}/T_{m2}), onset temperature (T_{onset}), and peak
1783 half-width ($\Delta T_{1/2}$) are labeled. (**c**) ELISA-derived EC_{50} (μg/ml) values of glycan-modified EBOV
1784 and SUDV GPΔmuc-WL^{2}P^4 trimers binding to five NAbs. Absorbance <0.5 at 10 μg/ml was used
1785 as a non-binding cutoff, as in **Fig. 1f**. (**d**) BLI profiles of the same glycan-modified trimers binding
1786 to five NAbs. Sensorgrams were obtained using the same protocol as in **Fig. 1h** (see **Fig. S4c**)
1787 Peak responses at the highest concentration are summarized in a matrix, as in **Fig. 1h**. (**e**) SEC
1788 profiles (top) and nsEM images (bottom) of glycan-modified EBOV and SUDV GPΔmuc-WL^{2}P^4-
1789 presenting SApNPs. Glycan modification was performed as in panel (a). EBOV GPΔmuc I3-
1790 01v9bs are not shown due to low yield. Scale bar: 50 nm. (**f**) Site-specific glycan profiles of SUDV
1791 GPΔmuc-WL^{2}P^4-presenting E2p and I3-01v9b SApNPs before and after Kif treatment, with
1792 glycan types colored as in **Fig. 1e**. (**g**) ELISA-derived EC_{50} (μg/ml) values for glycan-modified
1793 SUDV GPΔmuc-WL^{2}P^4-presenting E2p and I3-01v9b SApNPs binding to five NAbs. Absorbance
1794 <0.5 at 10 μg/ml was used as a non-binding cutoff, as in **Fig. 1g**. (**h**) BLI profiles of the same
1795 glycan-modified SApNPs binding to five NAbs. Sensorgrams were obtained using the same
1796 protocol as in **Fig. 1h** (see **Fig. S4h**). Peak responses are summarized in a matrix, as in **Fig. 1h**.

1797 **Fig. 5. Rational design and in vitro characterization of orthomarburgvirus GP trimers.** (**a**)
1798 Schematic of GP construct design based on the RAVV backbone, including MLD deletion (Δmuc,
1799 residues T256–T424), a P^2 (T578P) or P^4 (E580P) mutation in the HR1c bend, and a C-terminal
1800 double mutation (E631F/Q632V). (**b**) SEC profiles of four RAVV GP constructs expressed in 16

1801 ml ExpiCHO cultures and purified using a nickel column. Aggregation (A), trimer (T), and subunit
1802 (S) peaks are indicated. (**c**) BN-PAGE analysis of RAVV GPΔmuc-P^2CT trimer fractions purified
1803 by SEC. (**d**) DSC thermograms of nickel/SEC-purified RAVV GPΔmuc-P^2 and GPΔmuc-P^2CT
1804 trimers. Experimental data (black dots) and Gaussian fits (red lines) are shown, with melting
1805 temperatures (T_{m1}, T_{m2}, and T_{m3}) labeled. (**e**) nsEM analysis of RAVV GPΔmuc-P^2CT/MR78 Fab
1806 complex. Left: crystal structure (PDB ID: 5UQY) of RAVV GPΔmuc/MR78 Fab complex fitted
1807 into the nsEM density. Right: nsEM density map of RAVV GPΔmuc/MR78 Fab complex (EMDB:
1808 6233, orange surface) overlaid with the nsEM map obtained in this study. (**f**) Site-specific glycan
1809 profile of RAVV GPΔmuc-P^2CT trimer. Glycan types are colored as in **Fig. 1e**. (**g**) ELISA-derived
1810 EC_{50} (μg/ml) values for RAVV GPΔmuc-P^2 and GPΔmuc-P^2CT trimers binding to MARV NAbs
1811 MR78 and MR191. Absorbance <0.5 at 10 μg/ml was used as a non-binding cutoff, as in **Fig. 1f**.
1812 (**h**) BLI profiles of RAVV GPΔmuc-P^2 and GPΔmuc-P^2CT trimers binding to MARV NAbs MR78
1813 and MR191. Sensorgrams were obtained using the same protocol as in **Fig. 1h** (see **Fig. S5h**).
1814 Peak responses are summarized in a matrix, as in **Fig. 1h**.

1815 **Fig. 6. Retention of SUDV GPΔmuc-presenting SApNPs in lymph node follicles.** (**a, b**) Left:
1816 distribution of (**a**) E2p and (**b**) I3-01v9b SApNPs displaying SUDV GPΔmuc-WL^2P^4 trimers in
1817 lymph nodes 12 h after a single-dose injection (10 μg/injection, 40 μg/mouse). NAb CA45 was
1818 used to stain the sentinel lymph node sections. Right: schematic of SUDV SApNP accumulation
1819 in lymph node follicles. (**c**) Trafficking and retention of the SUDV GPΔmuc trimer and SApNPs
1820 in lymph node follicles 2 h to 8 weeks after a single-dose injection. Scale bar: 50 μm. (**d**) Time-
1821 dependent curve and (**e**) area under the curve (AUC) of CA45-stained areas in immunohistological
1822 images of SUDV vaccine retention in lymph node follicles over 8 weeks. (**f**) Quantification of
1823 SUDV vaccine accumulation in lymph node follicles 48 h after a single-dose injection. Data were

1824 collected from > 10 lymph node follicles (n = 3-5 mice/group). (**g**) Interaction of the SUDV
1825 GPΔmuc trimer and SApNPs with FDC networks in lymph node follicles 48 h after a single-dose
1826 injection. Both E2p and I3-01v9b SApNPs colocalized with FDC networks. Immunofluorescent
1827 images are pseudo-color-coded ($CD21^+$, green; $CD169^+$, red; CA45, white). Scale bars: 500 (whole
1828 lymph node) and 100 μm (enlarged follicle). Data are presented as mean ± SEM in (d), and mean
1829 ± SD in (e, f). Statistical analysis was performed using one-way ANOVA followed by Tukey's
1830 multiple comparison *post hoc* test. **$p < 0.01$, ****$p < 0.0001$.

1831 **Fig. 7. Interaction of SUDV GPΔmuc-presenting SApNPs with FDCs and phagocytic cells in**
1832 **lymph nodes. (a-c)** TEM images of (**a**) E2p and (**b, c**) I3-01v9b SApNPs (yellow arrows)
1833 displaying SUDV GPΔmuc-WL^2P^4 trimers aligned on FDC dendrites in lymph node follicles at (**a,**
1834 **b**) 12 h and (**c**) 48 h after a single-dose injection. Each mouse received 200 μl of antigen/aluminum
1835 phosphate (AP) adjuvant mix (100 μg SApNP + 100 μl adjuvant), administered into both hind
1836 footpads (2 footpads, 50 μg/footpad). Fresh popliteal lymph nodes were collected. No AP adjuvant
1837 was observed on FDC dendrites. (**d, e**) TEM images of (**d**) E2p and (**e**) I3-01v9b SApNPs (yellow
1838 arrows) displaying SUDV GPΔmuc-WL^2P^4 trimers on the surface and within endolysosomes of
1839 phagocytic cells at 12 h post-injection. (**f**) TEM images showing AP adjuvant (green arrows)
1840 aggregated in the extracellular matrix (ECM) at 2 h post-injection. (**g**) TEM images of Sudan
1841 GPΔmuc-presenting I3-01v9b SApNPs and AP adjuvant localized inside endolysosomes of
1842 phagocytic cells at 48 h post-injection.

1843 **Fig. 8. Induction of germinal center reactions by SUDV GPΔmuc-presenting SApNPs in**
1844 **lymph nodes**. (**a**) Top: representative immunofluorescent images of germinal centers (GCs)
1845 induced by the SUDV GPΔmuc-presenting SApNP vaccine 2 weeks after a single-dose injection
1846 (10 μg/injection, 40 μg/mouse). Each dose consisted of 80 μl of antigen/aluminum phosphate (AP)

1847 adjuvant mix. Bottom: robust GC formation with well-organized light zone (LZ) and dark zone
1848 (DZ) compartments in lymph node follicles. GC B cells ($GL7^+$, red) attached to FDCs ($CD21^+$,
1849 green) and T_{fh} cells located in the LZ. Scale bars: 500 μm (whole lymph node), 100 μm (enlarged
1850 follicle). (**b**, **c**) Assessment of GC responses from immunofluorescent images at 2, 5, and 8 weeks
1851 after a single-dose injection, or 2 and 5 weeks after a boost administered 3 weeks post-prime (n =
1852 5 mice/group). The GC/FDC ratio and GC size were measured and plotted. (**d**, **e**) Representative
1853 GC immunofluorescent images from lymph nodes collected at week 8 after single-dose or prime-
1854 boost immunization with SUDV GPΔmuc vaccines. Scale bar: 50 μm. (**f, g**) Quantification of GCs
1855 by flow cytometry after single-dose or prime-boost regimens (n = 5 mice/group). Frequency and
1856 number of GC B cells and T_{fh} cells were characterized and plotted. Data are shown as mean ± SD.
1857 Statistical analysis was performed using one-way ANOVA followed by Tukey's multiple
1858 comparison *post hoc* test at each timepoint. ns (not significant), *$p < 0.05$, **$p < 0.01$, ***$p <$
1859 0.001, ****$p < 0.0001$.

1860 **Fig. 9**. **Antibody responses to rationally designed filovirus vaccines in mice.** (a) Schematic of
1861 the mouse immunization regimen for in vivo evaluation of EBOV, SUDV, and RAVV GPΔmuc
1862 vaccines (n = 8 mice/group). Each dose consisted of 200 μl of antigen/AH + CpG adjuvant mix
1863 containing 10 μg of immunogen and 100 μl of adjuvant. Mice were immunized at weeks 0, 3, 9,
1864 and 15 via the intraperitoneal (i.p.) route, with 6-week intervals between the second and third, and
1865 third and fourth doses. (**b-d**) EBOV vaccine-induced binding antibody (bAb) responses against (**b**)
1866 EBOV GPΔmuc-WL^2P^4(1TD0), (**c**) SUDV GPΔmuc-WL^2P^4(1TD0), and (**d**) RAVV GPΔmuc-
1867 P^2CT(1TD0). (**e-g**) EBOV vaccine-induced NAb responses against (**e**) EBOV Makona, (**f**) SUDV
1868 Gulu, and (**g**) BDBV Uganda pseudoviruses. (**h-j**) SUDV vaccine-induced bAb responses against
1869 (**h**) SUDV GPΔmuc-WL^2P^4(1TD0), (**i**) EBOV GPΔmuc-WL^2P^4(1TD0), and (**j**) RAVV GPΔmuc-

1870 $P^2CT(1TD0)$. (**k-m**) SUDV vaccine-induced NAb responses against (**k**) SUDV Gulu, (**l**) EBOV
1871 Makona, and (**m**) BDBV Uganda pseudoviruses. (**n-p**) RAVV vaccine-induced bAb responses
1872 against (**n**) RAVV GPΔmuc-$P^2CT(1TD0)$, (**o**) EBOV GPΔmuc-$WL^2P^4(1TD0)$, and (**p**) SUDV
1873 GPΔmuc-$WL^2P^4(1TD0)$. (**q**) RAVV vaccine-induced NAb responses against MARV Angola
1874 pseudovirus (using purified IgG) and pseudotyped orthoebolaviruses (using serum). EC_{50} titers
1875 were derived from serum ELISA against coating antigens, and ID_{50}/IC_{50} titers were determined
1876 from pseudovirus neutralization assays. Geometric means are labeled on the plots. ID_{50}/IC_{50} values
1877 were calculated using a % neutralization range of 0.0–100.0%. Color coding indicates ID_{50}
1878 magnitude (green to red: low to high neutralization). Data are presented as the mean ± SD.
1879 Statistical analysis was performed using one-way ANOVA followed by Tukey's multiple
1880 comparison *post hoc* test at each timepoint. ns (not significant), $*p < 0.05$, $**p < 0.01$, $***p <$
1881 0.001, and $****p < 0.0001$. The schematic in (a) was created with BioRender.com.

1882 **Fig. 10. Effect of glycan modification on antibody responses elicited by filovirus vaccines.**
1883 Schematic of the mouse immunization regimen for in vivo evaluation of glycan-modified EBOV,
1884 SUDV, and RAVV vaccines (n = 8 mice/group). Each dose consisted of 200 µl of antigen/AH +
1885 CpG adjuvant mix containing 10 µg of glycan-modified immunogen and 100 µl of adjuvant. Mice
1886 were immunized at weeks 0, 3, 6, and 9 via the intraperitoneal (i.p.) route, with 3-week intervals
1887 between doses. Vaccine immunogenicity was compared across three conditions: wild-type, Kif-
1888 treated (oligomannose-enriched), and Kif/Endo H-treated (a monolayer of GlcNAc stumps). (**b-d**)
1889 Glycan-modified EBOV vaccine-induced bAb responses against EBOV GPΔmuc-$WL^2P^4(1TD0)$.
1890 (**e-g**) Glycan-modified EBOV vaccine-induced NAb responses against EBOV Makona
1891 pseudovirus. (**h-j**) Glycan-modified SUDV vaccine-induced bAb responses against SUDV
1892 GPΔmuc-$WL^2P^4(1TD0)$. (**k-m**) Glycan-modified SUDV vaccine-induced NAb responses against

1893 Gulu pseudovirus. (**n**) Glycan-trimmed RAVV vaccine-induced bAb responses against RAVV
1894 GPΔmuc-P^2CT(1TD0). (**o**) Glycan-trimmed RAVV vaccine-induced NAb responses against
1895 MARV Angola and pseudotyped orthoebolaviruses using purified IgG. EC_{50} titers were derived
1896 from serum ELISA against coating antigens, and ID_{50}/IC_{50} titers were determined from the
1897 pseudovirus neutralization assays. Geometric means are labeled on the plots. ID_{50}/IC_{50} values were
1898 calculated using a % neutralization range of 0.0–100.0%. Color coding indicates IC50 magnitude
1899 (green to red: low to high neutralization). Data for wild-type EBOV GPΔmuc trimer and SApNPs,
1900 SUDV GPΔmuc trimer, and RAVV GPΔmuc trimer from the long-interval immunization study
1901 were included for comparison. Boost timepoints (W11 and W17) were labeled but were excluded
1902 from statistical analysis. Data are presented as the mean ± SD. Statistical analysis was performed
1903 using one-way ANOVA, followed by Tukey's multiple comparison *post hoc* test at each timepoint.
1904 Two-tailed unpaired t-tests were used to compare geometric means between two groups. ns (not
1905 significant), *$p < 0.05$, **$p < 0.01$, ***$p < 0.001$, and ****$p < 0.0001$. The schematic in (a) was
1906 created with BioRender.com.

Figure 1

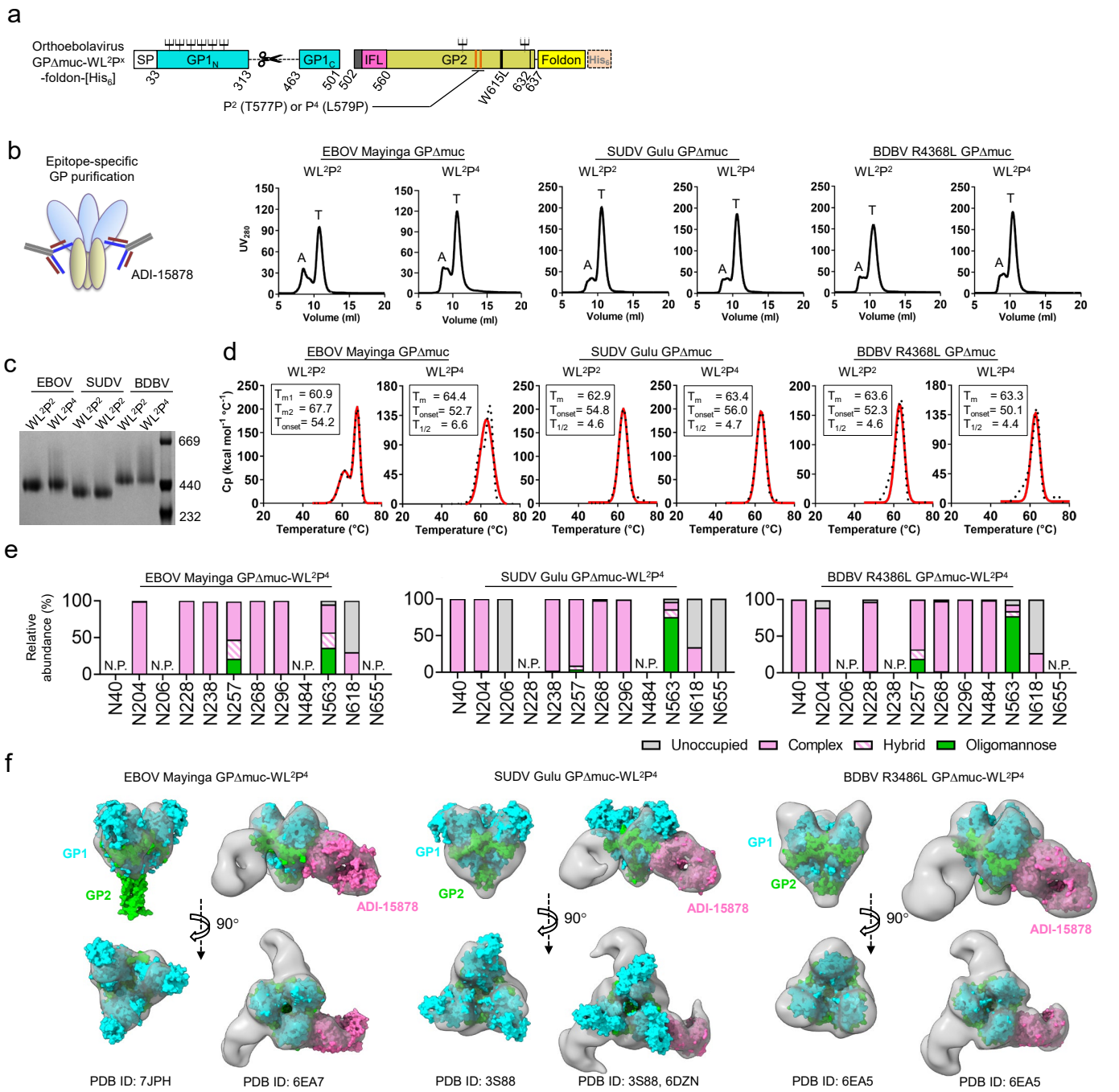

	CA45	ADI-15878	ADI-15946	BDBV-289	MR78
EBOV Mayinga GPΔmuc-WL^{2}P^2	0.68	0.58	0.38	0.41	0.00
EBOV Mayinga GPΔmuc-WL^{2}P^4	0.69	0.59	0.37	0.39	0.00
SUDV Gulu GPΔmuc-WL^{2}P^2	0.51	0.63	0.32	0.21	0.00
SUDV Gulu GPΔmuc-WL^{2}P^4	0.54	0.68	0.38	0.22	0.00
BDBV R4386L GPΔmuc-WL^{2}P^2	0.54	0.62	0.44	0.48	0.01
BDBV R4386L GPΔmuc-WL^{2}P^4	0.59	0.65	0.44	0.48	0.00

Figure 2

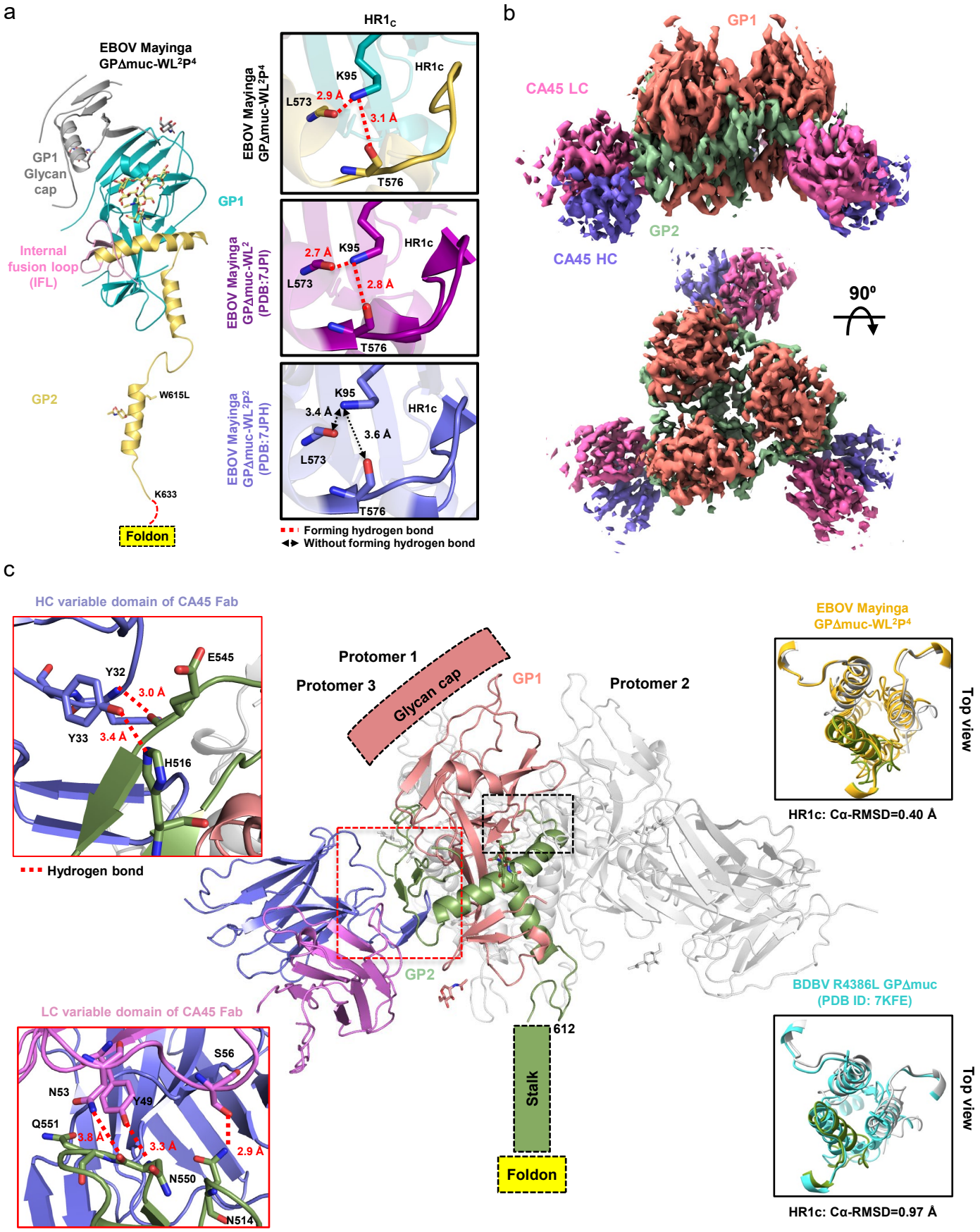
a
EBOV Mayinga
GPΔmuc-WL2P4
GP1
Glycan
cap
GP1
Internal
fusion loop
(IFL)
GP2
W615L
K633
Foldon
HR1c
EBOV Mayinga
GPΔmuc-WL2P4
K95
HR1c
L573
2.9 Å
3.1 Å
T576
EBOV Mayinga
GPΔmuc-WL2
(PDB:7JPI)
2.7 Å
K95
HR1c
L573
2.8 Å
T576
EBOV Mayinga
GPΔmuc-WL2P2
(PDB:7JPH)
K95
3.4 Å
HR1c
3.6 Å
L573
T576
Forming hydrogen bond
Without forming hydrogen bond
b
GP1
CA45 LC
GP2
CA45 HC
90º
c
HC variable domain of CA45 Fab
E545
Y32
3.0 Å
Y33
3.4 Å
H516
Hydrogen bond
Protomer 1
Protomer 3
Glycan cap
GP1
Protomer 2
GP2
612
Stalk
Foldon
EBOV Mayinga
GPΔmuc-WL2P4
Top view
HR1c: Cα-RMSD=0.40 Å
BDBV R4386L GPΔmuc
(PDB ID: 7KFE)
Top view
HR1c: Cα-RMSD=0.97 Å
LC variable domain of CA45 Fab
S56
N53
Y49
Q551
3.8 Å
3.3 Å
2.9 Å
N550
N514

Figure 3

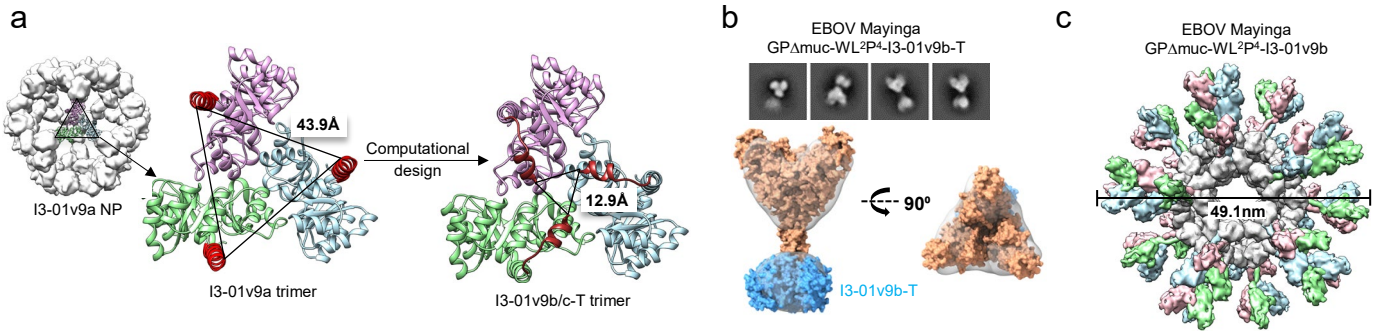

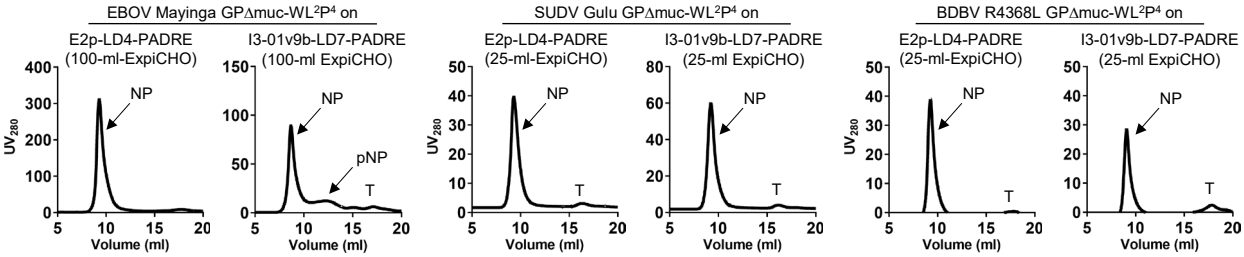

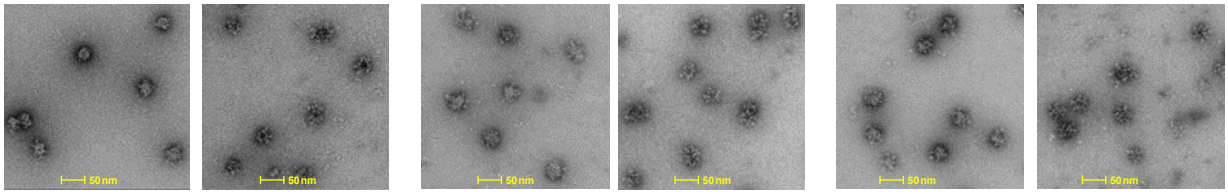

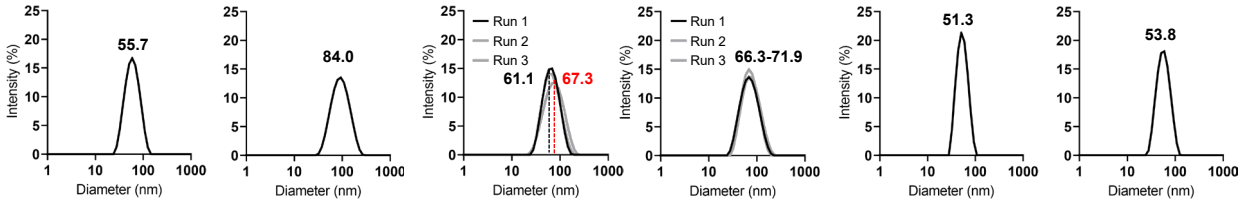

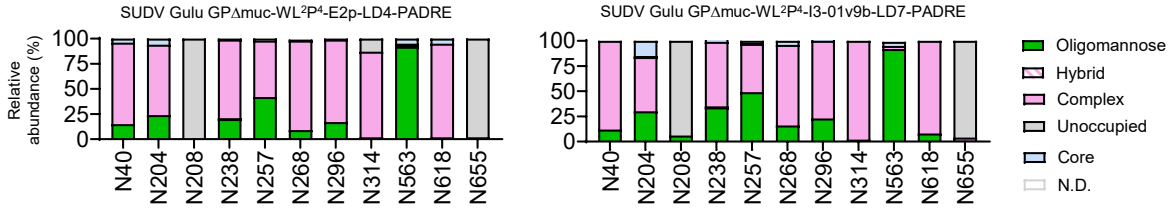

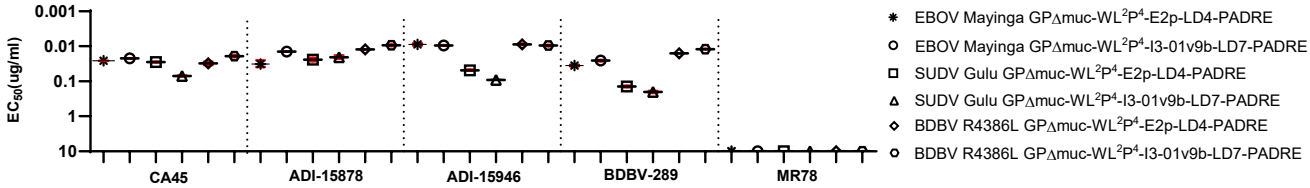

i

	CA45	ADI-15878	ADI-15946	BDBV-289	MR78
EBOV Mayinga GPΔmuc-WL^{2}P^4-E2p-LD4-PADRE	0.71	0.90	0.73	0.79	0.01
EBOV Mayinga GPΔmuc-WL^{2}P^4-I3-01v9b-LD7-PADRE	0.90	0.83	0.66	0.68	0.03
SUDV Gulu GPΔmuc-WL^{2}P^4-E2p-LD4-PADRE	1.37	1.60	1.37	0.51	0.00
SUDV Gulu GPΔmuc-WL^{2}P^4-I3-01v9b-LD7-PADRE	0.72	1.44	1.06	0.39	0.01
BDBV R4386L GPΔmuc-WL^{2}P^4-E2p-LD4-PADRE	0.95	1.68	1.24	2.03	0.01
BDBV R4386L GPΔmuc-WL^{2}P^4-I3-01v9b-LD7-PADRE	0.50	1.21	1.24	0.87	0.00

Figure 4

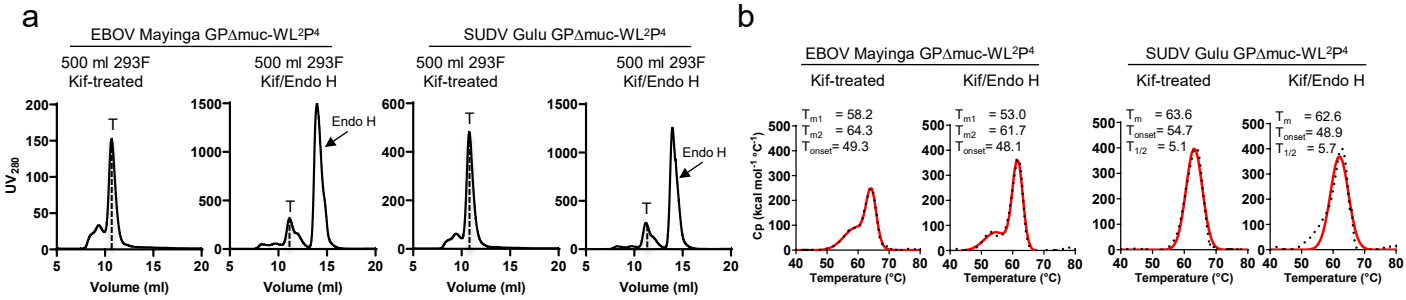

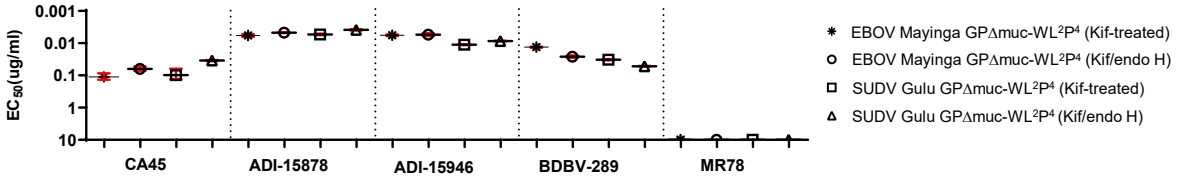

d

	CA45	ADI-15878	ADI-15946	BDBV-289	MR78
EBOV Mayinga GPΔmuc-WL^{2}P^4 (Kif-treated)	0.80	0.71	0.53	0.58	0.00
EBOV Mayinga GPΔmuc-WL^{2}P^4 (Kif/endo H)	0.74	0.62	0.45	0.51	0.00
SUDV Gulu GPΔmuc-WL^{2}P^4 (Kif-treated)	0.76	0.70	0.51	0.44	0.00
SUDV Gulu GPΔmuc-WL^{2}P^4 (Kif/endo H)	0.75	0.71	0.55	0.49	0.00

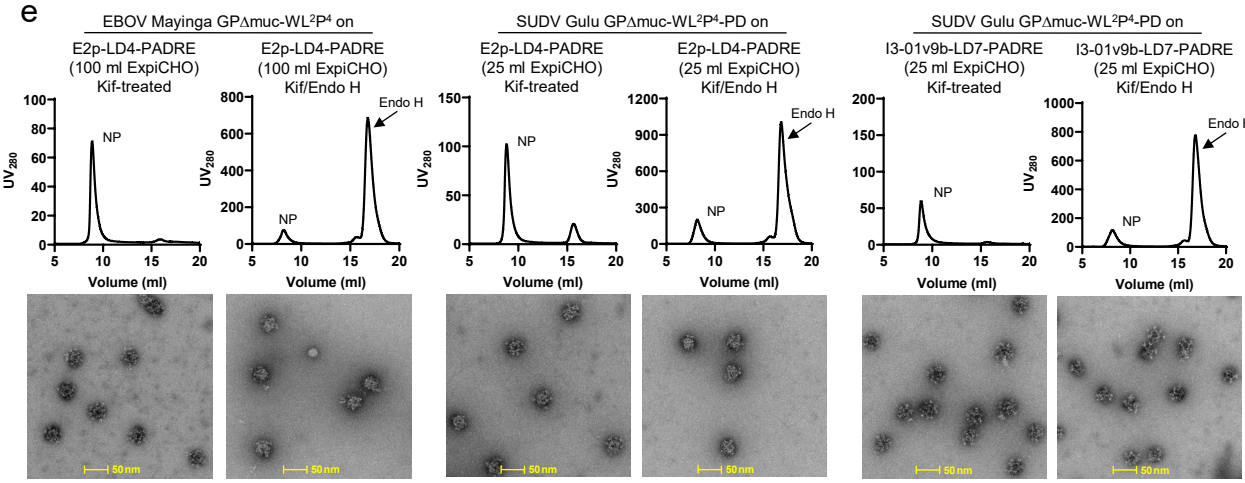

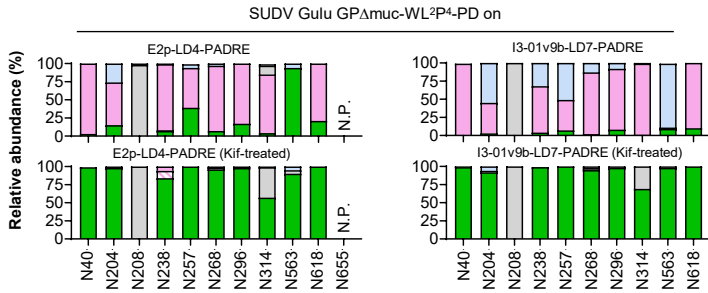

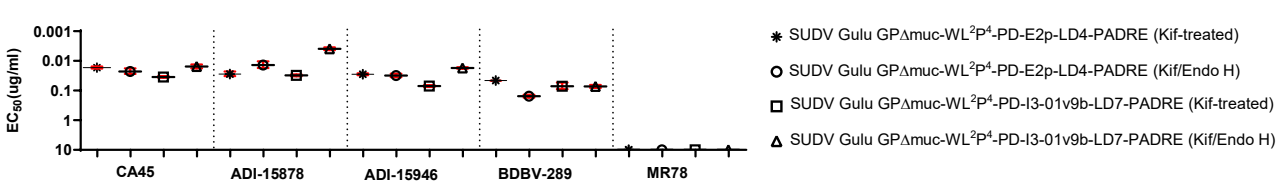

h

	CA45	ADI-15878	ADI-15946	BDBV-289	MR78
SUDV Gulu GPΔmuc-WL^{2}P^4-PD-E2p-LD4-PADRE (Kif-treated)	1.29	1.46	1.44	0.48	0.01
SUDV Gulu GPΔmuc-WL^{2}P^4-PD-E2p-LD4-PADRE (Kif/Endo H)	1.63	2.23	1.78	0.58	0.00
SUDV Gulu GPΔmuc-WL^{2}P^4-PD-I3-01v9b-LD7-PADRE (Kif-treated)	0.89	1.43	1.20	0.42	0.01
SUDV Gulu GPΔmuc-WL^{2}P^4-PD-I3-01v9b-LD7-PADRE (Kif/Endo H)	1.00	1.60	1.35	0.64	0.00

Figure 5

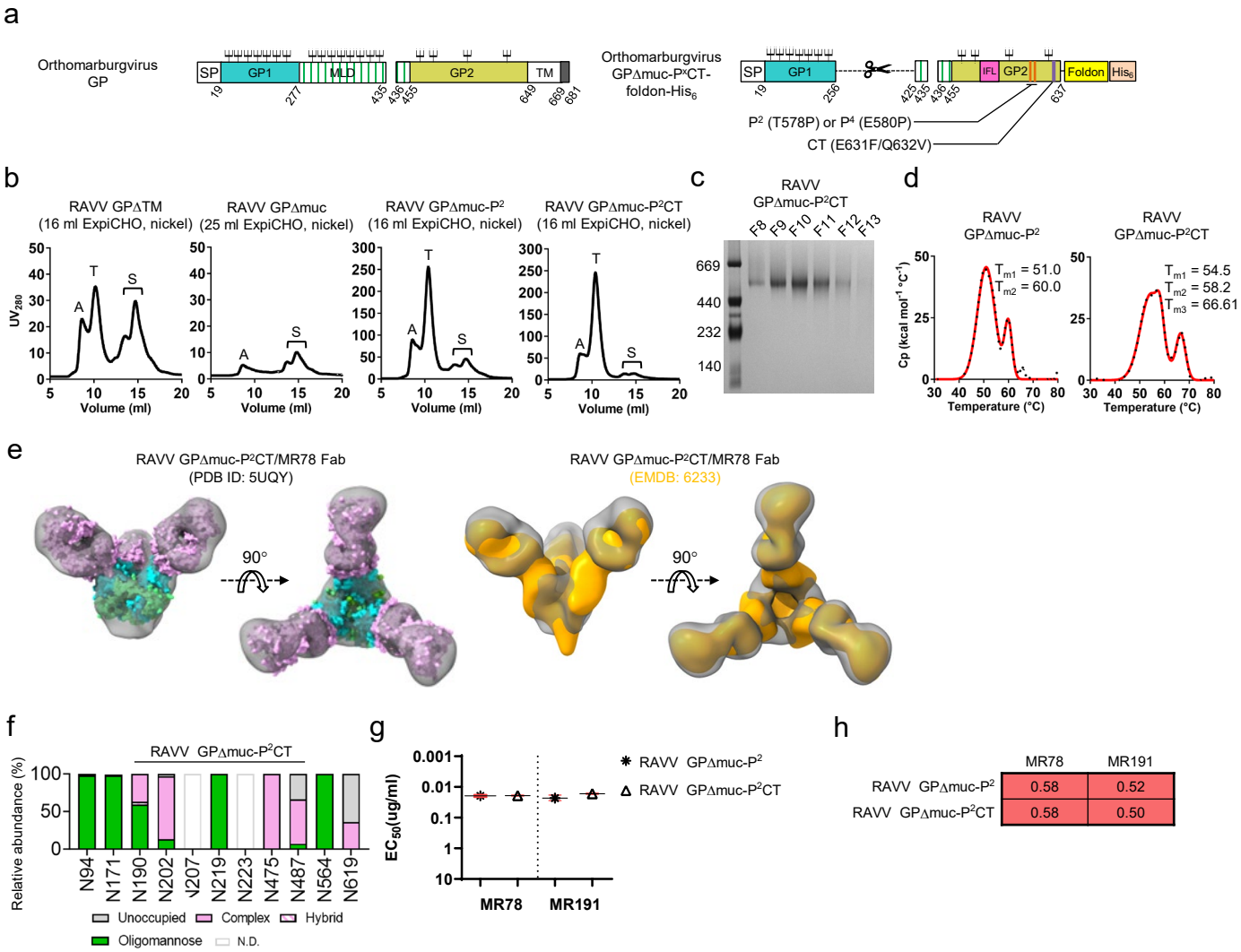
a
Orthomarburgvirus GP
SP
GP1
MLD
GP2
TM
19
277
435
436
455
649
669
681
Orthomarburgvirus GPΔmuc-P^X CT-foldon-His6
IFL
Foldon
His6
256
425
637
P2 (T578P) or P4 (E580P)
CT (E631F/Q632V)
b
RAVV GPΔTM (16 ml ExpiCHO, nickel)
RAVV GPΔmuc (25 ml ExpiCHO, nickel)
RAVV GPΔmuc-P2 (16 ml ExpiCHO, nickel)
RAVV GPΔmuc-P2CT (16 ml ExpiCHO, nickel)
UV280
Volume (ml)
A
T
S
c
RAVV GPΔmuc-P2CT
F8
F9
F10
F11
F12
F13
669
440
232
140
d
RAVV GPΔmuc-P2
RAVV GPΔmuc-P2CT
Cp (kcal mol-1 °C-1)
Temperature (°C)
Tm1 = 51.0
Tm2 = 60.0
Tm1 = 54.5
Tm2 = 58.2
Tm3 = 66.61
e
RAVV GPΔmuc-P2CT/MR78 Fab (PDB ID: 5UQY)
RAVV GPΔmuc-P2CT/MR78 Fab (EMDB: 6233)
90°
f
RAVV GPΔmuc-P2CT
Relative abundance (%)
N94
N171
N190
N202
N207
N219
N223
N475
N487
N564
N619
Unoccupied
Complex
Hybrid
Oligomannose
N.D.
g
EC50 (ug/ml)
RAVV GPΔmuc-P2
RAVV GPΔmuc-P2CT
MR78
MR191
h
MR78
MR191
RAVV GPΔmuc-P2
0.58
0.52
RAVV GPΔmuc-P2CT
0.58
0.50

Figure 6

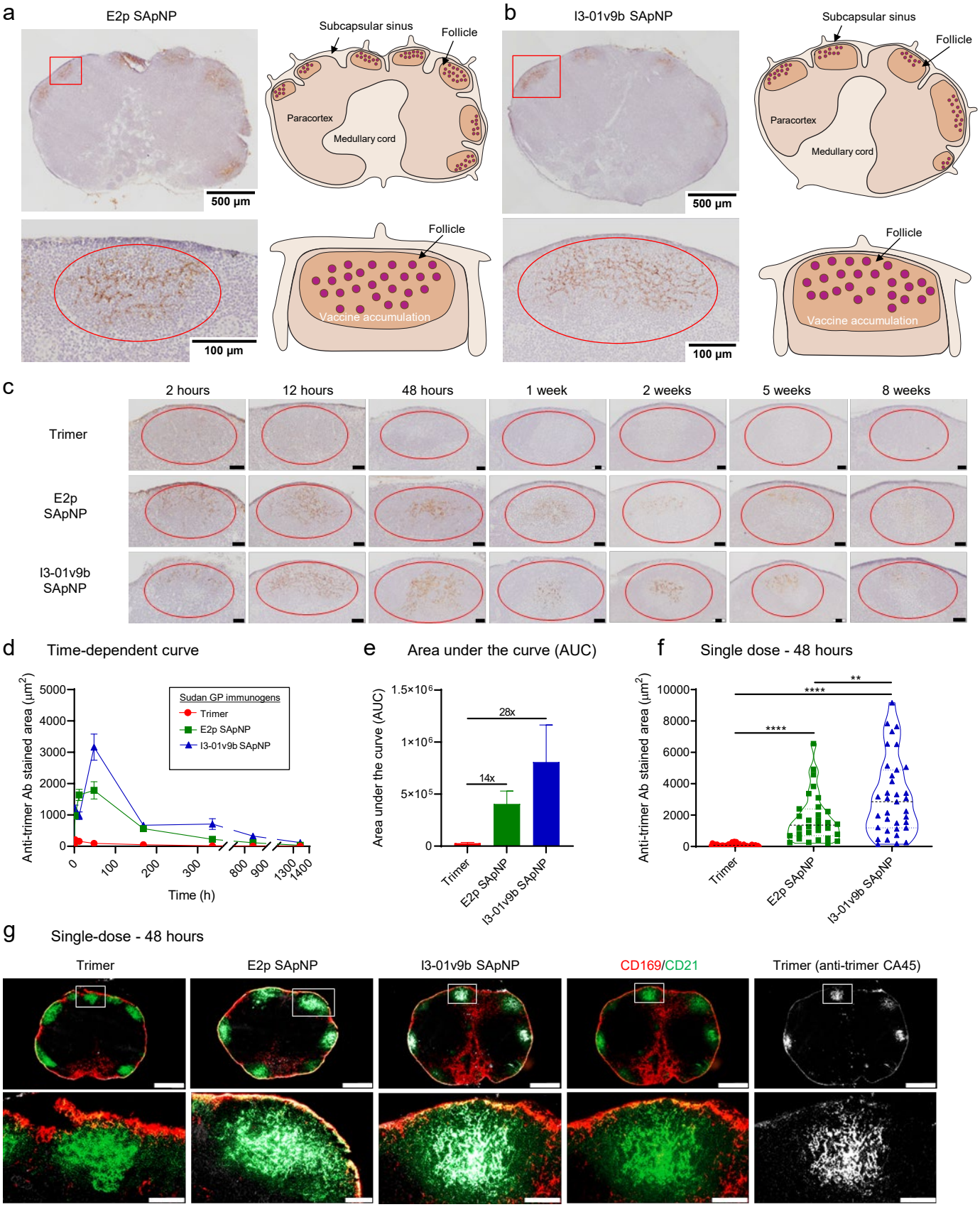
a
E2p SApNP
Subcapsular sinus
Follicle
Paracortex
Medullary cord
500 µm
Follicle
Vaccine accumulation
100 µm
b
I3-01v9b SApNP
Subcapsular sinus
Follicle
Paracortex
Medullary cord
500 µm
Follicle
Vaccine accumulation
100 µm
c
2 hours
12 hours
48 hours
1 week
2 weeks
5 weeks
8 weeks
Trimer
E2p SApNP
I3-01v9b SApNP
d
Time-dependent curve
Anti-trimer Ab stained area (µm²)
Sudan GP immunogens
Trimer
E2p SApNP
I3-01v9b SApNP
Time (h)
e
Area under the curve (AUC)
Area under the curve (AUC)
28x
14x
Trimer
E2p SApNP
I3-01v9b SApNP
f
Single dose - 48 hours
Anti-trimer Ab stained area (µm²)
****
****
**
Trimer
E2p SApNP
I3-01v9b SApNP
g
Single-dose - 48 hours
Trimer
E2p SApNP
I3-01v9b SApNP
CD169/CD21
Trimer (anti-trimer CA45)

Figure 7

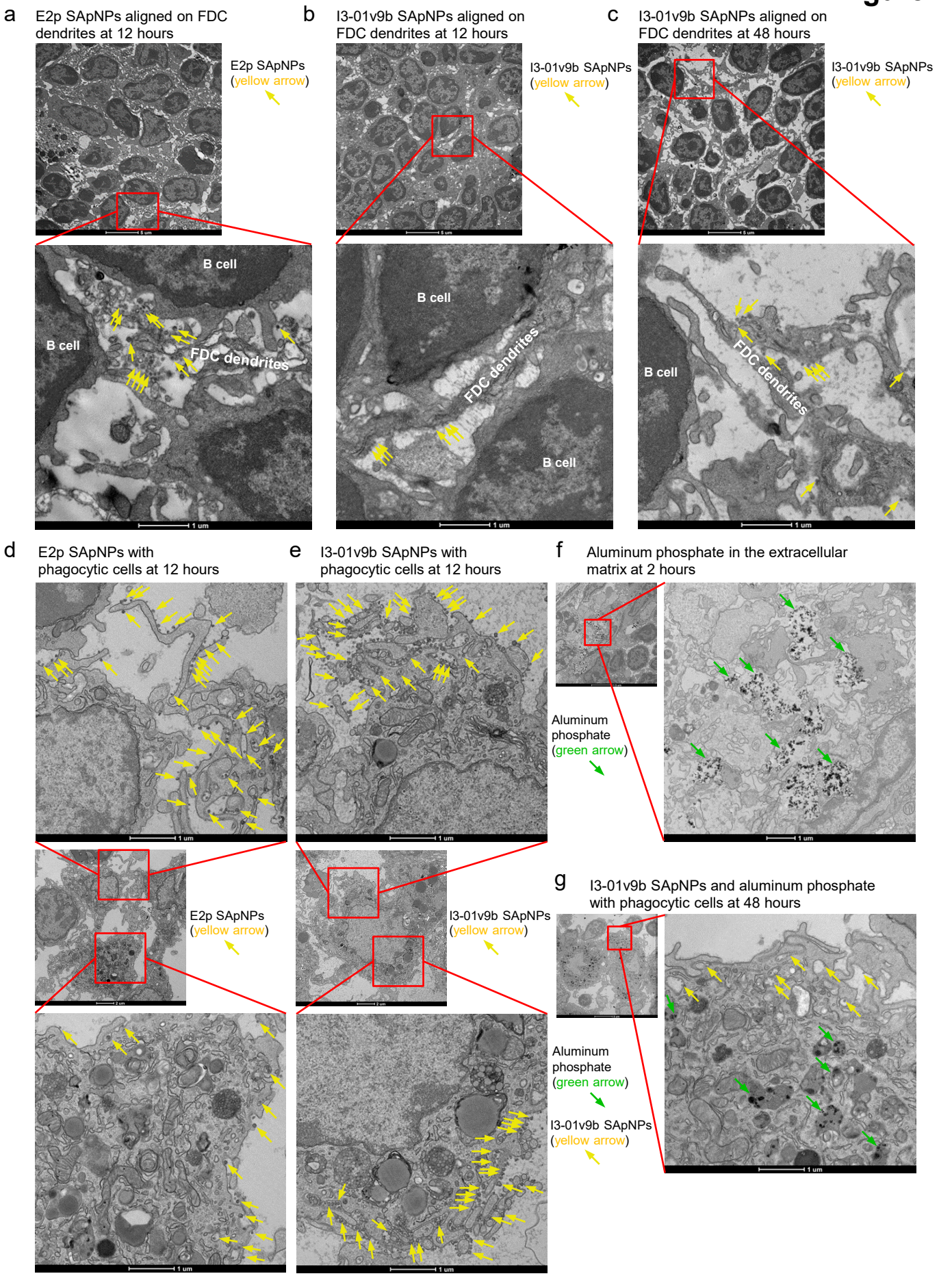
a
E2p SApNPs aligned on FDC dendrites at 12 hours
E2p SApNPs (yellow arrow)
B cell
B cell
FDC dendrites
b
I3-01v9b SApNPs aligned on FDC dendrites at 12 hours
I3-01v9b SApNPs (yellow arrow)
B cell
FDC dendrites
B cell
c
I3-01v9b SApNPs aligned on FDC dendrites at 48 hours
I3-01v9b SApNPs (yellow arrow)
B cell
FDC dendrites
d
E2p SApNPs with phagocytic cells at 12 hours
E2p SApNPs (yellow arrow)
e
I3-01v9b SApNPs with phagocytic cells at 12 hours
I3-01v9b SApNPs (yellow arrow)
f
Aluminum phosphate in the extracellular matrix at 2 hours
Aluminum phosphate (green arrow)
g
I3-01v9b SApNPs and aluminum phosphate with phagocytic cells at 48 hours
Aluminum phosphate (green arrow)
I3-01v9b SApNPs (yellow arrow)

Figure 8

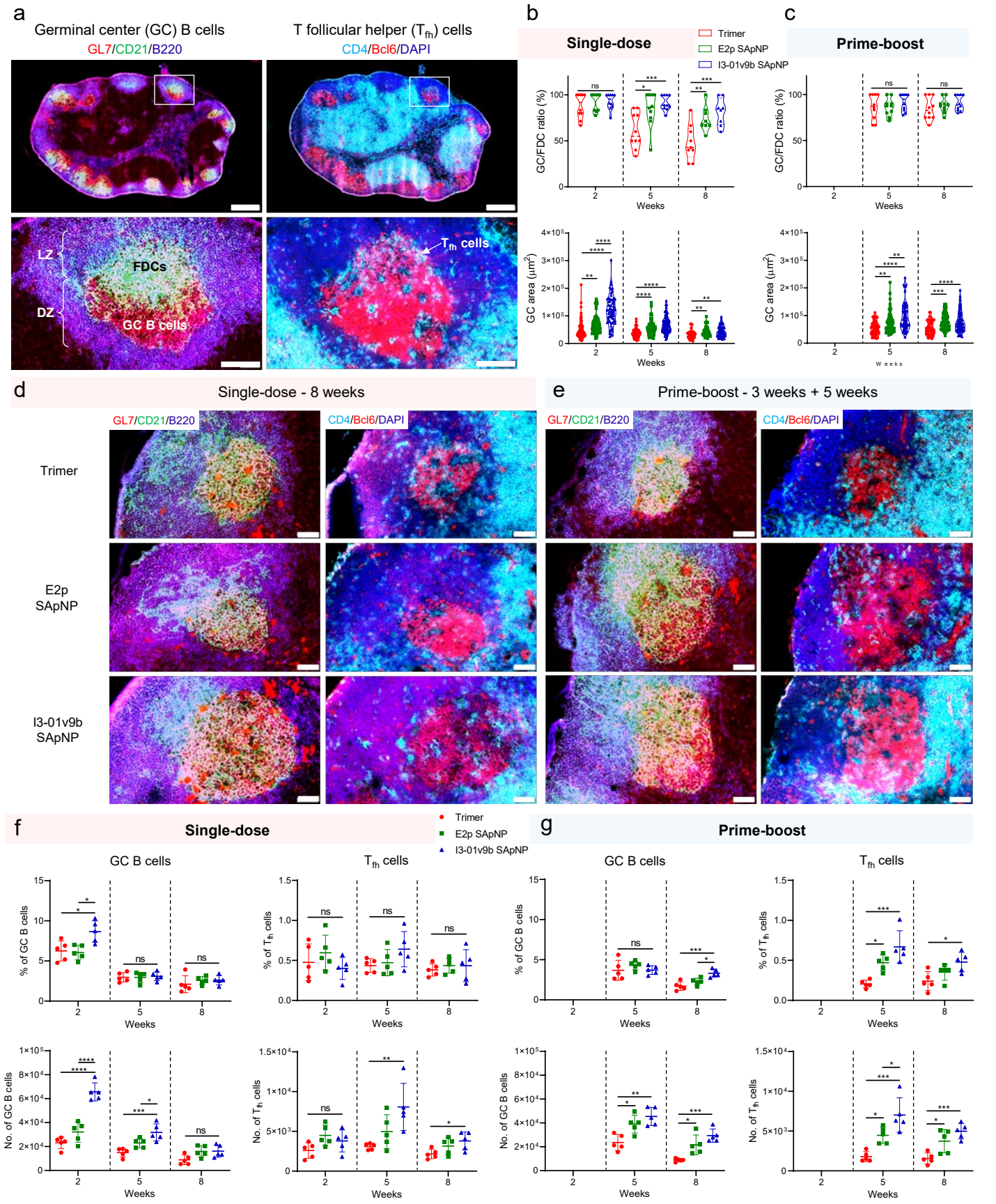
a
Germinal center (GC) B cells
GL7/CD21/B220
T follicular helper (Tfh) cells
CD4/Bcl6/DAPI
LZ
FDCs
DZ
GC B cells
Tfh cells
b
Single-dose
Trimer
E2p SApNP
I3-01v9b SApNP
c
Prime-boost
GC/FDC ratio (%)
GC area (μm2)
Weeks
d
Single-dose - 8 weeks
e
Prime-boost - 3 weeks + 5 weeks
GL7/CD21/B220
CD4/Bcl6/DAPI
Trimer
E2p SApNP
I3-01v9b SApNP
f
Single-dose
g
Prime-boost
GC B cells
Tfh cells
% of GC B cells
% of Tfh cells
No. of GC B cells
No. of Tfh cells
Weeks

Figure 9

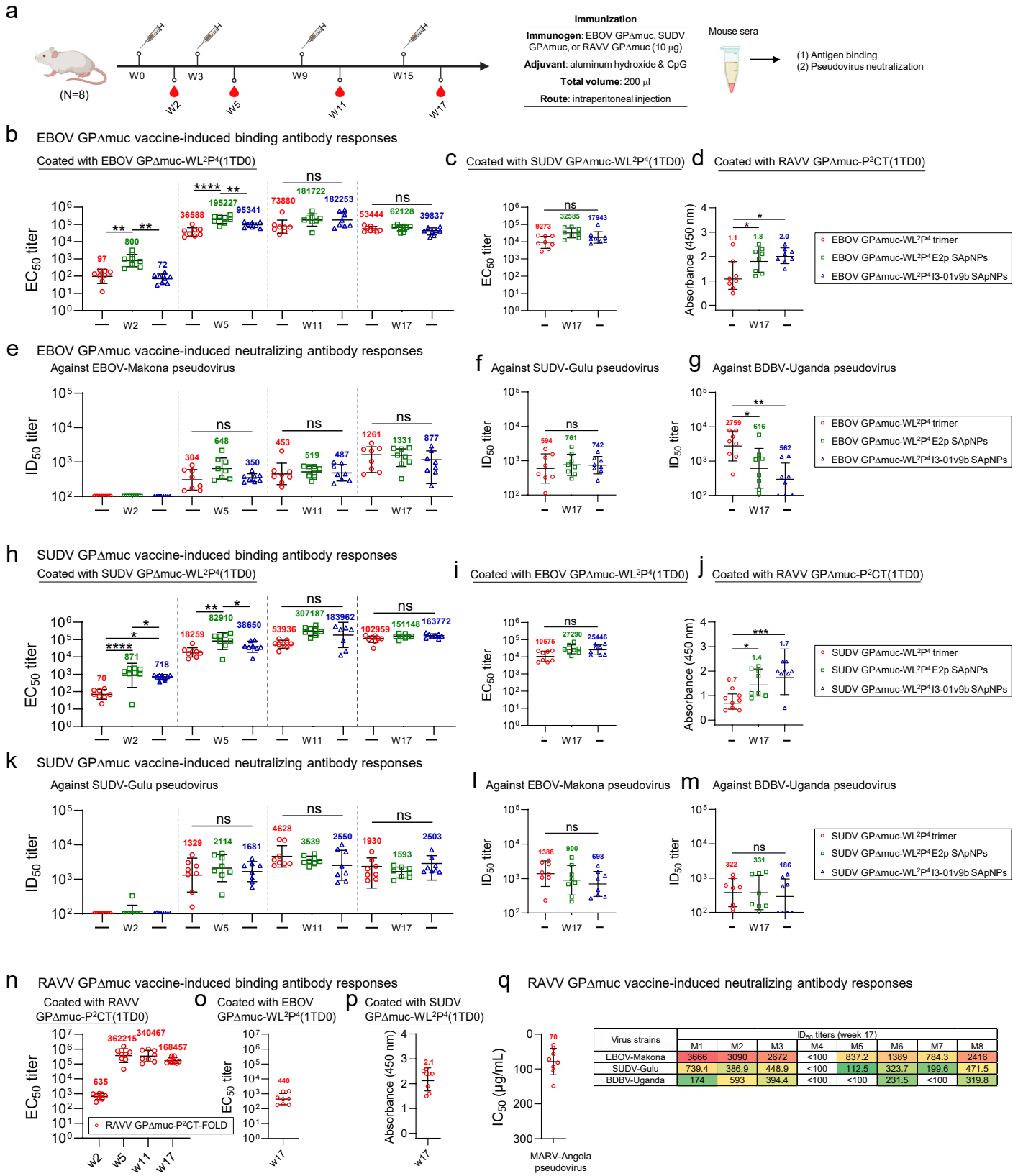

Virus strains	ID_{50} titers (week 17)							
	M1	M2	M3	M4	M5	M6	M7	M8
EBOV-Makona	3666	3090	2672	<100	837.2	1389	784.3	2416
SUDV-Gulu	739.4	386.9	448.9	<100	112.5	323.7	199.6	471.5
BDBV-Uganda	174	593	394.4	<100	<100	231.5	<100	319.8

Figure 10

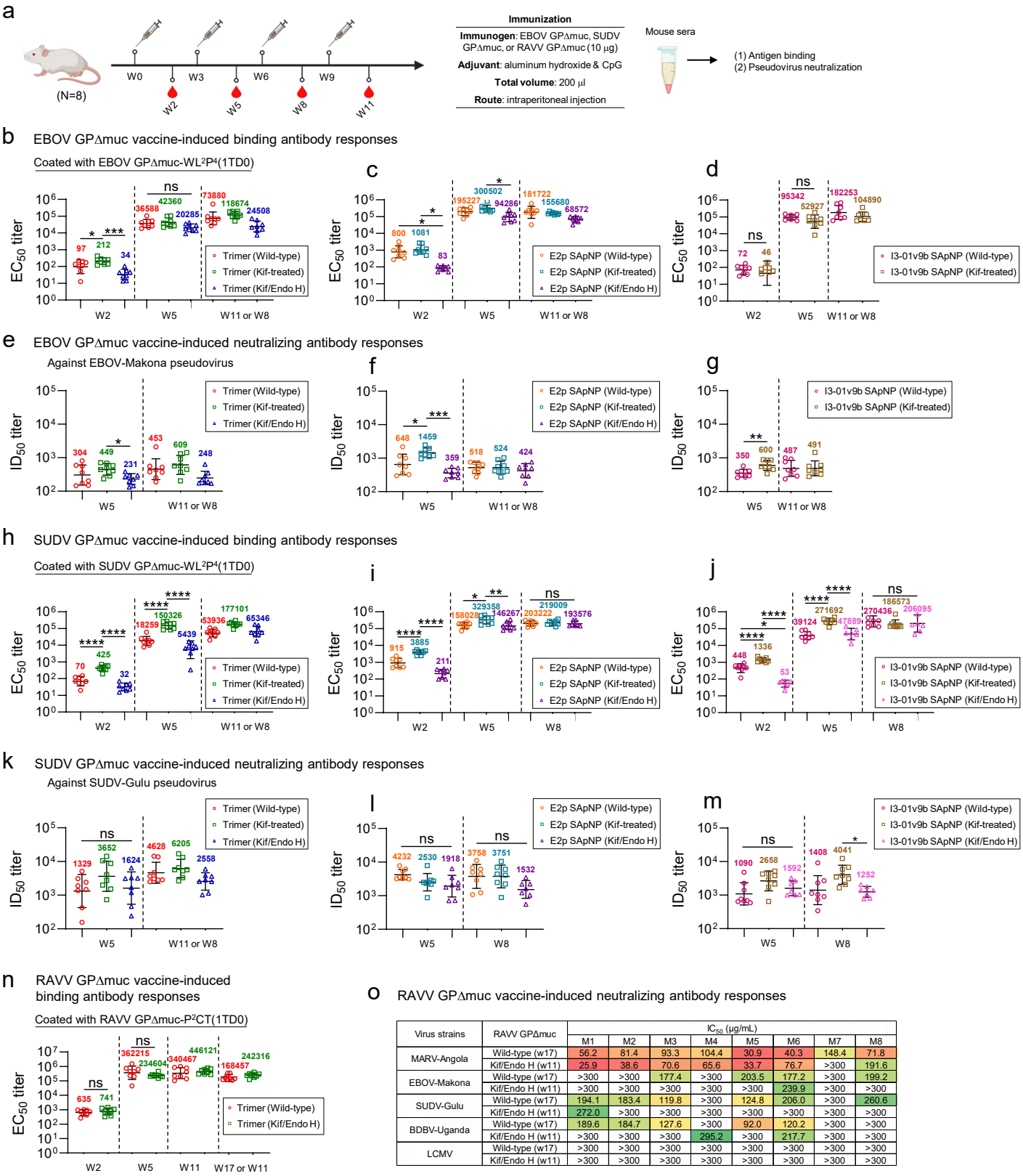

Virus strains	RAVV GPΔmuc	IC_{50} (μg/mL)							
		M1	M2	M3	M4	M5	M6	M7	M8
MARV-Angola	Wild-type (w17)	56.2	81.4	93.3	104.4	30.9	40.3	148.4	71.8
	Kif/Endo H (w11)	25.9	38.6	70.6	65.6	33.7	76.7	>300	191.6
EBOV-Makona	Wild-type (w17)	>300	>300	177.4	>300	203.5	177.2	>300	199.2
	Kif/Endo H (w11)	>300	>300	>300	>300	>300	239.9	>300	>300
SUDV-Gulu	Wild-type (w17)	194.1	183.4	119.8	>300	124.8	206.0	>300	260.6
	Kif/Endo H (w11)	272.0	>300	>300	>300	>300	>300	>300	>300
BDBV-Uganda	Wild-type (w17)	189.6	184.7	127.6	>300	92.0	120.2	>300	>300
	Kif/Endo H (w11)	>300	>300	>300	295.2	>300	217.7	>300	>300
LCMV	Wild-type (w17)	>300	>300	>300	>300	>300	>300	>300	>300
	Kif/Endo H (w11)	>300	>300	>300	>300	>300	>300	>300	>300

a

>EBOV Mayinga GPΔmuc-WL^{2}P^2-foldon-[His$_6$]

MGVTGILQLPRDRFKRTSFFLWVIILFQRTFSIPLGVIHNSALQVSDVDKLVCRDKLSSTNQLRSVGLNLEGNGVATDVPSATKRWGFRSGVPPKVVNYEAGEWAENC
YNLEIKKPDGSECLPAAPDGIRGFPRCRYVHKVSGTGPCAGDFAFHKEGAFFLYDRLASTVIYRGTTFAEGVVAFLILPQAKKDFFSSHPLREPVNATEDPSSGYYST
TIRYQATGFGTNETEYLFEVDNLTYVQLESRFTPQFLLQLNETIYTSGKRSNTTGKLIWKVNPEIDTTIGEWAFWETKKNLTRKIRSEELSFTVVSTHHQDTGEESAS
SGKLGLITNTIAGVAGLITGGRRTRREAIVNAQPKCNPNLHYWTTQDEGAAIGLAWIPYFGPAAEGIYIEGLMHNQDGLICGLRQLANETTQALQLFLRATPELRTFS
ILNRKAIDFLLQRWGGTCHILGPDCCIEPHDLTKNITDKIDQIIHDFVDKTLPDASGYIPEAPRDGQAYVRKDGEWVLLSTFL[GSHHHHHH]

>EBOV Mayinga GPΔmuc-WL^{2}P^4-foldon-[His$_6$]

MGVTGILQLPRDRFKRTSFFLWVIILFQRTFSIPLGVIHNSALQVSDVDKLVCRDKLSSTNQLRSVGLNLEGNGVATDVPSATKRWGFRSGVPPKVVNYEAGEWAENC
YNLEIKKPDGSECLPAAPDGIRGFPRCRYVHKVSGTGPCAGDFAFHKEGAFFLYDRLASTVIYRGTTFAEGVVAFLILPQAKKDFFSSHPLREPVNATEDPSSGYYST
TIRYQATGFGTNETEYLFEVDNLTYVQLESRFTPQFLLQLNETIYTSGKRSNTTGKLIWKVNPEIDTTIGEWAFWETKKNLTRKIRSEELSFTVVSTHHQDTGEESAS
SGKLGLITNTIAGVAGLITGGRRTRREAIVNAQPKCNPNLHYWTTQDEGAAIGLAWIPYFGPAAEGIYIEGLMHNQDGLICGLRQLANETTQALQLFLRATTEPRTFS
ILNRKAIDFLLQRWGGTCHILGPDCCIEPHDLTKNITDKIDQIIHDFVDKTLPDASGYIPEAPRDGQAYVRKDGEWVLLSTFL[GSHHHHHH]

>SUDV Gulu GPΔmuc-WL^{2}P^2-foldon-[His$_6$]

MGILPSPGMPALLSLVSLLSVLLMGCVAEMPLGVVTNSTLEVTEIDQLVCKDHLASTDQLKSVGLNLEGSGVSTDIPSATKRWGFRSGVPPKVVSYEAGEWAENCYNL
EIKKPDGSECLPPPPDGVRGFPRCRYVHKAQGTGPCPGDYAFHKDGAFFLYDRLASTVIYRGVNFAEGVIAFLILAKPKETFLQSPPIREAVNYTENTSSYYATSYLE
YEIENFGAQHSTTLFKIDNNTFVRLDRPHTPQFLFQLNDTIHLHQQLSNTTGRLIWTLDANINADIGEWAFWENKKNLSEQLRGEELSFEALSLNETEDDDAASSSTS
NGLITSTVTGILGSLGLRKRSRRQTNTKATGKCNPNLHYWTAQEQHNAAGIAWIPYFGPGAEGIYTEGLMHNQNALVCGLRQLANETTQALQLFLRATPELRTYTILN
RKAIDFLLRRWGGTCRILGPDCCIEPHDLTKNITDKINQIIHDFIDNPLPNASGYIPEAPRDGQAYVRKDGEWVLLSTFL[GSHHHHHH]

>SUDV Gulu GPΔmuc-WL^{2}P^4-foldon-[His$_6$]

MGILPSPGMPALLSLVSLLSVLLMGCVAEMPLGVVTNSTLEVTEIDQLVCKDHLASTDQLKSVGLNLEGSGVSTDIPSATKRWGFRSGVPPKVVSYEAGEWAENCYNL
EIKKPDGSECLPPPPDGVRGFPRCRYVHKAQGTGPCPGDYAFHKDGAFFLYDRLASTVIYRGVNFAEGVIAFLILAKPKETFLQSPPIREAVNYTENTSSYYATSYLE
YEIENFGAQHSTTLFKIDNNTFVRLDRPHTPQFLFQLNDTIHLHQQLSNTTGRLIWTLDANINADIGEWAFWENKKNLSEQLRGEELSFEALSLNETEDDDAASSSTS
NGLITSTVTGILGSLGLRKRSRRQTNTKATGKCNPNLHYWTAQEQHNAAGIAWIPYFGPGAEGIYTEGLMHNQNALVCGLRQLANETTQALQLFLRATTEPRTYTILN
RKAIDFLLRRWGGTCRILGPDCCIEPHDLTKNITDKINQIIHDFIDNPLPNASGYIPEAPRDGQAYVRKDGEWVLLSTFL[GSHHHHHH]

>BDBV R4386L GPΔmuc-WL^{2}P^2-foldon-[His$_6$]

MGILPSPGMPALLSLVSLLSVLLMGCVAEIPLGVVHNNTLQVSDIDKLVCRDKLSSTSQLKSVGLNLEGNGVATDVPTATKRWGFRAGVPPKVVNYEAGEWAENCYNL
DIKKADGSECLPEAPEGVRGFPRCRYVHKVSGTGPCPEGYAFHKEGAFFLYDRLASTIIYRSTTFSEGVVAFLILPETKKDFFQSPPLHEPANMTTDPSSYYHTVTLN
YVADNFGTNMTNFLFQVDHLTYVQLEPRFTPQFLVQLNETIYTNGRRSNTTGTLIWKVNPTVDTGVGEWAFWENKKNFTKTLSSEELSVIFVPRAQDPGSNDISESTE
PGPLTNTTRGAANLLTGSRRTRREITLRTQAKCNPNLHYWTTQDEGAAIGLAWIPYFGPAAEGIYTEGIMHNQNGLICGLRQLANETTQALQLFLRATPELRTFSILN
RKAIDFLLQRWGGTCHILGPDCCIEPHDLTKNITDKIDQIIHDFIDKPLPDASGYIPEAPRDGQAYVRKDGEWVLLSTFL[GSHHHHHH]

>BDBV R4386L GPΔmuc-WL^{2}P^4-foldon-[His$_6$]

MGILPSPGMPALLSLVSLLSVLLMGCVAEIPLGVVHNNTLQVSDIDKLVCRDKLSSTSQLKSVGLNLEGNGVATDVPTATKRWGFRAGVPPKVVNYEAGEWAENCYNL
DIKKADGSECLPEAPEGVRGFPRCRYVHKVSGTGPCPEGYAFHKEGAFFLYDRLASTIIYRSTTFSEGVVAFLILPETKKDFFQSPPLHEPANMTTDPSSYYHTVTLN
YVADNFGTNMTNFLFQVDHLTYVQLEPRFTPQFLVQLNETIYTNGRRSNTTGTLIWKVNPTVDTGVGEWAFWENKKNFTKTLSSEELSVIFVPRAQDPGSNDISESTE
PGPLTNTTRGAANLLTGSRRTRREITLRTQAKCNPNLHYWTTQDEGAAIGLAWIPYFGPAAEGIYTEGIMHNQNGLICGLRQLANETTQALQLFLRATTEPRTFSILN
RKAIDFLLQRWGGTCHILGPDCCIEPHDLTKNITDKIDQIIHDFIDKPLPDASGYIPEAPRDGQAYVRKDGEWVLLSTFL[GSHHHHHH]

b

SEC profile of 6 orthoebolavirus GPΔmuc constructs expressed in HEK293F cells and purified by nickel and IAC columns

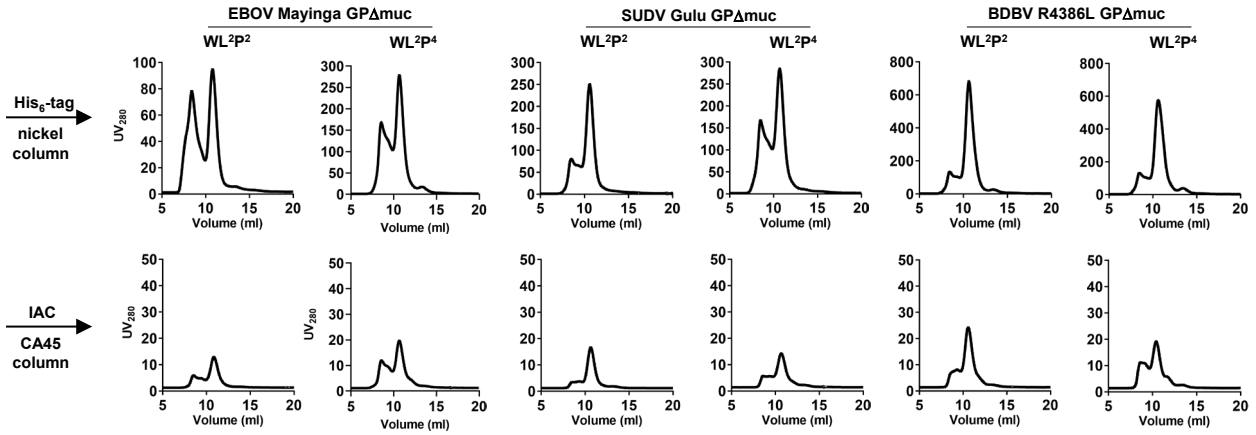

Fig. S1

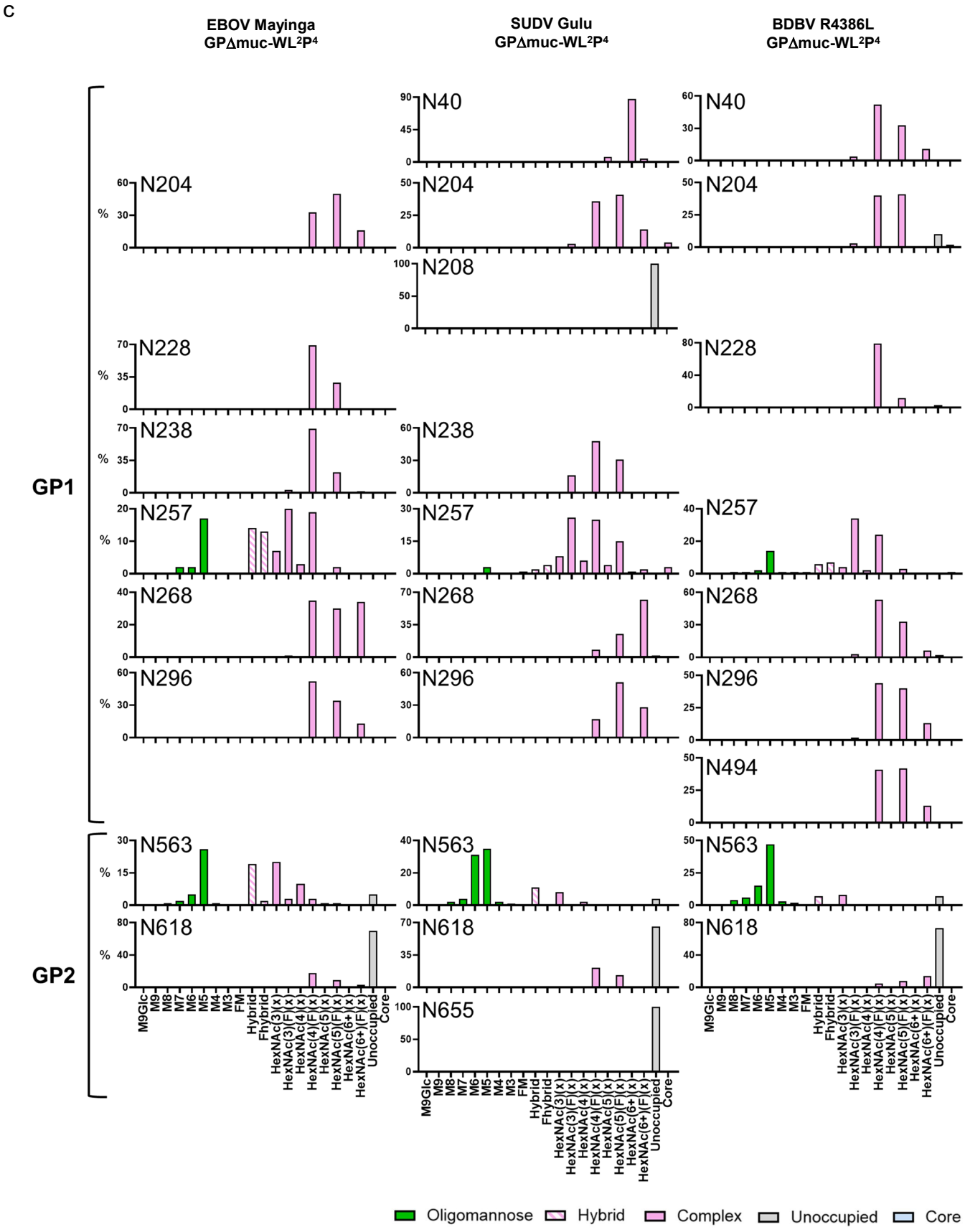
C
EBOV Mayinga GPΔmuc-WL2P4
SUDV Gulu GPΔmuc-WL2P4
BDBV R4386L GPΔmuc-WL2P4
GP1
GP2
N40
N204
N208
N228
N238
N257
N268
N296
N494
N563
N618
N655
%
M9Glc
M9
M8
M7
M6
M5
M4
M3
FM
Hybrid
Fhybrid
HexNAc(3)(x)
HexNAc(3)(F)(x)
HexNAc(4)(x)
HexNAc(4)(F)(x)
HexNAc(5)(x)
HexNAc(5)(F)(x)
HexNAc(6+)(x)
HexNAc(6+)(F)(x)
Unoccupied
Core
Oligomannose
Hybrid
Complex
Unoccupied
Core

d Flowchart of image processing and model building protocol

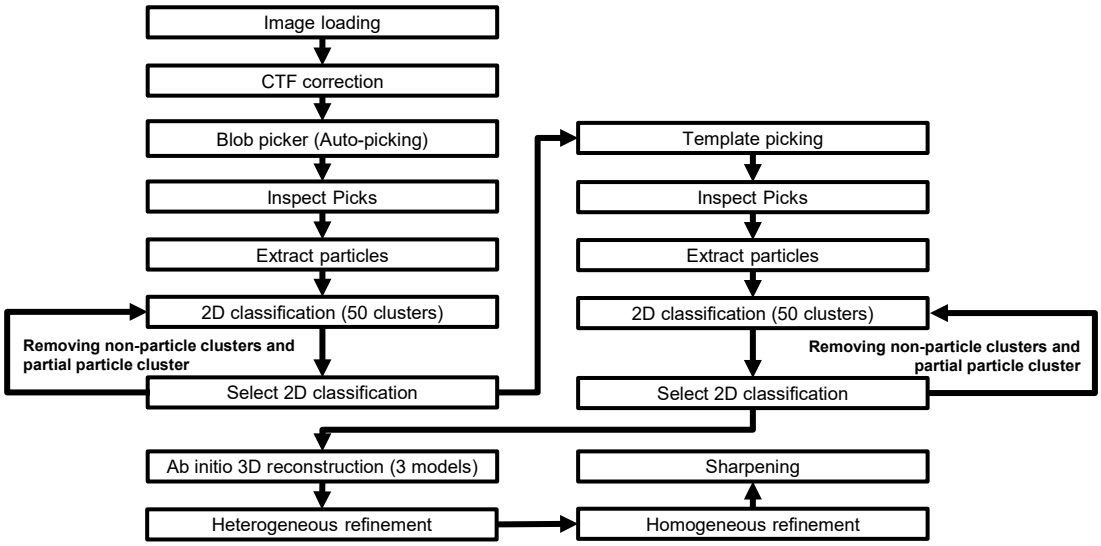

e **Selected 2D classifications for 3D modeling of EBOV Mayinga GPΔmuc**

GPΔmuc-WL^{2}P^4 trimer/ADI-15878 Fab complex

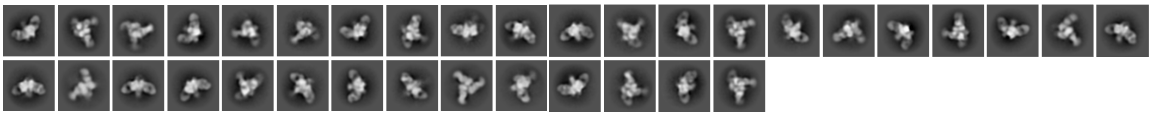

GPΔmuc-WL^{2}P^4 trimer

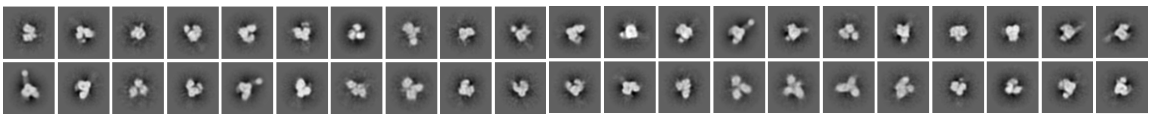

f **Selected 2D classifications for 3D modeling of SUDV Gulu GPΔmuc**

GPΔmuc-WL^{2}P^4 trimer/ADI-15878 Fab complex

GPΔmuc-WL^{2}P^4 trimer

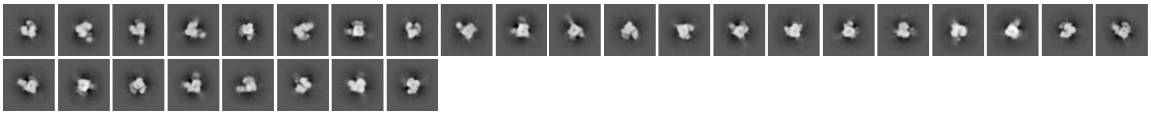

g **Selected 2D classifications for 3D modeling of BDBV R3486L GPΔmuc**

GPΔmuc-WL^{2}P^4 trimer/ADI-15878 Fab complex

GPΔmuc-WL^{2}P^4 trimer

h ELISA analysis of 6 rationally designed orthoebolavirus GPΔmuc trimers binding to 5 filovirus NAbs

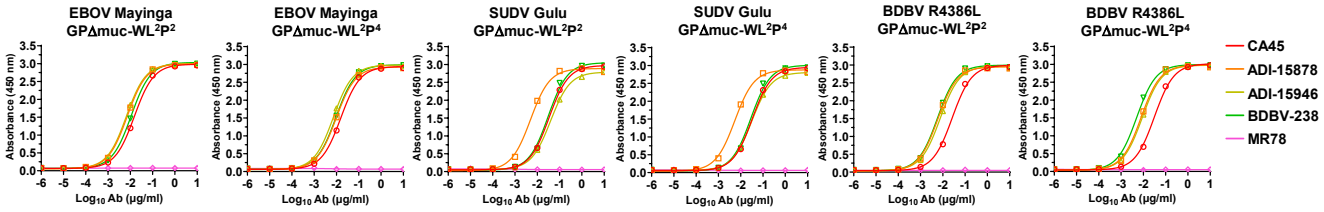

EBOV Mayinga GPΔmuc-WL^{2}P^2									
CA45		ADI-15878		ADI-15946		BDBV-289		MR78	
EC50	STD	EC50	STD	EC50	STD	EC50	STD	EC50	STD
0.01520	0.00023	0.00727	0.00072	0.00669	0.00017	0.01109	0.00029	N.D.	N.D.

EBOV Mayinga GPΔmuc-WL^{2}P^4									
CA45		ADI-15878		ADI-15946		BDBV-289		MR78	
EC50	STD	EC50	STD	EC50	STD	EC50	STD	EC50	STD
0.015639	0.000587	0.009683	0.001136	0.007233	0.000747	0.009632	0.00102	N.D.	N.D.

SUDV Gulu GPΔmuc-WL^{2}P^2									
CA45		ADI-15878		ADI-15946		BDBV-289		MR78	
EC50	STD	EC50	STD	EC50	STD	EC50	STD	EC50	STD
0.0338	2.83E-05	0.004959	7.07E-06	0.039574	0.002213	0.030734	0.000834	N.D.	N.D.

SUDV Gulu GPΔmuc-WL^{2}P^4									
CA45		ADI-15878		ADI-15946		BDBV-289		MR78	
EC50	STD	EC50	STD	EC50	STD	EC50	STD	EC50	STD
0.032764	0.001209	0.005461	0.000156	0.031179	0.002638	0.028805	0.000792	N.D.	N.D.

BDBV R4386L GPΔmuc-WL^{2}P^2									
CA45		ADI-15878		ADI-15946		BDBV-289		MR78	
EC50	STD	EC50	STD	EC50	STD	EC50	STD	EC50	STD
0.026339	0.001499	0.005969	0.000224	0.007626	0.000158	0.005773	3.39E-05	N.D.	N.D.

BDBV R4386L GPΔmuc-WL^{2}P^4									
CA45		ADI-15878		ADI-15946		BDBV-289		MR78	
EC50	STD	EC50	STD	EC50	STD	EC50	STD	EC50	STD
0.031360	0.000170	0.007866	0.000318	0.008934	0.000208	0.005026	0.000132	N.D.	N.D.

i BLI analysis of 6 rationally designed orthoebolavirus GPΔmuc trimers binding to 5 filovirus NAbs

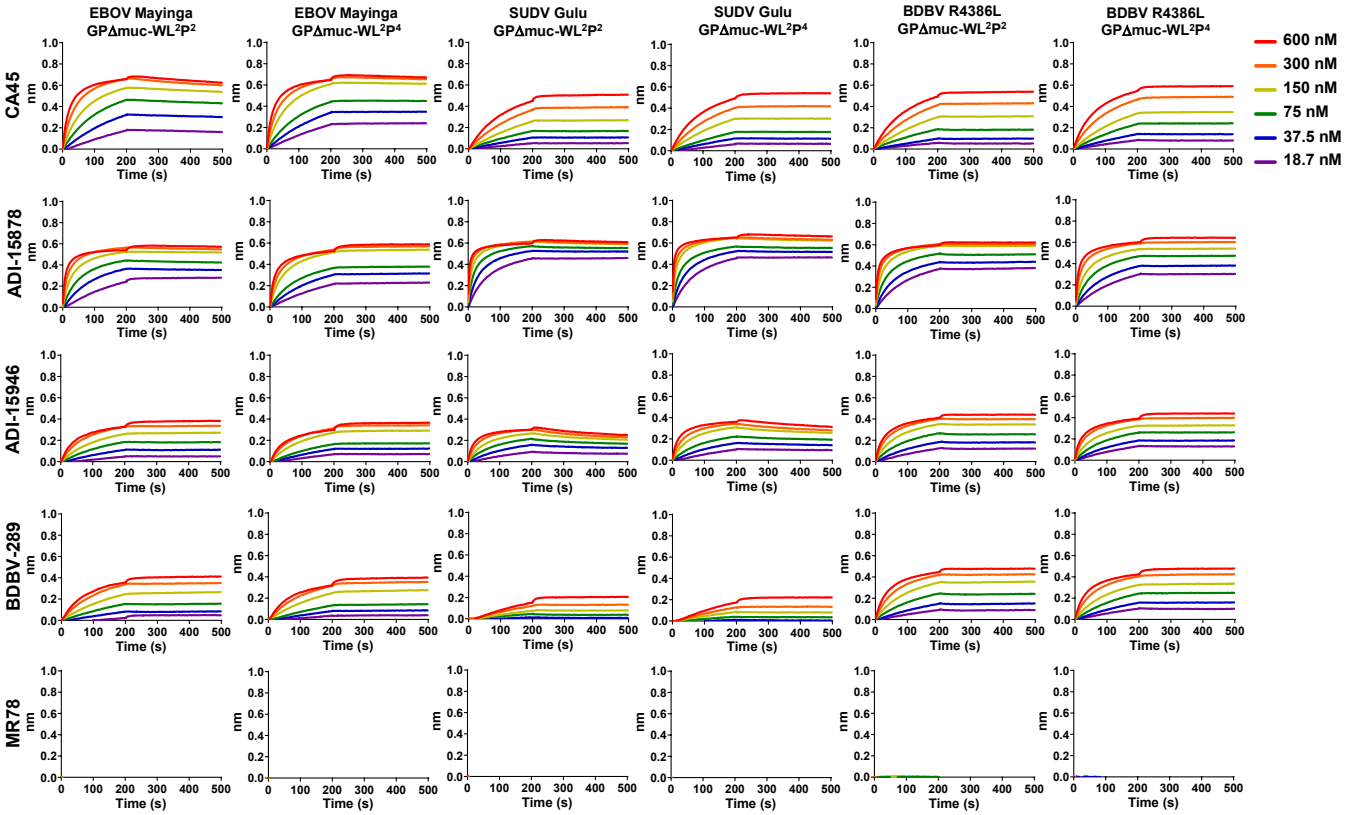

K_D values for 6 rationally designed orthoebolavirus GPΔmuc trimers binding to 5 filovirus NAbs (nM) [a]

	CA45	ADI-15878	ADI-15946	BDBV-289	MR78
EBOV Mayinga GPΔmuc-WL^{2}P^2	2.62	<1.0E-3	<1.0E-3	<1.0E-3	— [b]
EBOV Mayinga GPΔmuc-WL^{2}P^4	<1.0E-3	<1.0E-3	<1.0E-3	<1.0E-3	— [b]
SUDV Gulu GPΔmuc-WL^{2}P^2	<1.0E-3	<1.0E-3	7.22	<1.0E-3	— [b]
SUDV Gulu GPΔmuc-WL^{2}P^4	<1.0E-3	<1.0E-3	4.89	<1.0E-3	— [b]
BDBV R4386L GPΔmuc-WL^{2}P^2	<1.0E-3	<1.0E-3	<1.0E-3	<1.0E-3	— [b]
BDBV R4386L GPΔmuc-WL^{2}P^4	<1.0E-3	<1.0E-3	<1.0E-3	<1.0E-3	— [b]

[a] K_D values were derived from biolayer interferometry (BLI) using the binding equations describing a 1:1 interaction.
[b] "—" indicates cases where the peak signal value at the highest ebolavirus antigen concentration is 0.2 or lower.

Fig. S1. Construct design and in vitro characterization of orthoebolavirus GPΔmuc trimers. (**a**) Amino acid sequences of EBOV Mayinga , SUDV Gulu, and BDBV R3486L GPΔmuc-WL^{2}P^x-foldon-[His$_6$] constructs containing either the P^2 or P^4 mutation. Signal peptide, GP, restriction site (AS), foldon, linker (GS), and His$_6$ tag are highlighted in yellow, grey, green, orange, pink, and teal, respectively. The WL^{2}P^x mutations are shown in red. Note: Foldon is a C-terminal trimerization motif used in all orthoebolavirus GPΔmuc constructs and therefore will not be included in the construct names (except here in the sequence definition) to avoid redundancy. The GS linker and His$_6$ tag are enclosed in [ ] to indicate that they are included only in a subset of constructs used for evaluating nickel-based purification. (**b**) SEC profiles of EBOV Mayinga, SUDV Gulu, and BDBV R3486L GPΔmuc proteins produced in 165 ml HEK293F cultures and purified using either a nickel affinity column or a CA45 immunoaffinity column. (**c**) Compositional site-specific glycan analysis of three orthoebolavirus GPΔmuc-WL^{2}P^4 trimers. The graphs summarize quantitative mass spectrometric analysis of the glycan population present at individual N-linked glycosylation sites simplified into categories of glycans. The oligomannose-type glycan series (M9 to M5; Man$_9$GlcNAc$_2$ to Man$_5$GlcNAc$_2$) is colored green, afucosylated and fucosylated hybrid-type glycans (hybrid and F hybrid) are dashed pink, and complex glycans are grouped according to the number of antennae and presence of core fucosylation and are colored pink. Unoccupancy of an N-linked glycan site is represented in gray. Glycan sites that could not be determined are denoted as “N.D.”. (**d**) Flowchart illustrating image processing, 2D classification, and 3D reconstruction of negative stain EM (nsEM) data for EBOV, SUDV, and BDBV GPΔmuc trimers and their complexes with ADI-15878 Fab, using CryoSPARC. (**e**)-(**f**) Representative 2D classification images of EBOV, SUDV, and BDBV GPΔmuc-WL^{2}P^4 trimers and their complexes with ADI-15878 Fab. (**g**) ELISA analysis of EBOV, SUDV, and BDBV GPΔmuc trimers binding to 5 filovirus NAbs in IgG form. Briefly, each well was coated with 0.1 μg of the appropriate antigen, and IgG was diluted in a 10-fold dilution series from a starting concentration of 10 μg/ml for all tested antibodies. Error bars represent the difference between duplicate measurements at each concentration for each sample. (**h**) BLI analysis of EBOV, SUDV, and BDBV GPΔmuc trimers binding to 5 filovirus NAbs in IgG form. Sensorgrams were obtained from an Octet RED96 instrument using AHC biosensors. A two-fold concentration gradient of antigen, starting at 600 nM, was used in a dilution series of six. K_D values derived from a 1:1 fitting model are summarized in a table.

Fig. S2

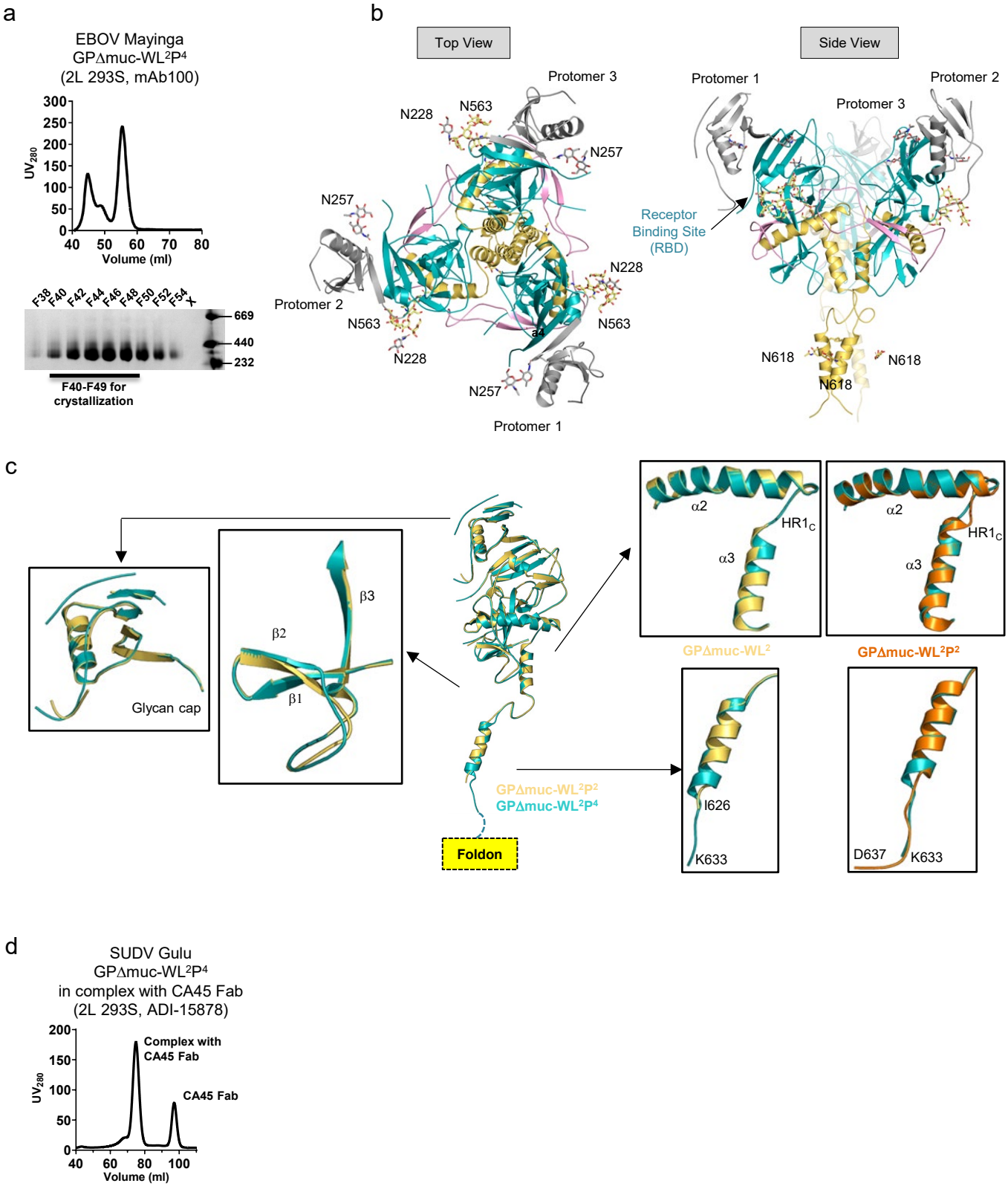
a
EBOV Mayinga
GPΔmuc-WL2P4
(2L 293S, mAb100)
UV280
Volume (ml)
F38 F40 F42 F44 F46 F48 F50 F52 F54 X
669
440
232
F40-F49 for crystallization
b
Top View
Side View
Protomer 1
Protomer 2
Protomer 3
N228
N563
N257
Receptor Binding Site (RBD)
N618
α4
c
Glycan cap
β1
β2
β3
α2
α3
HR1C
GPΔmuc-WL2
GPΔmuc-WL2P2
GPΔmuc-WL2P4
Foldon
I626
K633
D637
d
SUDV Gulu
GPΔmuc-WL2P4
in complex with CA45 Fab
(2L 293S, ADI-15878)
Complex with CA45 Fab
CA45 Fab

Fig. S2

e

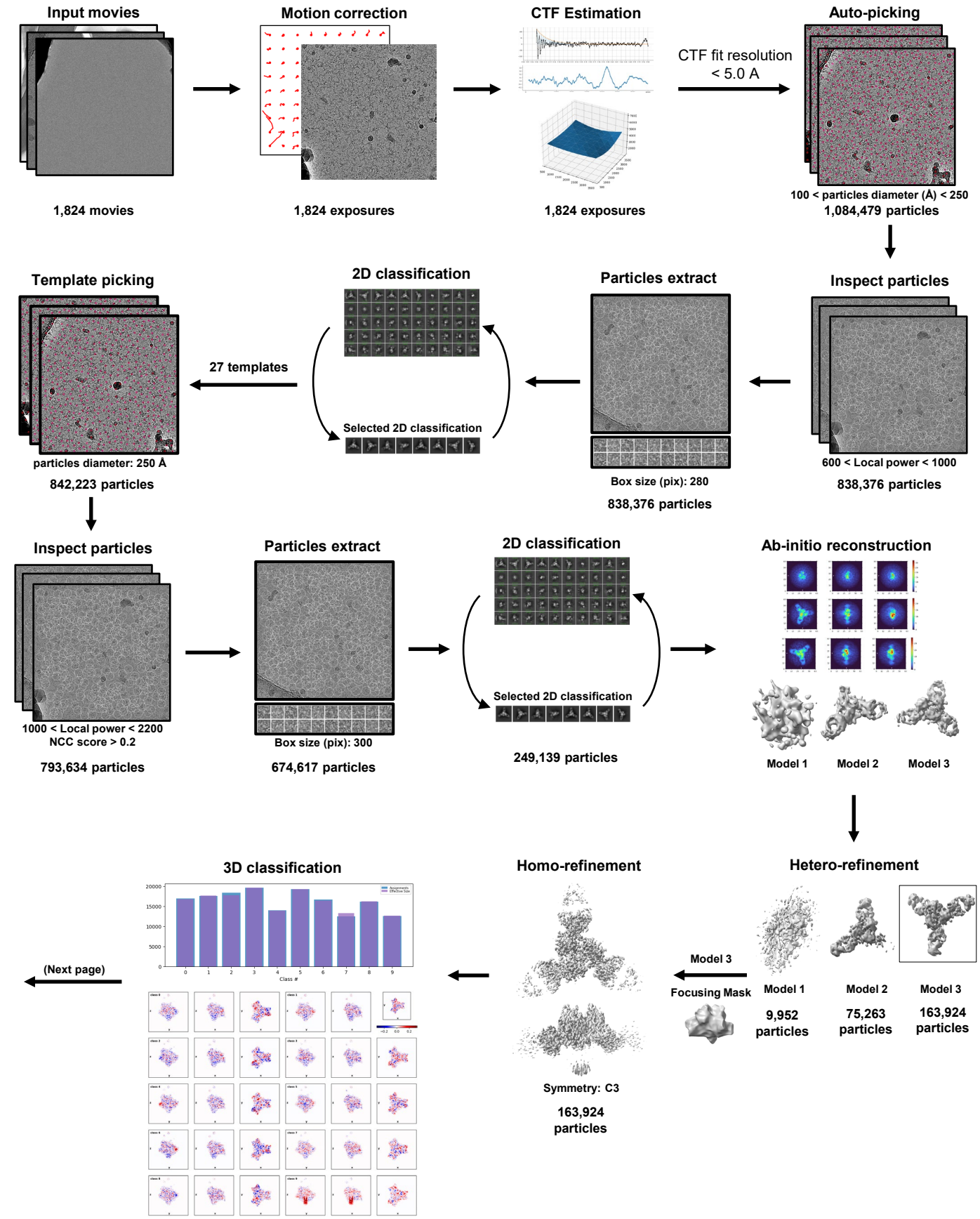
Input movies
1,824 movies
Motion correction
1,824 exposures
CTF Estimation
1,824 exposures
CTF fit resolution
< 5.0 A
Auto-picking
100 < particles diameter (Å) < 250
1,084,479 particles
Inspect particles
600 < Local power < 1000
838,376 particles
Particles extract
Box size (pix): 280
838,376 particles
2D classification
Selected 2D classification
27 templates
Template picking
particles diameter: 250 Å
842,223 particles
Inspect particles
1000 < Local power < 2200
NCC score > 0.2
793,634 particles
Particles extract
Box size (pix): 300
674,617 particles
2D classification
Selected 2D classification
249,139 particles
Ab-initio reconstruction
Model 1
Model 2
Model 3
Hetero-refinement
Model 1
9,952 particles
Model 2
75,263 particles
Model 3
163,924 particles
Model 3
Focusing Mask
Homo-refinement
Symmetry: C3
163,924 particles
3D classification
Class #
(Next page)

Fig. S2

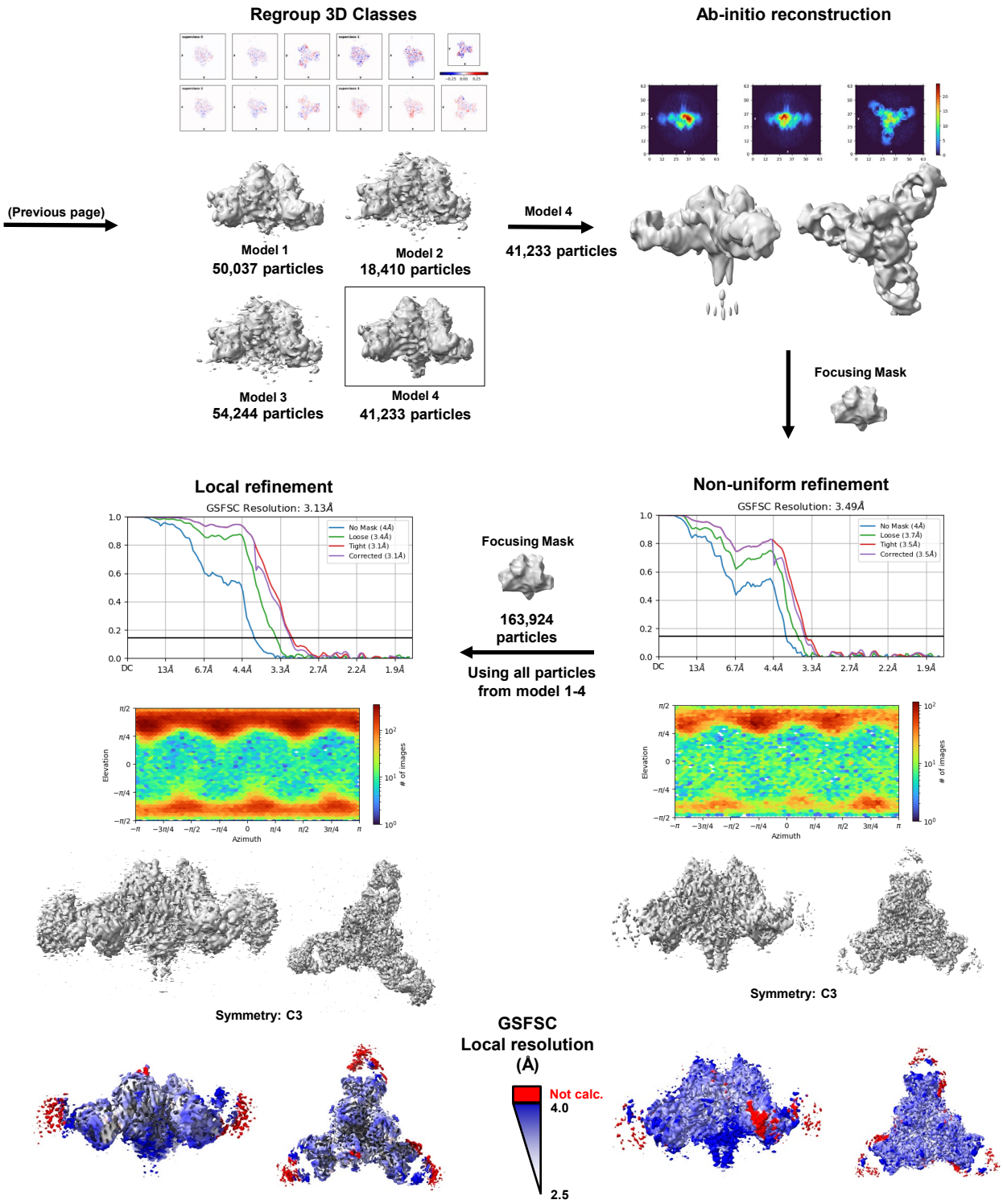
Regroup 3D Classes
Ab-initio reconstruction
(Previous page)
Model 1
50,037 particles
Model 2
18,410 particles
Model 3
54,244 particles
Model 4
41,233 particles
Model 4
41,233 particles
Focusing Mask
Local refinement
GSFSC Resolution: 3.13Å
No Mask (4Å)
Loose (3.4Å)
Tight (3.1Å)
Corrected (3.1Å)
Focusing Mask
163,924
particles
Using all particles
from model 1-4
Non-uniform refinement
GSFSC Resolution: 3.49Å
No Mask (4Å)
Loose (3.7Å)
Tight (3.5Å)
Corrected (3.5Å)
Elevation
Azimuth
# of images
Symmetry: C3
Symmetry: C3
GSFSC
Local resolution
(Å)
Not calc.
4.0
2.5

f

SUDV GPΔmuc-WL^{2}P^4 in complex with CA45 Fab

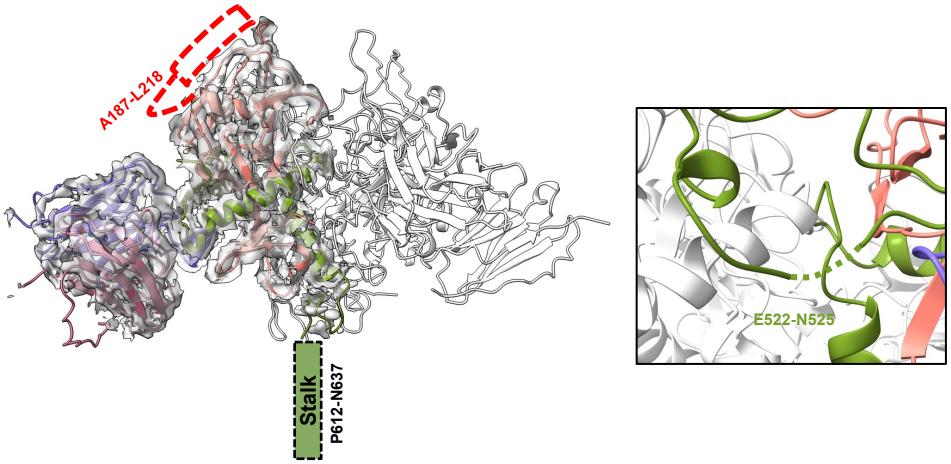

g

EBOV Mayinga GPΔmuc-WL^{2}P^4

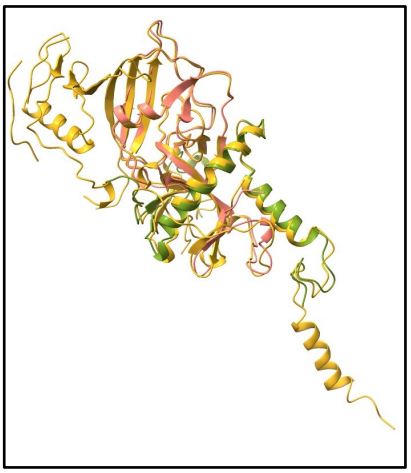

Cα-RMSD: 0.71 Å

EBOV Mayinga GPΔmuc in complex with CA45 Fab (PDB ID: 6EAY)

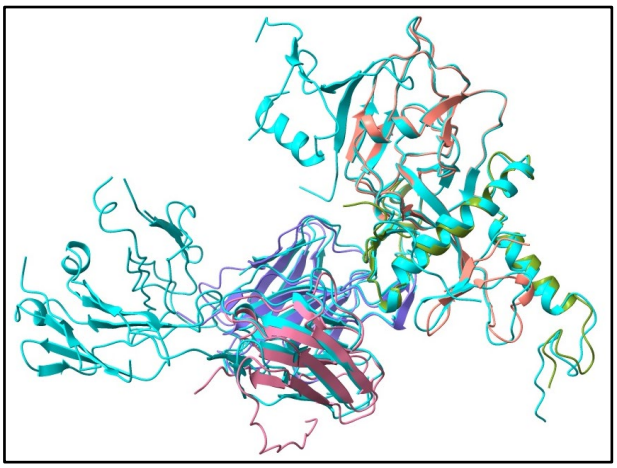

Cα-RMSD: 0.69 Å

h

Crystal structure of EBOV GPΔmuc in complex with CA45 Fab (PDB ID: 6EAY)

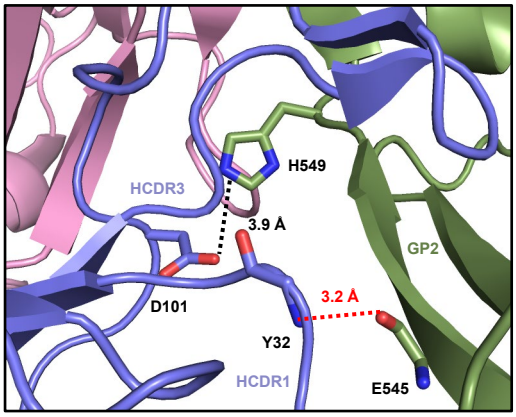

Heavy chain variable domain of CA45 Fab

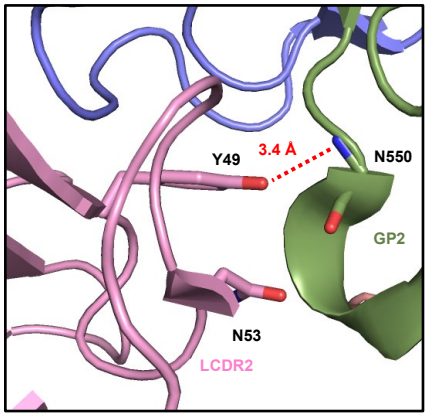

Light chain variable domain of CA45 Fab

Hydrogen bond
Salt-bridge

i

Interface between SUDV Gulu GPΔmuc-WL^{2}P^4 and CA45

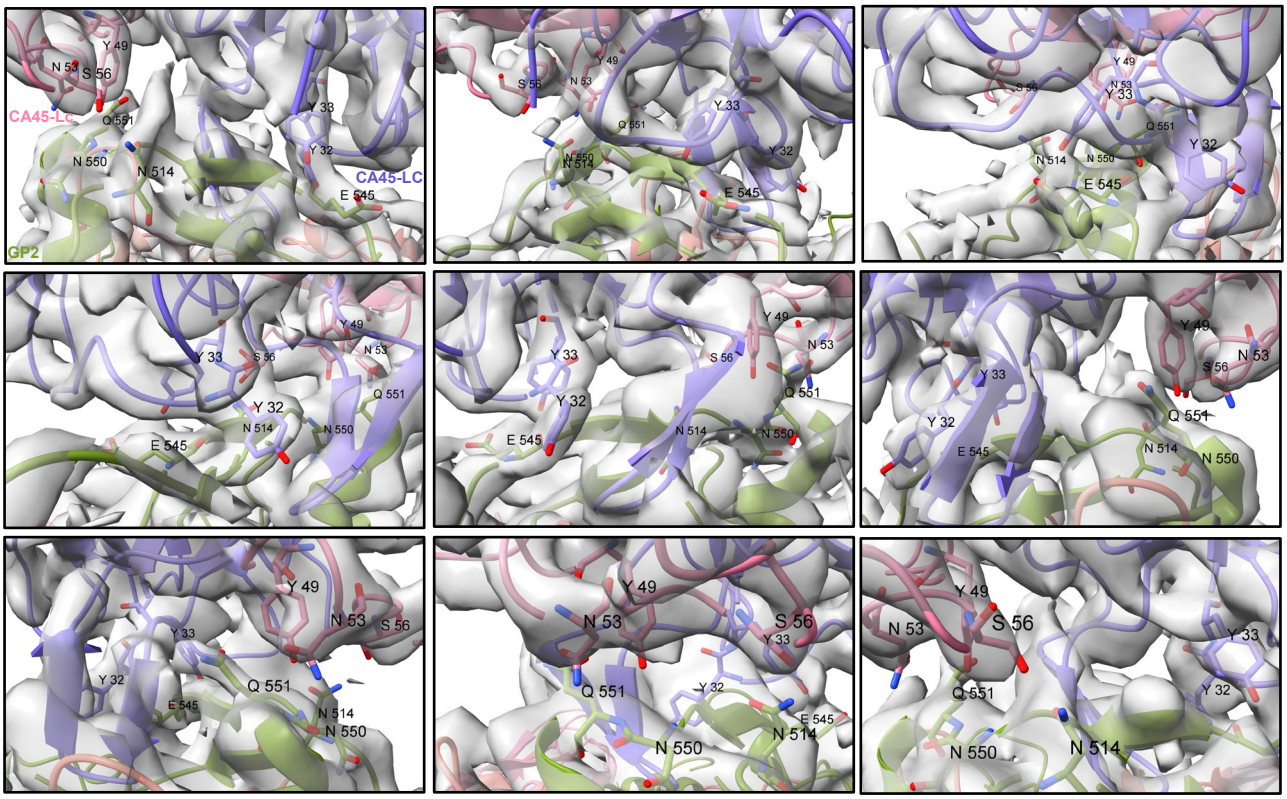

j

Local resolution at the interface between SUDV Gulu GPΔmuc-WL^{2}P^4 and CA45

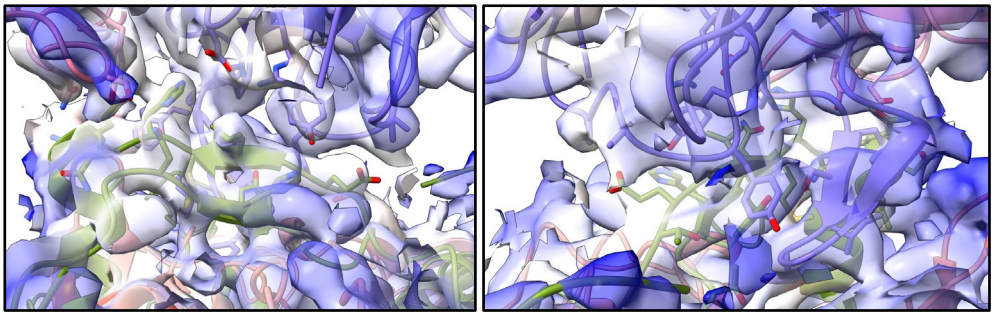

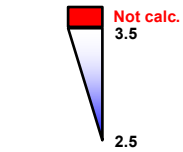

k

EBOV GPΔmuc in complex with ADI-15878

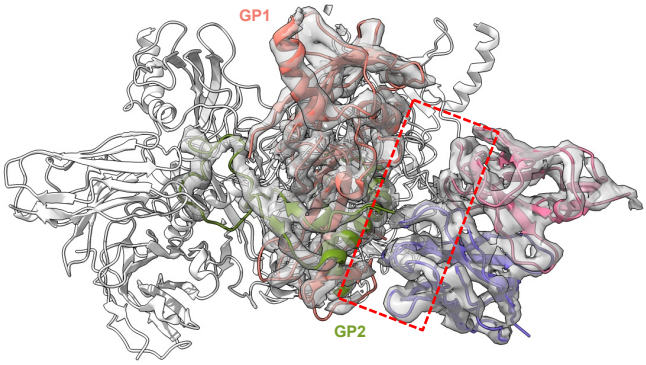

PDB ID: 6DZL (EMDB-8935)

Interface between EBOV GPΔmuc and ADI-15878

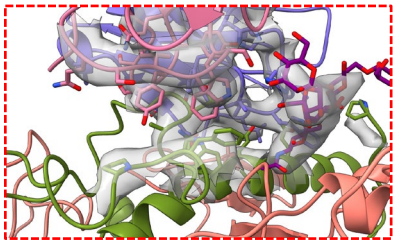

l

Fig. S2

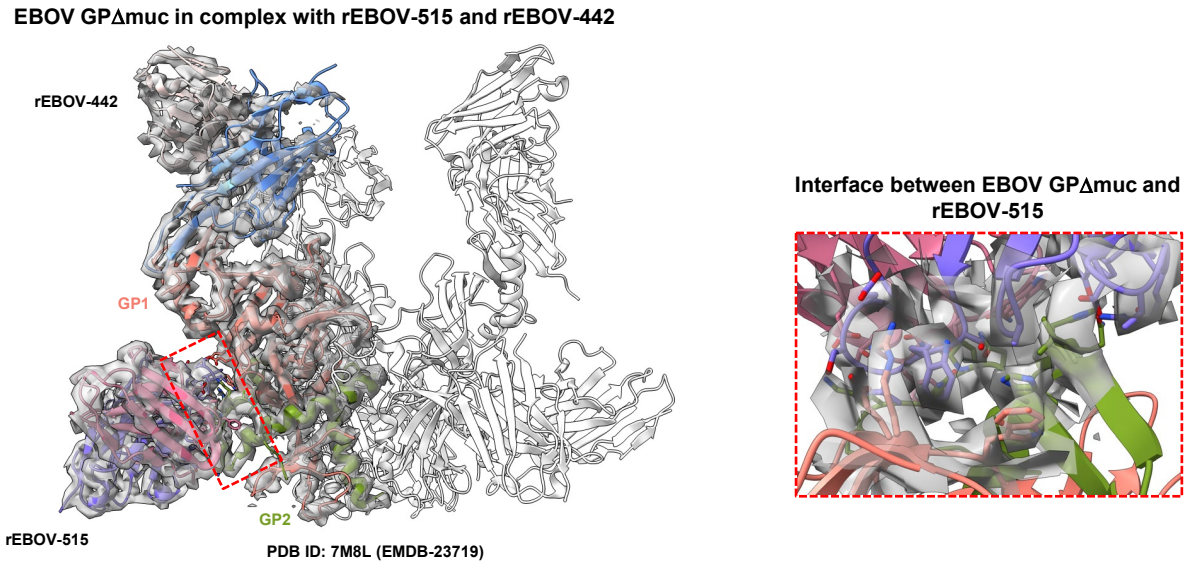

m

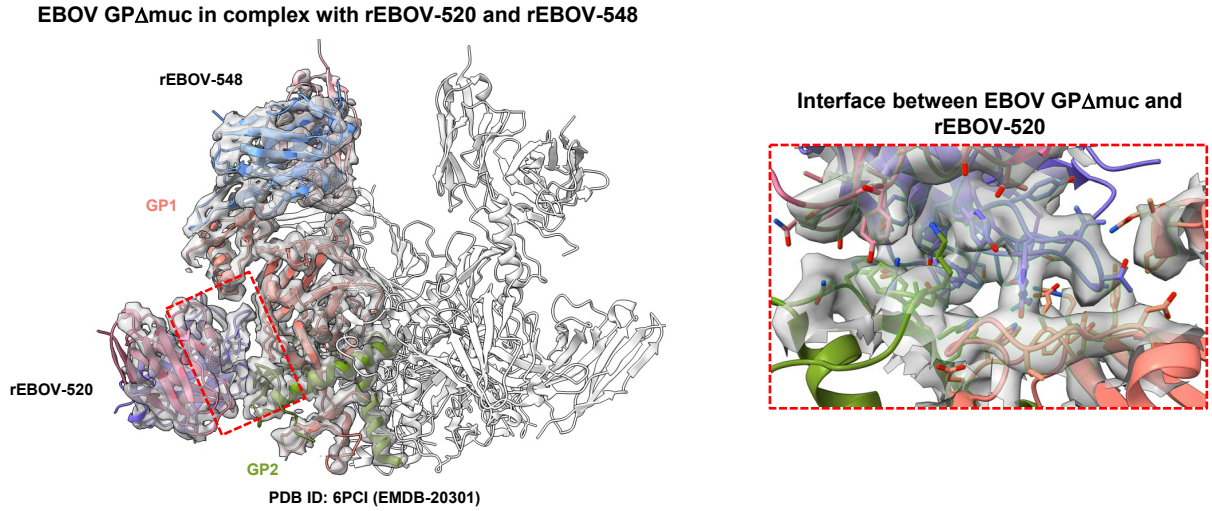

Fig. S2. Structural characterization of ligand-free EBOV GPΔmuc-WL^{2}P^4 and CA45 Fab-bound SUDV GPΔmuc-WL^{2}P^4 trimers. (**a**) SEC profile of EBOV GPΔmuc-WL^{2}P^4 trimer expressed in 2L HEK293S cells and BN-PAGE of ADI-15878/SEC-purified EBOV GPΔmuc-WL^{2}P^4 trimer. Fractions F40 to F49 were used for crystallization screening. The SEC profile was generated from a HiLoad Superdex 200 16/600 PG column (Cytiva). (**b**) Ribbon representation of EBOV GPΔmuc-WL^{2}P^4 trimer structure (Left: top view; Right: side view). The structure is colored as follows: glycan cap (gray), RBS (cyan), GP2 (yellow), and IFL (pink). *N*-linked glycans at N228, N257, N563, and N618 are shown as color-coded (by atom type) sticks. (**c**) Structural comparison of GPΔmuc-WL^{2}P^4 and previously reported GPΔmuc-WL^2 and GPΔmuc-WL^{2}P^2 trimers. The ribbon models of three GPΔmuc trimers containing WL^{2}P^4, WL^2, and WL^{2}P^2 mutations are shown in cyan, gold, and orange, respectively. Regions that are critical to the GP structure and exhibit appreciable differences in structure are superposed and shown as enlarged insects. (**d**) SEC profile of ADI-15878/SEC-purified SUDV GPΔmuc-WL^{2}P^4 trimer expressed in 2L HEK293S cells and complexed with ADI-15878 Fab. The SEC profile was generated from a Superose 6 10/300 increase column. (**e**) Schematic representation of image processing, 2D classification, and 3D reconstruction of cryo-EM data obtained for SUDV GPΔmuc-WL^{2}P^4 trimer in complex with ADI-15878 Fab using CryoSPARC. (**f**) Regions not modeled in the GP–CA45 complex structure due to limited density resolution. (**g**) Left: cryo-EM structure of SUDV GPΔmuc-WL^{2}P^4 superposed with the crystal structure of EBOV GPΔmuc-WL^{2}P^4 for comparison at the monomer level. The Cα root mean square deviation (Cα-RMSD) is 0.66 Å for 154 matching Cα atoms. Right: cryo-EM structure of SUDV GPΔmuc-WL^{2}P^4 in complex with ADI-15878 Fab superposed with the previously reported crystal structure of EBOV GPΔmuc in complex with CA45 Fab (PDB ID: 6EAY). Cα-RMSD is 0.63 Å for 149 matching Cα atoms. (**h**) Structural details of the GP-CA45 interface as illustrated in the crystal structure of EBOV GPΔmuc in complex with CA45 Fab (PDB ID: 6EAY). Hydrogen bonds are shown as red dashed lines, and the salt bridge is indicated with a black dashed line. Distances are labeled. (**i**) Snapshots of the GP-CA45 interface from different views with the density map shown. Interacting residues are displayed in ribbon representation. (**j**) Local resolution map overlaid with the built model at the GP-CA45 interface. (**k**) Published cryo-EM structure of EBOV GPΔmuc in complex with ADI-15878 (PDB ID: 6DZL; EMDB-8935), highlighting structural details at the interface. (**l**) Published cryo-EM structure of EBOV GPΔmuc in complex with rEBOV-515 and rEBOV-442 (PDB ID: 7M8L; EMDB-23719), with interface details shown. (**m**) Published cryo-EM structure of EBOV GPΔmuc in complex with rEBOV-520 and rEBOV-548 (PDB ID: 6PCI; EMDB-20301), highlighting interface details.

Fig. S3

a

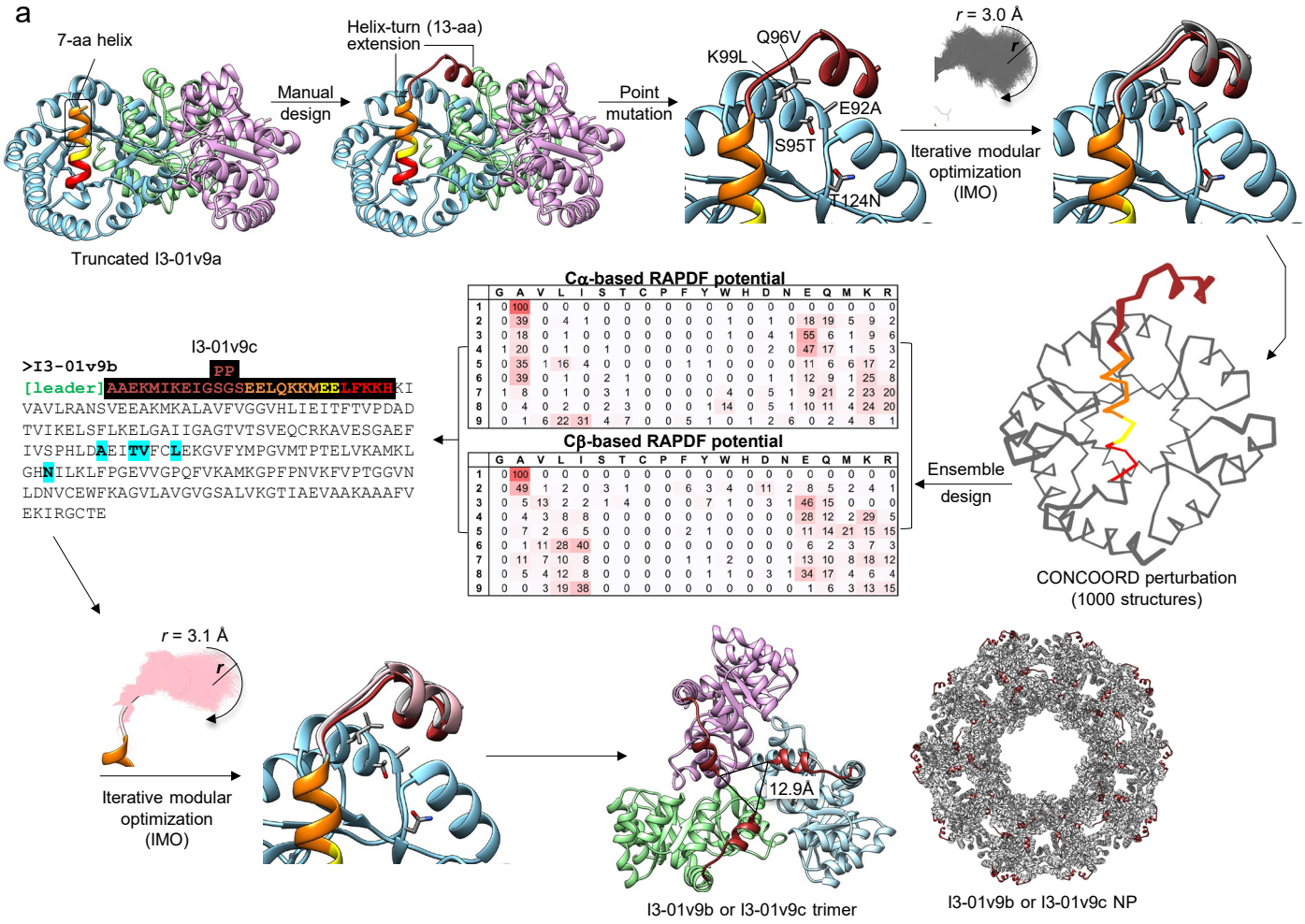

Cα-based RAPDF potential

	G	A	V	L	I	S	T	C	P	F	Y	W	H	D	N	E	Q	M	K	R
1	0	100	0	0	0	0	0	0	0	0	0	0	0	0	0	0	0	0	0	0
2	0	39	0	4	1	0	0	0	0	0	0	1	0	1	0	18	19	5	9	2
3	0	18	0	1	0	0	0	0	0	0	0	1	0	4	1	55	6	1	9	6
4	1	20	0	1	0	1	0	0	0	0	0	0	0	2	0	47	17	1	5	3
5	0	35	1	16	4	0	0	0	0	1	1	0	0	0	0	11	6	6	17	2
6	0	39	0	1	0	2	1	0	0	0	0	0	0	1	1	12	9	1	25	8
7	1	8	0	1	0	3	1	0	0	0	0	4	0	5	1	9	21	2	23	20
8	0	4	0	2	0	2	3	0	0	0	1	14	0	5	1	10	11	4	24	20
9	0	1	6	22	31	4	7	0	0	5	1	0	1	2	6	0	2	4	8	1

Cβ-based RAPDF potential

	G	A	V	L	I	S	T	C	P	F	Y	W	H	D	N	E	Q	M	K	R
1	0	100	0	0	0	0	0	0	0	0	0	0	0	0	0	0	0	0	0	0
2	0	49	1	2	0	3	1	0	0	6	3	4	0	11	2	8	5	2	4	1
3	0	5	13	2	2	1	4	0	0	0	7	1	0	3	1	46	15	0	0	0
4	0	4	3	8	8	0	0	0	0	0	0	0	0	0	0	28	12	2	29	5
5	0	7	2	6	5	0	0	0	0	2	1	0	0	0	0	11	14	21	15	15
6	0	1	11	28	40	0	0	0	0	0	0	0	0	0	0	6	2	3	7	3
7	0	11	7	10	8	0	0	0	0	1	1	2	0	0	1	13	10	8	18	12
8	0	5	4	12	8	0	0	0	0	0	1	1	0	3	1	34	17	4	6	4
9	0	0	3	19	38	0	0	0	0	0	0	0	0	0	0	1	6	3	13	15

b

>EBOV Mayinga GPΔmuc-WL^{2}P^4-I3-01v9b-T

MGVTGILQLPRDRFKRTSFFLWVIILFQRTFSIPLGVIHNSALQVSDVDKLVCRDKLSSTNQLRSVGLNLEGNGVATDVPSATKRWGFRSGVPPKVVNYEAGEWAENCYNLEI
KKPDGSECLPAAPDGIRGFPRCRYVHKVSGTGPCAGDFAFHKEGAFFLYDRLASTVIYRGTTFAEGVVAFLILPQAKKDFFSSHPLREPVNATEDPSSGYYSTTIRYQATGFG
TNETEYLFEVDNLTYVQLESRFTPQFLLQLNETIYTSGKRSNTTGKLIWKVNPEIDTTIGEWAFWETKKNLTRKIRSEELSFTVVSTHHQDTGEESASSGKLGLITNTIAGVA
GLITGGRRTRREAIVNAQPKCNPNLHYWTTQDEGAAIGLAWIPYFGPAAEGIYIEGLMHNQDGLICGLRQLANETTQALQLFLRATTEPRTFSILNRKAIDFLLQRWGGTCHI
LGPDCCIEPHDLTKNITDKIDQIIHDFVDKTLPDASGAEKMIKEIGSGSEELQKKMEELFKKHKIVAVLRANSVEEAKEKALAVFEGGVHLIEITFTVPDADTVIKELSFLKE
KGAIIGAGTVTSVEQCRKAVESGAEFIVSPHLDAEITVFCLEKGVFYMPGVMTPTELVKAMKLGHNILKLFPGEVVGPQFVKAMKGPFPNVKFVPTGGVNLDNVCEWFKAGVL
AVGVGSALVKGTPDEVREKAKAFVEKIRGCTE

>EBOV Mayinga GPΔmuc-WL^{2}P^4-I3-01v9c-T

MGVTGILQLPRDRFKRTSFFLWVIILFQRTFSIPLGVIHNSALQVSDVDKLVCRDKLSSTNQLRSVGLNLEGNGVATDVPSATKRWGFRSGVPPKVVNYEAGEWAENCYNLEI
KKPDGSECLPAAPDGIRGFPRCRYVHKVSGTGPCAGDFAFHKEGAFFLYDRLASTVIYRGTTFAEGVVAFLILPQAKKDFFSSHPLREPVNATEDPSSGYYSTTIRYQATGFG
TNETEYLFEVDNLTYVQLESRFTPQFLLQLNETIYTSGKRSNTTGKLIWKVNPEIDTTIGEWAFWETKKNLTRKIRSEELSFTVVSTHHQDTGEESASSGKLGLITNTIAGVA
GLITGGRRTRREAIVNAQPKCNPNLHYWTTQDEGAAIGLAWIPYFGPAAEGIYIEGLMHNQDGLICGLRQLANETTQALQLFLRATTEPRTFSILNRKAIDFLLQRWGGTCHI
LGPDCCIEPHDLTKNITDKIDQIIHDFVDKTLPDASGAEKMIKEIGPPSEELQKKMEELFKKHKIVAVLRANSVEEAKEKALAVFEGGVHLIEITFTVPDADTVIKELSFLKE
KGAIIGAGTVTSVEQCRKAVESGAEFIVSPHLDAEITVFCLEKGVFYMPGVMTPTELVKAMKLGHNILKLFPGEVVGPQFVKAMKGPFPNVKFVPTGGVNLDNVCEWFKAGVL
AVGVGSALVKGTPDEVREKAKAFVEKIRGCTE

c

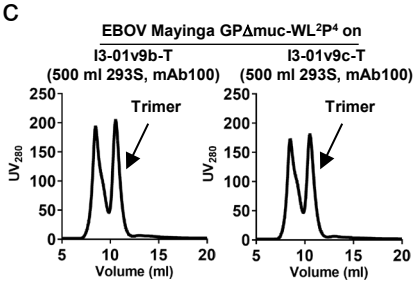

d

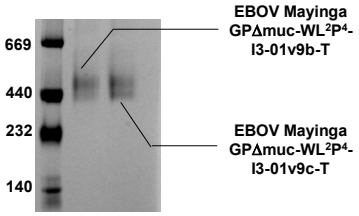

e

2D classes of EBOV Mayinga GPΔmuc-WL^{2}P^4-I3-01v9b-T

Selected 2D classification for modeling

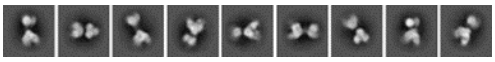

f

2D classes of EBOV Mayinga GPΔmuc-WL^{2}P^4-I3-01v9c-T

Selected 2D classification for modeling

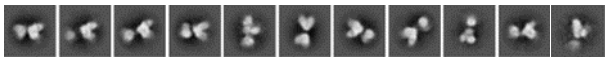

g

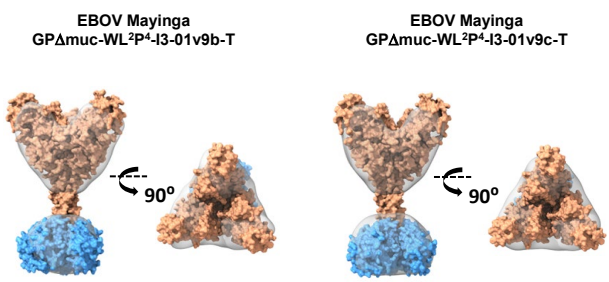

h

>EBOV Mayinga GPΔmuc-WL^{2}P^4-E2p-LD4-PADRE

MGVTGILQLPRDRFKRTSFFLWVIILFQRTFSIPLGVIHNSALQVSDVDKLVCRDKLSSTNQLRSVGLNLEGNGVATDVPSATKRWGFRSGVPPKVVNYEAGEWAENCYNLEI
KKPDGSECLPAAPDGIRGFPRCRYVHKVSGTGPCAGDFAFHKEGAFFLYDRLASTVIYRGTTFAEGVVAFLILPQAKKDFFSSHPLREPVNATEDPSSGYYSTTIRYQATGFG
TNETEYLFEVDNLTYVQLESRFTPQFLLQLNETIYTSGKRSNTTGKLIWKVNPEIDTTIGEWAFWETKKNLTRKIRSEELSFTVVSTHHQDTGEESASSGKLGLITNTIAGVA
GLITGGRRTRREAIVNAQPKCNPNLHYWTTQDEGAAIGLAWIPYFGPAAEGIYIEGLMHNQDGLICGLRQLANETTQALQLFLRATTEPRTFSILNRKAIDFLLQRWGGTCHI
LGPDCCIEPHDLTKNITDKIDQIIHDFVDKTLPDASGAAAKPATTEGEFPETREKMSGIRRAIAKAMVHSKHTAPHVTLMDEADVKLVAHRKKFKAIAAEKGIKLTFLPYVVK
ALVSALREYPVLNTAIDDETEEIIQKHYYNIGIAADTDRGLLVPVIKHADRKPIFALAQEINELAEKARDGKLTPGEMKGASCTITNIGSAGGQWFTPVINHPEVAILGIGRI
AEKPIVRDGEIVAAPMLALSLSFDHRMIDGATAQKALNHIKRLLSDPELLLMGGGGSFSEEQKKALDLAFYFDRRLTPEWRRYLSQRLGLNEEQIERWFRRKEQQIGWSHPQF
EKGSAKFVAAWTLKAAA

>EBOV Mayinga GPΔmuc-WL^{2}P^4-I3-01v9b-LD7-PADRE

MGVTGILQLPRDRFKRTSFFLWVIILFQRTFSIPLGVIHNSALQVSDVDKLVCRDKLSSTNQLRSVGLNLEGNGVATDVPSATKRWGFRSGVPPKVVNYEAGEWAENCYNLEI
KKPDGSECLPAAPDGIRGFPRCRYVHKVSGTGPCAGDFAFHKEGAFFLYDRLASTVIYRGTTFAEGVVAFLILPQAKKDFFSSHPLREPVNATEDPSSGYYSTTIRYQATGFG
TNETEYLFEVDNLTYVQLESRFTPQFLLQLNETIYTSGKRSNTTGKLIWKVNPEIDTTIGEWAFWETKKNLTRKIRSEELSFTVVSTHHQDTGEESASSGKLGLITNTIAGVA
GLITGGRRTRREAIVNAQPKCNPNLHYWTTQDEGAAIGLAWIPYFGPAAEGIYIEGLMHNQDGLICGLRQLANETTQALQLFLRATTEPRTFSILNRKAIDFLLQRWGGTCHI
LGPDCCIEPHDLTKNITDKIDQIIHDFVDKTLPDASGAEKMIKEIGSGSEELQKKMEELFKKHKIVAVLRANSVEEAKMKALAVFVGGVHLIEITFTVPDADTVIKELSFLKE
LGAIIGAGTVTSVEQCRKAVESGAEFIVSPHLDAEITVFCLEKGVFYMPGVMTPTELVKAMKLGHNILKLFPGEVVGPQFVKAMKGPFPNVKFVPTGGVNLDNVCEWFKAGVL
AVGVGSALVKGTIAEVAAKAAAFVEKIRGCTEGGGGSSPAVDIGDRLDELEKALEALSAEDGHDDVGQRLESLLRRWNSRRADGSAKFVAAWTLKAAA

>SUDV Gulu GPΔmuc-WL^{2}P^4-E2p-LD4-PADRE

MGILPSPGMPALLSLVSLLSVLLMGCVAEMPLGVVTNSTLEVTEIDQLVCKDHLASTDQLKSVGLNLEGSGVSTDIPSATKRWGFRSGVPPKVVSYEAGEWAENCYNLEIKKP
DGSECLPPPPDGVRGFPRCRYVHKAQGTGPCPGDYAFHKDGAFFLYDRLASTVIYRGVNFAEGVIAFLILAKPKETFLQSPPIREAVNYTENTSSYYATSYLEYEIENFGAQH
STTLFKIDNNTFVRLDRPHTPQFLFQLNDTIHLHQQLSNTTGRLIWTLDANINADIGEWAFWENKKNLSEQLRGEELSFEALSLNETEDDDAASSSTSNGLITSTVTGILGSL
GLRKRSRRQTNTKATGKCNPNLHYWTAQEQHNAAGIAWIPYFGPGAEGIYTEGLMHNQNALVCGLRQLANETTQALQLFLRATTEPRTYTILNRKAIDFLLRRWGGTCRILGP
DCCIEPHDLTKNITDKINQIIHDFIDNPLPNASGAAAKPATTEGEFPETREKMSGIRRAIAKAMVHSKHTAPHVTLMDEADVTKLVAHRKKFKAIAAEKGIKLTFLPYVVKAL
VSALREYPVLNTAIDDETEEIIQKHYYNIGIAADTDRGLLVPVIKHADRKPIFALAQEINELAEKARDGKLTPGEMKGASCTITNIGSAGGQWFTPVINHPEVAILGIGRIAE
KPIVRDGEIVAAPMLALSLSFDHRMIDGATAQKALNHIKRLLSDPELLLMGGGGSFSEEQKKALDLAFYFDRRLTPEWRRYLSQRLGLNEEQIERWFRRKEQQIGWSHPQFEK
GSAKFVAAWTLKAAA

>SUDV Gulu GPΔmuc-WL^{2}P^4-I3-01v9b-LD7-PADRE

MGILPSPGMPALLSLVSLLSVLLMGCVAEMPLGVVTNSTLEVTEIDQLVCKDHLASTDQLKSVGLNLEGSGVSTDIPSATKRWGFRSGVPPKVVSYEAGEWAENCYNLEIKKP
DGSECLPPPPDGVRGFPRCRYVHKAQGTGPCPGDYAFHKDGAFFLYDRLASTVIYRGVNFAEGVIAFLILAKPKETFLQSPPIREAVNYTENTSSYYATSYLEYEIENFGAQH
STTLFKIDNNTFVRLDRPHTPQFLFQLNDTIHLHQQLSNTTGRLIWTLDANINADIGEWAFWENKKNLSEQLRGEELSFEALSLNETEDDDAASSSTSNGLITSTVTGILGSL
GLRKRSRRQTNTKATGKCNPNLHYWTAQEQHNAAGIAWIPYFGPGAEGIYTEGLMHNQNALVCGLRQLANETTQALQLFLRATTEPRTYTILNRKAIDFLLRRWGGTCRILGP
DCCIEPHDLTKNITDKINQIIHDFIDNPLPNASGAEKMIKEIGSGSEELQKKMEELFKKHKIVAVLRANSVEEAKMKALAVFVGGVHLIEITFTVPDADTVIKELSFLKELGA
IIGAGTVTSVEQCRKAVESGAEFIVSPHLDAEITVFCLEKGVFYMPGVMTPTELVKAMKLGHNILKLFPGEVVGPQFVKAMKGPFPNVKFVPTGGVNLDNVCEWFKAGVLAVG
VGSALVKGTIAEVAAKAAAFVEKIRGCTEGGGGSSPAVDIGDRLDELEKALEALSAEDGHDDVGQRLESLLRRWNSRRADGSAKFVAAWTLKAAA

>BDBV R4386L GPΔmuc-WL^{2}P^4-E2p-LD4-PADRE

MGILPSPGMPALLSLVSLLSVLLMGCVAEIPLGVVHNNTLQVSDIDKLVCRDKLSSTSQLKSVGLNLEGNGVATDVPTATKRWGFRAGVPPKVVNYEAGEWAENCYNLDIKKA
DGSECLPEAPEGVRGFPRCRYVHKVSGTGPCPEGYAFHKEGAFFLYDRLASTIIYRSTTFSEGVVAFLILPETKKDFFQSPPLHEPANMTTDPSSYYHTVTLNYVADNFGTNM
TNFLFQVDHLTYVQLEPRFTPQFLVQLNETIYTNGRRSNTTGTLIWKVNPTVDTGVGEWAFWENKKNFTKTLSSEELSVIFVPRAQDPGSNDISESTEPGPLTNTTRGAANLL
TGSRRTRREITLRTQAKCNPNLHYWTTQDEGAAIGLAWIPYFGPAAEGIYTEGIMHNQNGLICGLRQLANETTQALQLFLRATTEPRTFSILNRKAIDFLLQRWGGTCHILGP
DCCIEPHDLTKNITDKIDQIIHDFIDKPLPDASGAAAKPATTEGEFPETREKMSGIRRAIAKAMVHSKHTAPHVTLMDEADVTKLVAHRKKFKAIAAEKGIKLTFLPYVVKAL
VSALREYPVLNTAIDDETEEIIQKHYYNIGIAADTDRGLLVPVIKHADRKPIFALAQEINELAEKARDGKLTPGEMKGASCTITNIGSAGGQWFTPVINHPEVAILGIGRIAE
KPIVRDGEIVAAPMLALSLSFDHRMIDGATAQKALNHIKRLLSDPELLLMGGGGSFSEEQKKALDLAFYFDRRLTPEWRRYLSQRLGLNEEQIERWFRRKEQQIGWSHPQFEK
GSAKFVAAWTLKAAA

>BDBV R4386L GPΔmuc-WL^{2}P^4-I3-01v9b-LD7-PADRE

MGILPSPGMPALLSLVSLLSVLLMGCVAEIPLGVVHNNTLQVSDIDKLVCRDKLSSTSQLKSVGLNLEGNGVATDVPTATKRWGFRAGVPPKVVNYEAGEWAENCYNLDIKKA
DGSECLPEAPEGVRGFPRCRYVHKVSGTGPCPEGYAFHKEGAFFLYDRLASTIIYRSTTFSEGVVAFLILPETKKDFFQSPPLHEPANMTTDPSSYYHTVTLNYVADNFGTNM
TNFLFQVDHLTYVQLEPRFTPQFLVQLNETIYTNGRRSNTTGTLIWKVNPTVDTGVGEWAFWENKKNFTKTLSSEELSVIFVPRAQDPGSNDISESTEPGPLTNTTRGAANLL
TGSRRTRREITLRTQAKCNPNLHYWTTQDEGAAIGLAWIPYFGPAAEGIYTEGIMHNQNGLICGLRQLANETTQALQLFLRATTEPRTFSILNRKAIDFLLQRWGGTCHILGP
DCCIEPHDLTKNITDKIDQIIHDFIDKPLPDASGAEKMIKEIGSGSEELQKKMEELFKKHKIVAVLRANSVEEAKMKALAVFVGGVHLIEITFTVPDADTVIKELSFLKELGA
IIGAGTVTSVEQCRKAVESGAEFIVSPHLDAEITVFCLEKGVFYMPGVMTPTELVKAMKLGHNILKLFPGEVVGPQFVKAMKGPFPNVKFVPTGGVNLDNVCEWFKAGVLAVG
VGSALVKGTIAEVAAKAAAFVEKIRGCTEGGGGSSPAVDIGDRLDELEKALEALSAEDGHDDVGQRLESLLRRWNSRRADGSAKFVAAWTLKAAA

i

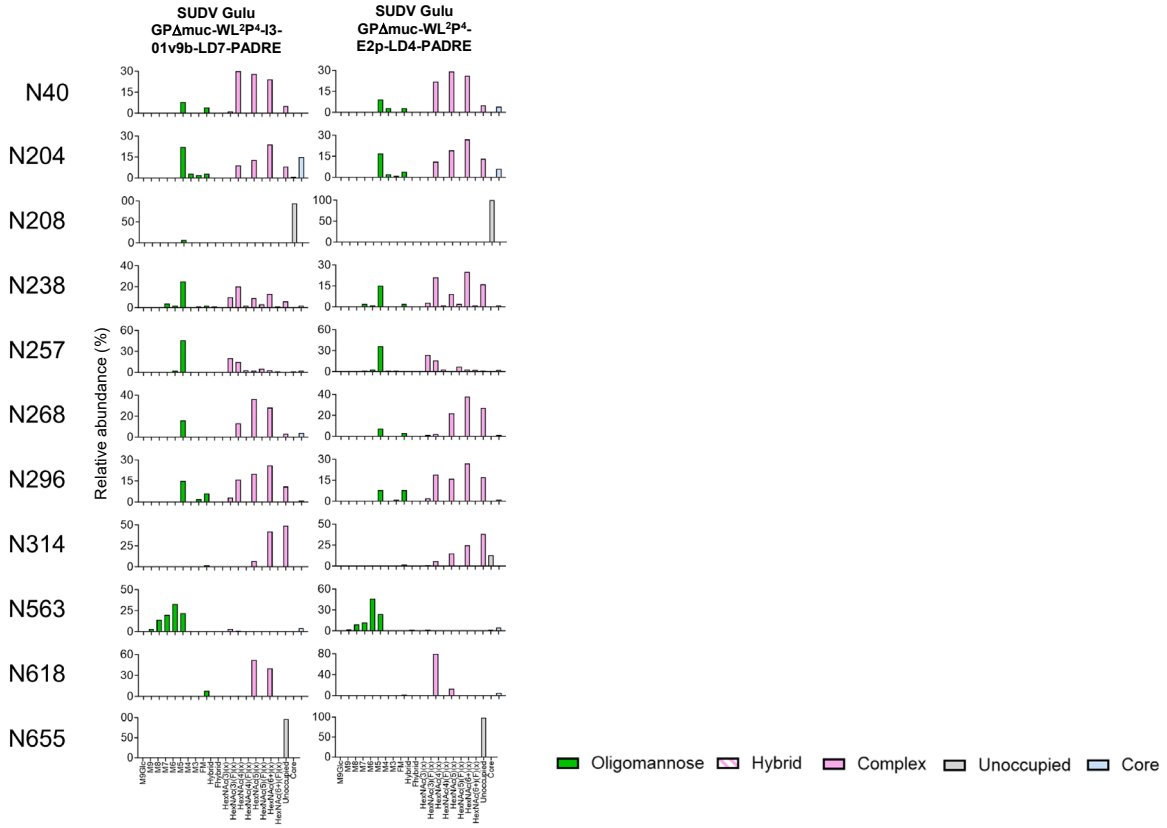

j

ELISA analysis of 6 rationally designed ebolavirus GPΔmuc SApNPs binding to 5 filovirus NAbs

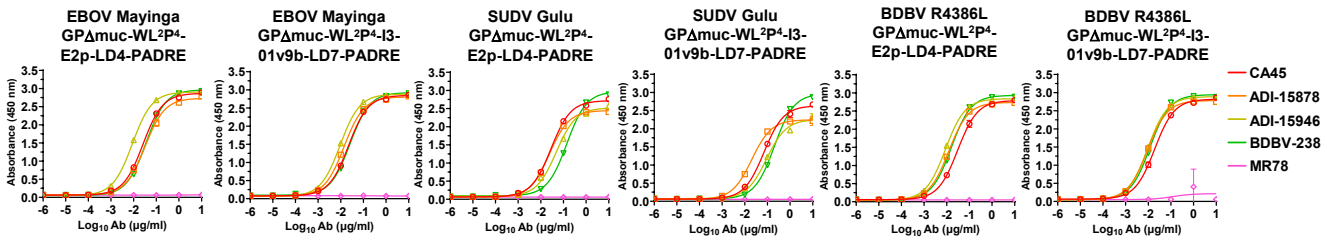

EBOV Mayinga GPΔmuc-WL^{2}P^{4}E2p-LD4-PADRE									
CA45		ADI-15878		ADI-15946		BDBV-289		MR78	
EC50	STD	EC50	STD	EC50	STD	EC50	STD	EC50	STD
0.02593	0.00030	0.03197	0.00696	0.00879	0.00075	0.03550	0.00212	N.D.	N.D.

EBOV Mayinga GPΔmuc-WL^{2}P^{4}I3-01v9b-LD7-PADRE									
CA45		ADI-15878		ADI-15946		BDBV-289		MR78	
EC50	STD	EC50	STD	EC50	STD	EC50	STD	EC50	STD
0.022141	0.000587	0.014095	0.000148	0.009384	0.000164	0.025555	0.00123	N.D.	N.D.

SUDV Gulu GPΔmuc-WL^{2}P^{4}E2p-LD4-PADRE									
CA45		ADI-15878		ADI-15946		BDBV-289		MR78	
EC50	STD	EC50	STD	EC50	STD	EC50	STD	EC50	STD
0.02819	0.00070	0.02407	0.00284	0.04811	0.00204	0.14057	0.00849	N.D.	N.D.

SUDV Gulu GPΔmuc-WL^{2}P^{4}I3-01v9b-LD7-PADRE									
CA45		ADI-15878		ADI-15946		BDBV-289		MR78	
EC50	STD	EC50	STD	EC50	STD	EC50	STD	EC50	STD
0.0699	0.0024	0.0204	0.0024	0.0910	0.0007	0.2017	0.0139	N.D.	N.D.

BDBV R4386L GPΔmuc-WL^{2}P^{4}E2p-LD4-PADRE									
CA45		ADI-15878		ADI-15946		BDBV-289		MR78	
EC50	STD	EC50	STD	EC50	STD	EC50	STD	EC50	STD
0.0307	0.0035	0.0123	0.0002	0.0087	0.0004	0.0159	0.0002	N.D.	N.D.

BDBV R4386L GPΔmuc-WL^{2}P^{4}I3-01v9b-LD7-PADRE									
CA45		ADI-15878		ADI-15946		BDBV-289		MR78	
EC50	STD	EC50	STD	EC50	STD	EC50	STD	EC50	STD
0.0191	0.0014	0.0093	0.0005	0.0095	0.0005	0.0120	0.0003	N.D.	N.D.

k **BLI analysis of 6 rationally designed orthoebolavirus GPΔmuc SApNPs binding to 5 filovirus NAbs**

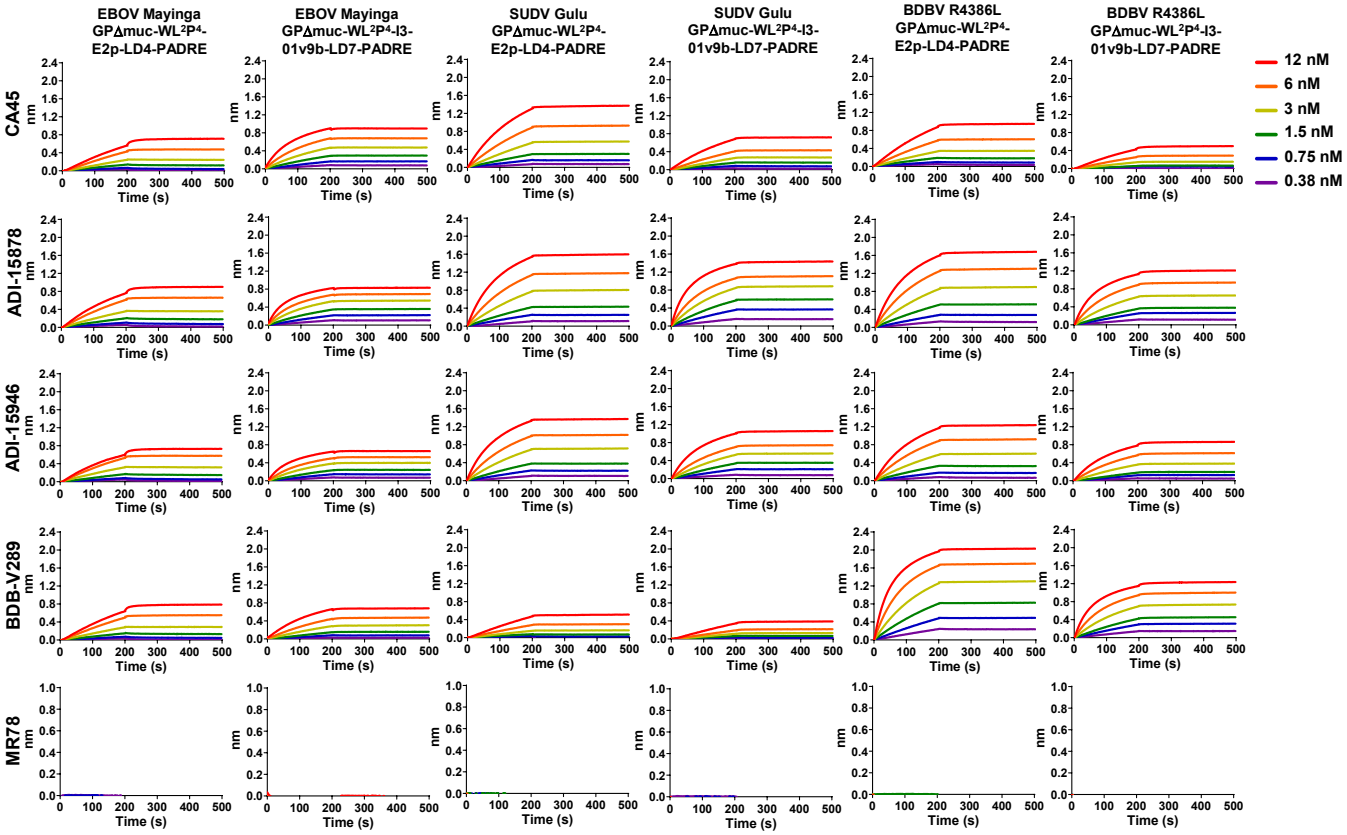

K_D values for 6 redesigned Filo-virus GP NP binding to 5 representative antibodies (nM) [a]

	CA45	ADI-15878	ADI-15946	BDBV-289	MR78
EBOV Mayinga GPΔmuc-WL^{2}P^4-E2p-LD4-PADRE	<1.0E-3	<1.0E-3	<1.0E-3	<1.0E-3	— [b]
EBOV Mayinga GPΔmuc-WL^{2}P^4-I3-01v9b-LD7-PADRE	<1.0E-3	<1.0E-3	<1.0E-3	<1.0E-3	— [b]
SUDV Gulu GPΔmuc-WL^{2}P^4-E2p-LD4-PADRE	<1.0E-3	<1.0E-3	<1.0E-3	<1.0E-3	— [b]
SUDV Gulu GPΔmuc-WL^{2}P^4-I3-01v9b-LD7-PADRE	<1.0E-3	<1.0E-3	<1.0E-3	<1.0E-3	— [b]
BDBV R4386L GPΔmuc-WL^{2}P^4-E2p-LD4-PADRE	<1.0E-3	<1.0E-3	<1.0E-3	<1.0E-3	— [b]
BDBV R4386L GPΔmuc-WL^{2}P^4-I3-01v9b-LD7-PADRE	<1.0E-3	<1.0E-3	<1.0E-3	<1.0E-3	— [b]

[a] K_D values were derived from biolayer interferometry (BLI) using the binding equations describing a 1:1 interaction.
[b] "—" indicates cases where the peak signal value at the highest orthoebolavirus antigen concentration is 0.2 or lower.

Fig. S3. Rational design of I3-01v9b/c and in vitro characterization of orthoebolavirus GPΔmuc-presenting SApNPs. (**a**) Schematic representation of computational design of I3-01v9b/c. Top left: structural model of I3-01v9a with the 11-aa N-terminal helix truncated to 7 aa; Top middle left: a 13-aa helix-turn fragment (9-aa helix + 4-aa turn, all alanine) was fused to the 7-aa N-terminal helix of the truncated I3-01v9a in such a way the new 9-aa N-terminal helix from the fused fragment would pack within the groove of two helices that are part of the I3-01 core; Top middle right: four mutations, E92A, S95T, Q96V, and K99L, were introduced to the I3-01 core helices to remove their steric clashes with the new N-terminal helix; Top right: iterative modular optimization (IMO) of the helix-turn backbone, with a radius of 3.0 Å measured for the first amino acid at the N-terminus; Middle right: 1000 slightly perturbed backbone conformations generated by CONCOORD, a torsion-space sampling program; Middle middle: results from an ensemble-based protein design program used to predict the optimal sequence for the 9-aa N-terminal helix within the fragment using Cα and Cβ-based RAPDF potentials. The 4-aa turn was set to "GSGS"; Middle left: sequence of I3-01v9b designed by combining data from both RAPDF potentials, with the difference between I3-01v9b and I3-01v9c (the "PP" mutation) labeled on the sequence; Bottom left: further backbone relaxation using IMO with a minimum perturbation angle; Bottom right: a structural model of the trimeric I3-01v9b/c, termed I3-01v9b/c-T, in which the N-termini form a triangle of 12.9 Å, and a structural model of fully assembled I3-01v9b/c NP. (**b**) Amino acids sequences of EBOV GPΔmuc-WL2P4-I3-01v9b/c-T, which are EBOV Mayinga GPΔmuc-WL^{2}P^4 anchored to the trimeric I3-01v9b/c-T scaffolds. Signal peptide, GP, restriction site (AS), and I3-01v9b/c-T are highlighted in yellow, grey, green and pink, respectively. The double proline mutation in the N-terminus of I3-01v9c-T that differs from I3-01v9b-T is highlighted in red. (**c**) SEC profiles of EBOV GPΔmuc-WL2P4-I3-01v9b/c-T expressed in 500 ml HEK293S cells and purified using an ADI-15878 column. (**d**) BN-PAGE of ADI-15878/SEC-purified EBOV GPΔmuc-WL2P4-I3-01v9b/c-T. (**e**) and (**f**) Representative 2D classification images of ADI-15878/SEC-purified EBOV GPΔmuc-WL2P4-I3-01v9b/c-T trimers. (**g**) 3D reconstructions of ADI-15878/SEC-purified EBOV GPΔmuc-WL2P4-I3-01v9b/c-T trimers. Crystal structures of EBOV GPΔmuc-WL^{2}P^2 (PDB ID:7JPH) and the bacterial enzyme from which I3-01 was derived (PDB ID:1VLW) were fitted into the model and shown in orange and blue, respectively. (**h**) Amino acids sequences of EBOV, SUDV, and BDBV GPΔmuc-WL^{2}P^4-E2P-LD4-PADRE and -I3-01v9b-LD7-PADRE SApNP constructs. LD stands for locking domain (LD), which is fused to the C-terminus of the NP backbone and forms an inner layer to stabilize the NP shell from the inside. PADRE is a helper T-cell epitope and forms a hydrophobic core at the center of the assembled NP to further stabilize the NP structure and to induce a strong T-help response upon vaccination. (**i**) Compositional site-specific glycan analysis of SUDV GPΔmuc-WL^{2}P^4-E2P-LD4-PADRE and I3-01v9b-LD7-PADRE SApNPs, as in **Fig. S1c**. (**j**) ELISA analysis of EBOV, SUDV, and BDBV GPΔmuc-WL^{2}P^4-E2P-LD4-PADRE and I3-01v9b-LD7-PADRE SApNPs binding to 5 filovirus NAbs, as in **Fig. S1h**. (**k**) BLI analysis of EBOV, SUDV, and BDBV GPΔmuc-WL^{2}P^4-E2P-LD4-PADRE and I3-01v9b-LD7-PADRE SApNPs binding to 5 filovirus NAbs. A two-fold concentration gradient of antigen, starting at 12 nM, was used in a dilution series of six. K_D values derived from a 1:1 fitting model are summarized in a table.

Fig. S4

a

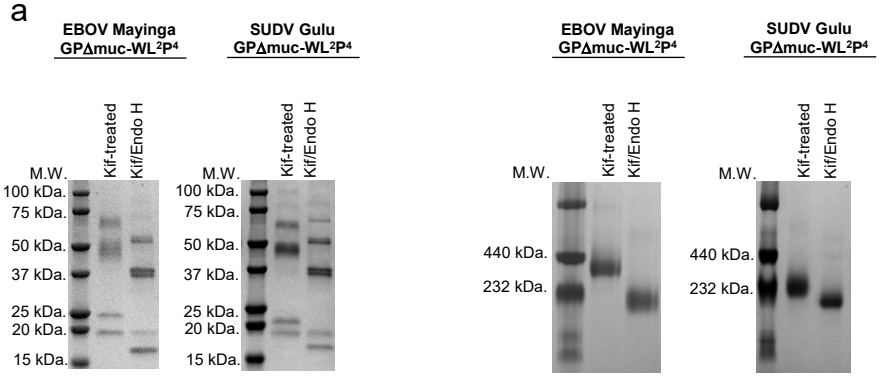

b **ELISA analysis of Kif-treated and glycan-trimmed EBOV and SUDV GPΔmuc-WL^{2}P^4 trimers binding to 5 filovirus NAbs**

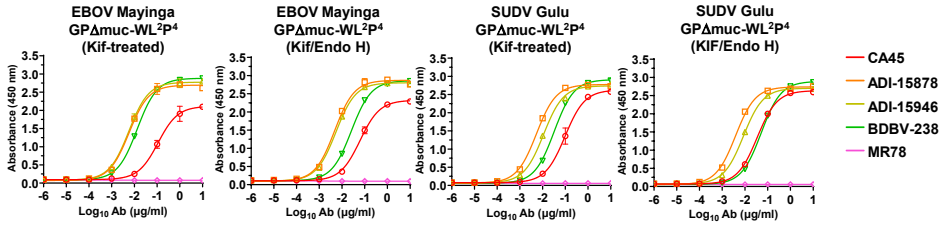

EBOV Mayinga GPΔmuc-WL^{2}P^4 (Kif-treated)									
CA45		ADI-15878		ADI-15946		BDBV-289		MR78	
EC50	STD	EC50	STD	EC50	STD	EC50	STD	EC50	STD
0.1110	0.0252	0.0058	0.0006	0.0057	0.0003	0.0133	0.0004	N.D.	N.D.

EBOV Mayinga GPΔmuc-WL^{2}P^4 (Kif/Endo H)									
CA45		ADI-15878		ADI-15946		BDBV-289		MR78	
EC50	STD	EC50	STD	EC50	STD	EC50	STD	EC50	STD
0.0624	0.0093	0.0047	0.0001	0.0055	0.0006	0.0261	0.0021	N.D.	N.D.

SUDV Gulu GPΔmuc-WL^{2}P^4 (Kif-treated)									
CA45		ADI-15878		ADI-15946		BDBV-289		MR78	
EC50	STD	EC50	STD	EC50	STD	EC50	STD	EC50	STD
0.0973	0.0354	0.0054	0.0003	0.0111	0.0003	0.0325	0.0013	N.D.	N.D.

SUDV Gulu GPΔmuc-WL^{2}P^4 (Kif/Endo H)									
CA45		ADI-15878		ADI-15946		BDBV-289		MR78	
EC50	STD	EC50	STD	EC50	STD	EC50	STD	EC50	STD
0.0347	0.0012	0.0039	0.0002	0.0086	0.0002	0.0518	0.0010	N.D.	N.D.

c **BLI analysis of Kif-treated and glycan-trimmed EBOV and SUDV GPΔmuc-WL^{2}P^4 trimers binding to 5 filovirus NAbs**

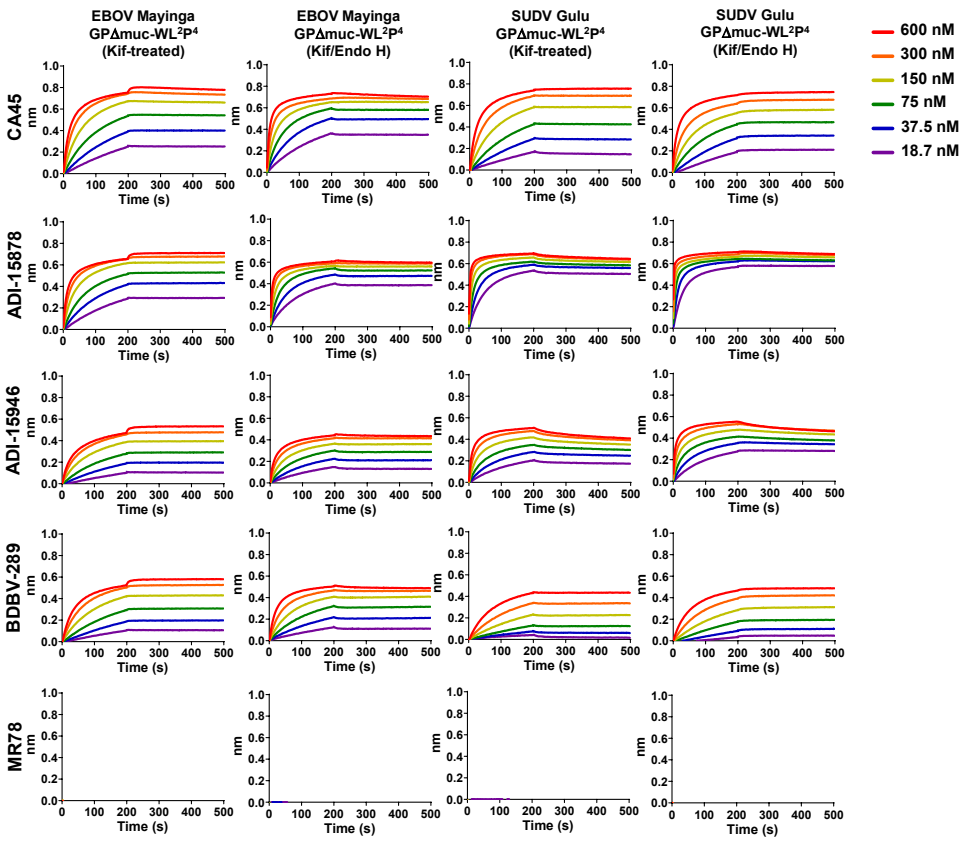

K_D values for 4 glycan-modified orthoebolavirus GPΔmuc trimers binding to 5 filovirus NAbs (nM) [a]

	CA45	ADI-15878	ADI-15946	BDBV-289	MR78
EBOV Mayinga GPΔmuc-WL^{2}P^4 (Kif-treated)	<1.0E-3	<1.0E-3	<1.0E-3	<1.0E-3	— [b]
EBOV Mayinga GPΔmuc-WL^{2}P^4 (Kif/Endo H)	<1.0E-3	<1.0E-3	<1.0E-3	<1.0E-3	— [b]
SUDV Gulu GPΔmuc-WL^{2}P^4 (Kif-treated)	<1.0E-3	2.99E-2	2.03	<1.0E-3	— [b]
SUDV Gulu GPΔmuc-WL^{2}P^4 (Kif/Endo H)	<1.0E-3	<1.0E-3	9.52E-1	<1.0E-3	— [b]

[a] K_D values were derived from bio-layer interferometry (BLI) using the binding equations describing a 1:1 interaction.
[b] "—" indicates cases where the peak signal value at the highest orthoebolavirus antigen concentration is 0.2 or lower.

d

>SUDV Gulu GPΔmuc-WL^{2}P^4-PD-E2p-LD4-PADRE

MGILPSPGMPALLSLVSLLSVLLMGCVAEMPLGVVTNSTLEVTEIDQLVCKDHLASTDQLKSVGLNLEGSGVSTDIPSATKRWGFRSGVPPKVVSYEAGEWAENCYNLEIKKP
DGSECLPPPPDGVRGFPRCRYVHKAQGTGPCPGDYAFHKDGAFFLYDRLASTVIYRGVNFAEGVIAFLILAKPKETFLQSPPIREAVNYTENTSSYYATSYLEYEIENFGAQH
STTLFKIDNNTFVRLDRPHTPQFLFQLNDTIHLHQQLSNTTGRLIWTLDANINADIGEWAFWENKKNLSEQLRGEELSFEALSLNETEDDDAASSSTSNGLITSTVTGILGSL
GLRKRSRRQTNTKATGKCNPNLHYWTAQEQHNAAGIAWIPYFGPGAEGIYTEGLMHNQNALVCGLRQLANETTQALQLFLRATTEPRTYTILNRKAIDFLLRRWGGTCRILGP
DCCIEPHDLTKNITDKINQIIHDFIDNPLPDASGAAAKPATTEGEFPETREKMSGIRRAIAKAMVHSKHTAPHVTLMDEADVT
KLVAHRKKFKAIAAEKGIKLTFLPYVVKALVSALREYPVLNTAIDDETEEIIQKHYYNIGIAADTDRGLLVPVIKHADRKPIFALAQEINELAEKARDGKLTPGEMKGASCTI
TNIGSAGGQWFTPVINHPEVAILGIGRIAEKPIVRDGEIVAAPMLALSLSFDHRMIDGATAQKALNHIKRLLSDPELLLMGGGGSFSEEQKKALDLAFYFDRRLTPEWRRYLS
QRLGLNEEQIERWFRRKEQQIGWSHPQFEKGSAKFVAAWTLKAAA

>SUDV Gulu GPΔmuc-WL^{2}P^4-PD-I3-01v9b-LD7-PADRE

MGILPSPGMPALLSLVSLLSVLLMGCVAEMPLGVVTNSTLEVTEIDQLVCKDHLASTDQLKSVGLNLEGSGVSTDIPSATKRWGFRSGVPPKVVSYEAGEWAENCYNLEIKKP
DGSECLPPPPDGVRGFPRCRYVHKAQGTGPCPGDYAFHKDGAFFLYDRLASTVIYRGVNFAEGVIAFLILAKPKETFLQSPPIREAVNYTENTSSYYATSYLEYEIENFGAQH
STTLFKIDNNTFVRLDRPHTPQFLFQLNDTIHLHQQLSNTTGRLIWTLDANINADIGEWAFWENKKNLSEQLRGEELSFEALSLNETEDDDAASSSTSNGLITSTVTGILGSL
GLRKRSRRQTNTKATGKCNPNLHYWTAQEQHNAAGIAWIPYFGPGAEGIYTEGLMHNQNALVCGLRQLANETTQALQLFLRATTEPRTYTILNRKAIDFLLRRWGGTCRILGP
DCCIEPHDLTKNITDKINQIIHDFIDNPLPDASGAEKMIKEIGSGSEELQKKMEELFKKHKIVAVLRANSVEEAKEKALAVFEGGVHLIEITFTVPDADTVIKELSFLKEKGA
IIGAGTVTSVEQCRKAVESGAEFIVSPHLDAEITVFCLEKGVFYMPGVMTPTELVKAMKLGHNILKLFPGEVVGPQFVKAMKGPFPNVKFVPTGGVNLDNVCEWFKAGVLAVG
VGSALVKGTPDEVREKAKAFVEKIRGCTEGGGGSSPAVDIGDRLDELEKALEALSAEDGHDDVGQRLESLLRRWNSRRADGSAKFVAAWTLKAAA

e

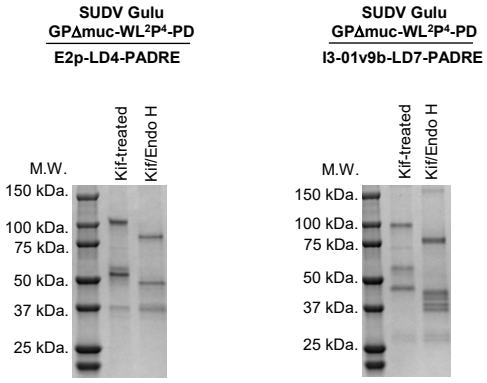

f **Site-specific glycan profiles of wild-type and Kif-treated SUDV GPΔmuc-WL^{2}P^4-PD-presenting SApNPs**

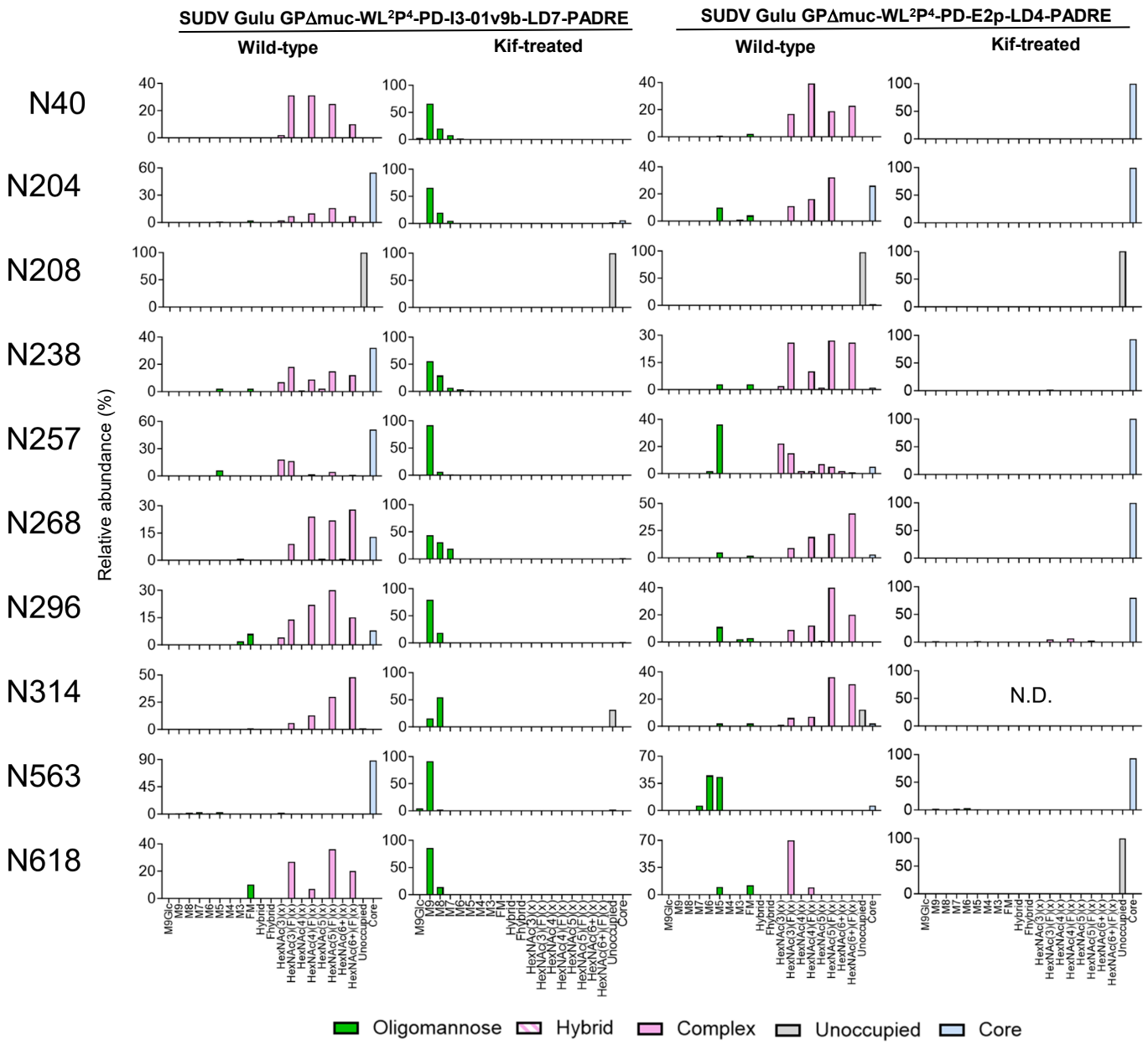

g

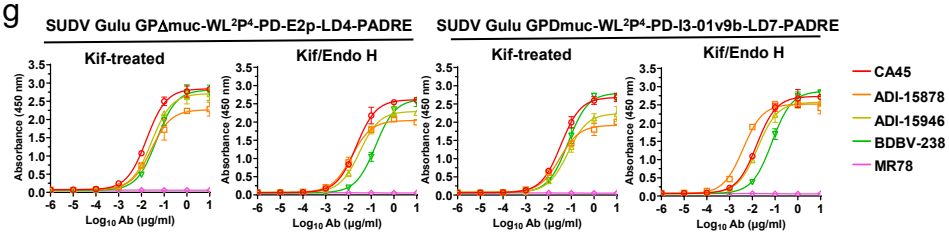

SUDV Gulu GPΔmuc-WL2P4-PD-E2p-LD4-PADRE (Kif-treated)									
CA45		ADI-15878		ADI-15946		BDBV-829		MR78	
EC50	STD	EC50	STD	EC50	STD	EC50	STD	EC50	STD
0.0168	0.0014	0.0277	0.0049	0.0283	0.0021	0.0462	0.0006	N.D.	N.D.

SUDV Gulu GPΔmuc-WL2P4-PD-E2p-LD4-PADRE (Kif/Endo H)									
CA45		ADI-15878		ADI-15946		BDBV-829		MR78	
EC50	STD	EC50	STD	EC50	STD	EC50	STD	EC50	STD
0.0226	0.0048	0.0308	0.002	0.0312	0.0043	0.1550	0.0179	N.D.	N.D.

SUDV Gulu GPΔmuc-WL2P4-PD-I3-01v9b-LD7-PADRE (Kif-treated)									
CA45		ADI-15878		ADI-15946		BDBV-829		MR78	
EC50	STD	EC50	STD	EC50	STD	EC50	STD	EC50	STD
0.0348	0.0024	0.0254	0.0163	0.0708	0.0049	0.0718	0.0181	N.D.	N.D.

SUDV Gulu GPΔmuc-WL2P4-PD-I3-01v9b-LD7-PADRE (Kif/Endo H)									
CA45		ADI-15878		ADI-15946		BDBV-829		MR78	
EC50	STD	EC50	STD	EC50	STD	EC50	STD	EC50	STD
0.0155	0.0023	0.0039	0.0004	0.0174	0.0011	0.0726	0.0083	N.D.	N.D.

h

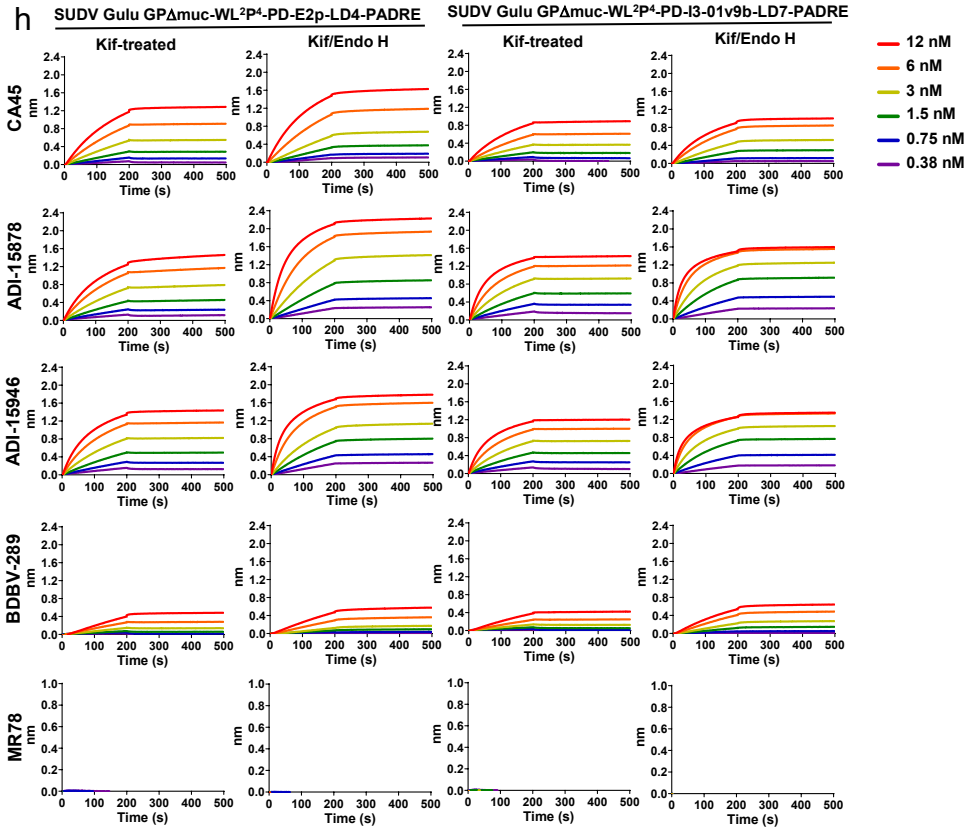

***K_D* values for 4 glycan-modified SUDVGPΔmuc-WL^{2}P^4-PD-presenting SApNPs binding to 5 filovirus NAbs (nM) [a]**

	CA45	ADI-15878	ADI-15946	BDBV-289	MR78
SUDV Gulu GPΔmuc-WL^{2}P^4-PD-E2p-LD4-PADRE (Kif-treated)	<1.0E-3	<1.0E-3	<1.0E-3	<1.0E-3	—[b]
SUDV Gulu GPΔmuc-WL^{2}P^4-PD-E2p-LD4-PADRE (Kif/Endo H)	<1.0E-3	<1.0E-3	<1.0E-3	<1.0E-3	—[b]
SUDV Gulu GPΔmuc-WL^{2}P^4-PD-I3-01v9b-LD7-PADRE (Kif-treated)	<1.0E-3	<1.0E-3	<1.0E-3	<1.0E-3	—[b]
SUDV Gulu GPΔmuc-WL^{2}P^4-PD-I3-01v9b-LD7-PADRE (Kif/Endo H)	<1.0E-3	<1.0E-3	<1.0E-3	<1.0E-3	—[b]

[a] K_D values were derived from biolayer interferometry (BLI) using the binding equations describing a 1:1 interaction.
[b] "—" indicates cases where the peak signal value at the highest SUDV antigen concentration is 0.2 or lower.

Fig. S4. In vitro characterization for glycan-modified orthoebolavirus GPΔmuc trimers and SApNPs. (**a**) SDS-PAGE and BN-PAGE of glycan-modified EBOV Mayinga and SUDV Gulu GPΔmuc-WL^{2}P^4 trimers. They were either expressed in the presence of kifunensine (Kif-treated) to obtain oligomannose-only glycans or further trimmed using endo H (Kif/Endo H) to obtain a mono-layer of GlcNAc stumps. (**b**) ELISA analysis of glycan-modified EBOV Mayinga and SUDV Gulu GPΔmuc-WL^{2}P^4 trimers binding to 5 filovirus NAbs in the IgG form, as in **Fig S1h.** (**c**) BLI analysis of glycan-modified EBOV Mayinga and SUDV Gulu GPΔmuc-WL^{2}P^4 trimers binding to 5 filovirus NAbs in the IgG form, as in **Fig S1i**. (**d**) Construct sequences for "multilayered" E2p (E2p-LD4-PADRE) and I3-01v9b (I3-0v9b-LD7-PADRE) SApNPs presenting 20 copies of a SUDV Gulu GPΔmuc-WL^{2}P^4-PD trimer, which contains a mutation (N637D) at the C-terminus to remove a potential glycosylation site between GP and NP. (**e**) SDS-PAGE of 3 glycan-modified SApNPs corresponding to EBOV Mayinga GPΔmuc-WL^{2}P^4 on the E2p-LD4-PADRE scaffold and SUDV Gulu GPΔmuc-WL^{2}P^4-PD on the E2p-LD4-PADRE and I3-01v9b-LD7-PADRE scaffolds. (**f**) Compositional site-specific glycan analysis of SUDV GPΔmuc-WL^{2}P^4-PD-presenting E2p and I3-01v9b SApNPs, as in **Fig. S1c**. (**g**) ELISA analysis of glycan-modified SUDV Gulu GPΔmuc-WL2P4-PD-presenting E2P and I3-01v9b SApNPs binding to 5 filovirus NAbs in the IgG form, as in **Fig S1h**. (**h**) BLI analysis of glycan-modified SUDV Gulu GPΔmuc-WL^{2}P^4-PD-presenting E2P and I3-01v9b SApNPs binding to 5 filovirus NAbs in the IgG form, as in **Fig S3k**.

a

>RAVV GPΔTM-foldon-His$_6$

MGVTGILQLPRDRFKRTSFFLWVIILFQRTFSIKTLPVLEIASNSQPQDVDSVCSGTLQKTEDVHLMGFTLSGQKVADSPLEASKRWAFRTGVPPKNVEYTEGEEAKTCYNIS
VTDPSGKSLLLDPPSNIRDYPKCKTVHHIQGQNPHAQGIALHLWGAFFLYDRVASTTMYRGKVFTEGNIAAMIVNKTVHRMIFSRQGQGYRHMNLTSTNKYWTSSNETQRNDT
GCFGILQEYNSTNNQTCPPSLKPPSLPTVTPSIHSTNTQINTAK**SGT**MNPSSDDEDLMISGSGSGEQGPHTTLNVVTEQKQSSTILSTPSLHPSTSQHEQNSTNPSRHAVTEH
NGTDPTTQPATLLNNTNTTPTYNTLKYNLSTPSPPTRNITNNDTQRELAESEQTNAQLNTTLDPTENPTTGQDTNSTTNIIMTTSDITSKHPTNSSPDSSPTT**RPPI**YFRKKR
SIFWKEGDIFPFLDGLINTEIDFDPIPNTETIFDESPSFNTSTNEEQHTPPNISLTFSYFPDKNGDTAYSGENENDCDAELRIWSVQEDDLAAGLSWIPFFGPGIEGLYTAGL
IKNQNNLVCRLRRLANQTAKSLELLLRVTTEERTFSLINRHAIDFLLTRWGGTCKVLGPDCCIGIEDLSKNISEQIDKIRKDEQKEETGASGYIPEAPRDGQAYVRKDGEWVL
LSTFLGSHHHHHH

>RAVV GPΔmuc-foldon-His$_6$

MGVTGILQLPRDRFKRTSFFLWVIILFQRTFSIKTLPVLEIASNSQPQDVDSVCSGTLQKTEDVHLMGFTLSGQKVADSPLEASKRWAFRTGVPPKNVEYTEGEEAKTCYNIS
VTDPSGKSLLLDPPSNIRDYPKCKTVHHIQGQNPHAQGIALHLWGAFFLYDRVASTTMYRGKVFTEGNIAAMIVNKTVHRMIFSRQGQGYRHMNLTSTNKYWTSSNETQRNDT
GCFGILQEYNSTNNQTCPPSLKPPSLPTVTPSIHSTNTQINTAK**SGTRPP**IYFRKKRSIFWKEGDIFPFLDGLINTEIDFDPIPNTETIFDESPSFNTSTNEEQHTPPNISLT
FSYFPDKNGDTAYSGENENDCDAELRIWSVQEDDLAAGLSWIPFFGPGIEGLYTAGLIKNQNNLVCRLRRLANQTAKSLELLLRVTTEERTFSLINRHAIDFLLTRWGGTCKV
LGPDCCIGIEDLSKNISEQIDKIRKDEQKEETGASGYIPEAPRDGQAYVRKDGEWVLLSTFLGSHHHHHH

>RAVV GPΔmuc-P^2-foldon-His$_6$

MGVTGILQLPRDRFKRTSFFLWVIILFQRTFSIKTLPVLEIASNSQPQDVDSVCSGTLQKTEDVHLMGFTLSGQKVADSPLEASKRWAFRTGVPPKNVEYTEGEEAKTCYNIS
VTDPSGKSLLLDPPSNIRDYPKCKTVHHIQGQNPHAQGIALHLWGAFFLYDRVASTTMYRGKVFTEGNIAAMIVNKTVHRMIFSRQGQGYRHMNLTSTNKYWTSSNETQRNDT
GCFGILQEYNSTNNQTCPPSLKPPSLPTVTPSIHSTNTQINTAK**SGTRPP**IYFRKKRSIFWKEGDIFPFLDGLINTEIDFDPIPNTETIFDESPSFNTSTNEEQHTPPNISLT
FSYFPDKNGDTAYSGENENDCDAELRIWSVQEDDLAAGLSWIPFFGPGIEGLYTAGLIKNQNNLVCRLRRLANQTAKSLELLLRVT**P**EERTFSLINRHAIDFLLTRWGGTCKV
LGPDCCIGIEDLSKNISEQIDKIRKDEQKEETGASGYIPEAPRDGQAYVRKDGEWVLLSTFLGSHHHHHH

>RAVV GPΔmuc-P^4-foldon-His$_6$

MGVTGILQLPRDRFKRTSFFLWVIILFQRTFSIKTLPVLEIASNSQPQDVDSVCSGTLQKTEDVHLMGFTLSGQKVADSPLEASKRWAFRTGVPPKNVEYTEGEEAKTCYNIS
VTDPSGKSLLLDPPSNIRDYPKCKTVHHIQGQNPHAQGIALHLWGAFFLYDRVASTTMYRGKVFTEGNIAAMIVNKTVHRMIFSRQGQGYRHMNLTSTNKYWTSSNETQRNDT
GCFGILQEYNSTNNQTCPPSLKPPSLPTVTPSIHSTNTQINTAK**SGTRPP**IYFRKKRSIFWKEGDIFPFLDGLINTEIDFDPIPNTETIFDESPSFNTSTNEEQHTPPNISLT
FSYFPDKNGDTAYSGENENDCDAELRIWSVQEDDLAAGLSWIPFFGPGIEGLYTAGLIKNQNNLVCRLRRLANQTAKSLELLLRVTTE**P**RTFSLINRHAIDFLLTRWGGTCKV
LGPDCCIGIEDLSKNISEQIDKIRKDEQKEETGASGYIPEAPRDGQAYVRKDGEWVLLSTFLGSHHHHHH

>RAVV GPΔmuc-P^{2}CT-foldon-His$_6$

MGVTGILQLPRDRFKRTSFFLWVIILFQRTFSIKTLPVLEIASNSQPQDVDSVCSGTLQKTEDVHLMGFTLSGQKVADSPLEASKRWAFRTGVPPKNVEYTEGEEAKTCYNIS
VTDPSGKSLLLDPPSNIRDYPKCKTVHHIQGQNPHAQGIALHLWGAFFLYDRVASTTMYRGKVFTEGNIAAMIVNKTVHRMIFSRQGQGYRHMNLTSTNKYWTSSNETQRNDT
GCFGILQEYNSTNNQTCPPSLKPPSLPTVTPSIHSTNTQINTAK**SGTRPP**IYFRKKRSIFWKEGDIFPFLDGLINTEIDFDPIPNTETIFDESPSFNTSTNEEQHTPPNISLT
FSYFPDKNGDTAYSGENENDCDAELRIWSVQEDDLAAGLSWIPFFGPGIEGLYTAGLIKNQNNLVCRLRRLANQTAKSLELLLRVT**P**EERTFSLINRHAIDFLLTRWGGTCKV
LGPDCCIGIEDLSKNISEQIDKIRKD**FV**KEETGASGYIPEAPRDGQAYVRKDGEWVLLSTFLGSHHHHHH

b

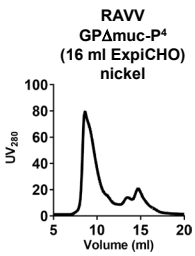

c

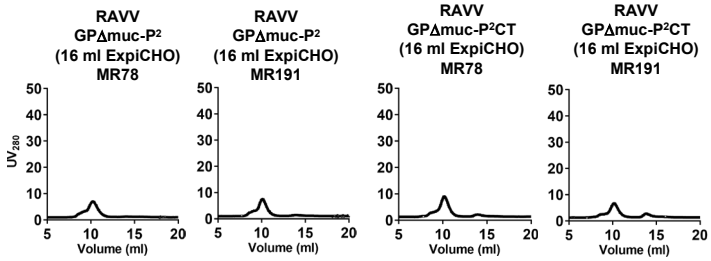

d

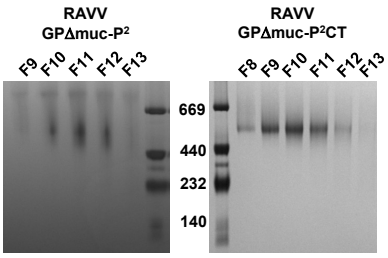

e

2D classes of RAVV GPΔmuc-P^{2}CT / MR78 Fab complex

Selected 2D classifications for 3D modeling

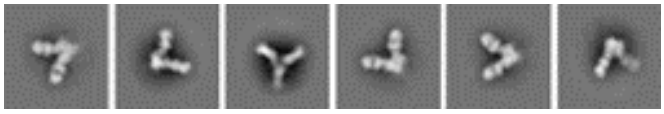

f

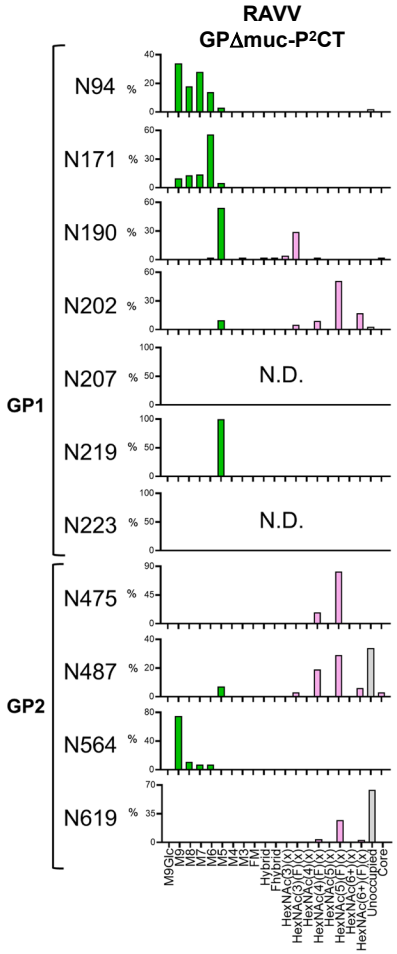

g

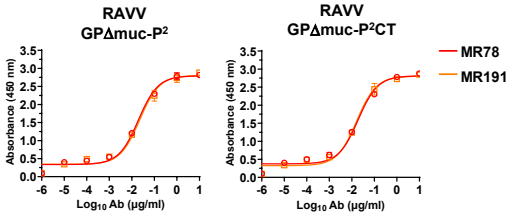

RAVV GPΔmuc-P2			
MR78		MR191	
EC50	STD	EC50	STD
0.0191	0.0007	0.0166	0.0007

RAVV GPΔmuc-P2CT			
MR78		MR191	
EC50	STD	EC50	STD
0.0196	0.0015	0.0230	0.0046

h

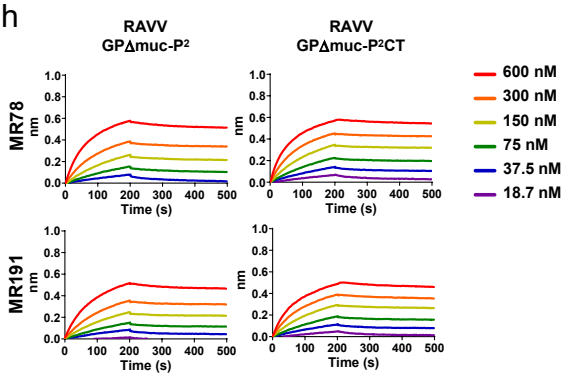

K_D values for two RAVV GPΔmuc trimers binding to 2 marburgvirus NAbs in the IgG form (nM) [a]

	MR78	MR191
RAVV GPΔmuc-P2	6.61E-1	1.55E+1
RAVV GPΔmuc-P2CT	8.06	1.30E+1

[a] K_D values were derived from bio-layer interferometry (BLI) using the binding equations describing a 1:1 interaction.
[b] "—" indicates cases where the peak signal value at the highest RSV-F concentration is 0.2 or lower.

i

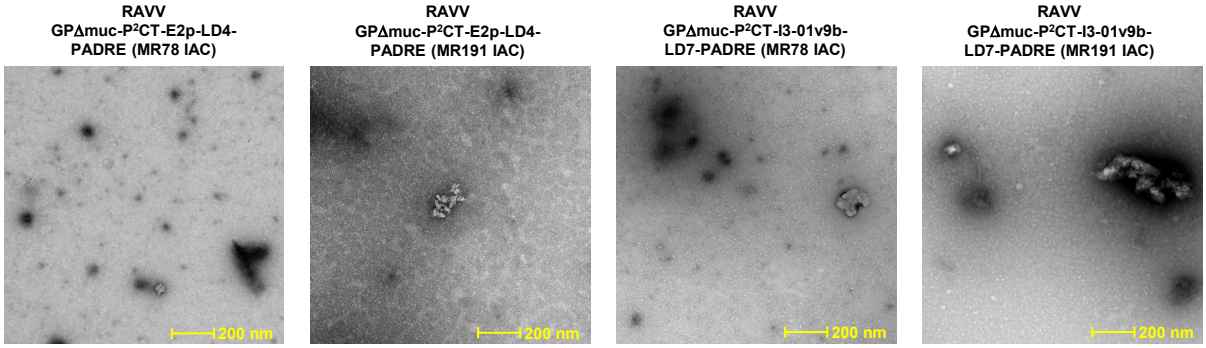

Fig. S5. Construct design and in vitro characterization of RAVV GP trimers. (**a**) Constructs sequences of RAVV GP designs. Signal peptide, mucin-like domain (MLD), HR1c, restriction site (AS), foldon, linker (GS), and His_6-tag are highlighted in yellow, gray, cyan, green, orange, light pink, and light sea green, respectively. The proline mutation on HR1c and CT are shown in red. Notably, the foldon motif, GS linker, and His_6 tag are present in all RAVV GP trimers tested in this study and will not be included in the construct names to avoid redundancy. (**b**) SEC profile of nickel-purified RAVV GPΔmuc-P^4 expressed in 16 ml ExpiCHO cells. (**c**) SECs profile of NAb MR78/MR191-purified RAVV GPΔmuc-P^2 and GPΔmuc-P^2CT each expressed in 16 ml ExpiCHO cells. (**d**) BN-PAGE of the trimer fractions from the SEC analysis of nickel-purified RAVV GPΔmuc-P^2 and GPΔmuc-P^2CT. (**e**) Representative 2D classification images of the RAVV GPΔmuc-P^2CT trimer in complex with MR78 Fab. (**f**) Compositional site-specific glycan analysis for RAVV GPΔmuc-P^2CT trimer, as in **Fig. S1c**. (**g**) ELISA analysis of RAVV GPΔmuc-P^2 and GPΔmuc-P^2CT trimers binding to NAbs MR78 and MR191 in the IgG form. Briefly, each well was coated with 0.1 μg of the appropriate antigen and IgG antibodies were diluted in a 10-fold dilution series from a starting concentration of 10 μg/ml for all antibodies. Error bars represent the difference between duplicate measurements at each concentration for each sample. (**h**) BLI analysis of RAVV GPΔmuc-P^2 and GPΔmuc-P^2CT trimers binding to NAbs MR78 and MR191 in the IgG form, as in **Fig. S1i**. (i) nsEM analysis of RAVV GPΔmuc-P^2CT E2p and I3-01v9b constructs following ExpiCHO expression and MR78- or MR191-based IAC purification. Scale bar is labeled in yellow on the EM micrographs. No discernible protein NPs are shown in any of the EM micrographs.

Fig. S6

a

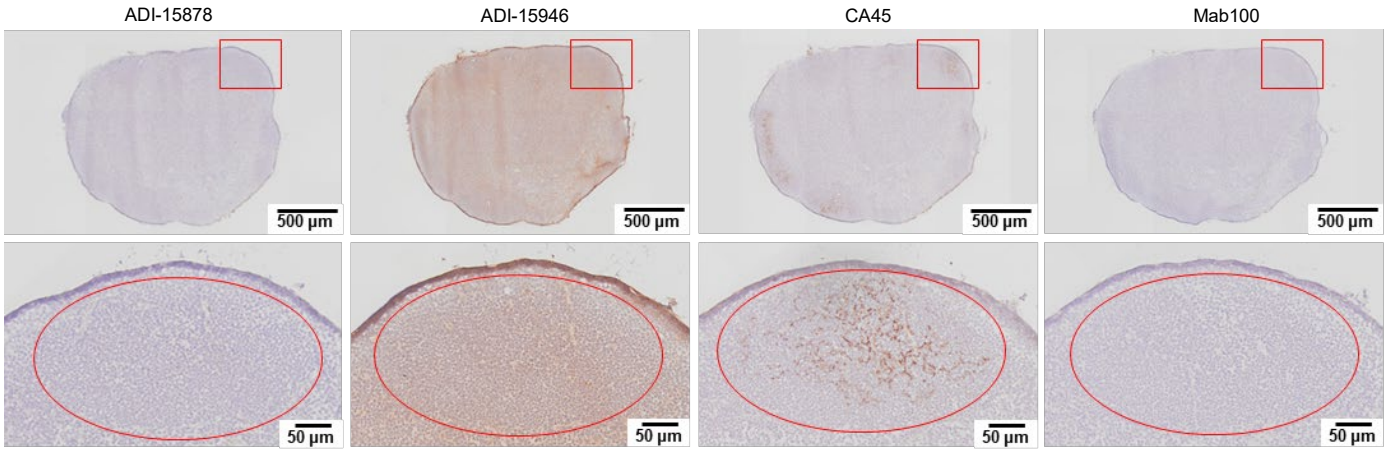

b Single-dose - 2 hours

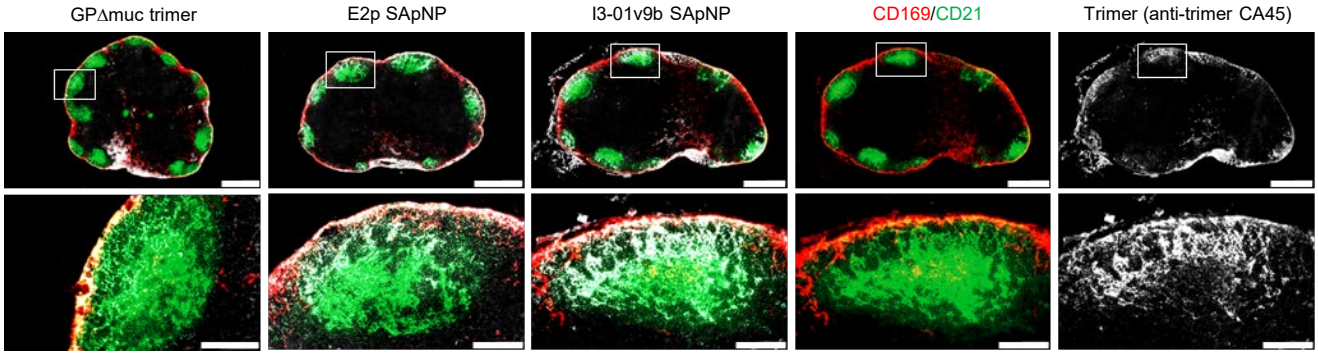

c Single-dose - 12 hours

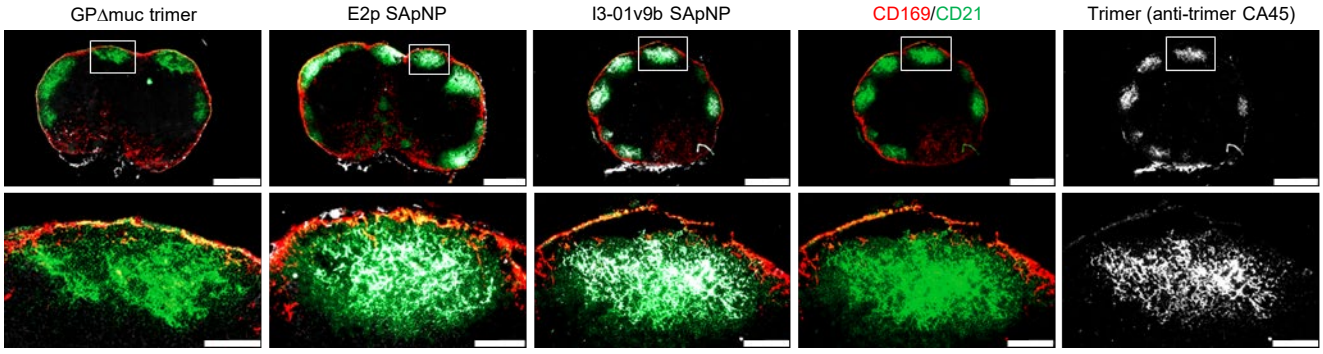

d Single-dose - 1 week

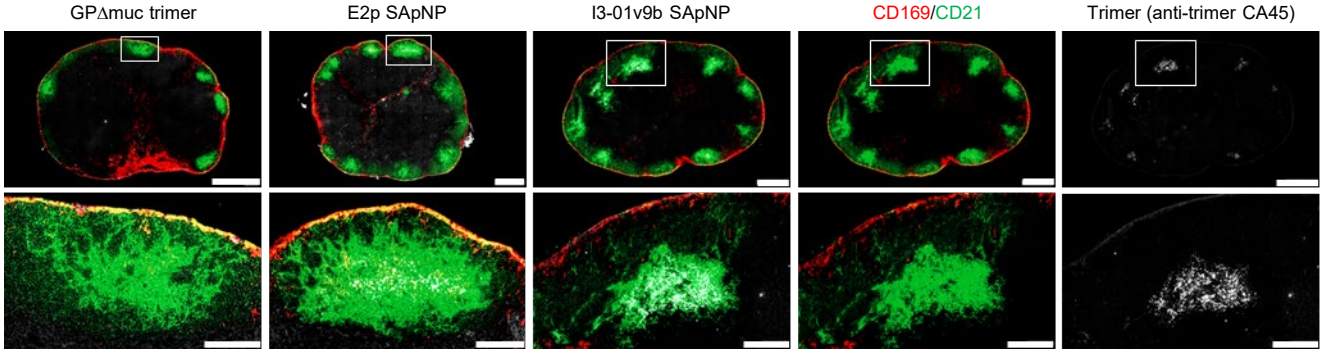

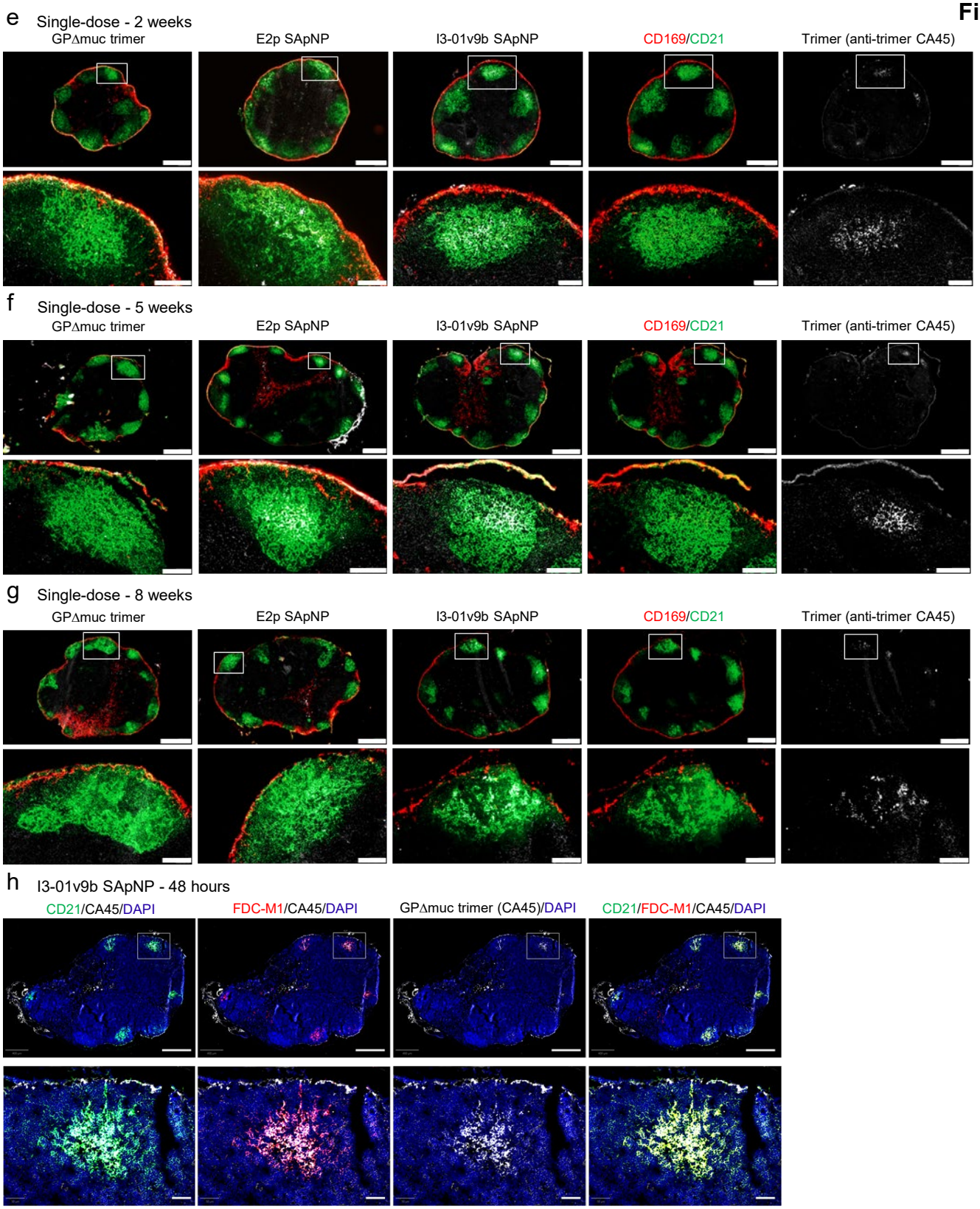

Fig. S6. Immunohistological images of SUDV GPΔmuc trimer and SApNPs in lymph nodes. (**a**) Immunostaining images of lymph node tissues from mice injected with SUDV GPΔmuc-presenting SApNPs, stained using antibodies ADI-15878, ADI-15946, CA45, and mAb100. **(b–g)** Colocalization of SUDV GPΔmuc trimer, E2p SApNP, and I3-01v9b SApNP with FDC networks in lymph node follicles at various time points following a single-dose injection (10 μg per injection, 40 μg total per mouse): (**b**) 2 hours, (**c**) 12 hours, (**d**) 1 week, (**e**) 2 weeks, (**f**) 5 weeks, and (**g**) 8 weeks. Immunofluorescent images are pseudo-color-coded as follows: $CD21^+$ (green), $CD169^+$ (red), and CA45 (white). (**h**) Colocalization of SUDV GPΔmuc-presenting I3-01v9b SApNPs (labeled by CA45, white) with FDC networks labeled by $CD21^+$ (green) and FDC-$M1^+$ (red) at 48 hours post-injection. Scale bars: 500 μm (entire lymph node) and 100 μm (enlarged follicle image).

Fig. S7

a E2p SApNPs (yellow arrow) are aligned on FDC dendrites at 2 hours after injection

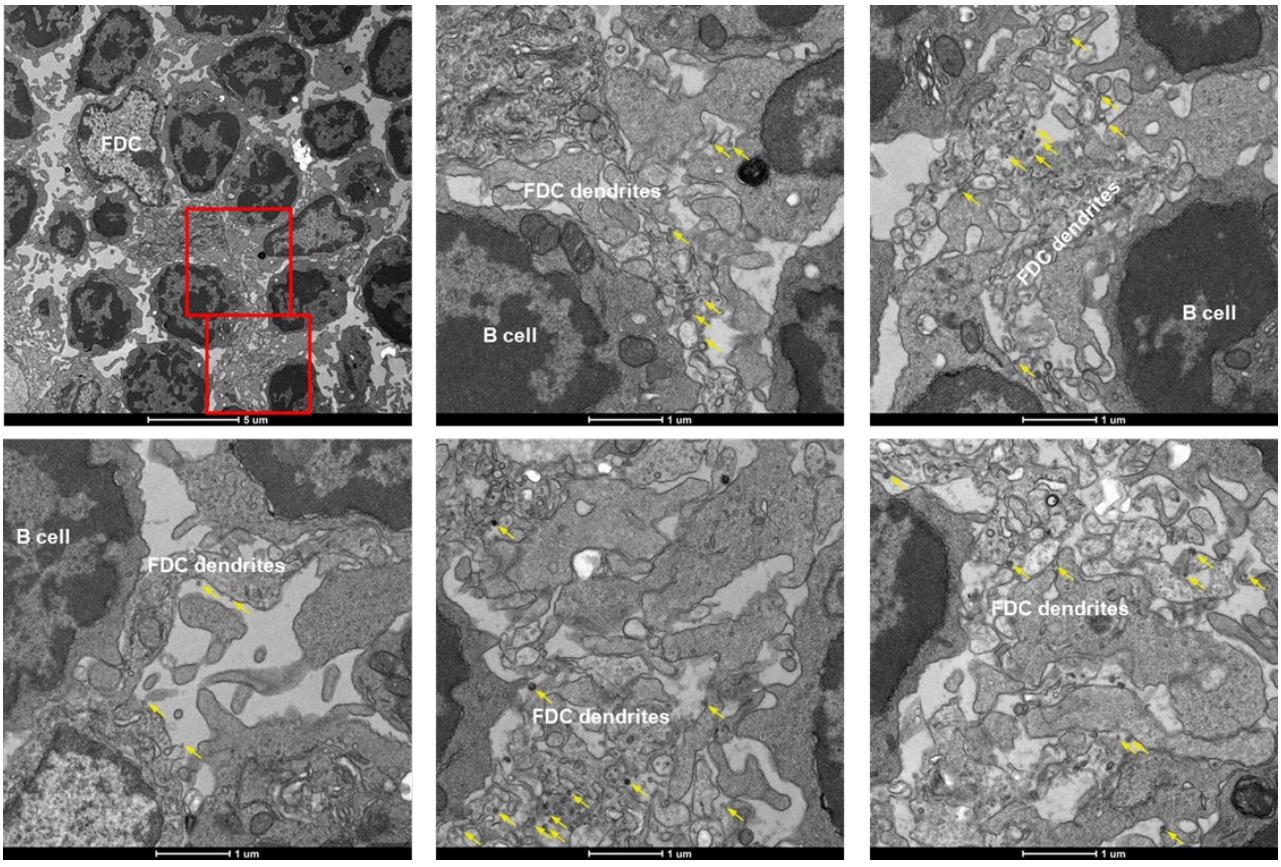

b E2p SApNPs (yellow arrow) are aligned on FDC dendrites at 12 hours after injection

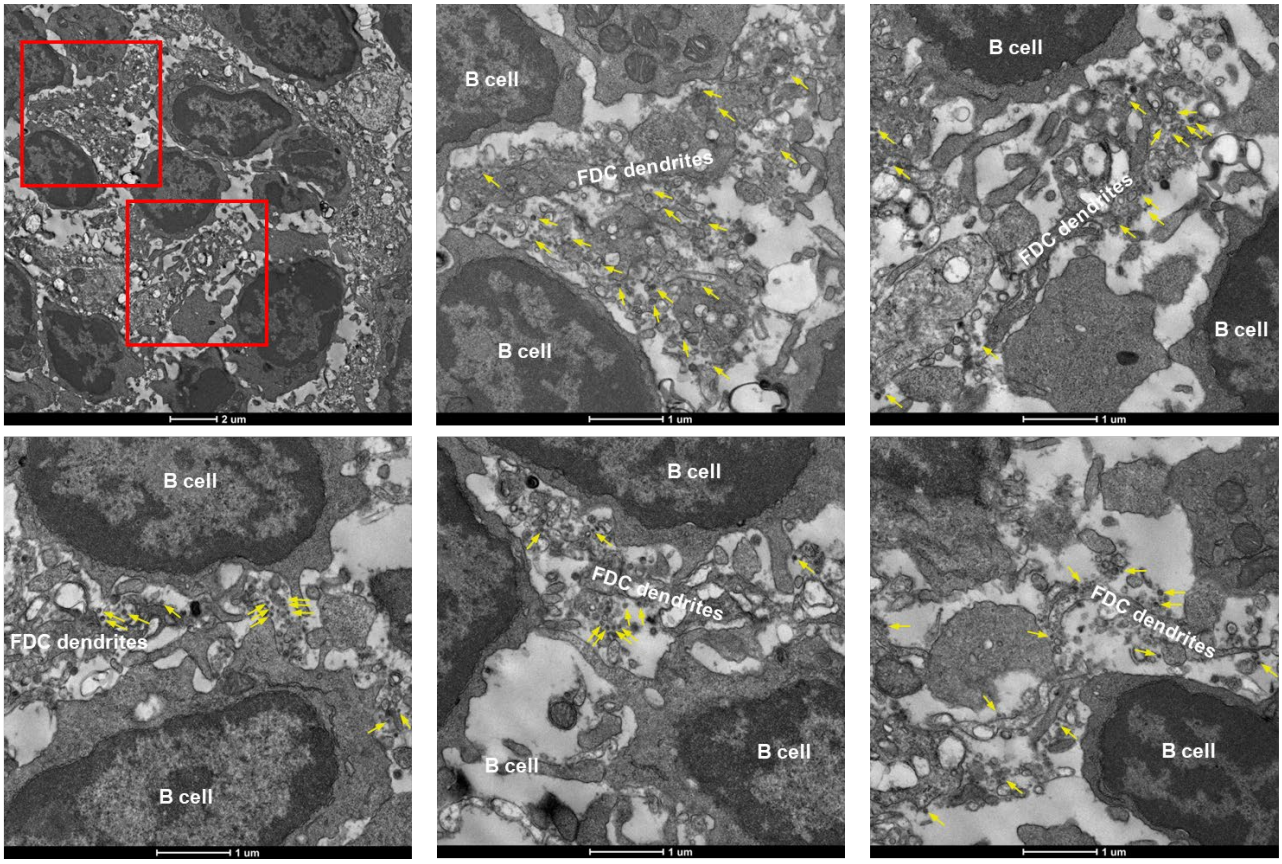

c E2p SApNPs (yellow arrow) are aligned on FDC dendrites or taken up by B cells at 48 hours after injection

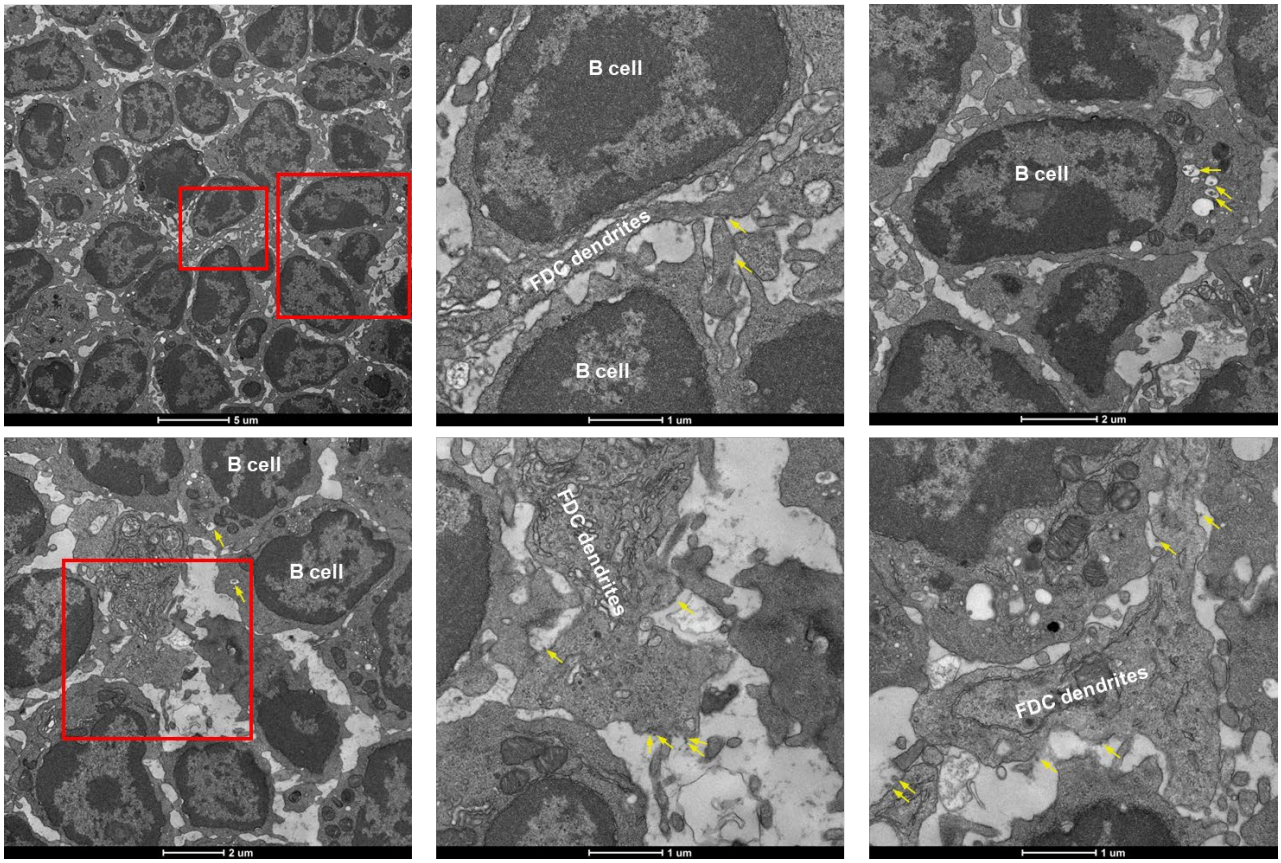

d I3-01v9b SApNPs (yellow arrow) are aligned on FDC dendrites or inside endolysosomes of FDC dendrities at 2 hours after injection

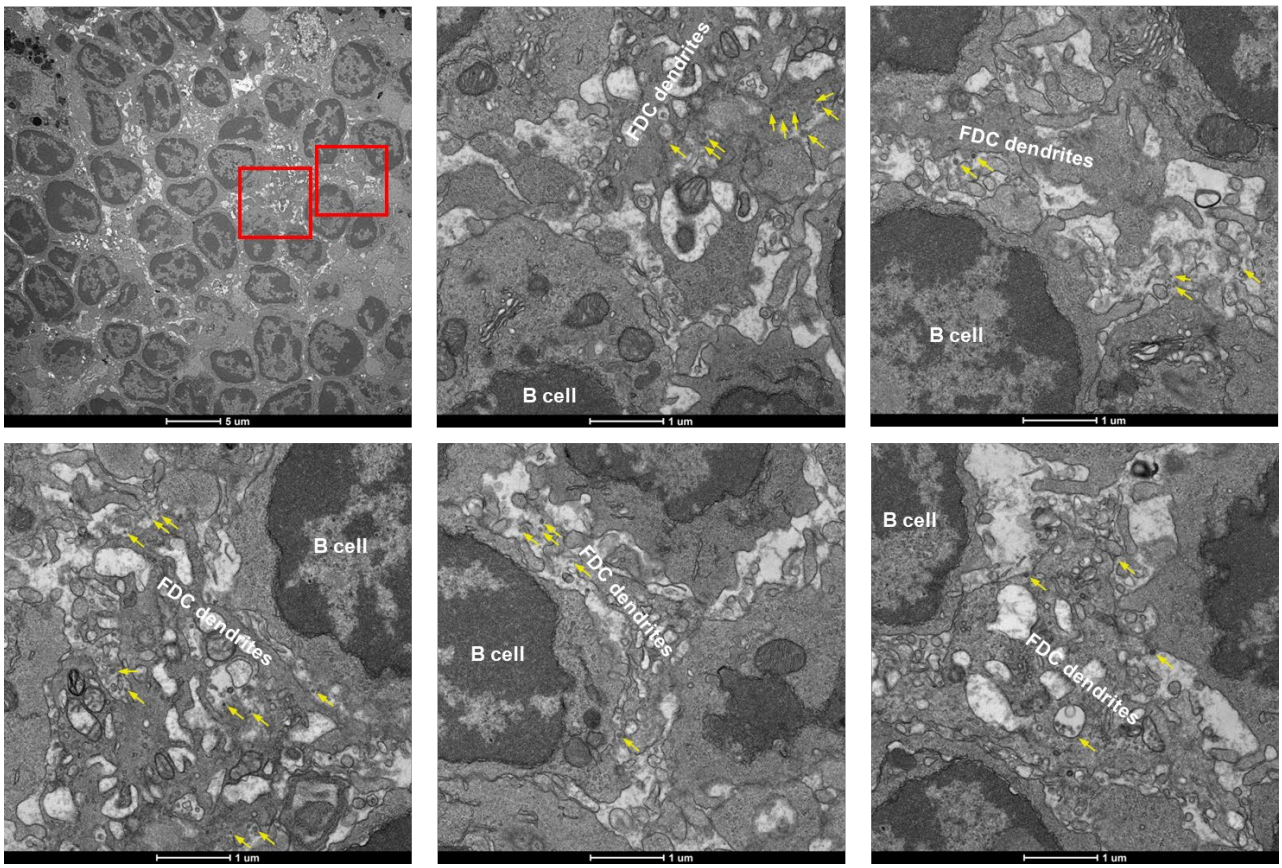

e I3-01v9b SApNPs (yellow arrow) are aligned on FDC dendrites or taken up by B cells at 12 hours after injection

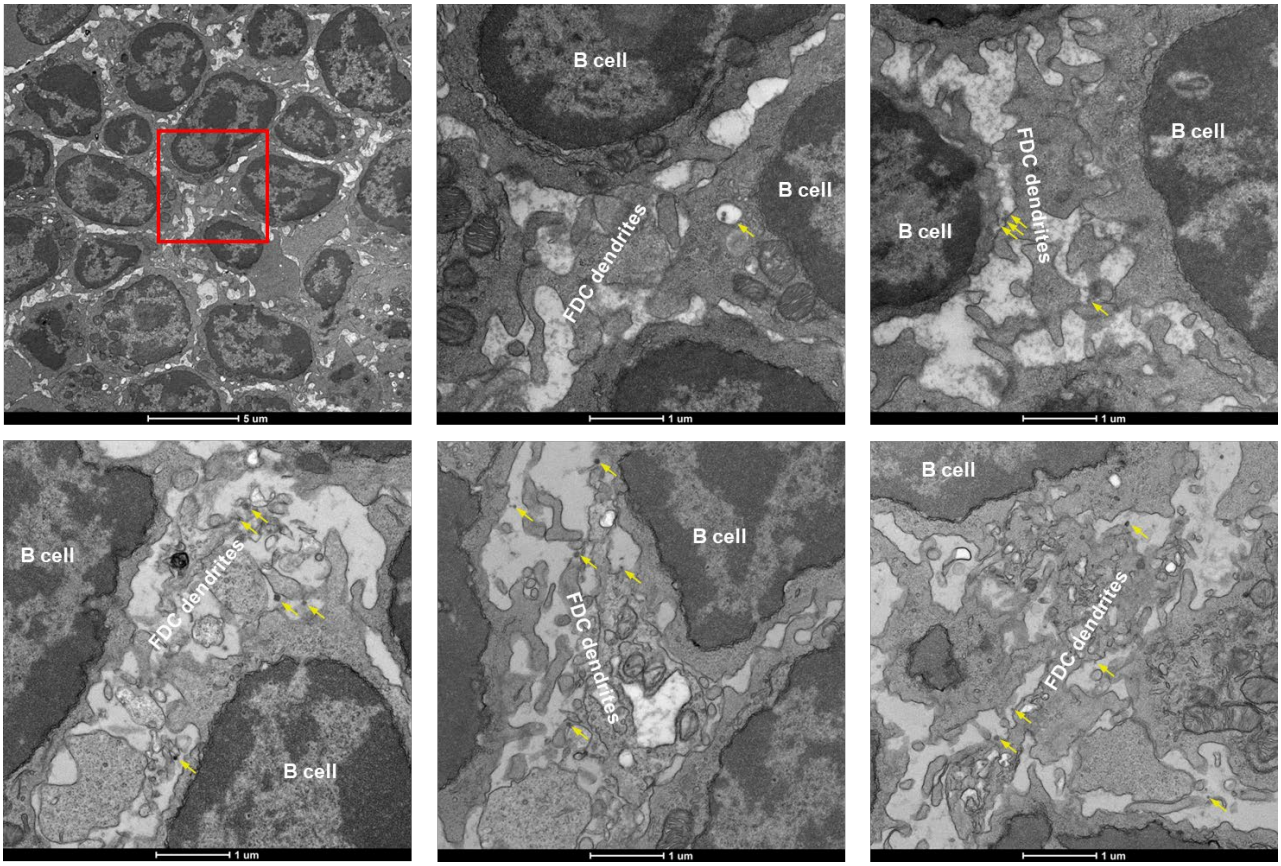

f I3-01v9b SApNPs (yellow arrow) are aligned on FDC dendrites at 48 hours after injection

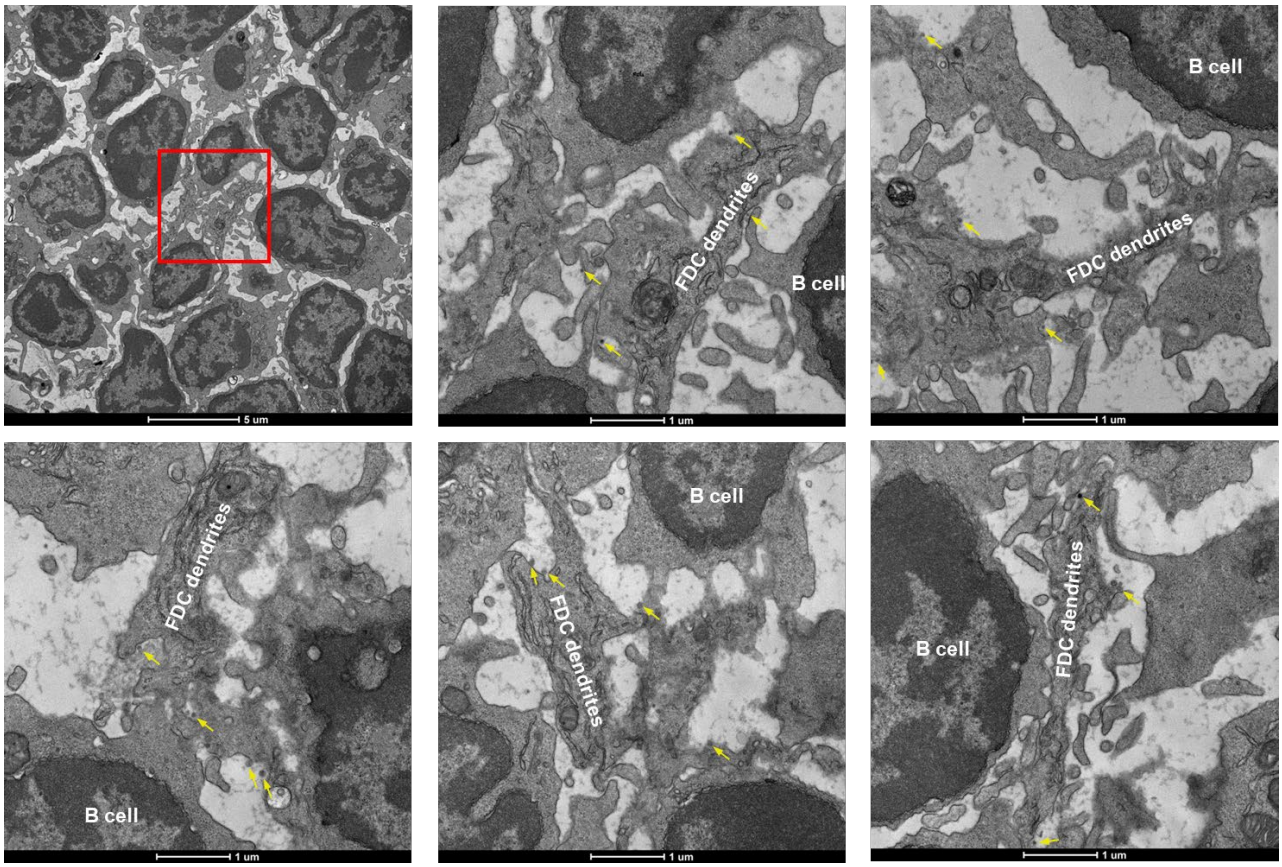

g E2p SApNPs (yellow arrow) are associated with phagocytic cells at 2 hours after injection

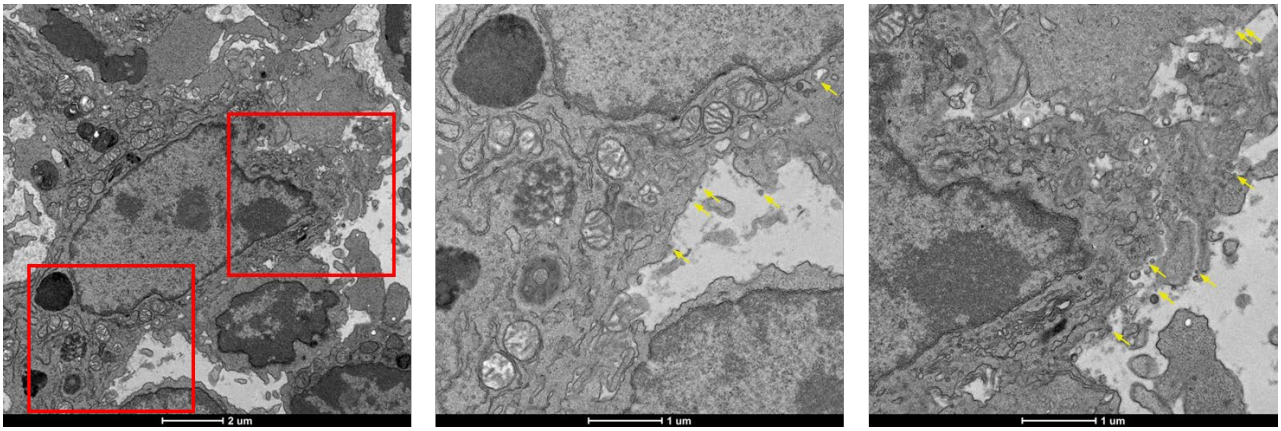

h E2p SApNPs (yellow arrow) are associated with phagocytic cells at 12 hours after injection

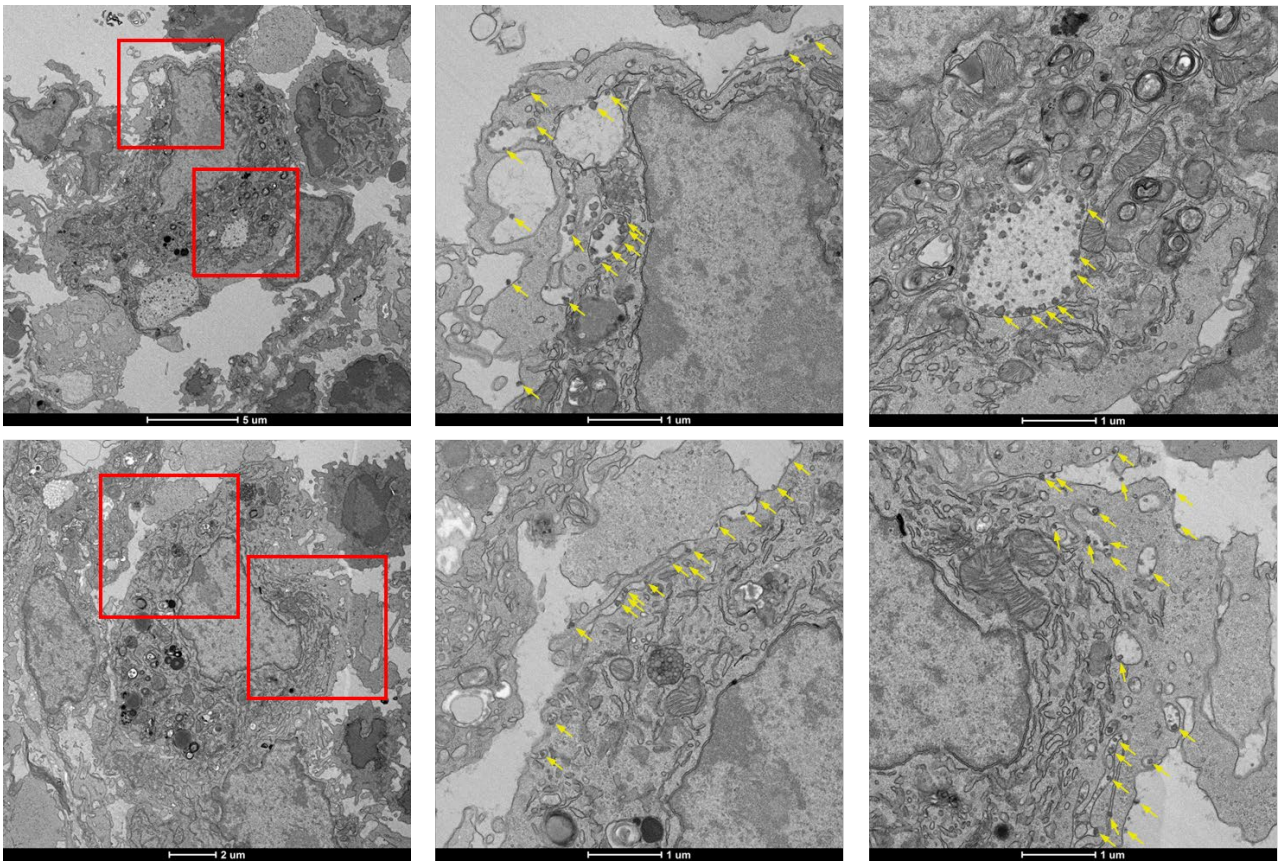

i E2p SApNPs (yellow arrow) are associated with phagocytic cells at 48 hours after injection

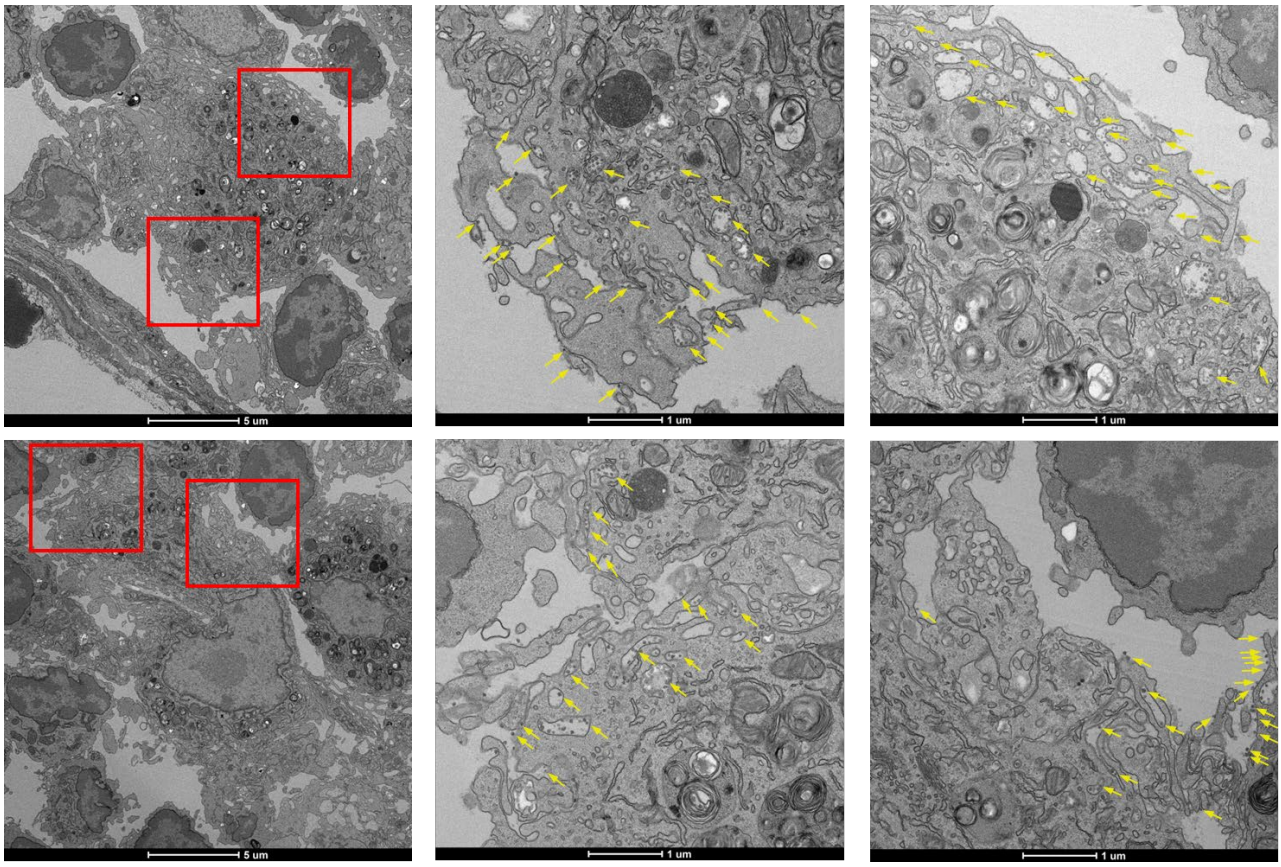

j I3-01v9b SApNPs (yellow arrow) are associated with phagocytic cells at 2 hours after injection

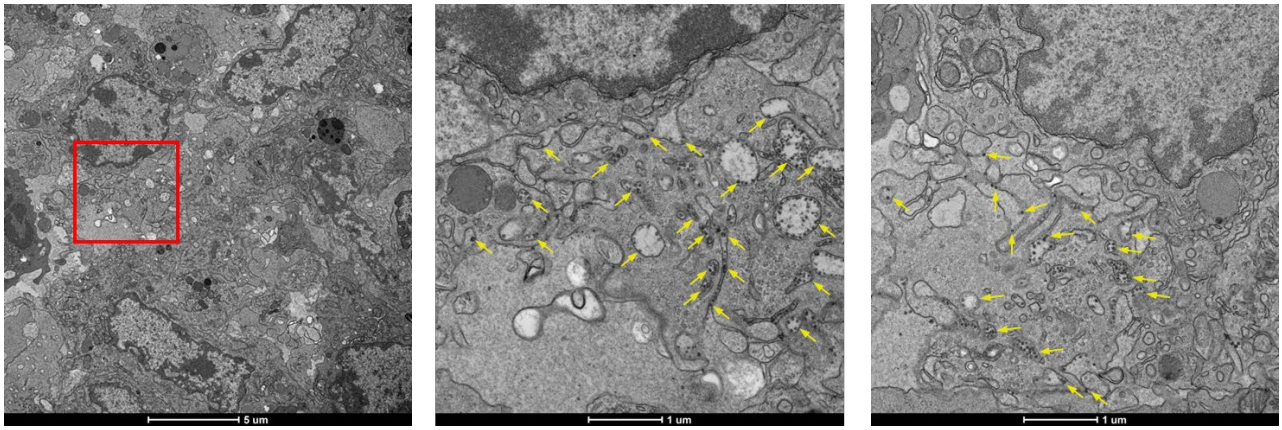

k I3-01v9b SApNPs (yellow arrow) are associated with phagocytic cells at 12 hours after injection

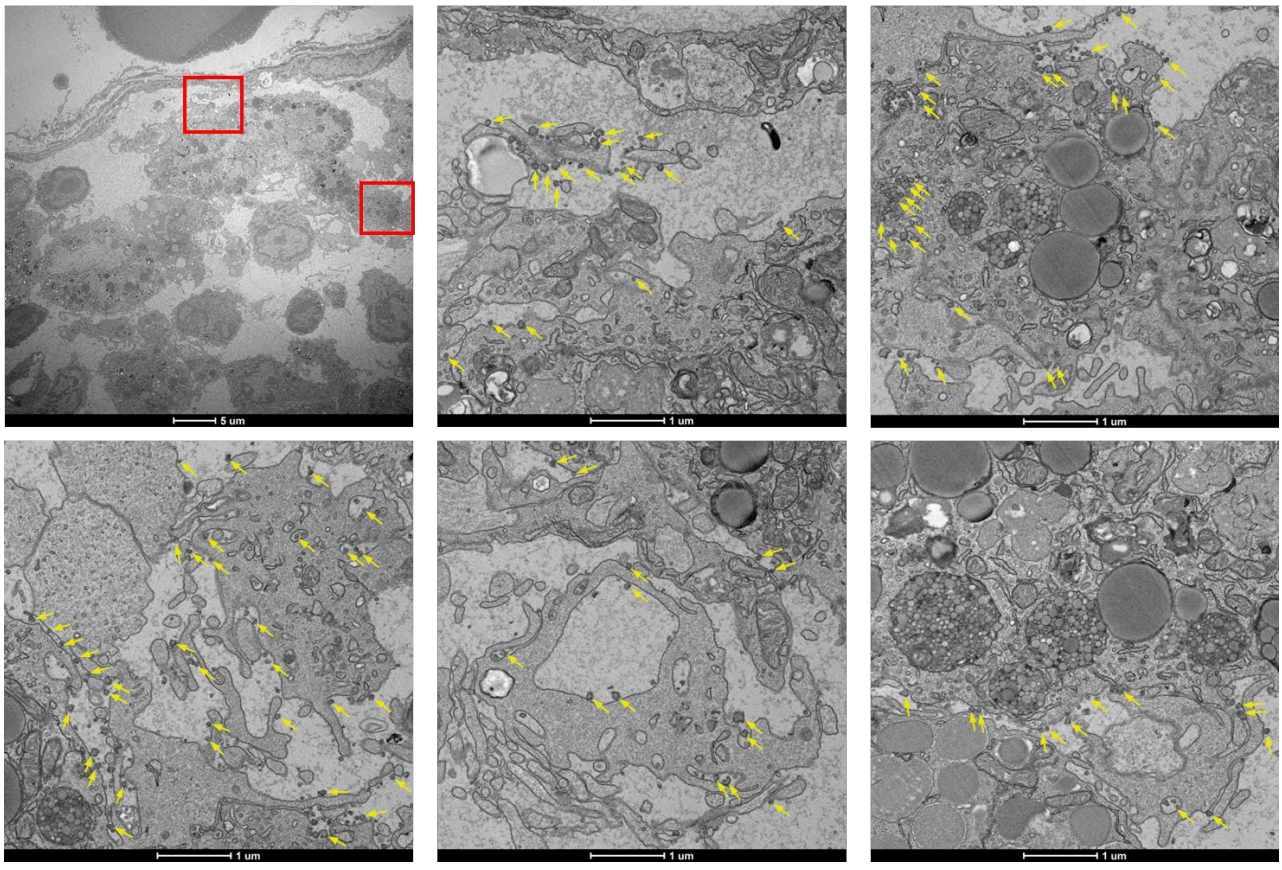

l I3-01v9b SApNPs (yellow arrow) are associated with phagocytic cells at 48 hours after injection

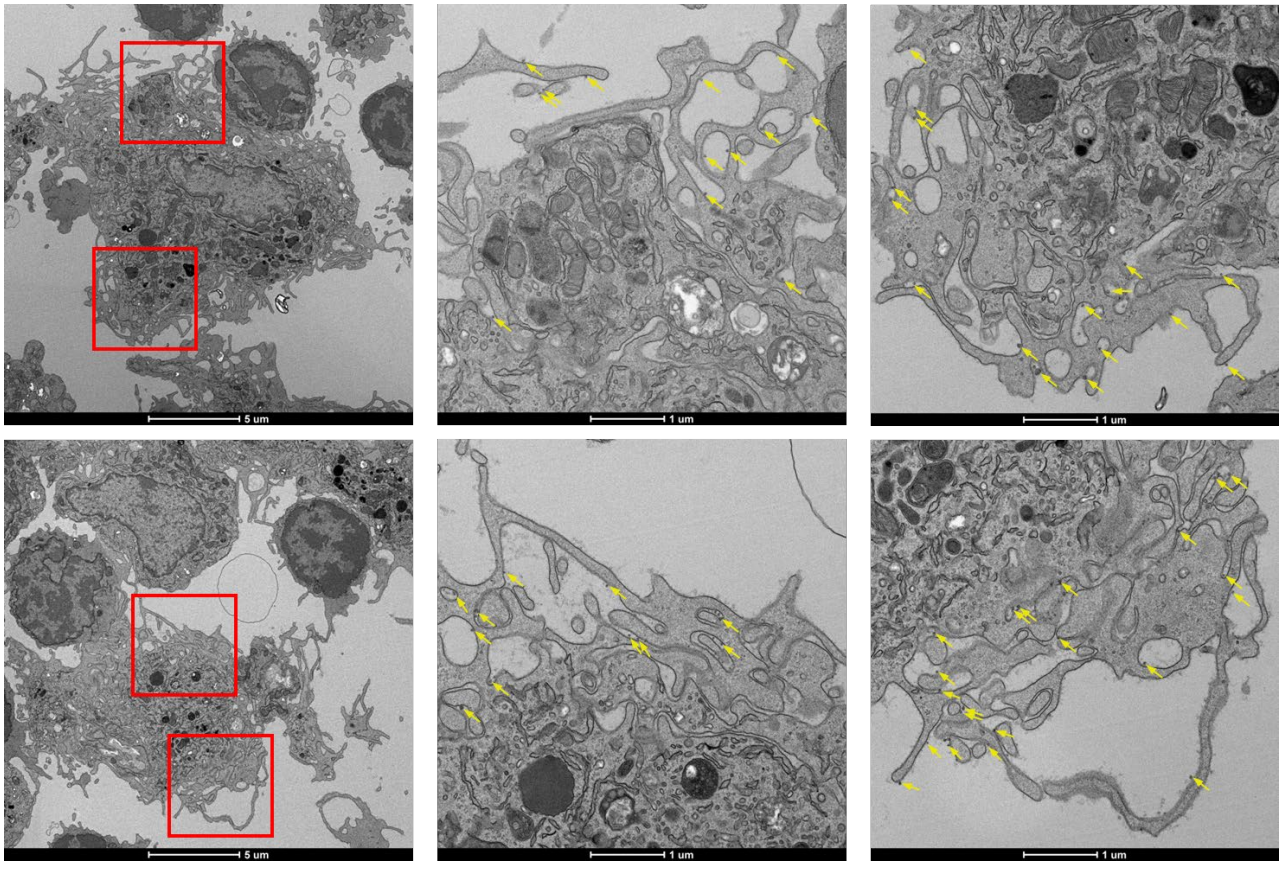

m Aluminum phosphate (green arrow) tends to aggregate in the ECM at 2 hours after injection

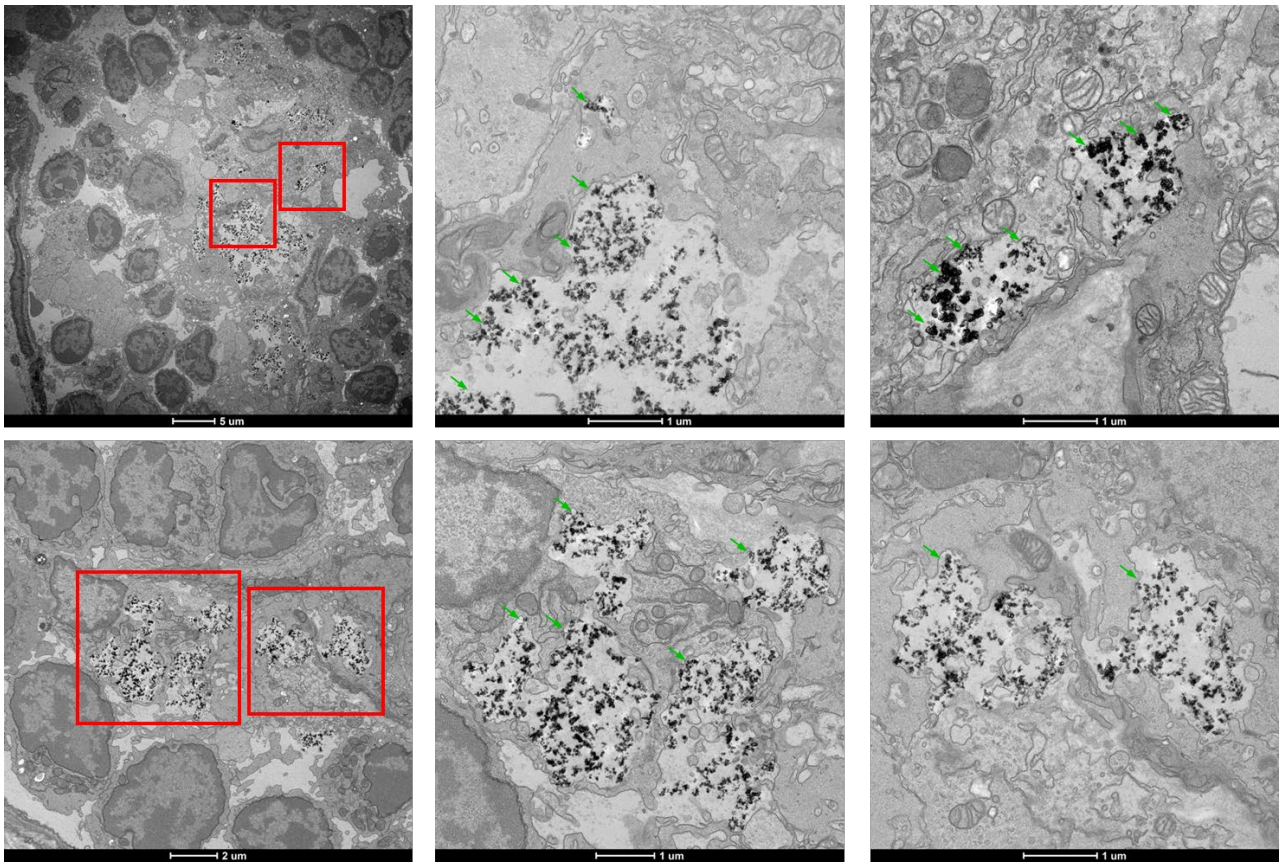

n I3-01v9b SApNPs (yellow arrow) and aluminum phosphate (green arrow) with phagocytic cells at 2 hours after injection

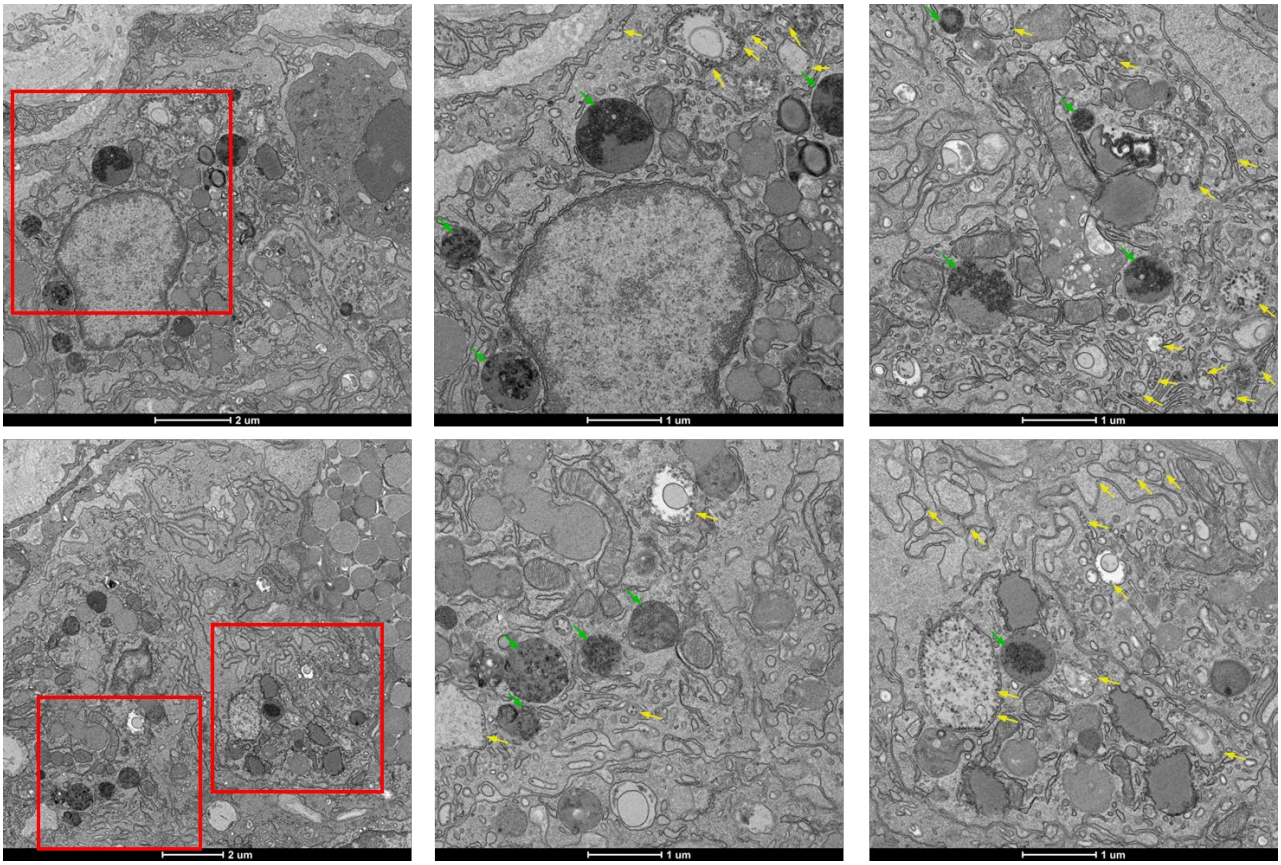

o I3-01v9b SApNPs (yellow arrow) and aluminum phosphate (green arrow) with phagocytic cells at 12 hours after injection

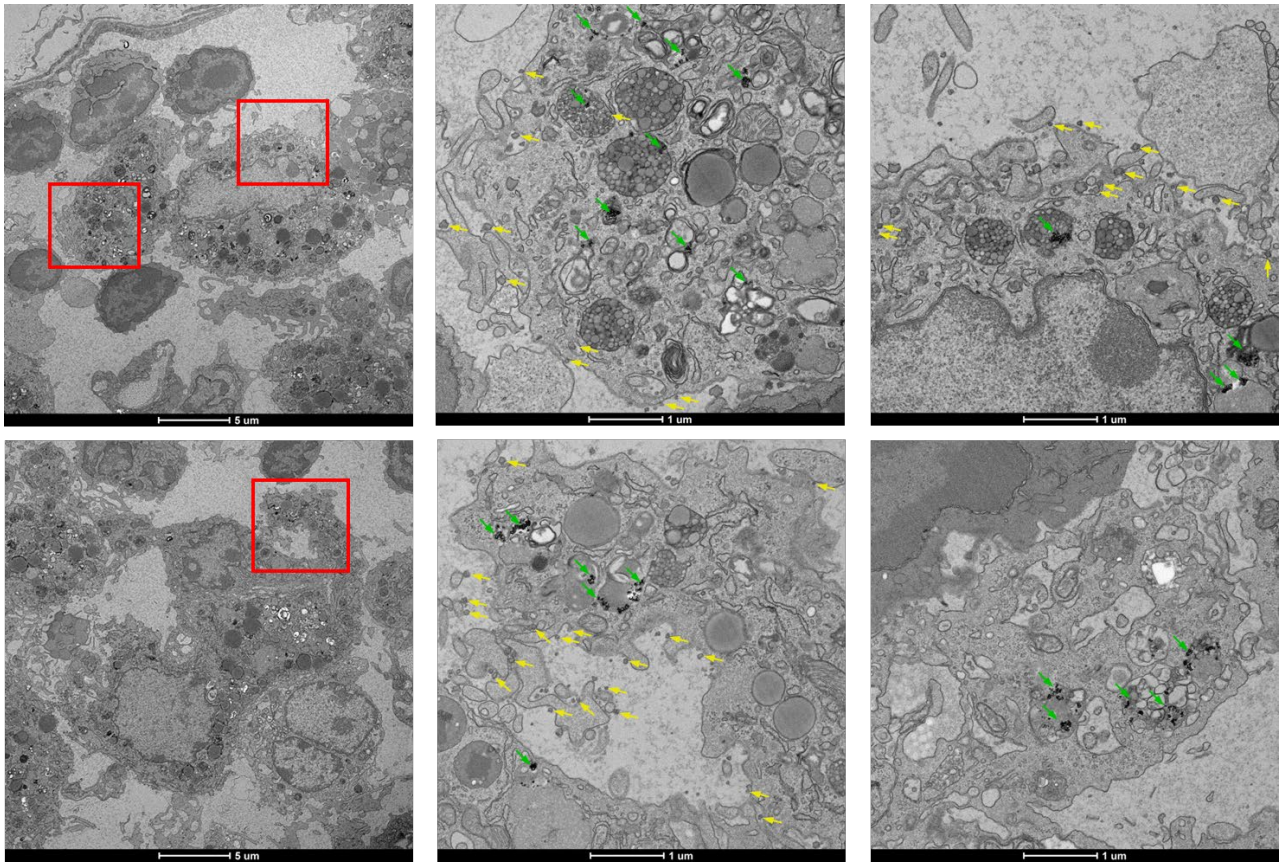

p I3-01v9b SApNPs (yellow arrow) and aluminum phosphate (green arrow) with phagocytic cells at 48 hours after injection

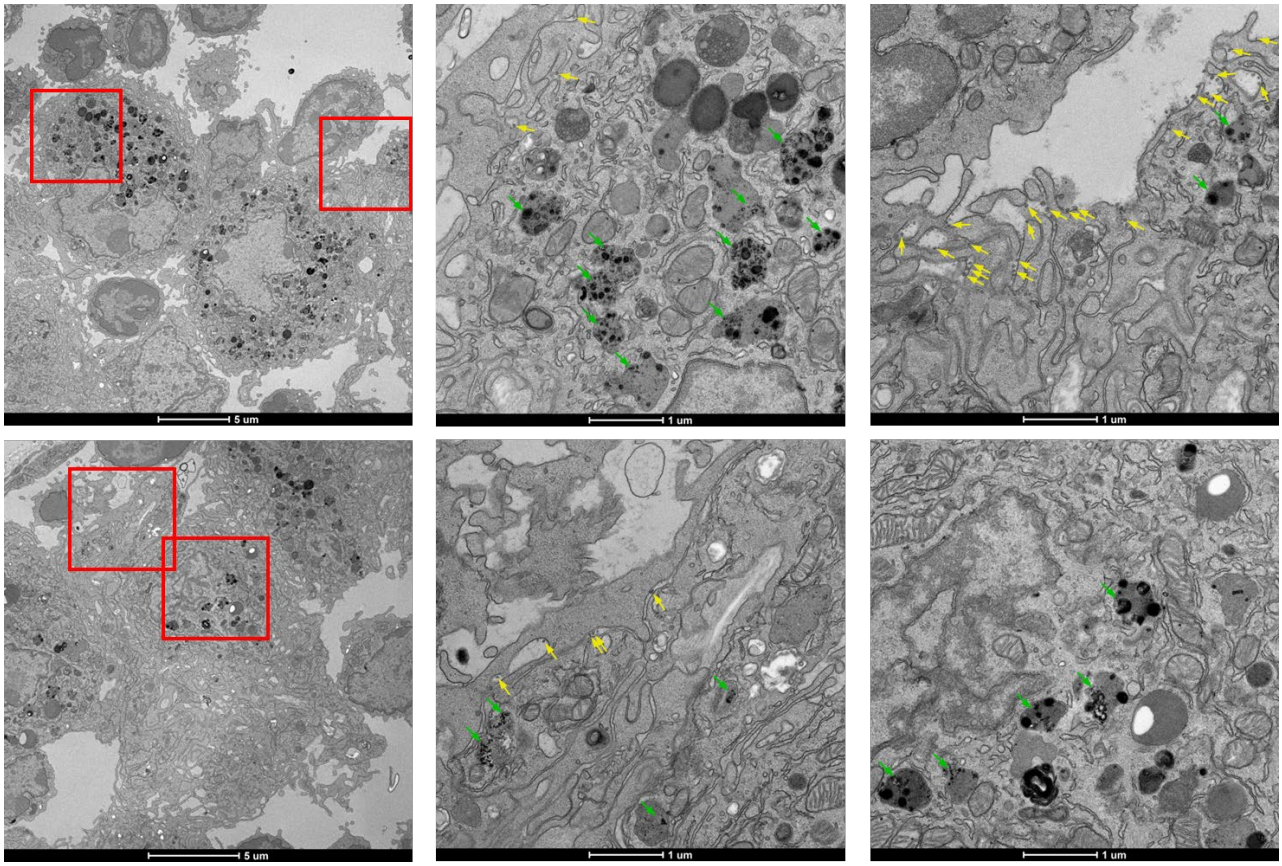

Fig. S7. TEM analysis of SUDV GPΔmuc-presenting SApNPs interacting with FDCs and phagocytic cells in lymph nodes. TEM images show the distribution and cellular interactions of SUDV GPΔmuc-presenting SApNPs following a single-dose injection (2 footpads, 50 µg/footpad). (**a–c**) E2p SApNPs aligned along FDC dendrites at 2 hours, 12 hours, and 48 hours post-injection, respectively. (**d–f**) I3-01v9b SApNPs aligned on FDC dendrites at the same time points. Aluminum phosphate (AP) adjuvant particles are not observed in association with SApNPs on FDC dendrites. (**g–i**) E2p SApNPs located on the surface or within endolysosomes of phagocytic cells at 2 hours, 12 hours, and 48 hours post-injection, respectively. (**j–l**) I3-01v9b SApNPs associated with phagocytic cells at the same time points. (**m**) AP adjuvant particles aggregating in the extracellular matrix 2 hours after injection. (**n–p**) I3-01v9b SApNPs formulated with AP observed within phagocytic cells at 2 hours, 12 hours, and 48 hours post-injection. TEM imaging was performed on two popliteal lymph nodes per SApNP construct. E2p and I3-01v9b SApNPs are indicated by yellow arrows; AP adjuvant particles are indicated by green arrows.

Fig. S8

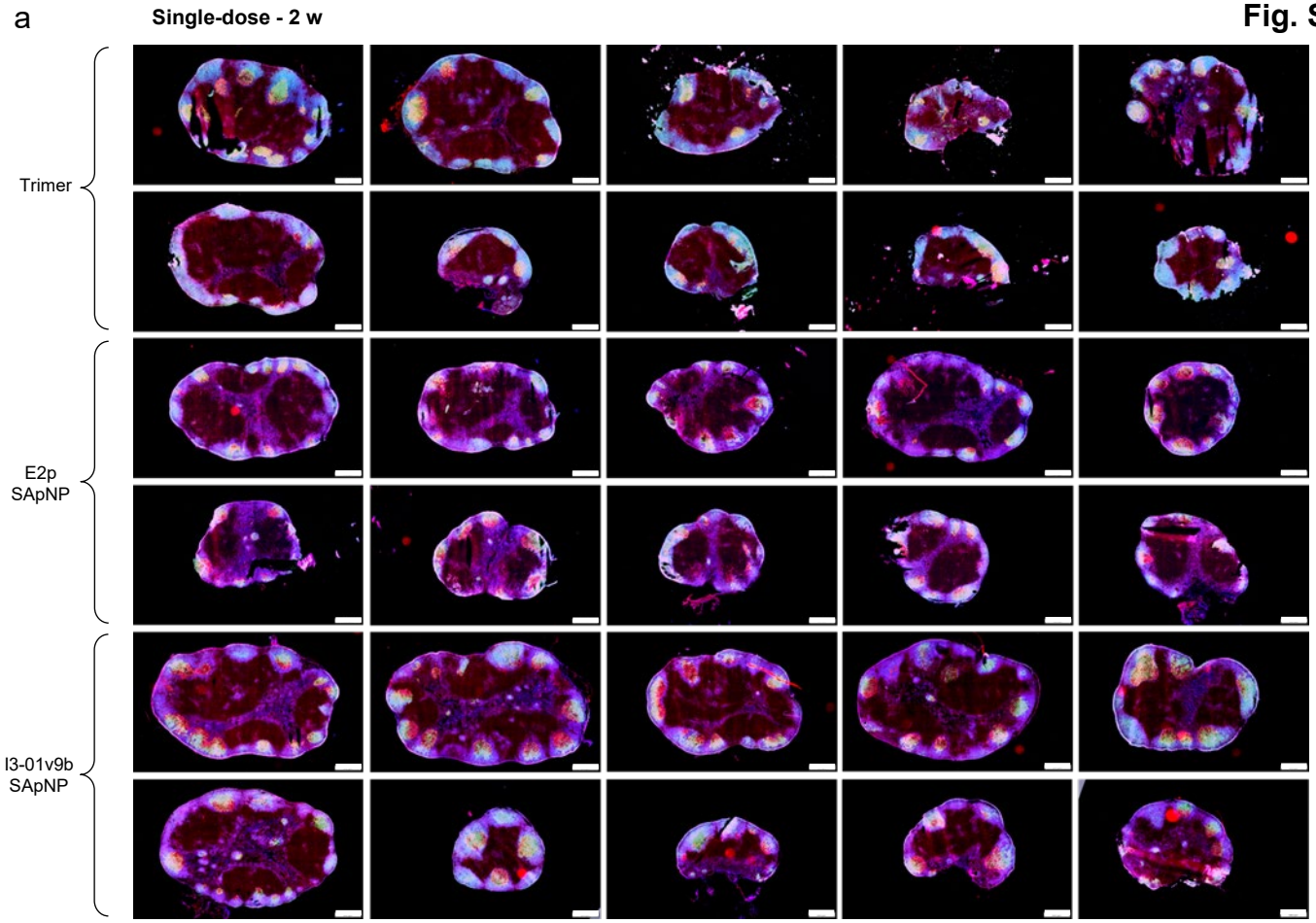
a
Single-dose - 2 w
Trimer
E2p
SApNP
I3-01v9b
SApNP

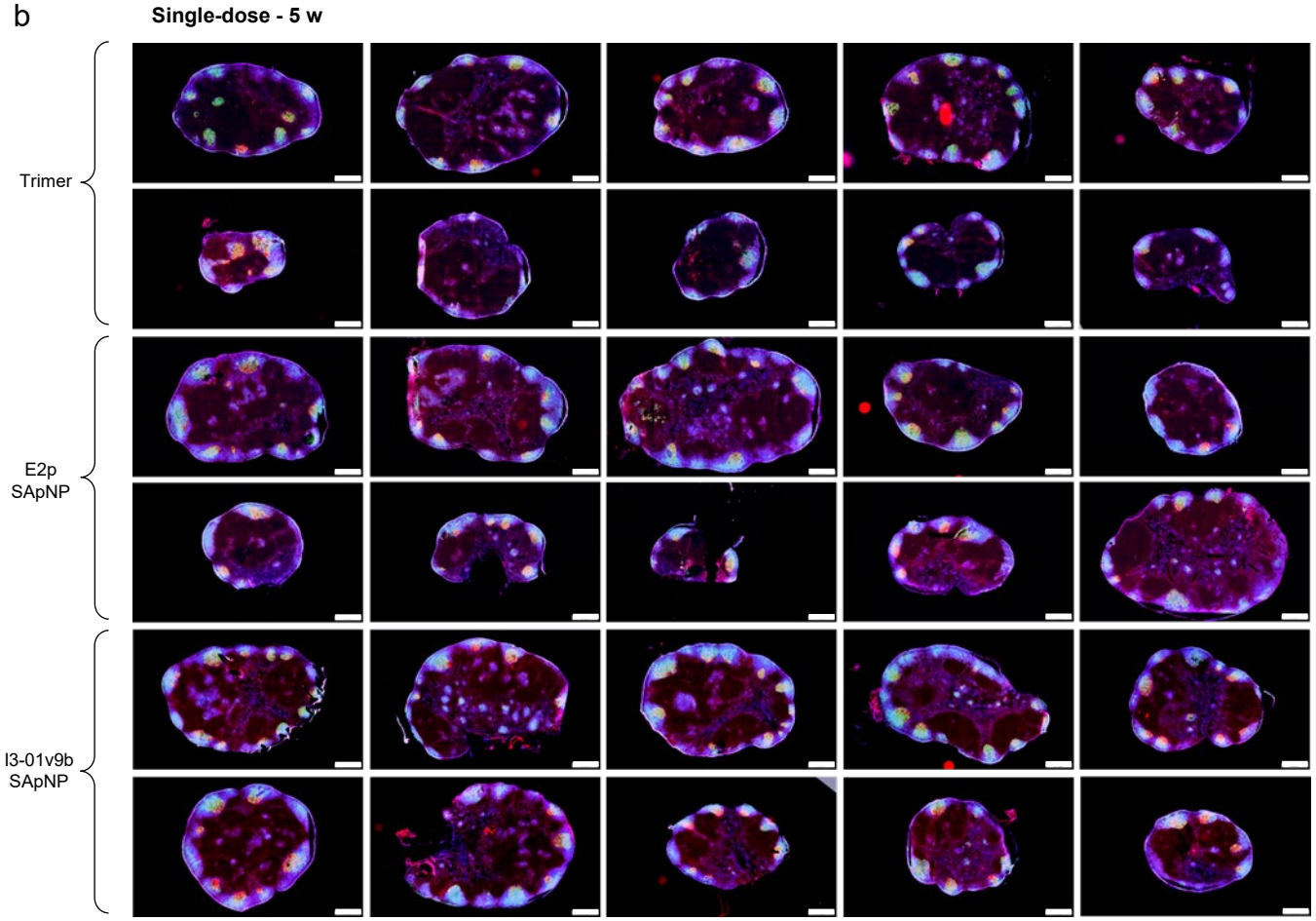
b
Single-dose - 5 w
Trimer
E2p
SApNP
I3-01v9b
SApNP

c

Single-dose - 8 w

Fig. S8

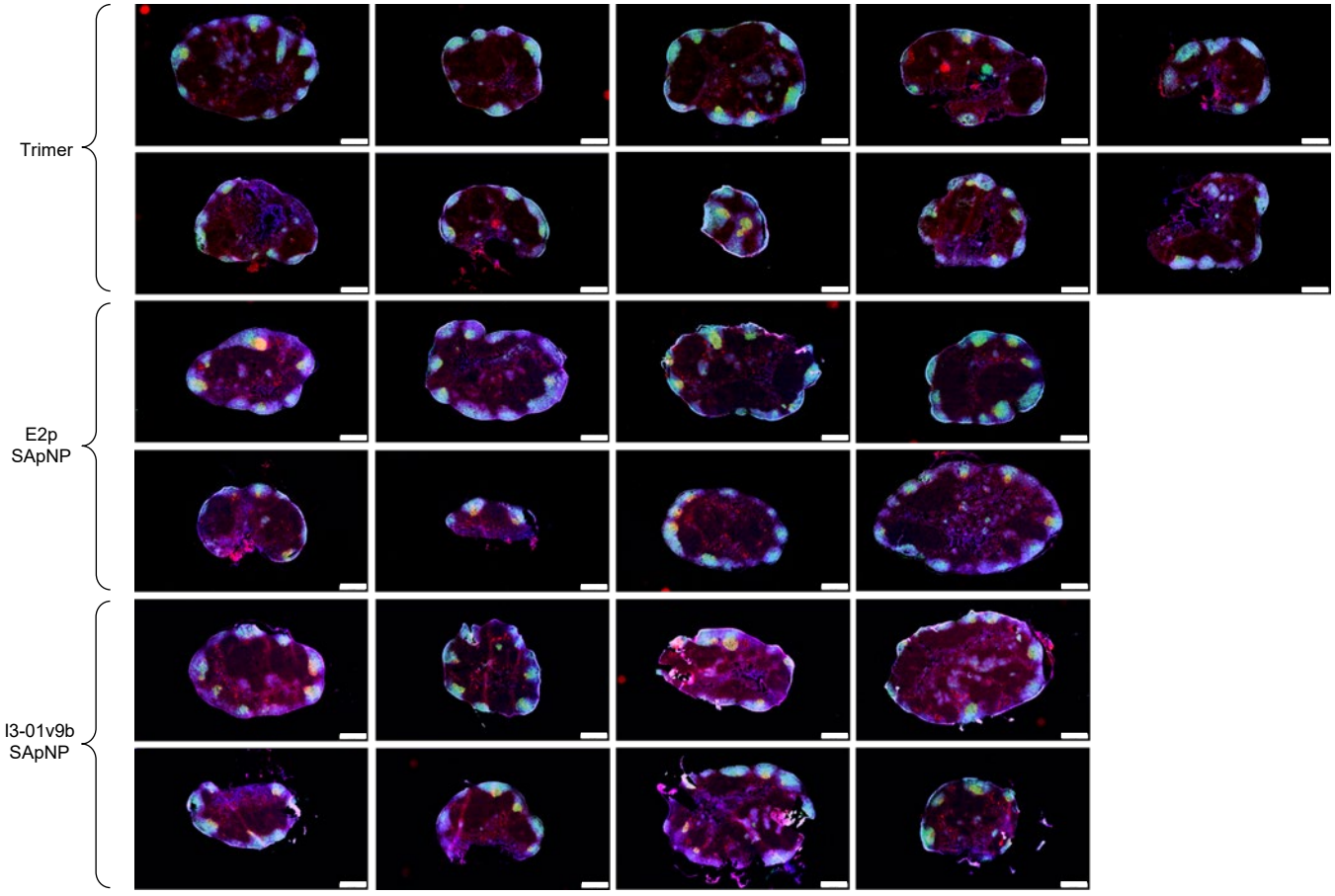

d

Prime-boost - 3 w + 2 w

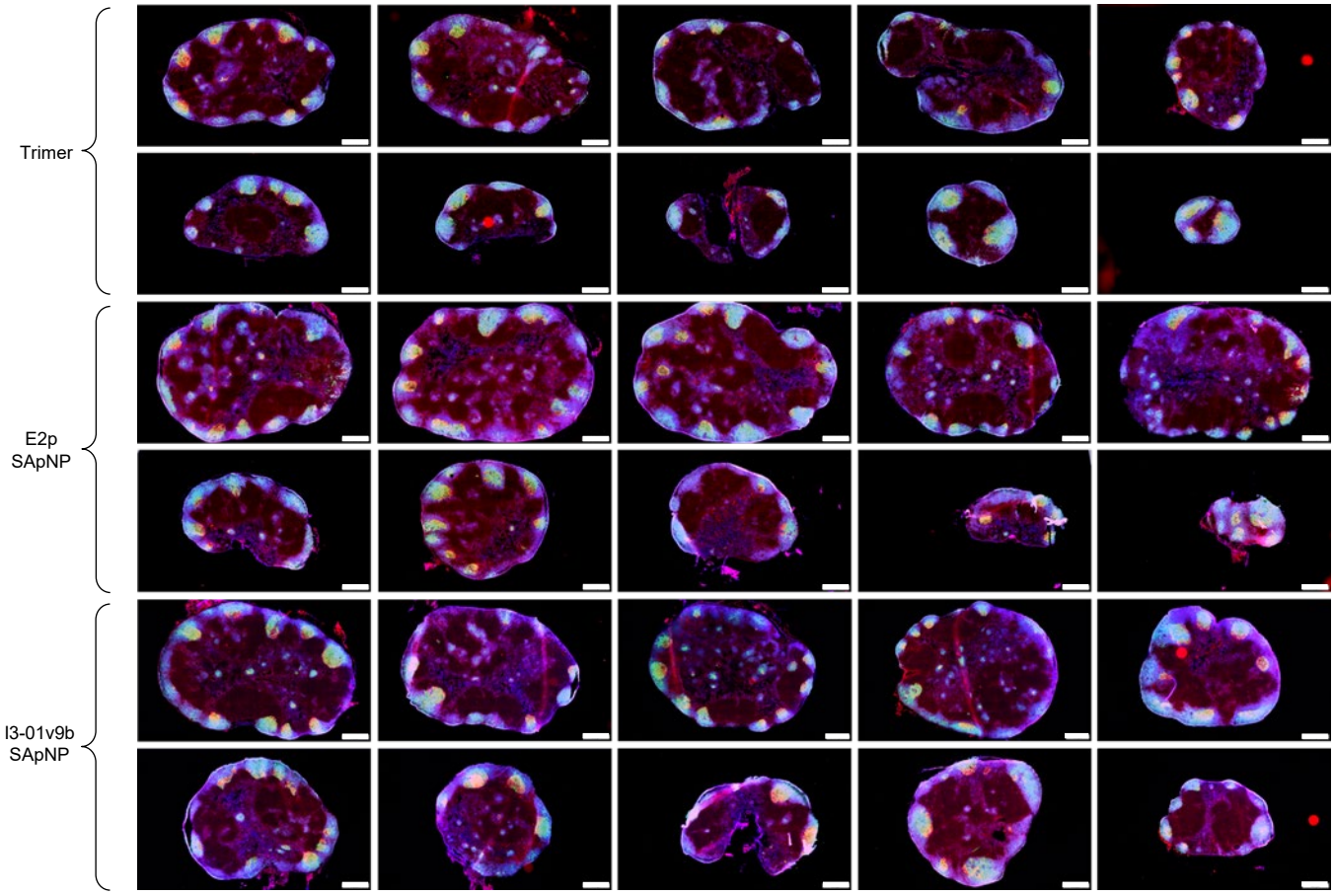

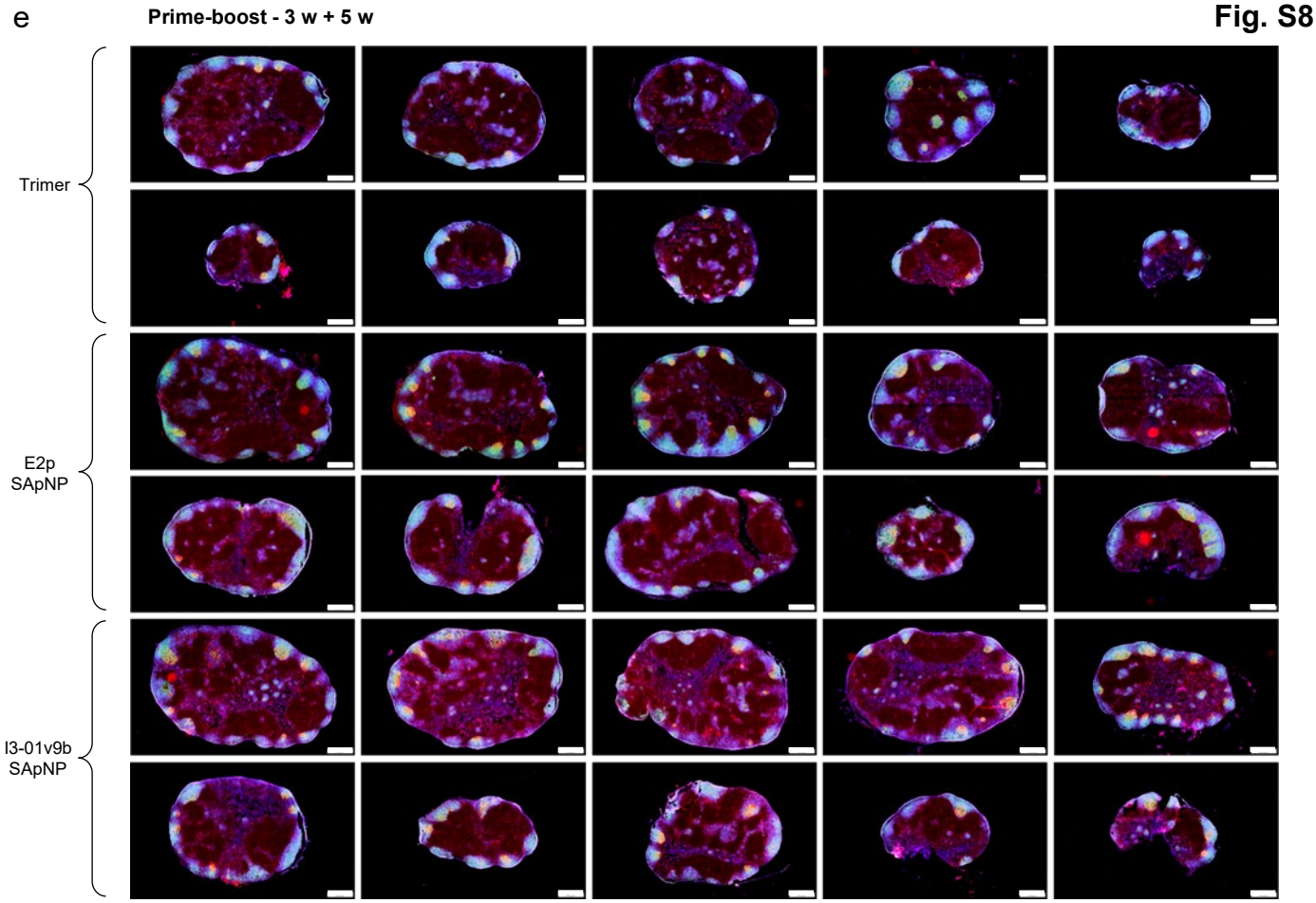

Fig. S8. Immunohistological analysis of SUDV GPΔmuc trimer and SApNP vaccine-induced germinal centers (GCs). Immunohistological images of GCs at (**a**) 2, (**b**) 5, and (**c**) 8 weeks following a single-dose injection of GPΔmuc trimer or GPΔmuc-presenting E2p and I3-01v9b SApNPs (10 μg per injection; total of 40 μg per mouse). GC images at (**d**) 2 and (**e**) 5 weeks after a booster dose, administered 3 weeks after the initial immunization (n = 5 mice/group). Immunofluorescent images are pseudo-color coded (GL7^{+}, red; CD21^{+}, green; B220, blue). Scale bars = 500 μm for each lymph node image.

a

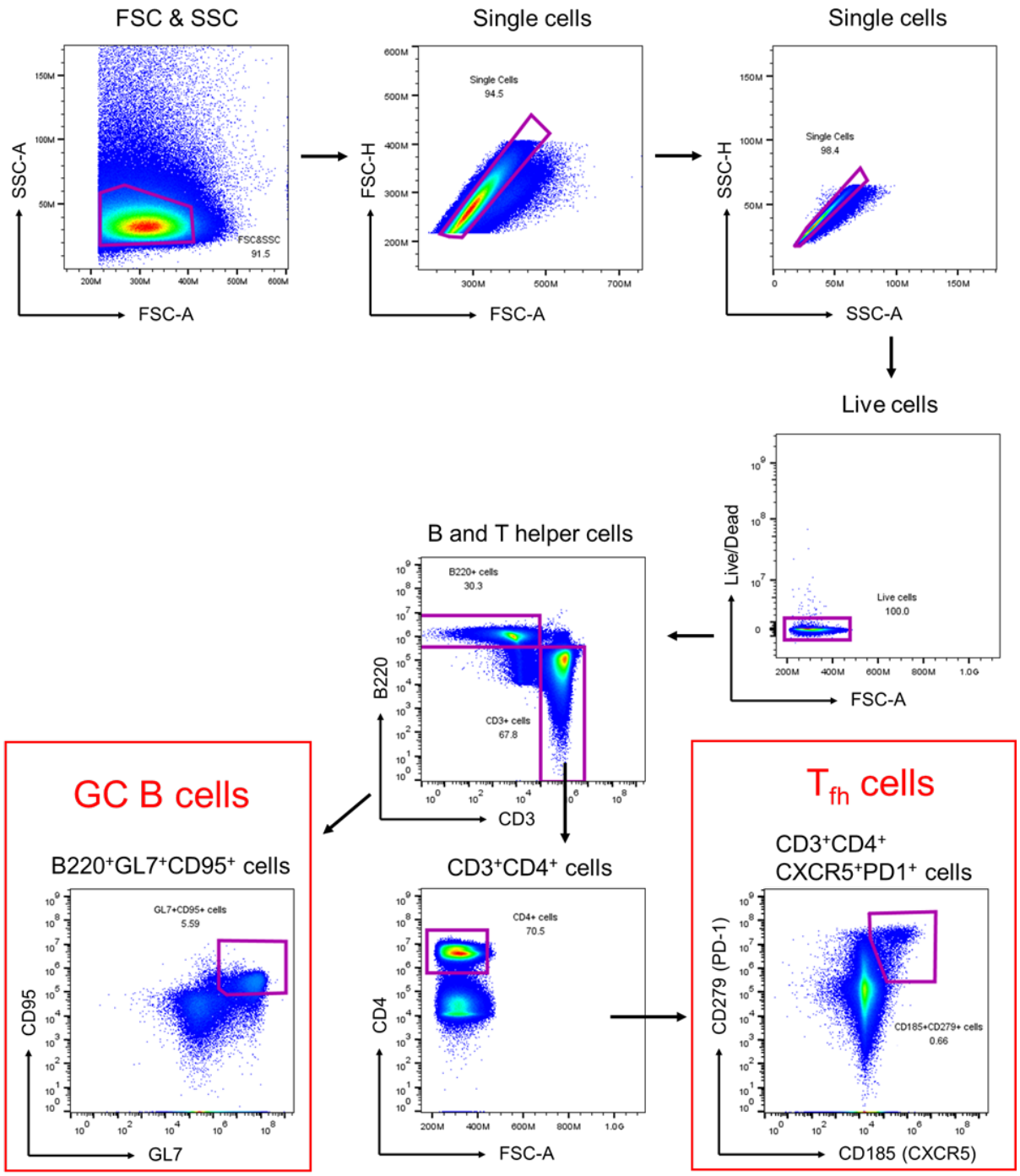

Fig. S9. Flow cytometry analysis of germinal centers (GCs) induced by SUDV GPΔmuc trimer and SApNPs vaccines. Gating strategy for identifying GC B cells and T follicular helper (Tfh) cells by flow cytometry (n = 5 mice per group).

a Sera of individual mice immunized with EBOV vaccines binding to EBOV GPΔmuc-WL^{2}P^4(1TD0) trimer

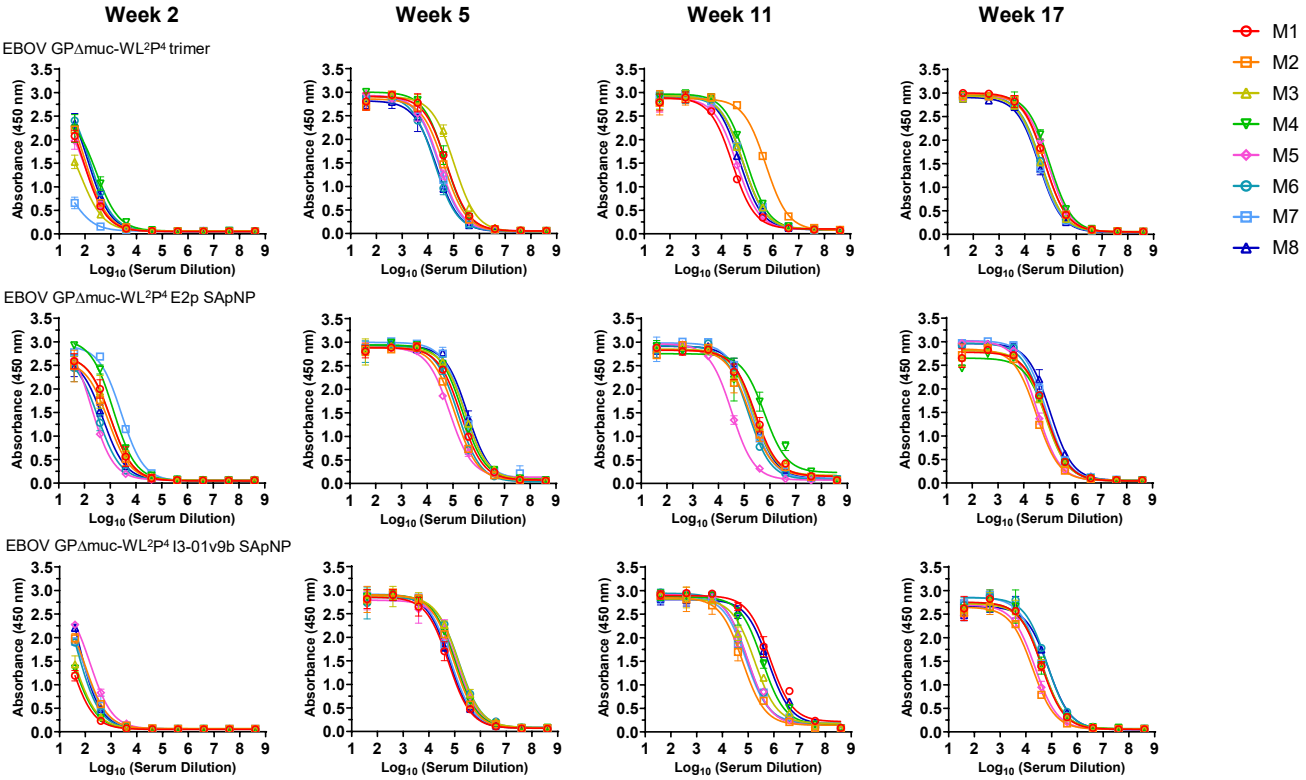

b Mouse serum ELISA EC_{50} titers

Week 2

Antigen	EC_{50} titers (week 2)								Geometric Mean
	M1	M2	M3	M4	M5	M6	M7	M8	
EBOV GPΔmuc-WL^{2}P^4 trimer	111.7	136.3	51.3	227.2	103.0	200.2	12.6	173.3	97.3
EBOV GPΔmuc-WL^{2}P^4 E2p SApNP	985.3	706.4	970.8	1772.0	271.5	336.1	3145.0	486.4	799.6
EBOV GPΔmuc-WL^{2}P^4 I3-01v9b SApNP	30.1	101.8	43.0	37.9	172.4	80.7	91.5	115.6	72.1

Week 5

Antigen	EC_{50} titers (week 5)								Geometric Mean
	M1	M2	M3	M4	M5	M6	M7	M8	
EBOV GPΔmuc-WL^{2}P^4 trimer	52545	41735	104914	48787	27947	18271	26144	21434	36588.3
EBOV GPΔmuc-WL^{2}P^4 E2p SApNP	199849	120954	303168	237335	74446	156667	282413	368341	195227.1
EBOV GPΔmuc-WL^{2}P^4 I3-01v9b SApNP	58458	93275	140476	104463	128829	148277	70114	63709	95341.8

Week 11

Antigen	EC_{50} titers (week 11)								Geometric Mean
	M1	M2	M3	M4	M5	M6	M7	M8	
EBOV GPΔmuc-WL^{2}P^4 trimer	26545	524033	69054	94400	39464	69865	68351	51944	73880.6
EBOV GPΔmuc-WL^{2}P^4 E2p SApNP	267135	163352	223491	606328	32762	143908	182928	233182	181721.7
EBOV GPΔmuc-WL^{2}P^4 I3-01v9b SApNP	703967	60730	178784	354031	97482	91294	82827	610293	182253.3

Week 17

Antigen	EC_{50} titers (week 17)								Geometric Mean
	M1	M2	M3	M4	M5	M6	M7	M8	
EBOV GPΔmuc-WL^{2}P^4-FOLD	59703	59841	42414	92526	80033	44111	36894	36448	53444.3
EBOV GPΔmuc-WL^{2}P^4 E2p SApNP	78072	31500	66659	79702	33830	63116	75359	105584	62128.2
EBOV GPΔmuc-WL^{2}P^4 I3-01v9b SApNP	40965	18206	43559	42711	22529	65820	41237	74760	39837.1

Statistical analysis

One-way ANOVA with Tukey's multiple comparisons test (w2)	Statistics	Adjusted P Value
EBOV GPΔmuc-WL^{2}P^4 trimer vs. EBOV GPΔmuc-WL^{2}P^4 E2p SApNP	**	0.0067
EBOV GPΔmuc-WL^{2}P^4 trimer vs. EBOV GPΔmuc-WL^{2}P^4 I3-01v9b SApNP	ns	0.9871
EBOV GPΔmuc-WL^{2}P^4 E2p SApNP vs. EBOV GPΔmuc-WL^{2}P^4 I3-01v9b SApNP	**	0.0047

One-way ANOVA with Tukey's multiple comparisons test (w5)	Statistics	Adjusted P Value
EBOV GPΔmuc-WL^{2}P^4 trimer vs. EBOV GPΔmuc-WL^{2}P^4 E2p SApNP	****	<0.0001
EBOV GPΔmuc-WL^{2}P^4 trimer vs. EBOV GPΔmuc-WL^{2}P^4 I3-01v9b SApNP	ns	0.1769
EBOV GPΔmuc-WL^{2}P^4 E2p SApNP vs. EBOV GPΔmuc-WL^{2}P^4 I3-01v9b SApNP	**	0.0034

One-way ANOVA with Tukey's multiple comparisons test (w11)	Statistics	Adjusted P Value
EBOV GPΔmuc-WL^{2}P^4 trimer vs. EBOV GPΔmuc-WL^{2}P^4 E2p SApNP	ns	0.5058
EBOV GPΔmuc-WL^{2}P^4 trimer vs. EBOV GPΔmuc-WL^{2}P^4 I3-01v9b SApNP	ns	0.2942
EBOV GPΔmuc-WL^{2}P^4 E2p SApNP vs. EBOV GPΔmuc-WL^{2}P^4 I3-01v9b SApNP	ns	0.9135

One-way ANOVA with Tukey's multiple comparisons test (w17)	Statistics	Adjusted P Value
EBOV GPΔmuc-WL^{2}P^4 trimer vs. EBOV GPΔmuc-WL^{2}P^4 E2p SApNP	ns	0.6171
EBOV GPΔmuc-WL^{2}P^4 trimer vs. EBOV GPΔmuc-WL^{2}P^4 I3-01v9b SApNP	ns	0.4761
EBOV GPΔmuc-WL^{2}P^4 E2p SApNP vs. EBOV GPΔmuc-WL^{2}P^4 I3-01v9b SApNP	ns	0.1078

C Week-7 sera of individual mice immunized with EBOV vaccines binding to SUDV GPΔmuc-WL^{2}P^4(1TD0) trimer

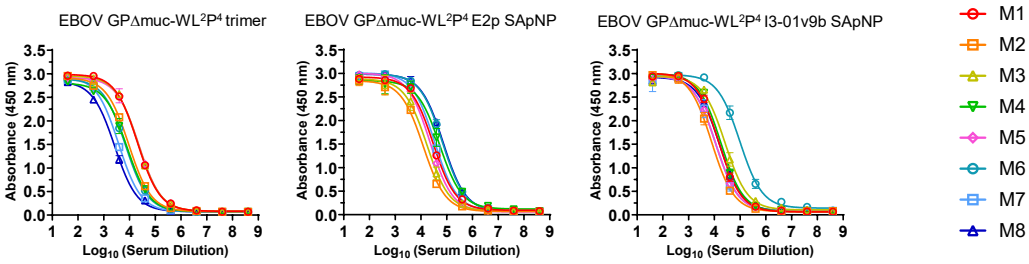

Mouse serum ELISA EC_{50} titers

	Antigen	EC_{50} titers (week 17)								Geometric Mean
		M1	M2	M3	M4	M5	M6	M7	M8	
Week 17	EBOV GPΔmuc-WL^{2}P^4 trimer	20545	9375	21603	8039	22891	7014	3805	2676	9273.3
	EBOV GPΔmuc-WL^{2}P^4 E2p SApNP	29973	12206	17018	52874	22735	68558	33997	72867	32585.3
	EBOV GPΔmuc-WL^{2}P^4 I3-01v9b SApNP	15023	7900	26186	17813	11241	97786	11184	15787	17943.0

Statistical analysis

One-way ANOVA with Tukey's multiple comparisons test (w17)	Statistics	Adjusted P Value
EBOV GPΔmuc-WL^{2}P^4 trimer vs. EBOV GPΔmuc-WL^{2}P^4 E2p SApNP	ns	0.0641
EBOV GPΔmuc-WL^{2}P^4 trimer vs. EBOV GPΔmuc-WL^{2}P^4 I3-01v9b SApNP	ns	0.4678
EBOV GPΔmuc-WL^{2}P^4 E2p SApNP vs. EBOV GPΔmuc-WL^{2}P^4 I3-01v9b SApNP	ns	0.4656

d Week-17 sera of individual mice immunized with EBOV vaccines binding to RAVV GPΔmuc-P^{2}CT(1TD0) trimer

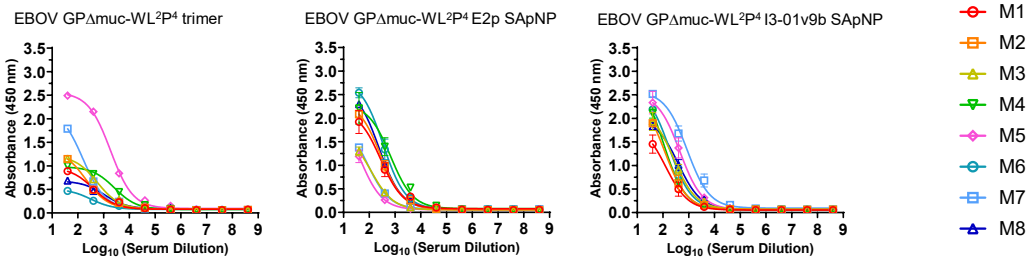

Mouse serum ELISA EC_{50} titers

	Antigen	Absorbance (450 nm) (week 17)								Geometric Mean
		M1	M2	M3	M4	M5	M6	M7	M8	
Week 17	EBOV GPΔmuc-WL^{2}P^4 trimer	0.9	1.1	1.2	1.0	2.5	0.5	1.8	0.7	1.1
	EBOV GPΔmuc-WL^{2}P^4 E2p SApNP	1.9	2.1	1.3	2.2	1.2	2.5	1.4	2.3	1.8
	EBOV GPΔmuc-WL^{2}P^4 I3-01v9b SApNP	1.5	1.9	1.9	2.1	2.3	2.2	2.5	1.8	2.0

Statistical analysis

One-way ANOVA with Tukey's multiple comparisons test (w17)	Statistics	Adjusted P Value
EBOV GPΔmuc-WL^{2}P^4 trimer vs. EBOV GPΔmuc-WL^{2}P^4 E2p SApNP	*	0.0449
EBOV GPΔmuc-WL^{2}P^4 trimer vs. EBOV GPΔmuc-WL^{2}P^4 I3-01v9b SApNP	*	0.0111
EBOV GPΔmuc-WL^{2}P^4 E2p SApNP vs. EBOV GPΔmuc-WL^{2}P^4 I3-01v9b SApNP	ns	0.7982

e Sera of individual mice immunized with EBOV vaccines neutralizing an EBOV Makona strain

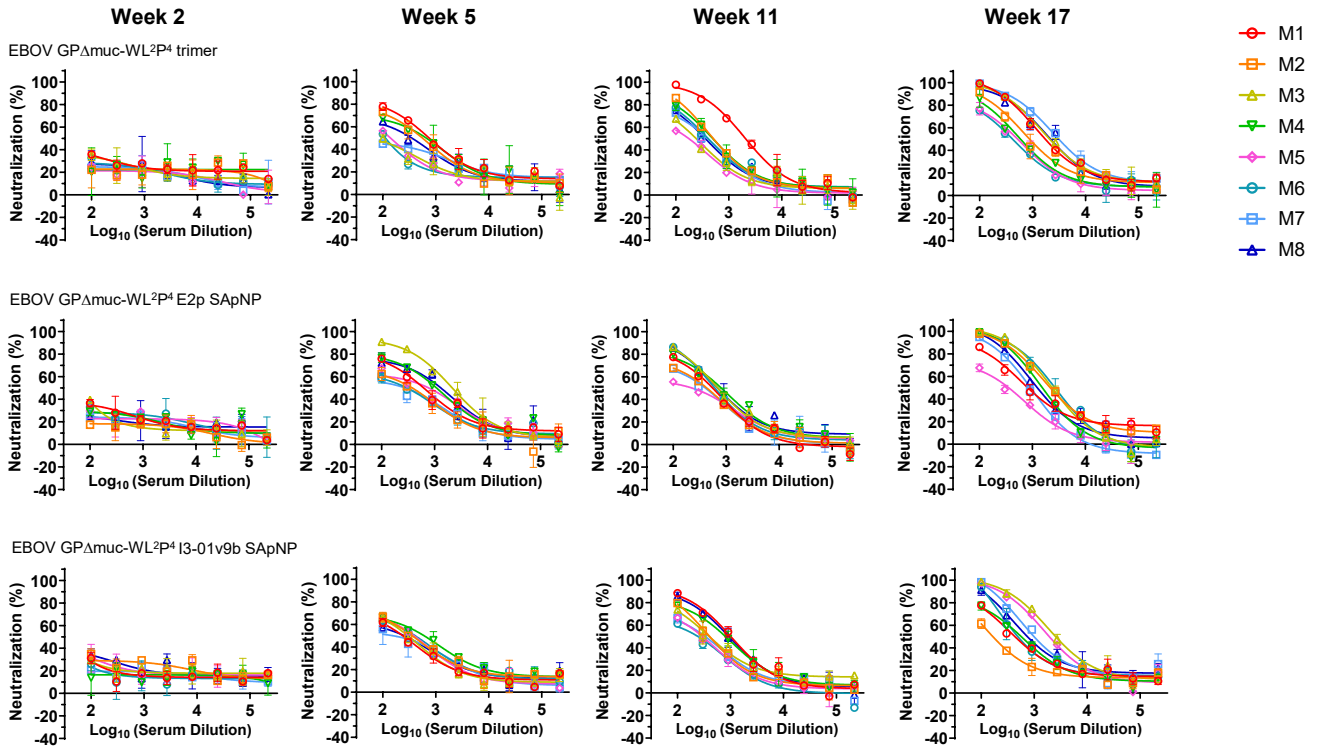

f Mouse serum neutralizing ID_{50} titers

Week 2

Antigen	ID_{50} titers (week 2)								Geometric Mean
	M1	M2	M3	M4	M5	M6	M7	M8	
EBOV GPΔmuc-WL^{2}P^4 trimer	<100	<100	<100	<100	<100	<100	<100	<100	N/A
EBOV GPΔmuc-WL^{2}P^4 E2p SApNP	<100	<100	<100	<100	<100	<100	<100	<100	N/A
EBOV GPΔmuc-WL^{2}P^4 I3-01v9b SApNP	<100	<100	<100	<100	<100	<100	<100	<100	N/A

Week 5

Antigen	ID_{50} titers (week 5)								Geometric Mean
	M1	M2	M3	M4	M5	M6	M7	M8	
EBOV GPΔmuc-WL^{2}P^4 trimer	805.4	559.3	149.3	588.2	174.1	145.1	203.2	360.5	304.1
EBOV GPΔmuc-WL^{2}P^4 E2p SApNP	636.9	358.8	2178.0	1002.0	555.2	322.9	299.4	1167.0	648.4
EBOV GPΔmuc-WL^{2}P^4 I3-01v9b SApNP	267.9	390.2	313.1	575.8	378.9	413.4	258.7	296.7	350.3

Week 11

Antigen	ID_{50} titers (week 11)								Geometric Mean
	M1	M2	M3	M4	M5	M6	M7	M8	
EBOV GPΔmuc-WL^{2}P^4 trimer	2117.0	560.6	254.4	521.5	188.7	430.2	369.3	377.3	453.2
EBOV GPΔmuc-WL^{2}P^4 E2p SApNP	494.5	392.0	734.2	747.4	275.3	643.8	365.2	759.9	518.6
EBOV GPΔmuc-WL^{2}P^4 I3-01v9b SApNP	1006.0	434.9	454.1	766.3	289.4	237.7	327.0	928.5	487.3

Week 17

Antigen	ID_{50} titers (week 17)								Geometric Mean
	M1	M2	M3	M4	M5	M6	M7	M8	
EBOV GPΔmuc-WL^{2}P^4 trimer	2106.0	1038.0	2482.0	641.1	505.0	437.0	3537.0	2352.0	1260.8
EBOV GPΔmuc-WL^{2}P^4 E2p SApNP	1000.0	2501.0	2393.0	1580.0	329.2	2587.0	875.5	1415.0	1333.1
EBOV GPΔmuc-WL^{2}P^4 I3-01v9b SApNP	513.1	205.2	2961.0	592.6	2154.0	693.4	1272.0	994.0	876.7

Statistical analysis

One-way ANOVA with Tukey's multiple comparisons test (w5)	Statistics	Adjusted P Value
EBOV GPΔmuc-WL^{2}P^4 trimer vs. EBOV GPΔmuc-WL^{2}P^4 E2p SApNP	ns	0.0919
EBOV GPΔmuc-WL^{2}P^4 trimer vs. EBOV GPΔmuc-WL^{2}P^4 I3-01v9b SApNP	ns	0.9982
EBOV GPΔmuc-WL^{2}P^4 E2p SApNP vs. EBOV GPΔmuc-WL^{2}P^4 I3-01v9b SApNP	ns	0.0824

One-way ANOVA with Tukey's multiple comparisons test (w11)	Statistics	Adjusted P Value
EBOV GPΔmuc-WL^{2}P^4 trimer vs. EBOV GPΔmuc-WL^{2}P^4 E2p SApNP	ns	0.9676
EBOV GPΔmuc-WL^{2}P^4 trimer vs. EBOV GPΔmuc-WL^{2}P^4 I3-01v9b SApNP	ns	0.9724
EBOV GPΔmuc-WL^{2}P^4 E2p SApNP vs. EBOV GPΔmuc-WL^{2}P^4 I3-01v9b SApNP	ns	0.9998

One-way ANOVA with Tukey's multiple comparisons test (w17)	Statistics	Adjusted P Value
EBOV GPΔmuc-WL^{2}P^4 trimer vs. EBOV GPΔmuc-WL^{2}P^4 E2p SApNP	ns	0.9938
EBOV GPΔmuc-WL^{2}P^4 trimer vs. EBOV GPΔmuc-WL^{2}P^4 I3-01v9b SApNP	ns	0.618
EBOV GPΔmuc-WL^{2}P^4 E2p SApNP vs. EBOV GPΔmuc-WL^{2}P^4 I3-01v9b SApNP	ns	0.6831

g Week-17 sera of individual mice immunized with EBOV vaccines neutralizing a SUDV Gulu strain

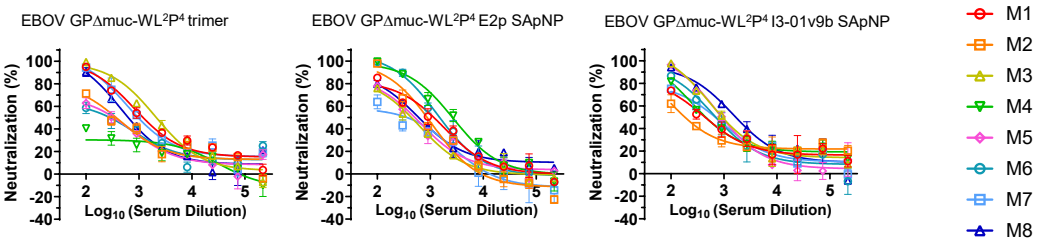

Mouse serum neutralizing ID_{50} titers

	Antigen	ID_{50} titers (week 17)								Geometric Mean
		M1	M2	M3	M4	M5	M6	M7	M8	
Week 17	EBOV GPΔmuc-WL^{2}P^4 trimer	1530.0	407.3	2200.0	113.8	341.2	323.2	1236.0	726.5	593.8
	EBOV GPΔmuc-WL^{2}P^4 E2p SApNP	956.0	759.0	403.8	2580.0	489.0	1564.0	301.3	647.6	761.3
	EBOV GPΔmuc-WL^{2}P^4 I3-01v9b SApNP	512.3	265.2	1198.0	608.8	1006.0	765.2	662.5	1824.0	742.3

Statistical analysis

One-way ANOVA with Tukey's multiple comparisons test (w17)	Statistics	Adjusted P Value
EBOV GPΔmuc-WL^{2}P^4 trimer vs. EBOV GPΔmuc-WL^{2}P^4 E2p SApNP	ns	0.9497
EBOV GPΔmuc-WL^{2}P^4 trimer vs. EBOV GPΔmuc-WL^{2}P^4 I3-01v9b SApNP	ns	>0.9999
EBOV GPΔmuc-WL^{2}P^4 E2p SApNP vs. EBOV GPΔmuc-WL^{2}P^4 I3-01v9b SApNP	ns	0.9453

h Week-17 sera of individual mice immunized with EBOV vaccines neutralizing a BDBV Uganda strain

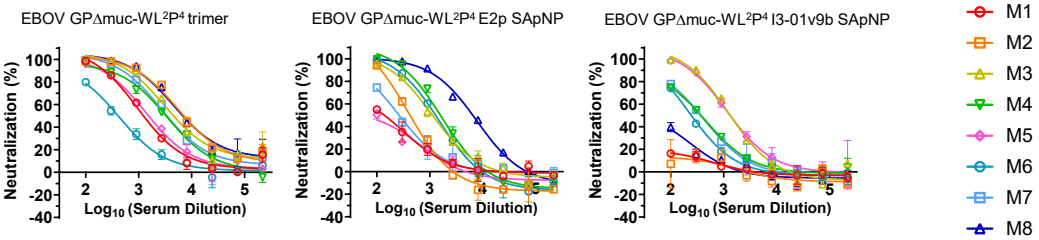

Mouse serum neutralizing ID_{50} titers

	Antigen	ID_{50} titers (week 17)								Geometric Mean
		M1	M2	M3	M4	M5	M6	M7	M8	
Week 17	EBOV GPΔmuc-WL^{2}P^4 trimer	1344.0	7809.0	5137.0	3217.0	1631.0	411.3	3729.0	7747.0	2759.4
	EBOV GPΔmuc-WL^{2}P^4 E2p SApNP	149.6	394.3	1109.0	1525.0	115.1	1174.0	261.1	5895.0	616.1
	EBOV GPΔmuc-WL^{2}P^4 I3-01v9b SApNP	<100	<100	1332.0	356.1	1397.0	240.1	352.0	<100	561.9

Statistical analysis

One-way ANOVA with Tukey's multiple comparisons test (w17)	Statistics	Adjusted P Value
EBOV GPΔmuc-WL^{2}P^4 trimer vs. EBOV GPΔmuc-WL^{2}P^4 E2p SApNP	*	0.0469
EBOV GPΔmuc-WL^{2}P^4 trimer vs. EBOV GPΔmuc-WL^{2}P^4 I3-01v9b SApNP	**	0.0076
EBOV GPΔmuc-WL^{2}P^4 E2p SApNP vs. EBOV GPΔmuc-WL^{2}P^4 I3-01v9b SApNP	ns	0.6882

i Sera of individual mice immunized with SUDV vaccines binding to SUDV GPΔmuc-WL^{2}P^4(1TD0) trimer

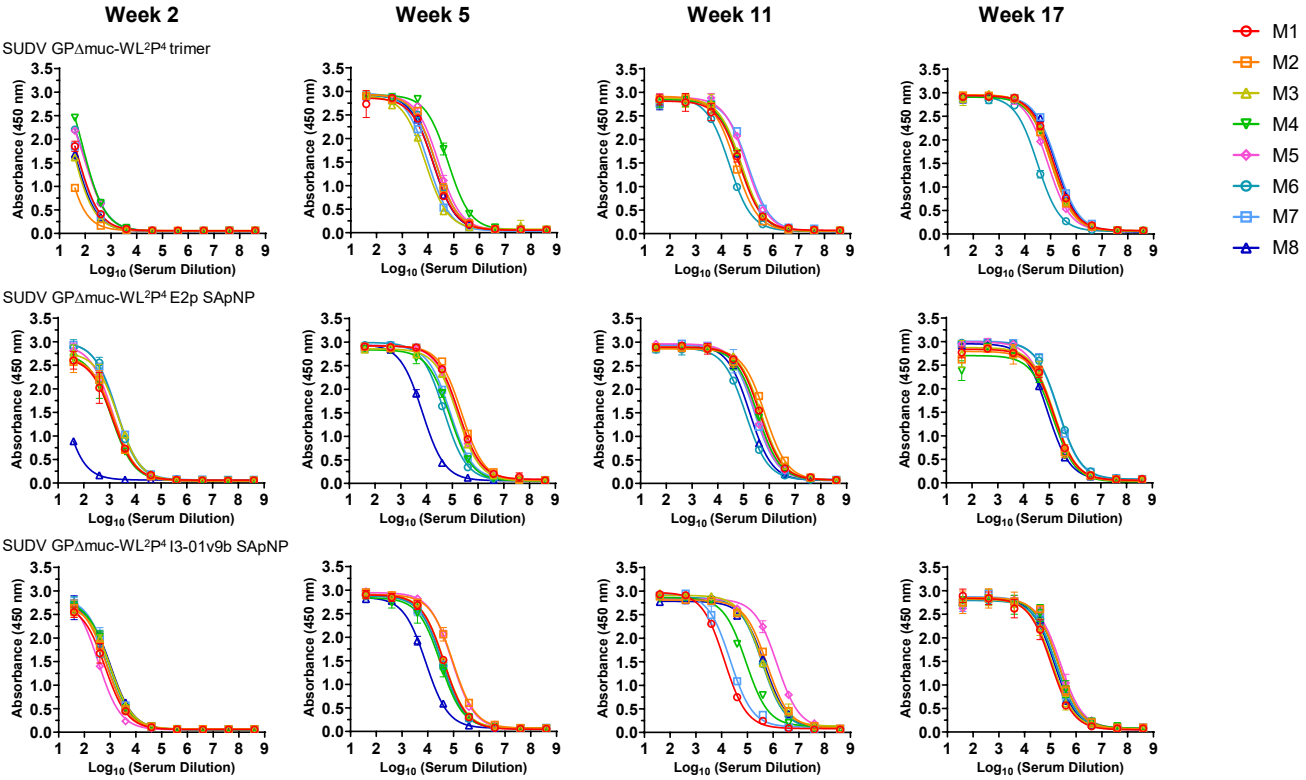

j Mouse serum ELISA EC_{50} titers

Week 2

Antigen	EC_{50} titers (week 2)								Geometric Mean
	M1	M2	M3	M4	M5	M6	M7	M8	
SUDV GPΔmuc-WL^{2}P^4 trimer	69.8	20.2	50.0	149.7	116.9	122.4	68.1	55.0	69.8
SUDV GPΔmuc-WL^{2}P^4 E2p SApNP	1058.0	1223.0	1977.0	1062.0	1419.0	2123.0	2262.0	17.9	871.0
SUDV GPΔmuc-WL^{2}P^4 I3-01v9b SApNP	550.3	700.2	876.2	893.5	373.7	741.1	903.2	940.0	718.4

Week 5

Antigen	EC_{50} titers (week 5)								Geometric Mean
	M1	M2	M3	M4	M5	M6	M7	M8	
SUDV GPΔmuc-WL^{2}P^4 trimer	16436	19941	7907	60277	25656	19754	9992	15619	18259.2
SUDV GPΔmuc-WL^{2}P^4 E2p SApNP	177305	230404	159220	79353	157784	47895	82714	6921	82910.4
SUDV GPΔmuc-WL^{2}P^4 I3-01v9b SApNP	42731	93470	42715	31125	87027	36180	35115	8482	38650.3

Week 11

Antigen	EC_{50} titers (week 11)								Geometric Mean
	M1	M2	M3	M4	M5	M6	M7	M8	
SUDV GPΔmuc-WL^{2}P^4 trimer	51852	34819	59219	58035	92570	20182	108658	56856	53935.6
SUDV GPΔmuc-WL^{2}P^4 E2p SApNP	427238	688825	479499	349324	289258	121660	264183	173015	307186.5
SUDV GPΔmuc-WL^{2}P^4 I3-01v9b SApNP	12804	573418	373590	88061	1405850	379235	21591	471753	183962.3

Week 17

Antigen	EC_{50} titers (week 17)								Geometric Mean
	M1	M2	M3	M4	M5	M6	M7	M8	
SUDV GPΔmuc-WL^{2}P^4 trimer	132375	104284	117314	112501	78562	31328	174100	161747	102958.9
SUDV GPΔmuc-WL^{2}P^4 E2p SApNP	150503	150658	156743	142867	124345	229353	218325	86164	151148.0
SUDV GPΔmuc-WL^{2}P^4 I3-01v9b SApNP	108351	204158	120591	200895	248727	170555	157838	144221	163771.7

Statistical analysis

One-way ANOVA with Tukey's multiple comparisons test (w2)	Statistics	Adjusted P Value
SUDV GPΔmuc-WL^{2}P^4 trimer vs. SUDV GPΔmuc-WL^{2}P^4 E2p SApNP	****	<0.0001
SUDV GPΔmuc-WL^{2}P^4 trimer vs. SUDV GPΔmuc-WL^{2}P^4 I3-01v9b SApNP	*	0.0169
SUDV GPΔmuc-WL^{2}P^4 E2p SApNP vs. SUDV GPΔmuc-WL^{2}P^4 I3-01v9b SApNP	*	0.0207

One-way ANOVA with Tukey's multiple comparisons test (w5)	Statistics	Adjusted P Value
SUDV GPΔmuc-WL^{2}P^4 trimer vs. SUDV GPΔmuc-WL^{2}P^4 E2p SApNP	**	0.0016
SUDV GPΔmuc-WL^{2}P^4 trimer vs. SUDV GPΔmuc-WL^{2}P^4 I3-01v9b SApNP	ns	0.5472
SUDV GPΔmuc-WL^{2}P^4 E2p SApNP vs. SUDV GPΔmuc-WL^{2}P^4 I3-01v9b SApNP	*	0.0187

One-way ANOVA with Tukey's multiple comparisons test (w11)	Statistics	Adjusted P Value
SUDV GPΔmuc-WL^{2}P^4 trimer vs. SUDV GPΔmuc-WL^{2}P^4 E2p SApNP	ns	0.1259
SUDV GPΔmuc-WL^{2}P^4 trimer vs. SUDV GPΔmuc-WL^{2}P^4 I3-01v9b SApNP	ns	0.0502
SUDV GPΔmuc-WL^{2}P^4 E2p SApNP vs. SUDV GPΔmuc-WL^{2}P^4 I3-01v9b SApNP	ns	0.885

One-way ANOVA with Tukey's multiple comparisons test (w17)	Statistics	Adjusted P Value
SUDV GPΔmuc-WL^{2}P^4 trimer vs. SUDV GPΔmuc-WL^{2}P^4 E2p SApNP	ns	0.1724
SUDV GPΔmuc-WL^{2}P^4 trimer vs. SUDV GPΔmuc-WL^{2}P^4 I3-01v9b SApNP	ns	0.0653
SUDV GPΔmuc-WL^{2}P^4 E2p SApNP vs. SUDV GPΔmuc-WL^{2}P^4 I3-01v9b SApNP	ns	0.8627

k Week-17 sera of individual mice immunized with SUDV vaccines binding to EBOV GPΔmuc-WL^{2}P^4(1TD0) trimer

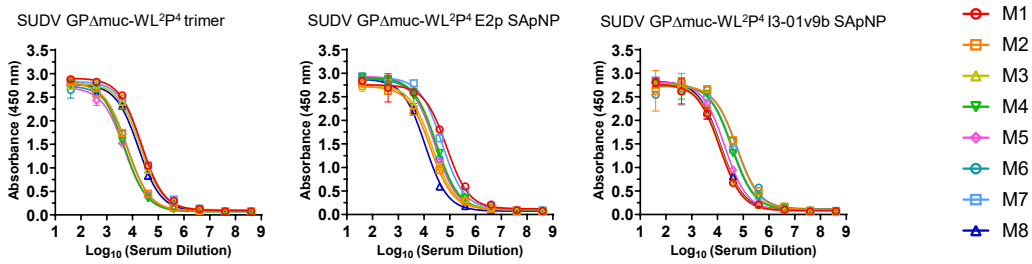

Mouse serum ELISA EC_{50} titers

	Antigen	EC_{50} titers (week 17)								Geometric Mean
		M1	M2	M3	M4	M5	M6	M7	M8	
Week 17	SUDV GPΔmuc-WL^{2}P^4 trimer	22131	6105	19939	4814	4809	6529	22832	16822	10574.9
	SUDV GPΔmuc-WL^{2}P^4 E2p SApNP	74857	17696	20913	30182	25142	26898	49408	11012	27290.2
	SUDV GPΔmuc-WL^{2}P^4 I3-01v9b SApNP	12210	55319	13273	35138	19190	57302	38054	13336	25446.4

Statistical analysis

One-way ANOVA with Tukey's multiple comparisons test (w17)	Statistics	Adjusted P Value
SUDV GPΔmuc-WL^{2}P^4 trimer vs. SUDV GPΔmuc-WL^{2}P^4 E2p SApNP	ns	0.0832
SUDV GPΔmuc-WL^{2}P^4 trimer vs. SUDV GPΔmuc-WL^{2}P^4 I3-01v9b SApNP	ns	0.1177
SUDV GPΔmuc-WL^{2}P^4 E2p SApNP vs. SUDV GPΔmuc-WL^{2}P^4 I3-01v9b SApNP	ns	0.9817

l Week-17 sera of individual mice immunized with SUDV vaccines binding to RAVV GPΔmuc-P^{2}CT(1TD0) trimer

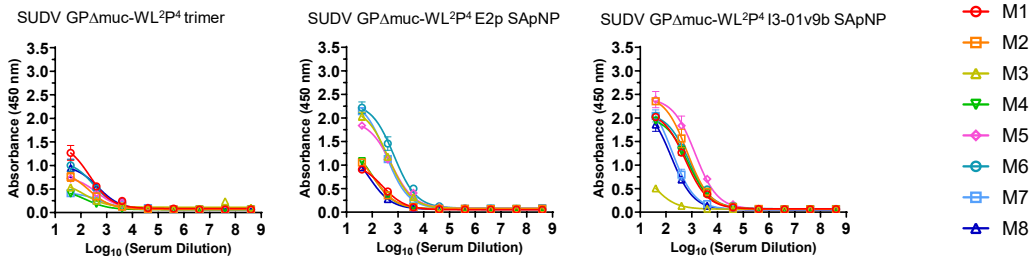

Mouse serum ELISA EC_{50} titers

	Antigen	Absorbance (450 nm) (week 17)								Geometric Mean
		M1	M2	M3	M4	M5	M6	M7	M8	
Week 17	SUDV GPΔmuc-WL^{2}P^4 trimer	1.3	0.8	0.5	0.4	0.7	1.0	0.4	0.9	0.7
	SUDV GPΔmuc-WL^{2}P^4 E2p SApNP	0.9	1.1	2.0	1.1	1.8	2.2	2.1	1.0	1.4
	SUDV GPΔmuc-WL^{2}P^4 I3-01v9b SApNP	2.0	2.4	0.5	1.9	2.4	2.0	2.0	1.9	1.7

Statistical analysis

One-way ANOVA with Tukey's multiple comparisons test (w17)	Statistics	Adjusted P Value
SUDV GPΔmuc-WL^{2}P^4 trimer vs. SUDV GPΔmuc-WL^{2}P^4 E2p SApNP	*	0.0149
SUDV GPΔmuc-WL^{2}P^4 trimer vs. SUDV GPΔmuc-WL^{2}P^4 I3-01v9b SApNP	***	0.0005
SUDV GPΔmuc-WL^{2}P^4 E2p SApNP vs. SUDV GPΔmuc-WL^{2}P^4 I3-01v9b SApNP	ns	0.338

m Sera of individual mice immunized with SUDV vaccines neutralizing a SUDV Gulu strain

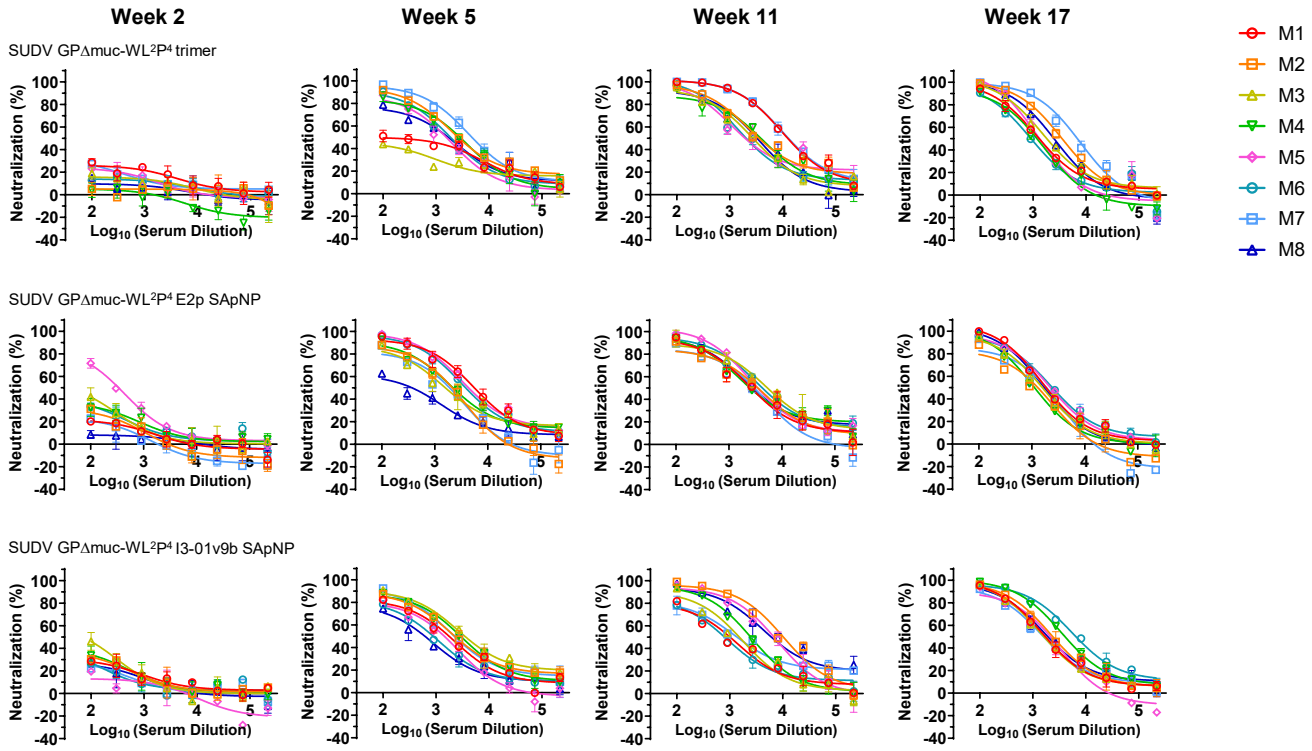

n Mouse serum neutralizing ID_{50} titers

Week 2

Antigen	ID_{50} titers (week 2)								Geometric Mean
	M1	M2	M3	M4	M5	M6	M7	M8	
SUDV GPΔmuc-WL^{2}P^4 trimer	<100	<100	<100	<100	<100	<100	<100	<100	N/A
SUDV GPΔmuc-WL^{2}P^4 E2p SApNP	<100	<100	<100	<100	331.1	<100	<100	<100	N/A
SUDV GPΔmuc-WL^{2}P^4 I3-01v9b SApNP	<100	<100	107.2	<100	<100	<100	<100	<100	N/A

Week 5

Antigen	ID_{50} titers (week 5)								Geometric Mean
	M1	M2	M3	M4	M5	M6	M7	M8	
SUDV GPΔmuc-WL^{2}P^4 trimer	420	3076	156.6	2417	1377	1896	5149	1477	1328.6
SUDV GPΔmuc-WL^{2}P^4 E2p SApNP	5677	1634	1754	2420	5081	4212	1332	355.5	2114.1
SUDV GPΔmuc-WL^{2}P^4 I3-01v9b SApNP	1582	2485	4102	2862	1119	843.6	2506	584.4	1681.2

Week 11

Antigen	ID_{50} titers (week 11)								Geometric Mean
	M1	M2	M3	M4	M5	M6	M7	M8	
SUDV GPΔmuc-WL^{2}P^4 trimer	13810	4694	2805	3670	2858	2497	14410	3069	4628.4
SUDV GPΔmuc-WL^{2}P^4 E2p SApNP	2835	3130	5528	3311	3940	4935	2323	3352	3538.7
SUDV GPΔmuc-WL^{2}P^4 I3-01v9b SApNP	889.3	10154	1391	2424	6257	808.9	1524	7608	2549.8

Week 17

Antigen	ID_{50} titers (week 17)								Geometric Mean
	M1	M2	M3	M4	M5	M6	M7	M8	
SUDV GPΔmuc-WL^{2}P^4 trimer	1389	3550	2017	1006	1354	931.1	6329	2409	1929.8
SUDV GPΔmuc-WL^{2}P^4 E2p SApNP	2035	928.9	1546	1147	2291	2536	1215	1753	1593.1
SUDV GPΔmuc-WL^{2}P^4 I3-01v9b SApNP	1853	2507	1746	4395	1648	7166	1695	2160	2503.1

Statistical analysis

One-way ANOVA with Tukey's multiple comparisons test (w5)	Statistics	Adjusted P Value
SUDV GPΔmuc-WL^{2}P^4 trimer vs. SUDV GPΔmuc-WL^{2}P^4 E2p SApNP	ns	0.5769
SUDV GPΔmuc-WL^{2}P^4 trimer vs. SUDV GPΔmuc-WL^{2}P^4 I3-01v9b SApNP	ns	0.9998
SUDV GPΔmuc-WL^{2}P^4 E2p SApNP vs. SUDV GPΔmuc-WL^{2}P^4 I3-01v9b SApNP	ns	0.5879

One-way ANOVA with Tukey's multiple comparisons test (w11)	Statistics	Adjusted P Value
SUDV GPΔmuc-WL^{2}P^4 trimer vs. SUDV GPΔmuc-WL^{2}P^4 E2p SApNP	ns	0.4294
SUDV GPΔmuc-WL^{2}P^4 trimer vs. SUDV GPΔmuc-WL^{2}P^4 I3-01v9b SApNP	ns	0.4956
SUDV GPΔmuc-WL^{2}P^4 E2p SApNP vs. SUDV GPΔmuc-WL^{2}P^4 I3-01v9b SApNP	ns	0.9925

One-way ANOVA with Tukey's multiple comparisons test (w17)	Statistics	Adjusted P Value
SUDV GPΔmuc-WL^{2}P^4 trimer vs. SUDV GPΔmuc-WL^{2}P^4 E2p SApNP	ns	0.6592
SUDV GPΔmuc-WL^{2}P^4 trimer vs. SUDV GPΔmuc-WL^{2}P^4 I3-01v9b SApNP	ns	0.7862
SUDV GPΔmuc-WL^{2}P^4 E2p SApNP vs. SUDV GPΔmuc-WL^{2}P^4 I3-01v9b SApNP	ns	0.2916

o Week-17 sera of individual mice immunized with SUDV vaccines neutralizing an EBOV Makona strain

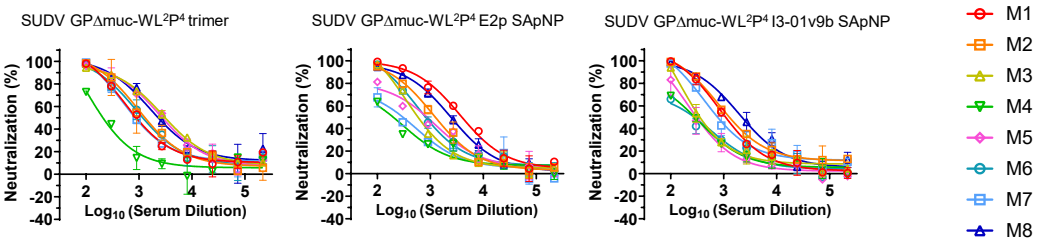

Mouse serum neutralizing ID_{50} titers

	Antigen	ID_{50} titers (week 17)								Geometric Mean
		M1	M2	M3	M4	M5	M6	M7	M8	
Week 17	SUDV GPΔmuc-WL^{2}P^4 trimer	1073	1510	3312	230.5	2932	1345	1075	2621	1387.6
	SUDV GPΔmuc-WL^{2}P^4 E2p SApNP	4144	1304	687.5	217	758.8	964.7	297	2453	899.9
	SUDV GPΔmuc-WL^{2}P^4 I3-01v9b SApNP	1214	1567	467.4	296.9	336.4	271	990.7	2370	698.3

Statistical analysis

One-way ANOVA with Tukey's multiple comparisons test (w17)	Statistics	Adjusted P Value
SUDV GPΔmuc-WL^{2}P^4 trimer vs. SUDV GPΔmuc-WL^{2}P^4 E2p SApNP	ns	0.7312
SUDV GPΔmuc-WL^{2}P^4 trimer vs. SUDV GPΔmuc-WL^{2}P^4 I3-01v9b SApNP	ns	0.2983
SUDV GPΔmuc-WL^{2}P^4 E2p SApNP vs. SUDV GPΔmuc-WL^{2}P^4 I3-01v9b SApNP	ns	0.7257

p Week-17 sera of individual mice immunized with SUDV vaccines neutralizing a BDBV Uganda strain

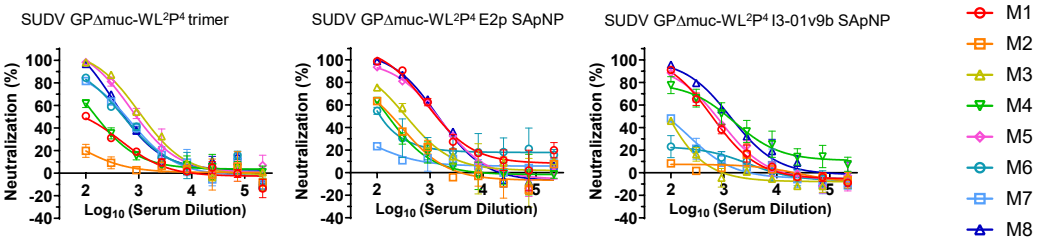

Mouse serum neutralizing ID_{50} titers

	Antigen	ID_{50} titers (week 17)								Geometric Mean
		M1	M2	M3	M4	M5	M6	M7	M8	
Week 17	SUDV GPΔmuc-WL^{2}P^4 trimer	126.7	26.1	1237.0	165.3	985.6	518.9	543.9	613.3	322.0
	SUDV GPΔmuc-WL^{2}P^4 E2p SApNP	1504.0	174.5	356.0	156.5	1298.0	151.8	35.5	1393.0	330.6
	SUDV GPΔmuc-WL^{2}P^4 I3-01v9b SApNP	580.4	9.7	69.0	1085.0	656.4	<100	<100	1280.0	185.5

Statistical analysis

One-way ANOVA with Tukey's multiple comparisons test (w17)	Statistics	Adjusted P Value
SUDV GPΔmuc-WL^{2}P^4 trimer vs. SUDV GPΔmuc-WL^{2}P^4 E2p SApNP	ns	0.913
SUDV GPΔmuc-WL^{2}P^4 trimer vs. SUDV GPΔmuc-WL^{2}P^4 I3-01v9b SApNP	ns	0.9893
SUDV GPΔmuc-WL^{2}P^4 E2p SApNP vs. SUDV GPΔmuc-WL^{2}P^4 I3-01v9b SApNP	ns	0.8492

q Sera of individual mice immunized with RAVV vaccines binding to RAVV GPΔmuc-P²CT(1TD0) trimer

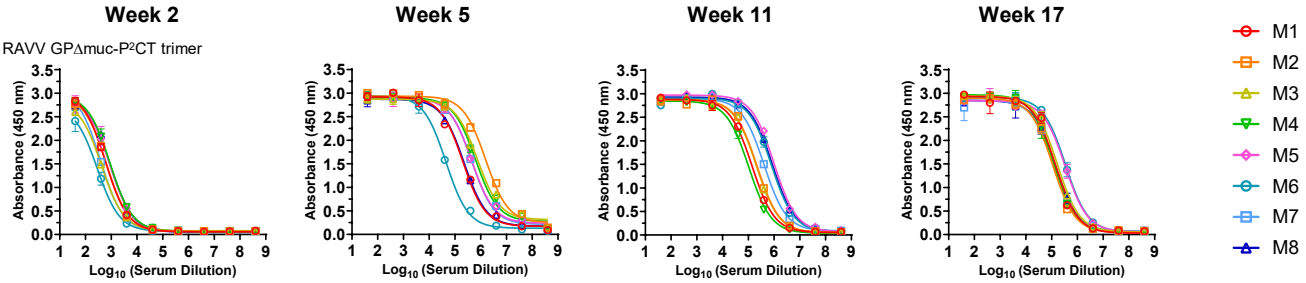

Mouse serum ELISA EC_{50} titers

Antigen	EC_{50} titers								Geometric Mean
	M1	M2	M3	M4	M5	M6	M7	M8	
RAVV GPΔmuc-P²CT trimer-w2	718.9	721.9	432.3	1030.0	946.3	262.3	481.5	958.5	635.1
RAVV GPΔmuc-P²CT trimer-w5	202735	1544554	746406	628189	447117	44771	446178	225949	362215.2
RAVV GPΔmuc-P²CT trimer-w11	139135	218951	208199	104125	998580	786127	408247	853062	340466.6
RAVV GPΔmuc-P²CT trimer-w17	140811	110900	164905	119990	336478	344895	127509	141835	168457.1

r Week-17 sera of individual mice immunized with RAVV vaccines binding to EBOV GPΔmuc-WL²P⁴(1TD0) trimer

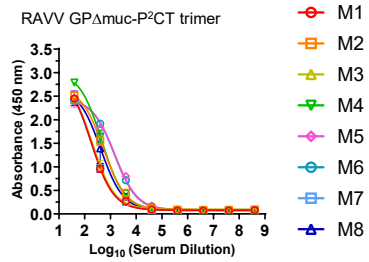

Mouse serum ELISA EC_{50} titers

Antigen	EC_{50} titers (week 17)								Geometric Mean
	M1	M2	M3	M4	M5	M6	M7	M8	
RAVV GPΔmuc-P²CT trimer	177.5	537.5	197.8	459.9	1477.0	1430.0	182.7	422.8	440.4

s Week-17 sera of individual mice immunized with RAVV vaccines binding to SUDV GPΔmuc-WL²P⁴(1TD0) trimer

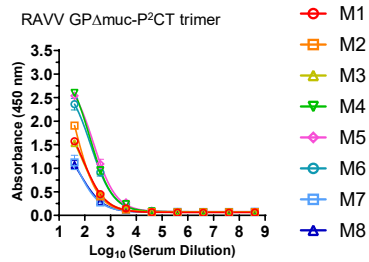

Mouse serum ELISA EC_{50} titers

Antigen	Absorbance (450 nm) (week 17)								Geometric Mean
	M1	M2	M3	M4	M5	M6	M7	M8	
RAVV GPΔmuc-P²CT trimer	1.6	1.9	1.5	2.6	2.5	2.4	2.4	2.4	2.1

t Week-17 IgG samples of individual mice immunized with RAVV vaccines neutralizing a MARV Angola strain

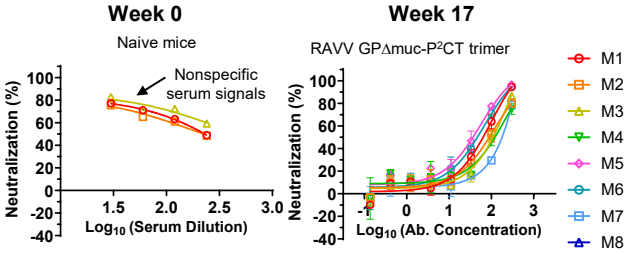

Week 17 mouse IgG neutralization

Virus strains	IC_{50} (μg/mL) (week 17)								Geometric Mean
	M1	M2	M3	M4	M5	M6	M7	M8	
MARV-Angola	56.2	81.4	93.3	104.4	30.9	40.3	148.4	71.8	70.2

u Week-17 sera of individual mice immunized with RAVV vaccines neutralizing three orthoebolavirus strains

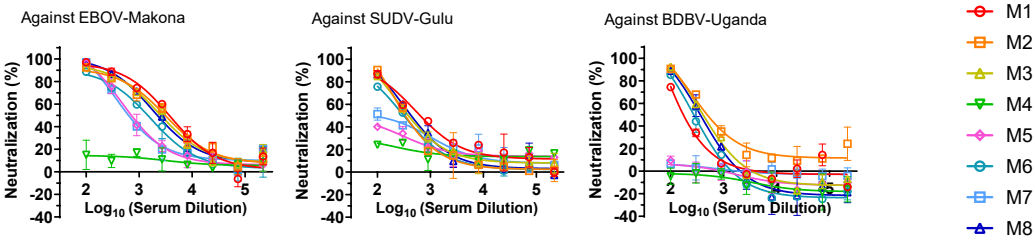

Fig. S10. Immunogenicity of EBOV, SUDV, and RAVV GPΔmuc vaccines in mice. (**a**) ELISA curves of mouse sera from EBOV GPΔmuc trimer and SApNP vaccine groups (n = 8 mice/group) binding to the coating antigen EBOV GPΔmuc-WL^{2}P^4(1TD0) trimer (**b**) (Top) Summary of geometric mean EC_{50} titers measured for Ebola GPΔmuc vaccine groups against EBOV GPΔmuc-WL^{2}P^4(1TD0) trimer. Color coding indicates EC_{50} levels (green to red: low to high binding). (Bottom) Summary of statistical analysis performed for each timepoint. Note: EC_{50} values at week 2 were derived by setting the minimum/maximum OD_{450} values to 0.0/2.8. (**c**) ELISA curves of mouse sera from EBOV GPΔmuc vaccine groups at week 17 after four immunizations binding to SUDV GPΔmuc-WL^{2}P^4(1TD0) trimer. Summary of geometric mean EC_{50} titers and statistical analysis. (**d**) ELISA curves of mouse sera from Ebola GPΔmuc vaccine groups at week 17 after four immunizations binding to RAVV GPΔmuc-P^{2}CT(1TD0) trimer. Summary of absorbance at 450 nm (A450) values was included. (**e**) Neutralization curves of mouse sera from EBOV GPΔmuc trimer and SApNP vaccine groups against EBOV Makona pseudovirus. (**f**) (Top) Summary of geometric mean ID_{50} titers measured for EBOV GPΔmuc vaccine groups against EBOV Makona pseudovirus. Color coding: white (no neutralization), green to red (low to high neutralization). Note: ID_{50} values were calculated using %neutralization constraints of 0.0 (min) and 100.0 (max). (Bottom) Summary of statistical analysis as in (**b**). (**g**) Neutralization curves of mouse sera from EBOV GPΔmuc vaccine groups at week 17 against SUDV Gulu pseudovirus. Summary of geometric means of ID_{50} values and statistical analysis. (**h**) Neutralization curves of mouse sera from EBOV GPΔmuc vaccine groups at week 17 against BDBV Uganda pseudovirus. Summary of geometric mean ID_{50} values and statistical analysis. (**i**) ELISA curves of mouse sera from SUDV GPΔmuc trimer and SApNP vaccine groups binding to SUDV GPΔmuc-WL^{2}P^4(1TD0) trimer. (**j**) (Top) Summary of geometric means of EC_{50} titers measured for SUDV GPΔmuc vaccine groups against SUDV GPΔmuc-WL^{2}P^4(1TD0) trimer. (Bottom) Summary of statistical analysis as in (**b**). Note: EC_{50} values at week 2 were derived by setting the minimum/maximum OD_{450} values to 0.0/2.9. (**k**) ELISA curves of mouse sera from SUDV GPΔmuc vaccine groups at week 17 after four immunizations binding to EBOV GPΔmuc-WL^{2}P^4(1TD0) trimer. Summary of geometric mean EC_{50} titers and statistical analysis. (**l**) ELISA curves of mouse sera from SUDV GPΔmuc vaccine groups at week 17 after four immunizations binding to RAVV GPΔmuc-P^{2}CT(1TD0) trimer. Summary of A450 values was included. (**m**) Neutralization curves of mouse sera from SUDV GPΔmuc trimer and SApNP vaccine groups against SUDV Gulu pseudovirus. (**n**) (Top) Summary of geometric means of ID_{50} titers measured for EBOV GPΔmuc vaccine groups against EBOV Makona pseudovirus. (Bottom) Summary of statistical analysis as in (**b**). (**o**) Neutralization curves of mouse sera from EBOV GPΔmuc vaccine groups at week 17 against EBOV Makona pseudovirus. Summary of geometric mean ID_{50} values and statistical analysis. (**p**) Neutralization curves of mouse sera from EBOV GPΔmuc vaccine groups at week 17 against BDBV Uganda pseudovirus. Summary of geometric means of ID_{50} values and statistical analysis. (**q**) (Top) ELISA curves of mouse sera from RAVV GPΔmuc trimer vaccine groups binding to RAVV GPΔmuc-P^{2}CT(1TD0) trimer. (Bottom) Summary of geometric mean EC_{50} values. Note: EC_{50} values at week 2 were derived by setting the minimum/maximum OD_{450} values to 0.0/2.9. (**r**) ELISA curves of mouse sera from RAVV GPΔmuc vaccine groups at week 17 after four immunizations binding to EBOV GPΔmuc-WL^{2}P^4(1TD0) trimer. Summary of geometric mean EC_{50} titers. (**s**) ELISA curves of mouse sera from RAVV GPΔmuc vaccine groups at week 17 after four immunizations binding to SUDV GPΔmuc-WL^{2}P^4(1TD0) trimer. Summary of A450 values was included. (**t**) Neutralization curves of purified IgG from RAVV GPΔmuc vaccine groups at week 17 against MARV Angola pseudovirus. Summary of IC_{50} values. Left panel: sera from three naive mice showed nonspecific background in MARV Angola pseudovirus assays, suggesting that IgG purification is required to eliminate the nonspecific serum reactivity. (**u**) Neutralization curves of mouse sera from RAVV GPΔmuc vaccine groups at week 17 against orthoebolavirus strains. Error bars represent the difference between duplicate measurements at each concentration for each sample. EC_{50}, ID_{50}, and IC_{50} values were calculated using GraphPad Prism version 10.3.1. Data were analyzed using one-way ANOVA, followed by Tukey's multiple comparison post hoc test for each timepoint. For significance, ns (not significant), *$p < 0.05$, **$p < 0.01$, ***$p < 0.001$, and ****$p < 0.0001$.

Figure S11

a **Sera of individual mice immunized with glycan-modified EBOV vaccines binding to EBOV GPΔmuc-WL^{2}P^4(1TD0) trimer**

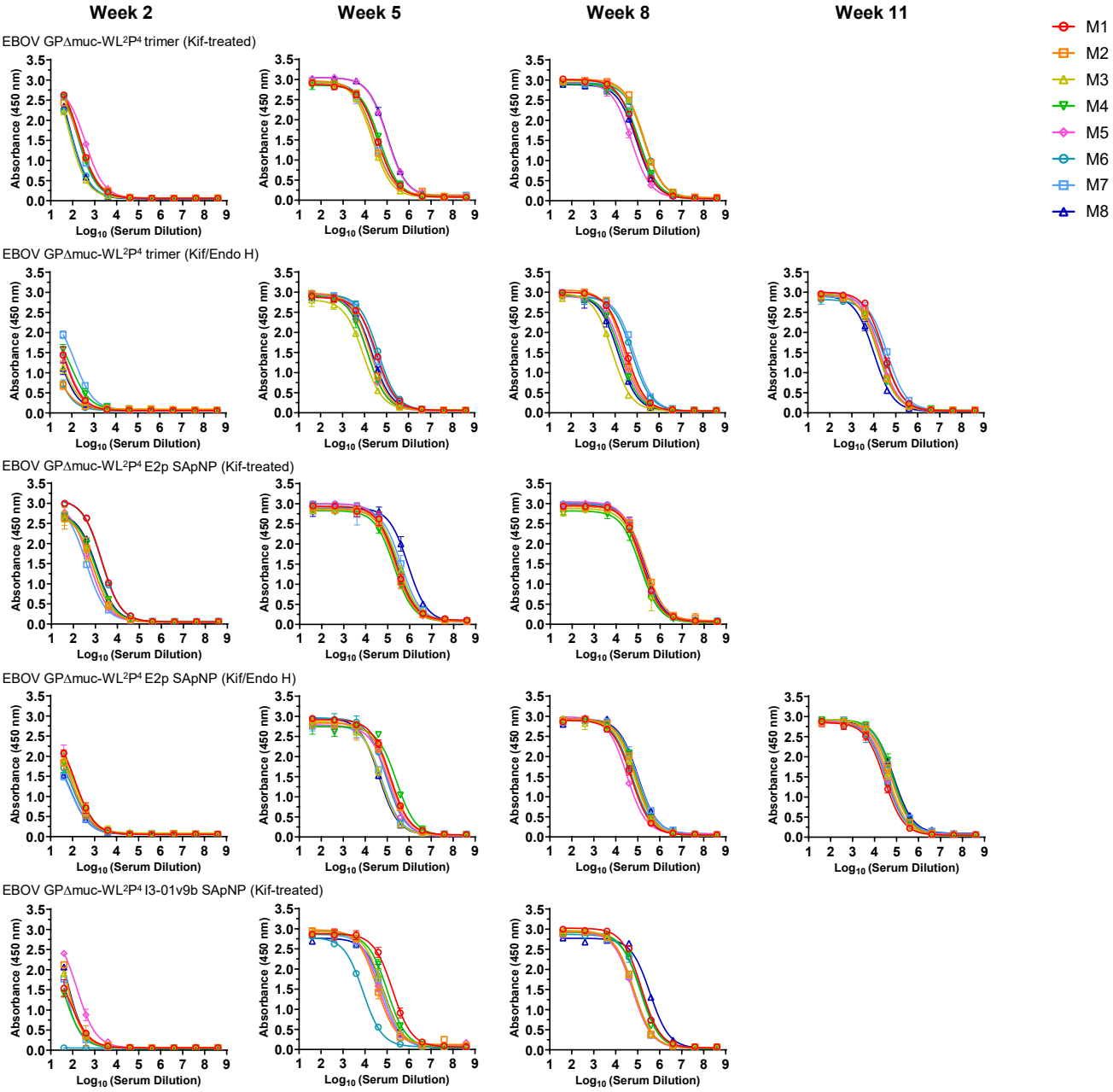

b Mouse serum ELISA EC_{50} titers

Week 2

Antigen	EC_{50} titers (week 2)								Geometric Mean
	M1	M2	M3	M4	M5	M6	M7	M8	
EBOV GPΔmuc-WL^{2}P^4 trimer-Wild-type	111.7	136.3	51.3	227.2	103.0	200.2	12.6	173.3	97.3
EBOV GPΔmuc-WL^{2}P^4 trimer-Kif-treated	283.7	255.1	119.5	248.0	423.8	133.4	239.1	141.3	212.1
EBOV GPΔmuc-WL^{2}P^4 trimer-Kif/Endo H	43.1	13.4	28.4	56.2	46.5	14.1	106.9	26.8	33.8
EBOV GPΔmuc-WL^{2}P^4 E2p SApNP-Wild-type	985.3	706.4	970.8	1772.0	271.5	336.1	3145.0	486.4	799.6
EBOV GPΔmuc-WL^{2}P^4 E2p SApNP-Kif-treated	2721.0	813.3	815.7	1046.0	678.3	2584.0	482.5	1166.0	1080.8
EBOV GPΔmuc-WL^{2}P^4 E2p SApNP-Kif/Endo H	126.0	84.5	104.9	95.8	122.8	69.1	50.0	51.4	83.4
EBOV GPΔmuc-WL^{2}P^4 I3-01v9b SApNP-Wild-type	30.1	101.8	43.0	37.9	172.4	80.7	91.5	115.6	72.1
EBOV GPΔmuc-WL^{2}P^4 I3-01v9b SApNP-Kif-treated	51.8	97.6	80.2	41.8	201.5	0.9	62.9	95.3	45.5

Week 5

Antigen	EC_{50} titers (week 5)								Geometric Mean
	M1	M2	M3	M4	M5	M6	M7	M8	
EBOV GPΔmuc-WL^{2}P^4 trimer-Wild-type	52545	41735	104914	48787	27947	18271	26144	21434	36588
EBOV GPΔmuc-WL^{2}P^4 trimer-Kif-treated	38706	25086	21695	47634	99875	36855	27014	103907	42360
EBOV GPΔmuc-WL^{2}P^4 trimer-Kif/Endo H	35186	18238	8909	13634	13630	41752	29227	22113	20285
EBOV GPΔmuc-WL^{2}P^4 E2p SApNP-Wild-type	199849	120954	303168	237335	74446	156667	282413	368341	195227
EBOV GPΔmuc-WL^{2}P^4 E2p SApNP-Kif-treated	241215	224657	335618	192147	216173	258075	406613	838779	300502
EBOV GPΔmuc-WL^{2}P^4 E2p SApNP-Kif/Endo H	141920	136153	48617	265817	117352	88543	56725	42434	94286
EBOV GPΔmuc-WL^{2}P^4 I3-01v9b SApNP-Wild-type	58458	93275	140476	104463	128829	148277	70114	63709	95342
EBOV GPΔmuc-WL^{2}P^4 I3-01v9b SApNP-Kif-treated	180905	34224	63566	102618	42941	8255	57374	74974	52927

Week 11 or 8

Antigen	EC_{50} titers (week 11 or 8)								Geometric Mean
	M1	M2	M3	M4	M5	M6	M7	M8	
EBOV GPΔmuc-WL^{2}P^4 trimer-Wild-type (w11)	26545	524033	69054	94400	39464	69865	68351	51944	73881
EBOV GPΔmuc-WL^{2}P^4 trimer-Kif-treated (w8)	93214	195305	183599	116631	50918	193472	114590	89398	118674
EBOV GPΔmuc-WL^{2}P^4 trimer-Kif/Endo H (w8)	31571	25030	7454	16954	21834	59045	72580	13927	24508
EBOV GPΔmuc-WL^{2}P^4 E2p SApNP-Wild-type (w11)	267135	163352	223491	606328	32762	143908	182928	233182	181722
EBOV GPΔmuc-WL^{2}P^4 E2p SApNP-Kif-treated (w8)	153387	211525	149619	126857	158759	131151	152440	176520	155680
EBOV GPΔmuc-WL^{2}P^4 E2p SApNP-Kif/Endo H (w8)	50455	81205	73372	89472	32112	55202	99817	102711	68571
EBOV GPΔmuc-WL^{2}P^4 I3-01v9b SApNP-Wild-type (w11)	703967	60730	178784	354031	97482	91294	82827	610293	182253
EBOV GPΔmuc-WL^{2}P^4 I3-01v9b SApNP-Kif-treated (w8)	146649	66233	62594	129059	58475	142777	61089	366113	104890

Statistical analysis

One-way ANOVA with Tukey's multiple comparisons test (w2)	Statistics	Adjusted P Value
EBOV GPΔmuc-WL^{2}P^4 trimer-Wild-type vs. EBOV GPΔmuc-WL^{2}P^4 trimer-Kif-treated	*	0.0276
EBOV GPΔmuc-WL^{2}P^4 trimer-Wild-type vs. EBOV GPΔmuc-WL^{2}P^4 trimer-Kif/Endo H	ns	0.0775
EBOV GPΔmuc-WL^{2}P^4 trimer-Kif-treated vs. EBOV GPΔmuc-WL^{2}P^4 trimer-Kif/Endo H	***	0.0001

One-way ANOVA with Tukey's multiple comparisons test (w5)	Statistics	Adjusted P Value
EBOV GPΔmuc-WL^{2}P^4 trimer-Wild-type vs. EBOV GPΔmuc-WL^{2}P^4 trimer-Kif-treated	ns	0.8381
EBOV GPΔmuc-WL^{2}P^4 trimer-Wild-type vs. EBOV GPΔmuc-WL^{2}P^4 trimer-Kif/Endo H	ns	0.2962
EBOV GPΔmuc-WL^{2}P^4 trimer-Kif-treated vs. EBOV GPΔmuc-WL^{2}P^4 trimer-Kif/Endo H	ns	0.1137

One-way ANOVA with Tukey's multiple comparisons test (w2)	Statistics	Adjusted P Value
EBOV GPΔmuc-WL^{2}P^4 E2p SApNP-Wild-type vs. EBOV GPΔmuc-WL^{2}P^4 E2p SApNP-Kif-treated	ns	0.8496
EBOV GPΔmuc-WL^{2}P^4 E2p SApNP-Wild-type vs. EBOV GPΔmuc-WL^{2}P^4 E2p SApNP-Kif/Endo H	*	0.0371
EBOV GPΔmuc-WL^{2}P^4 E2p SApNP-Kif-treated vs. EBOV GPΔmuc-WL^{2}P^4 E2p SApNP-Kif/Endo H	*	0.0112

One-way ANOVA with Tukey's multiple comparisons test (w5)	Statistics	Adjusted P Value
EBOV GPΔmuc-WL^{2}P^4 E2p SApNP-Wild-type vs. EBOV GPΔmuc-WL^{2}P^4 E2p SApNP-Kif-treated	ns	0.2278
EBOV GPΔmuc-WL^{2}P^4 E2p SApNP-Wild-type vs. EBOV GPΔmuc-WL^{2}P^4 E2p SApNP-Kif/Endo H	ns	0.3186
EBOV GPΔmuc-WL^{2}P^4 E2p SApNP-Kif-treated vs. EBOV GPΔmuc-WL^{2}P^4 E2p SApNP-Kif/Endo H	*	0.0119

Unpaired t test (w2)	Statistics	P Value
EBOV GPΔmuc-WL^{2}P^4 I3-01v9b SApNP-Wild-type vs. EBOV GPΔmuc-WL^{2}P^4 I3-01v9b SApNP-Kif-treated	ns	0.8507

Unpaired t test (w5)	Statistics	P Value
EBOV GPΔmuc-WL^{2}P^4 I3-01v9b SApNP-Wild-type vs. EBOV GPΔmuc-WL^{2}P^4 I3-01v9b SApNP-Kif-treated	ns	0.1978

Figure S11

c Sera of individual mice immunized with EBOV vaccines neutralizing an EBOV Makona strain

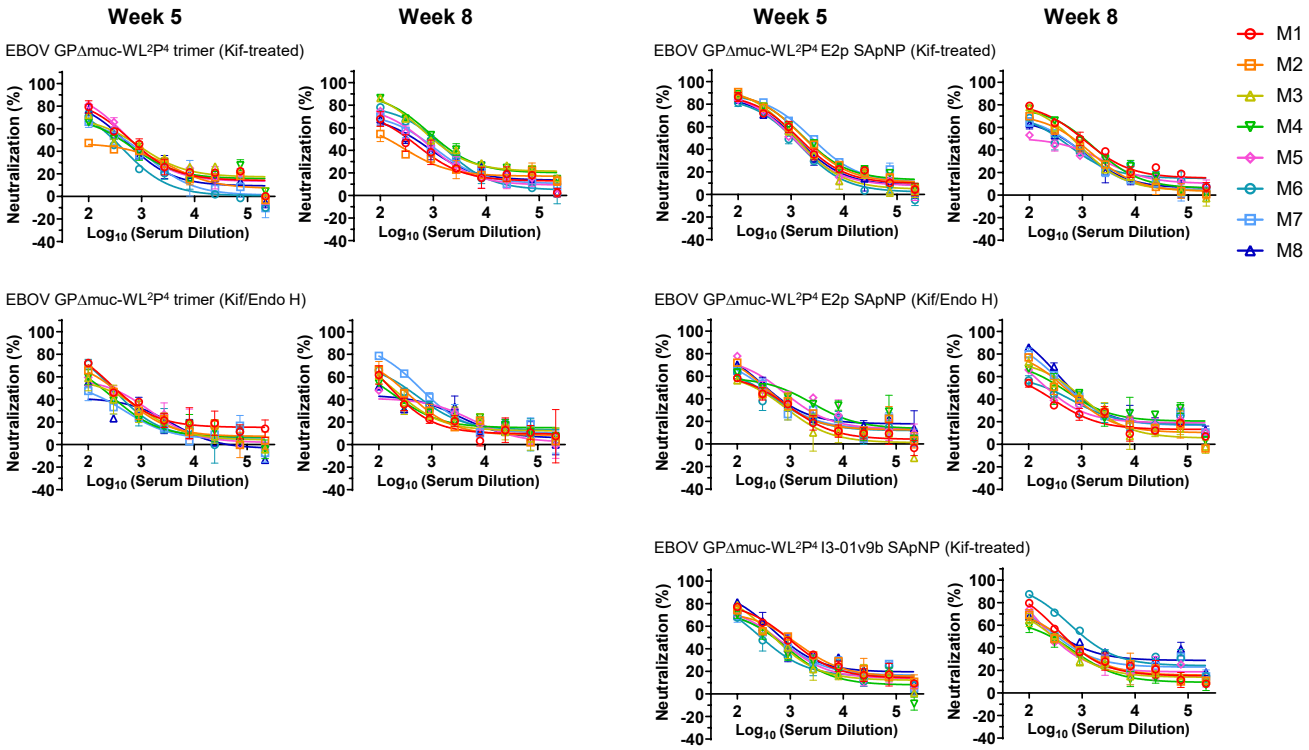

d Mouse serum neutralizing ID_{50} titers

Week 5

Antigen	ID_{50} titers (week 5)								Geometric Mean
	M1	M2	M3	M4	M5	M6	M7	M8	
EBOV GPΔmuc-WL^{2}P^4 trimer-Wild-type	805.4	559.3	149.3	588.2	174.1	145.1	203.2	360.5	304.1
EBOV GPΔmuc-WL^{2}P^4 trimer-Kif-treated	685.5	234.7	577.4	443.0	708.5	285.4	407.7	489.1	449.3
EBOV GPΔmuc-WL^{2}P^4 trimer-Kif/Endo H	383.7	299.7	227.6	199.9	271.6	298.0	132.4	145.5	231.2
EBOV GPΔmuc-WL^{2}P^4 E2p SApNP-Wild-type	636.9	358.8	2178.0	1002.0	555.2	322.9	299.4	1167.0	648.4
EBOV GPΔmuc-WL^{2}P^4 E2p SApNP-Kif-treated	1414.0	1867.0	1249.0	1961.0	1107.0	963.3	2480.0	1201.0	1459.0
EBOV GPΔmuc-WL^{2}P^4 E2p SApNP-Kif/Endo H	263.2	376.3	232.9	513.0	559.4	273.6	353.0	430.4	358.9
EBOV GPΔmuc-WL^{2}P^4 I3-01v9b SApNP-Wild-type	881.2	850.8	555.5	452.4	550.2	340.8	548.8	865.0	599.9
EBOV GPΔmuc-WL^{2}P^4 I3-01v9b SApNP-Kif-treated	267.9	390.2	313.1	575.8	378.9	413.4	258.7	296.7	350.3

Week 11 or 8

Antigen	ID_{50} titers (week 11 or 8)								Geometric Mean
	M1	M2	M3	M4	M5	M6	M7	M8	
EBOV GPΔmuc-WL^{2}P^4 trimer-Wild-type (w11)	2117.0	560.6	254.4	521.5	188.7	430.2	369.3	377.3	453.2
EBOV GPΔmuc-WL^{2}P^4 trimer-Kif-treated (w8)	370.3	204.5	1305	1425	578	911.8	569.1	448.8	609.1
EBOV GPΔmuc-WL^{2}P^4 trimer-Kif/Endo H (w8)	192.8	287.4	217.4	178.6	171.6	351.1	636.2	175.4	248.3
EBOV GPΔmuc-WL^{2}P^4 E2p SApNP-Wild-type (w11)	494.5	392.0	734.2	747.4	275.3	643.8	365.2	759.9	518.6
EBOV GPΔmuc-WL^{2}P^4 E2p SApNP-Kif-treated (w8)	1031	562.3	594.7	902.2	273	393.9	416.3	408.9	524.1
EBOV GPΔmuc-WL^{2}P^4 E2p SApNP-Kif/Endo H (w8)	179.2	499.6	538.7	486.6	301.2	292.4	649.2	772.1	423.6
EBOV GPΔmuc-WL^{2}P^4 I3-01v9b SApNP-Wild-type (w11)	1006.0	434.9	454.1	766.3	289.4	237.7	327.0	928.5	487.3
EBOV GPΔmuc-WL^{2}P^4 I3-01v9b SApNP-Kif-treated (w8)	562.9	429.3	326.9	281.2	376.1	1462	459.4	603.8	491.2

Statistical analysis

One-way ANOVA with Tukey's multiple comparisons test (w5)	Statistics	Adjusted P Value
EBOV GPΔmuc-WL^{2}P^4 trimer-Wild-type vs. EBOV GPΔmuc-WL^{2}P^4 trimer-Kif-treated	ns	0.489
EBOV GPΔmuc-WL^{2}P^4 trimer-Wild-type vs. EBOV GPΔmuc-WL^{2}P^4 trimer-Kif/Endo H	ns	0.3549
EBOV GPΔmuc-WL^{2}P^4 trimer-Kif-treated vs. EBOV GPΔmuc-WL^{2}P^4 trimer-Kif/Endo H	*	0.0453

One-way ANOVA with Tukey's multiple comparisons test (w5)	Statistics	Adjusted P Value
EBOV GPΔmuc-WL^{2}P^4 E2p SApNP-Wild-type vs. EBOV GPΔmuc-WL^{2}P^4 E2p SApNPr-Kif-treated	*	0.02
EBOV GPΔmuc-WL^{2}P^4 E2p SApNP-Wild-type vs. EBOV GPΔmuc-WL^{2}P^4 E2p SApNP-Kif/Endo H	ns	0.1792
EBOV GPΔmuc-WL^{2}P^4 E2p SApNPr-Kif-treated vs. EBOV GPΔmuc-WL^{2}P^4 E2p SApNP-Kif/Endo H	***	0.0003

Unpaired t test (w5)	Statistics	P Value
EBOV GPΔmuc-WL^{2}P^4 I3-01v9b SApNP-Wild-type vs. EBOV GPΔmuc-WL^{2}P^4 I3-01v9b SApNP-Kif-treated	**	0.0055

Figure S11

e Sera of individual mice immunized with wild-type/glycan-modified SUDV vaccines binding to SUDV GPΔmuc-WL^{2}P^4(1TD0) trimer

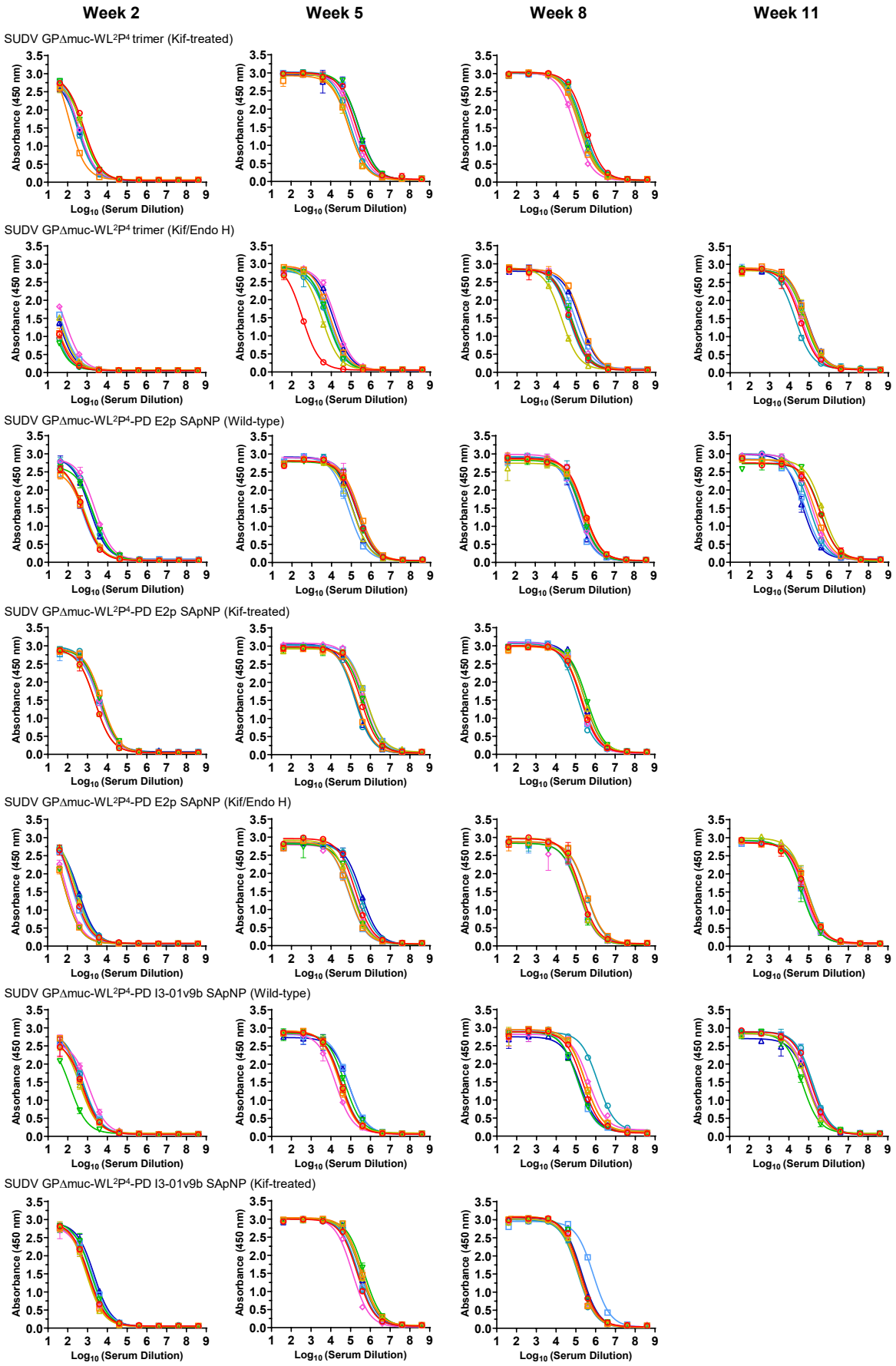

Figure S11

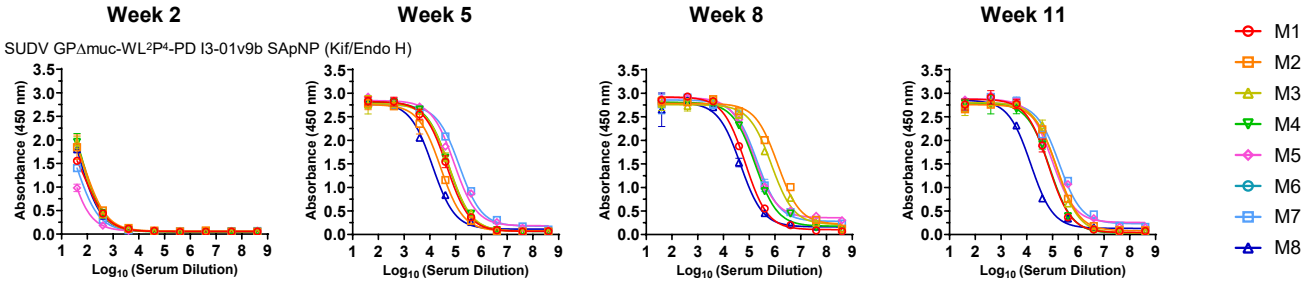

f Mouse serum ELISA EC_{50} titers

Week 2

Antigen	EC_{50} titers (week 2)								Geometric Mean
	M1	M2	M3	M4	M5	M6	M7	M8	
SUDV GPΔmuc-WL^{2}P^4 trimer-Wild-type	69.8	20.2	50.0	149.7	116.9	122.4	68.1	55.0	69.8
SUDV GPΔmuc-WL^{2}P^4 trimer-Kif-treated	714.8	192.9	605.3	591.0	412.8	343.0	419.8	362.8	425.0
SUDV GPΔmuc-WL^{2}P^4 trimer-Kif/Endo H	23.3	24.5	44.7	15.7	72.2	19.6	50.5	36.9	31.8
SUDV GPΔmuc-WL^{2}P^4-PD E2p SApNP-Wild-type	527.1	474.8	583.8	1483.0	2336.0	1545.0	475.4	1316.0	914.5
SUDV GPΔmuc-WL^{2}P^4-PD E2p SApNP-Kif-treated	2482.0	5568.0	2483.0	4798.0	4273.0	4408.0	3878.0	4312.0	3884.6
SUDV GPΔmuc-WL^{2}P^4-PD E2p SApNP-Kif/Endo H	271.0	99.3	330.9	99.8	124.0	375.7	234.7	410.6	211.4
SUDV GPΔmuc-WL^{2}P^4-PD I3-01v9b SApNP-Wild-type	469.6	479.9	387.3	115.2	890.0	616.4	586.8	503.1	448.2
SUDV GPΔmuc-WL^{2}P^4-PD I3-01v9b SApNP-Kif-treated	1206.0	1067.0	961.1	1644.0	1098.0	1237.0	1839.0	2248.0	1355.8
SUDV GPΔmuc-WL^{2}P^4-PD I3-01v9b SApNP-Kif/Endo H	49.8	73.8	77.8	80.5	20.8	N/A	38.4	65.2	53.1

Week 5

Antigen	EC_{50} titers (week 5)								Geometric Mean
	M1	M2	M3	M4	M5	M6	M7	M8	
SUDV GPΔmuc-WL^{2}P^4 trimer-Wild-type	16436	19941	7907	60277	25656	19754	9992	15619	18259.2
SUDV GPΔmuc-WL^{2}P^4 trimer-Kif-treated	187796	83838	82374	256237	143796	100245	199748	272537	150326.2
SUDV GPΔmuc-WL^{2}P^4 trimer-Kif/Endo H	337	8926	3406	6542	16601	6364	8124	13307	5439.3
SUDV GPΔmuc-WL^{2}P^4-PD E2p SApNP-Wild-type	194403	254967	120302	189915	195340	209194	72385	116111	158028.4
SUDV GPΔmuc-WL^{2}P^4-PD E2p SApNP-Kif-treated	328808	203797	637646	429942	440079	160965	596309	178438	329358.5
SUDV GPΔmuc-WL^{2}P^4-PD E2p SApNP-Kif/Endo H	174902	82685	108551	129398	143808	261848	79238	345641	146267.1
SUDV GPΔmuc-WL^{2}P^4-PD I3-01v9b SApNP-Wild-type	32933	27405	30608	50359	17406	34313	79188	83439	39124.1
SUDV GPΔmuc-WL^{2}P^4-PD I3-01v9b SApNP-Kif-treated	213630	375263	331165	484567	123702	233165	246351	324809	271692.3
SUDV GPΔmuc-WL^{2}P^4-PD I3-01v9b SApNP-Kif/Endo H	45679	26310	57270	55138	87196	N/A	138210	12630	47889.1

Week 11 or 8

Antigen	EC_{50} titers (week 11 or 8)								Geometric Mean
	M1	M2	M3	M4	M5	M6	M7	M8	
SUDV GPΔmuc-WL^{2}P^4 trimer-Wild-type (w11)	51852	34819	59219	58035	92570	20182	108658	56856	53935.6
SUDV GPΔmuc-WL^{2}P^4 trimer-Kif-treated (w8)	302797	144377	177306	198140	88084	235081	164275	185242	177101.1
SUDV GPΔmuc-WL^{2}P^4 trimer-Kif/Endo H (w8)	50453	172980	18107	59100	58943	44125	87452	156514	65346.1
SUDV GPΔmuc-WL^{2}P^4-PD E2p SApNP-Wild-type (w8)	299781	269350	317854	207812	165230	208403	120522	131427	203221.8
SUDV GPΔmuc-WL^{2}P^4-PD E2p SApNP-Kif-treated (w8)	192720	218683	292392	372944	179861	130425	179178	274004	219008.7
SUDV GPΔmuc-WL^{2}P^4-PD E2p SApNP-Kif/Endo H (w8)	180099	336638	152272	156367	145160	325977	149103	N/A	193576.0
SUDV GPΔmuc-WL^{2}P^4-PD I3-01v9b SApNP-Wild-type (w8)	219021	293708	296644	131589	450528	1270551	122274	162786	270436.4
SUDV GPΔmuc-WL^{2}P^4-PD I3-01v9b SApNP-Kif-treated (w8)	166508	138485	135652	171299	143035	129149	754862	196507	186573.4
SUDV GPΔmuc-WL^{2}P^4-PD I3-01v9b SApNP-Kif/Endo H (w8)	71039	1261224	728092	170130	156138	N/A	198137	45999	206095.4

Statistical analysis

One-way ANOVA with Tukey's multiple comparisons test (w2)	Statistics	Adjusted P Value
SUDV GPΔmuc-WL^{2}P^4 trimer-Wild-type vs. SUDV GPΔmuc-WL^{2}P^4 trimer-Kif-treated	****	<0.0001
SUDV GPΔmuc-WL^{2}P^4 trimer-Wild-type vs. SUDV GPΔmuc-WL^{2}P^4 trimer-Kif/Endo H	ns	0.6485
SUDV GPΔmuc-WL^{2}P^4 trimerKif-treated vs. SUDV GPΔmuc-WL^{2}P^4 trimer-Kif/Endo H	****	<0.0001

One-way ANOVA with Tukey's multiple comparisons test (w5)	Statistics	Adjusted P Value
SUDV GPΔmuc-WL^{2}P^4 trimer-Wild-type vs. SUDV GPΔmuc-WL^{2}P^4 trimer-Kif-treated	****	<0.0001
SUDV GPΔmuc-WL^{2}P^4 trimer-Wild-type vs. SUDV GPΔmuc-WL^{2}P^4 trimer-Kif/Endo H	ns	0.8066
SUDV GPΔmuc-WL^{2}P^4 trimerKif-treated vs. SUDV GPΔmuc-WL^{2}P^4 trimer-Kif/Endo H	****	<0.0001

One-way ANOVA with Tukey's multiple comparisons test (w2)	Statistics	Adjusted P Value
SUDV GPΔmuc-WL^{2}P^4-PD E2p SApNP-Wild-type vs. SUDV GPΔmuc-WL^{2}P^4-PD E2p SApNP-Kif-treated	****	<0.0001
SUDV GPΔmuc-WL^{2}P^4-PD E2p SApNP-Wild-type vs. SUDV GPΔmuc-WL^{2}P^4-PD E2p SApNP-Kif/Endo H	ns	0.0778
SUDV GPΔmuc-WL^{2}P^4-PD E2p SApNP-Kif-treated vs. SUDV GPΔmuc-WL^{2}P^4-PD E2p SApNP-Kif/Endo H	****	<0.0001

One-way ANOVA with Tukey's multiple comparisons test (w5)	Statistics	Adjusted P Value
SUDV GPΔmuc-WL^{2}P^4-PD E2p SApNP-Wild-type vs. SUDV GPΔmuc-WL^{2}P^4-PD E2p SApNP-Kif-treated	*	0.0103
SUDV GPΔmuc-WL^{2}P^4-PD E2p SApNP-Wild-type vs. SUDV GPΔmuc-WL^{2}P^4-PD E2p SApNP-Kif/Endo H	ns	0.9984
SUDV GPΔmuc-WL^{2}P^4-PD E2p SApNP-Kif-treated vs. SUDV GPΔmuc-WL^{2}P^4-PD E2p SApNP-Kif/Endo H	**	0.0091

One-way ANOVA with Tukey's multiple comparisons test (w2)	Statistics	Adjusted P Value
SUDV GPΔmuc-WL^{2}P^4-PD I3-01v9b SApNP-Wild-type vs. SUDV GPΔmuc-WL^{2}P^4-PD I3-01v9b SApNP-Kif-treated	****	<0.0001
SUDV GPΔmuc-WL^{2}P^4-PD I3-01v9b SApNP-Wild-type vs. SUDV GPΔmuc-WL^{2}P^4-PD I3-01v9b SApNP-Kif/Endo H	*	0.0224
SUDV GPΔmuc-WL^{2}P^4-PD I3-01v9b SApNP-Kif-treated vs. SUDV GPΔmuc-WL^{2}P^4-PD I3-01v9b SApNP-Kif/Endo H	****	<0.0001

One-way ANOVA with Tukey's multiple comparisons test (w5)	Statistics	Adjusted P Value
SUDV GPΔmuc-WL^{2}P^4-PD I3-01v9b SApNP-Wild-type vs. SUDV GPΔmuc-WL^{2}P^4-PD I3-01v9b SApNP-Kif-treated	****	<0.0001
SUDV GPΔmuc-WL^{2}P^4-PD I3-01v9b SApNP-Wild-type vs. SUDV GPΔmuc-WL^{2}P^4-PD I3-01v9b SApNP-Kif/Endo H	ns	0.903
SUDV GPΔmuc-WL^{2}P^4-PD I3-01v9b SApNP-Kif-treated vs. SUDV GPΔmuc-WL^{2}P^4-PD I3-01v9b SApNP-Kif/Endo H	****	<0.0001

Figure S11

g Sera of individual mice immunized with wild-type/glycan-modified SUDV vaccines neutralizing a SUDV Gulu strain

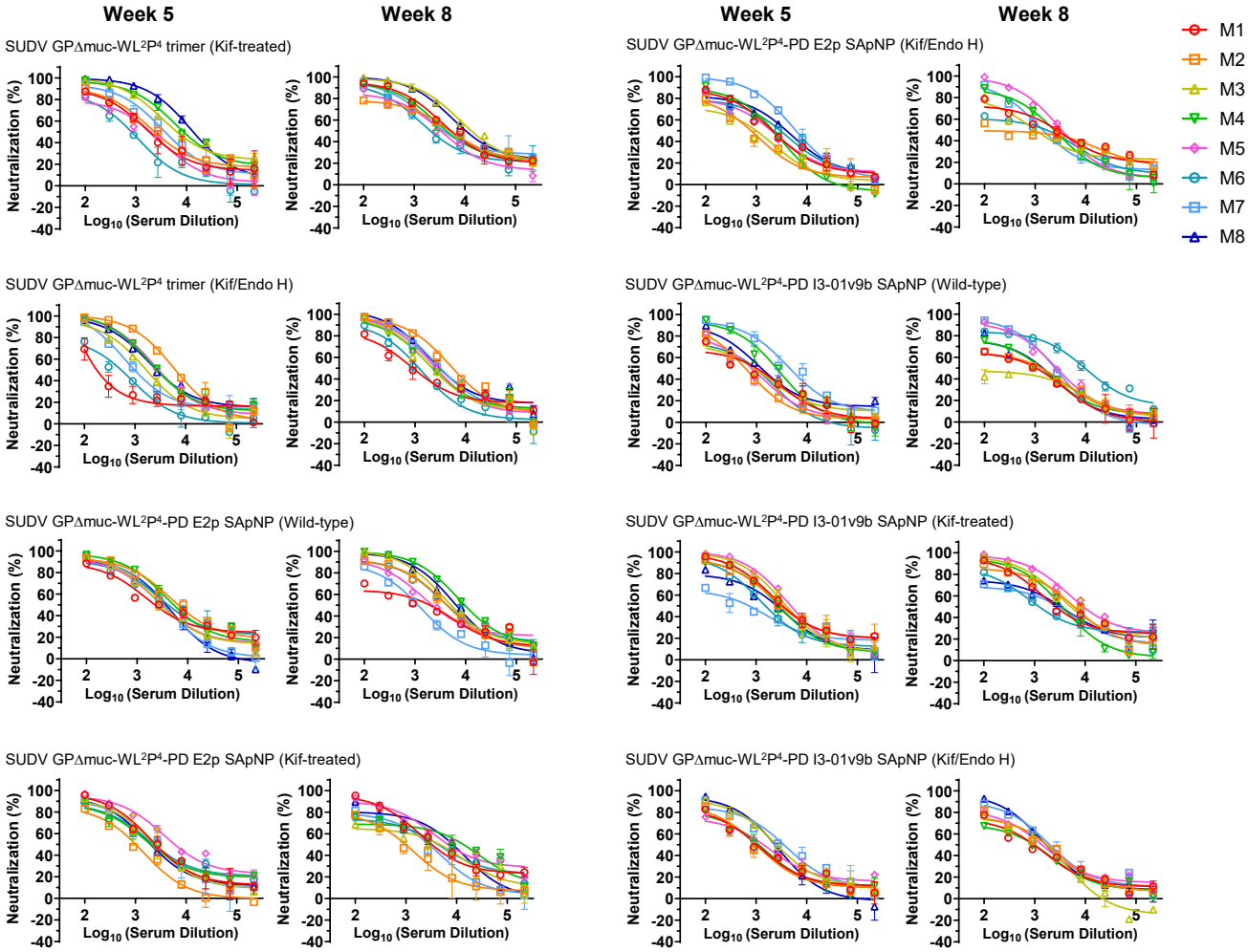

h Mouse serum neutralizing ID_{50} titers

Week 5

Antigen	ID_{50} titers (week 5)								Geometric Mean
	M1	M2	M3	M4	M5	M6	M7	M8	
SUDV GPΔmuc-WL^{2}P^4 trimer-Wild-type	420	3076	156.6	2417	1377	1896	5149	1477	1328.6
SUDV GPΔmuc-WL^{2}P^4 trimer-Kif-treated	1986	2709	8760	10520	1522	736.6	4016	14183	3652.3
SUDV GPΔmuc-WL^{2}P^4 trimer-Kif/Endo H	243.4	6460	1691	3127	3197.0	463.3	1201.0	3265.0	1623.6
SUDV GPΔmuc-WL^{2}P^4-PD E2p SApNP-Wild-type	3142	7835	3520	6205	3431	5382	3249	3187	4231.6
SUDV GPΔmuc-WL^{2}P^4-PD E2p SApNP-Kif-treated	2877	873.4	2512	2311	7871	2706	2473	2186	2530.2
SUDV GPΔmuc-WL^{2}P^4-PD E2p SApNP-Kif/Endo H	2075	721.3	713.9	1791	1742	2481	6384	3462	1917.5
SUDV GPΔmuc-WL^{2}P^4-PD I3-01v9b SApNP-Wild-type	662.4	592.3	758.7	2268	682.9	642.8	4778	1402	1089.5
SUDV GPΔmuc-WL^{2}P^4-PD I3-01v9b SApNP-Kif-treated	4252	3819	4262	2863	5193	1734	651.4	2141	2657.6
SUDV GPΔmuc-WL^{2}P^4-PD I3-01v9b SApNP-Kif/Endo H	1023	1000	2652	1043	1287	N/A	3262	2177	1591.5

Week 11 or 8

Antigen	ID_{50} titers (week 11 or 8)								Geometric Mean
	M1	M2	M3	M4	M5	M6	M7	M8	
SUDV GPΔmuc-WL^{2}P^4 trimer-Wild-type (w11)	13810	4694	2805	3670	2858	2497	14410	3069	4628.4
SUDV GPΔmuc-WL^{2}P^4 trimer-Kif-treated (w8)	6582	5258	16937	5674	3316	2649	5681	13235	6204.7
SUDV GPΔmuc-WL^{2}P^4 trimer-Kif/Endo H (w8)	1035	6006	2560	2543	2847	1139	3639	3835	2557.7
SUDV GPΔmuc-WL^{2}P^4-PD E2p SApNP-Wild-type (w8)	1224	4430	6202	11133	2887	4953	1083	6855	3757.6
SUDV GPΔmuc-WL^{2}P^4-PD E2p SApNP-Kif-treated (w8)	4414	880.9	2466	7047	10493	4060	2235	6092	3751.0
SUDV GPΔmuc-WL^{2}P^4-PD E2p SApNP-Kif/Endo H (w8)	2234	555.2	1224	2211	3512	1040	1615	N/A	1531.9
SUDV GPΔmuc-WL^{2}P^4-PD I3-01v9b SApNP-Wild-type (w8)	739.1	911.5	343.7	1130	2675	9196	2305	1040	1407.8
SUDV GPΔmuc-WL^{2}P^4-PD I3-01v9b SApNP-Kif-treated (w8)	3830	5923	6805	3469	12386	1653	2090	3103	4041.0
SUDV GPΔmuc-WL^{2}P^4-PD I3-01v9b SApNP-Kif/Endo H (w8)	810.8	1367	1095	777.2	1388	N/A	2057	1791	1252.0

Statistical analysis

One-way ANOVA with Tukey's multiple comparisons test (w5)	Statistics	Adjusted P Value
SUDV GPΔmuc-WL^{2}P^4 trimer-Wild-type vs. SUDV GPΔmuc-WL^{2}P^4 trimer-Kif-treated	ns	0.0934
SUDV GPΔmuc-WL^{2}P^4 trimer-Wild-type vs. SUDV GPΔmuc-WL^{2}P^4 trimer-Kif/Endo H	ns	0.9563
SUDV GPΔmuc-WL^{2}P^4 trimerKif-treated vs. SUDV GPΔmuc-WL^{2}P^4 trimer-Kif/Endo H	ns	0.1577

One-way ANOVA with Tukey's multiple comparisons test (w5)	Statistics	Adjusted P Value
SUDV GPΔmuc-WL^{2}P^4-PD E2p SApNP-Wild-type vs. SUDV GPΔmuc-WL^{2}P^4-PD E2p SApNP-Kif-treated	ns	0.2678
SUDV GPΔmuc-WL^{2}P^4-PD E2p SApNP-Wild-type vs. SUDV GPΔmuc-WL^{2}P^4-PD E2p SApNP-Kif/Endo H	ns	0.0973
SUDV GPΔmuc-WL^{2}P^4-PD E2p SApNP-Kif-treated vs. SUDV GPΔmuc-WL^{2}P^4-PD E2p SApNP-Kif/Endo H	ns	0.8296

One-way ANOVA with Tukey's multiple comparisons test (w8)	Statistics	Adjusted P Value
SUDV GPΔmuc-WL^{2}P^4-PD E2p SApNP-Wild-type vs. SUDV GPΔmuc-WL^{2}P^4-PD E2p SApNP-Kif-treated	ns	0.9947
SUDV GPΔmuc-WL^{2}P^4-PD E2p SApNP-Wild-type vs. SUDV GPΔmuc-WL^{2}P^4-PD E2p SApNP-Kif/Endo H	ns	0.1006
SUDV GPΔmuc-WL^{2}P^4-PD E2p SApNP-Kif-treated vs. SUDV GPΔmuc-WL^{2}P^4-PD E2p SApNP-Kif/Endo H	ns	0.1201

One-way ANOVA with Tukey's multiple comparisons test (w5)	Statistics	Adjusted P Value
SUDV GPΔmuc-WL^{2}P^4-PD I3-01v9b SApNP-Wild-type vs. SUDV GPΔmuc-WL^{2}P^4-PD I3-01v9b SApNP-Kif-treated	ns	0.0604
SUDV GPΔmuc-WL^{2}P^4-PD I3-01v9b SApNP-Wild-type vs. SUDV GPΔmuc-WL^{2}P^4-PD I3-01v9b SApNP-Kif/Endo H	ns	0.9009
SUDV GPΔmuc-WL^{2}P^4-PD I3-01v9b SApNP-Kif-treated vs. SUDV GPΔmuc-WL^{2}P^4-PD I3-01v9b SApNP-Kif/Endo H	ns	0.1599

One-way ANOVA with Tukey's multiple comparisons test (w8)	Statistics	Adjusted P Value
SUDV GPΔmuc-WL^{2}P^4-PD I3-01v9b SApNP-Wild-type vs. SUDV GPΔmuc-WL^{2}P^4-PD I3-01v9b SApNP-Kif-treated	ns	0.1544
SUDV GPΔmuc-WL^{2}P^4-PD I3-01v9b SApNP-Wild-type vs. SUDV GPΔmuc-WL^{2}P^4-PD I3-01v9b SApNP-Kif/Endo H	ns	0.7712
SUDV GPΔmuc-WL^{2}P^4-PD I3-01v9b SApNP-Kif-treated vs. SUDV GPΔmuc-WL^{2}P^4-PD I3-01v9b SApNP-Kif/Endo H	*	0.0468

Figure S11

i Sera of individual mice immunized with glycan-modified RAVV GPΔmuc-P²CT(1TD0) trimer

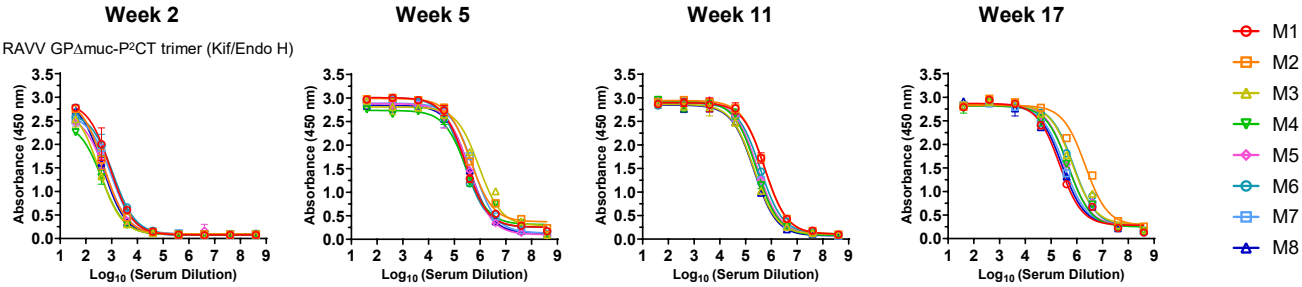

j Mouse serum ELISA EC_{50} titers

Week 2

Antigen	EC_{50} titers (week 2)								Geometric Mean
	M1	M2	M3	M4	M5	M6	M7	M8	
RAVV GPΔmuc-P²CT trimer-Wild-type	718.9	721.9	432.3	1030.0	946.3	262.3	481.5	958.5	635.1
RAVV GPΔmuc-P²CT trimer-Kif/Endo H	1088.0	842.6	372.8	326.6	773.6	1455.0	1260.0	571.6	740.6

Week 5

Antigen	EC_{50} titers (week 5)								Geometric Mean
	M1	M2	M3	M4	M5	M6	M7	M8	
RAVV GPΔmuc-P²CT trimer-Wild-type	202735	1544554	746406	628189	447117	44771	446178	225949	362215.2
RAVV GPΔmuc-P²CT trimer-Kif/Endo H	208318	261241	222068	150370	267446	198233	450054	211636	234603.9

Week 11 or 8

Antigen	EC_{50} titers (week 11 or 8)								Geometric Mean
	M1	M2	M3	M4	M5	M6	M7	M8	
RAVV GPΔmuc-P²CT trimer-Wild-type (w11)	139135	218951	208199	104125	998580	786127	408247	853062	340466.6
RAVV GPΔmuc-P²CT trimer-Kif/Endo H (w8)	770620	683058	388118	292655	294767	621323	524297	273292	446120.6

Week 17 or 11

Antigen	EC_{50} titers (week 17 or 11)								Geometric Mean
	M1	M2	M3	M4	M5	M6	M7	M8	
RAVV GPΔmuc-P²CT trimer-Wild-type (w17)	140811	110900	164905	119990	336478	344895	127509	141835	168457
RAVV GPΔmuc-P²CT trimer-Kif/Endo H (w11)	125144	295308	212027	173036	313400	398840	295603	237268	242316

Statistical analysis

Unpaired t test (w2)	Statistics	P Value
RAVV GPΔmuc-P²CT trimer-Wild-type vs. RAVV GPΔmuc-P²CT trimer-Kif/Endo H	ns	0.4307

Unpaired t test (w5)	Statistics	P Value
RAVV GPΔmuc-P²CT trimer-Wild-type vs. RAVV GPΔmuc-P²CT trimer-Kif/Endo H	ns	0.1079

k Purified IgG of individual mice immunized with RAVV vaccines neutralizing a MARV Angola strain

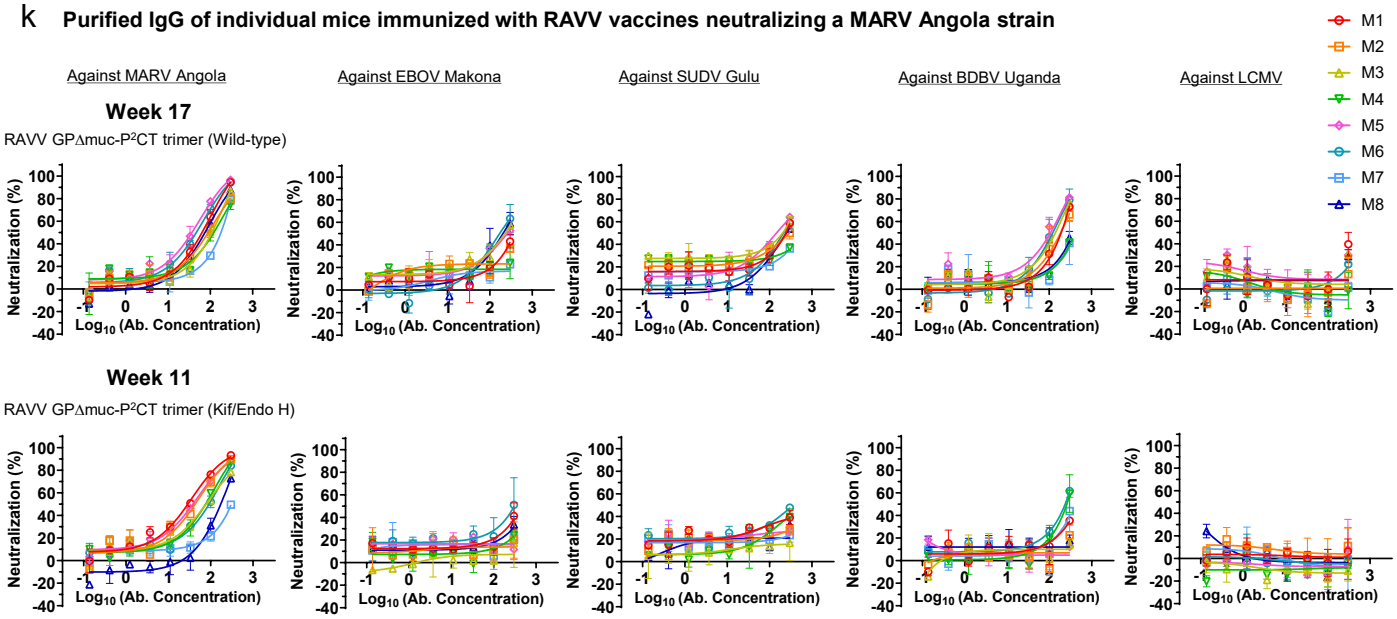

Fig. S11. Immunogenicity of glycan-modified EBOV, SUDV, and RAVV GPΔmuc vaccines in mice. (**a**) ELISA curves of mouse sera from glycan-modified EBOV GPΔmuc trimer and SApNP vaccine groups (n = 8 mice/group) binding to EBOV GPΔmuc-WL^{2}P^4(1TD0) trimer. (**b**) (Top) Summary of geometric mean EC_{50} titers measured for glycan-modified EBOV GPΔmuc vaccine groups against EBOV GPΔmuc-WL^{2}P^4(1TD0) trimer. Color coding indicates EC_{50} levels (green to red: low to high binding). (Bottom) Summary of statistical analysis performed for each timepoint. Note: EC_{50} values at week 2 were derived by setting the minimum/maximum OD_{450} values to 0.0/2.8. (**c**) Neutralization curves of mouse sera from glycan-modified EBOV GPΔmuc trimer and SApNP vaccine groups against EBOV Makona pseudovirus. (**d**) (Top) Summary of geometric means of ID_{50} titers measured for EBOV GPΔmuc vaccine groups against EBOV Makona pseudovirus. Color coding: white (no neutralization), green to red (low to high neutralization). Note: ID_{50} values were calculated using %neutralization constraints of 0.0 (min) and 100.0 (max). (Bottom) Summary of statistical analysis. (**e**) ELISA curves of mouse sera from glycan-modified SUDV GPΔmuc trimer and SApNP vaccine groups binding to SUDV GPΔmuc-WL^{2}P^4(1TD0) trimer. (**f**) (Top) Summary of geometric mean EC_{50} titers measured for glycan-modified SUDV GPΔmuc vaccine groups against SUDV GPΔmuc-WL^{2}P^4(1TD0) trimer. (Bottom) Summary of statistical analysis. Note: EC_{50} values at week 2 were derived by setting the minimum/maximum OD_{450} values to 0.0/2.9. (**g**) Neutralization curves of mouse sera from glycan-modified SUDV GPΔmuc trimer and SApNP vaccine groups against SUDV Gulu pseudovirus. (**h**) (Top) Summary of geometric means of ID_{50} titers measured for SUDV GPΔmuc vaccine groups against SUDV Gulu pseudovirus. (Bottom) Summary of statistical analysis. (**i**) ELISA curves of mouse sera from glycan modified RAVV GPΔmuc trimer vaccine groups binding to RAVV GPΔmuc-P^{2}CT(1TD0) trimer. (**j**) (Top) Summary of geometric mean EC_{50} titers measured for glycan-modified RAVV GPΔmuc vaccine groups against RAVV GPΔmuc-P^{2}CT(1TD0) trimer. (Bottom) Summary of statistical analysis. Note: EC_{50} values at week 2 were derived by setting the minimum/maximum OD_{450} values to 0.0/2.9. (**k**) Neutralization curves of purified mouse IgG from glycan-modified RAVV GPΔmuc vaccine groups after four immunizations at week 17 or week 11 against MARV Angola or orthoebolavirus strains. Lymphocytic choriomeningitis virus (LCMV) was included as a negative control to confirm the cross-NAb responses measured using purified IgG. Error bars represent the difference between duplicate measurements at each concentration for each sample. EC_{50} and ID_{50} values were calculated using GraphPad Prism version 10.3.1. Data were analyzed using one-way ANOVA, followed by Tukey's multiple comparison post hoc test for each timepoint. Two-tailed unpaired t-tests were used to compare the geometric means between two independent groups. Statistical significance was defined as follows: ns (not significant), *$p < 0.05$, **$p < 0.01$, ***$p < 0.001$, and ****$p < 0.0001$.

a

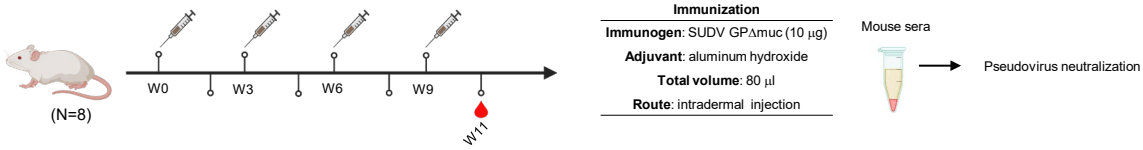

b **Week-11 sera of female and male mice immunized with wild-type SUDV vaccines neutralizing a SUDV Gulu strain**

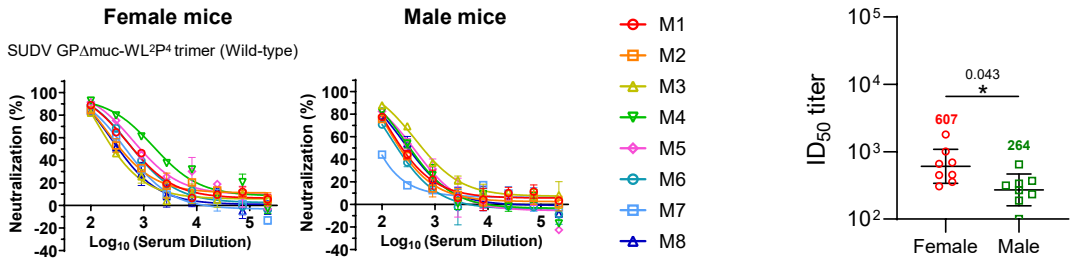

Sex	ID_{50} titers (week 11)								Geometric Mean
	M1	M2	M3	M4	M5	M6	M7	M8	
Female	690.2	454.8	307.7	1796	1007	660.1	449	355.5	606.9
Male	267.7	233.5	649.3	335.9	371.4	188.1	<100	314.3	263.9

Unpaired t test (w11)	Statistics	P Value
female vs. male	*	0.043

c **Week-11 sera of female and male mice immunized with glycan-modified SUDV vaccines neutralizing a SUDV Gulu strain**

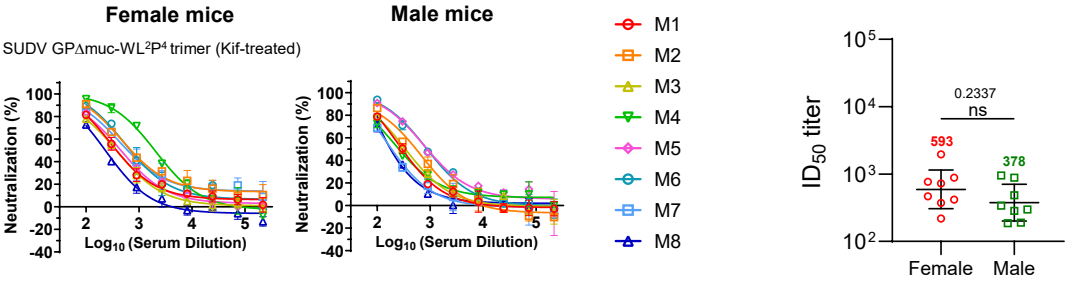

Sex	ID_{50} titers (week 11)								Geometric Mean
	M1	M2	M3	M4	M5	M6	M7	M8	
Female	417.3	885.7	374.1	1953	468	769.3	726	217.8	593.4
Male	297.6	485.6	340.5	283.6	954.3	880.1	185.9	190.2	377.7

Unpaired t test (w11)	Statistics	P Value
female vs. male	ns	0.2337

Fig. S12. Influence of sex on immunogenicity of SUDV GPΔmuc-induced neutralizing antibody responses in mice. (**a**) Schematic illustration of the mouse immunization regimen for SUDV GPΔmuc trimer vaccines (n = 8 mice per group). Each mouse received 80 μl of a vaccine antigen/aluminum hydroxide (AH) adjuvant mix containing 10 μg of SUDV antigen and 40 μl of AH. Mice were immunized via the intradermal route through four footpad injections at weeks 0, 3, 6, and 9, with 3-week intervals between doses. (**b**) Neutralization curves of female and male mouse sera from the wild-type SUDV GPΔmuc trimer group at week 11 (after four immunizations), tested against SUDV Gulu pseudovirus. (**c**) Neutralization curves of female and male mouse sera from the glycan-modified SUDV GPΔmuc trimer group under the same conditions. Comparison of NAb responses (by ID_{50} titers) between female and male mice is shown, along with a summary of geometric mean ID_{50} values for each group against SUDV Gulu pseudovirus. Error bars represent the difference between duplicate measurements at each concentration for each sample. ID_{50} values were calculated using GraphPad Prism version 10.3.1. Two-tailed unpaired t-tests were used to compare the geometric means between two independent groups. Statistical significance was defined as follows: ns (not significant), *$p < 0.05$.

Table S1. Data collection and refinement statistics for EBOV Mayinga GPΔmuc-WL^{2}P^4.

Data Collection	**EBOV Mayinga GPΔmuc-WL^{2}P^4**
Beamline	SSRL 12-1
Wavelength (Å)	0.97946
Resolution (Å)[a]	40.6 - 3.20 (3.29 - 3.20)
Space group	P321
Unit cell (Å)	114.47,114.47,133.38
(°)	90 90 120
Total reflections	189,316 (12,886)
Unique reflections	17,104 (815)
Multiplicity	11.1 (9.6)
Completeness (%)	99.8 (98.2)
Mean (I)/ σ_I	22.2 (1.2)
R_{merge} (%)	6.1 (>100)
R_{meas}[c] (%)	12.3 (>100)
R_{pim}[d] (%)	3.7 (69.3)
$CC_{1/2}$[e] (%)	99.8 (30.3)
Refinement	
Refinement resolution (Å)[a]	40.6 - 3.20 (3.29 - 3.20)
# reflections in refinement (work/free)	17,082 (1,323)
R_{work} (%)	21.5 (36.1)
R_{free} (%)	22.2 (33.0)
# Protein atoms	3,119
# Carbohydrate atoms	128
# Waters	0
# Protein residues	398
Bond r.m.s. deviation (Å)	0.013
Angle r.m.s. deviation (º)	1.60
Wilson B (Å^2)	114
Average B protein (Å^2)	119
carbohydrate (Å^2)	156
Ramachandran favored, allowed, outliers (%)	96.1, 3.9, 0.0, 0.0
Clashscore[f]	8.2
PDB ID	9N8E

[a]Numbers in parentheses are for highest resolution shell
[b]$R_{merge} = \Sigma_{hkl} \Sigma_{i=1,n}|I_i(hkl) - \langle I(hkl)\rangle| / \Sigma_{hkl} \Sigma_{i=1,n} I_i(hkl)$
[c]$R_{meas} = \Sigma_{hkl} \sqrt{(n/n-1)} \Sigma_{i=1,n}|I_i(hkl) - \langle I(hkl)\rangle| / \Sigma_{hkl} \Sigma_{i=1,n} I_i(hkl)$
[d]$R_{pim} = \Sigma_{hkl} \sqrt{(1/n-1)} \Sigma_{i=1,n}|I_i(hkl) - \langle I(hkl)\rangle| / \Sigma_{hkl} \Sigma_{i=1,n} I_i(hkl)$
[e]$CC_{1/2}$ = Pearson correlation coefficient between two random half datasets
[f] Number of unfavorable all-atom steric overlaps ≥ 0.4 Å per 1000 atoms

Table S2. Cryo-EM data collection information, model building, and refinement statistics.

Data collection information	**SUDV Gulu GPΔmuc-WL^{2}P^4/CA45 Fab**
Microscope	Titan Krios G4
Voltage (keV)	200
Detector	Falcon 4 camera with a Selectris-X energy filter
Recording mode	Counting
Magnification	130,000 x
Movie micrograph pixel size	0.89
Total dose (e^-/Å^2)	50
Under focus range (µm)	-1.0 to -2.0 um
Number of movie micrographs	1,824
Model building and refinement statistics	
Map Resolution (Å)	3.13
Residues	
Amino-acids	1473
Carbohydrates	9
RMSD Bonds (Å)	0.003
RMSD Angles (º)	0.746
Ramachandran	
Outliers (%)	0.00
Allowed (%)	7.2
Favored (%)	92.8
Rotamer outliers	1.67
Clash score	8.98
MolProbity score	2.10
PDB ID	9N8F
EMDB ID	EMD-49127

Figure 1

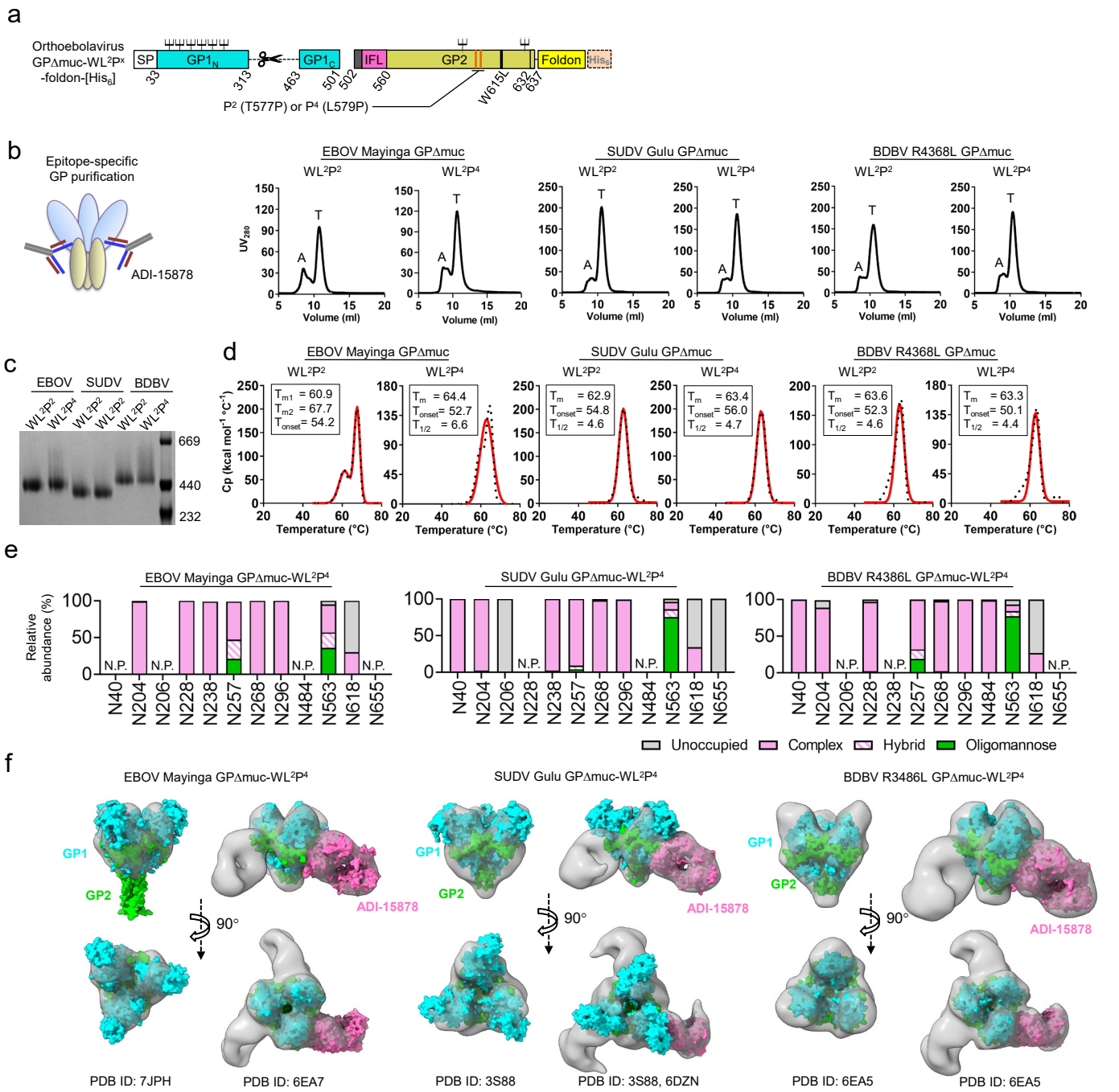

	CA45	ADI-15878	ADI-15946	BDBV-289	MR78
EBOV Mayinga GPΔmuc-WL^{2}P^2	0.68	0.58	0.38	0.41	0.00
EBOV Mayinga GPΔmuc-WL^{2}P^4	0.69	0.59	0.37	0.39	0.00
SUDV Gulu GPΔmuc-WL^{2}P^2	0.51	0.63	0.32	0.21	0.00
SUDV Gulu GPΔmuc-WL^{2}P^4	0.54	0.68	0.38	0.22	0.00
BDBV R4386L GPΔmuc-WL^{2}P^2	0.54	0.62	0.44	0.48	0.01
BDBV R4386L GPΔmuc-WL^{2}P^4	0.59	0.65	0.44	0.48	0.00

Figure 2

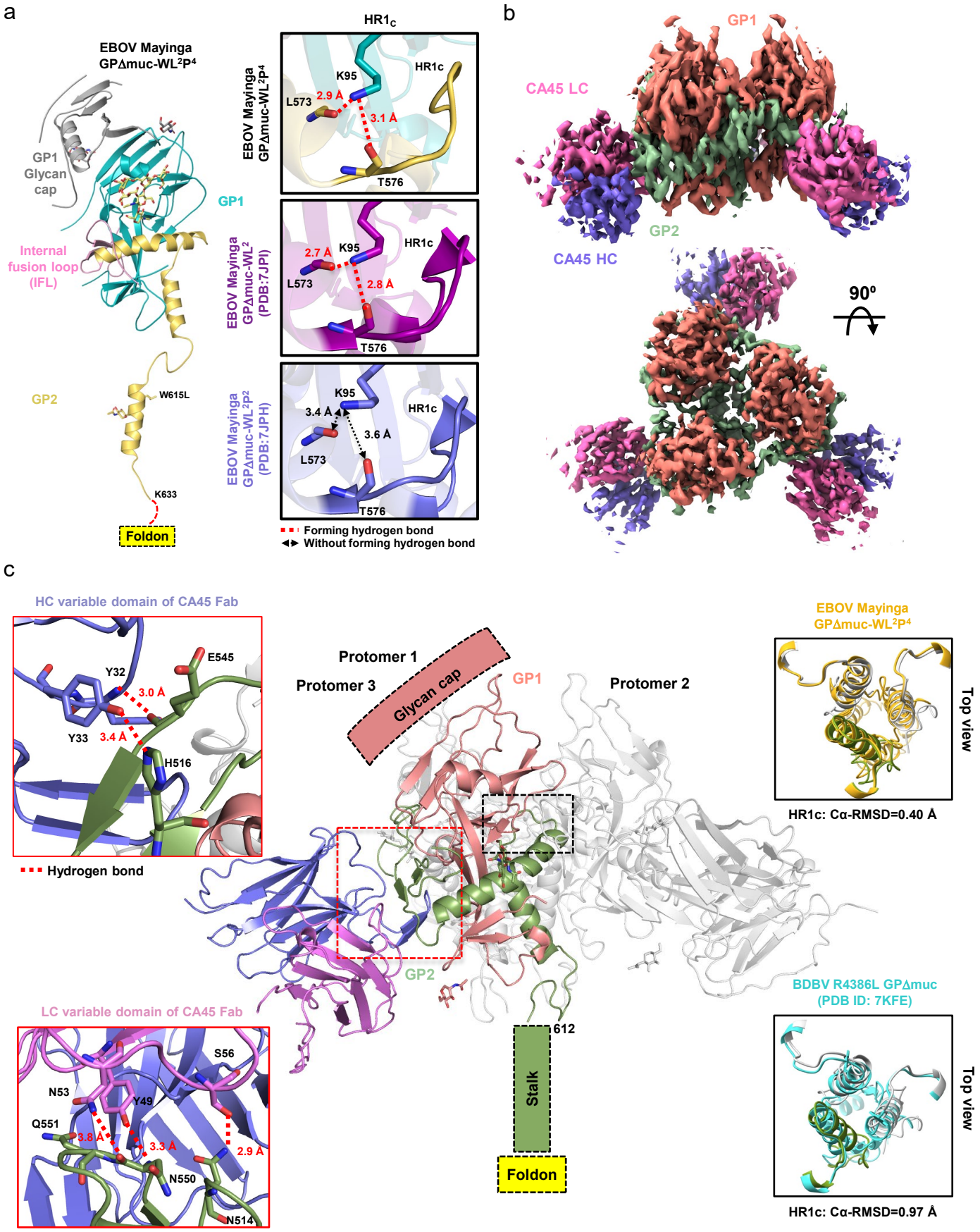
a
EBOV Mayinga
GPΔmuc-WL2P4
GP1
Glycan
cap
GP1
Internal
fusion loop
(IFL)
GP2
W615L
K633
Foldon
HR1c
EBOV Mayinga
GPΔmuc-WL2P4
K95
HR1c
L573
2.9 Å
3.1 Å
T576
EBOV Mayinga
GPΔmuc-WL2
(PDB:7JPI)
2.7 Å
K95
HR1c
L573
2.8 Å
T576
EBOV Mayinga
GPΔmuc-WL2P2
(PDB:7JPH)
K95
3.4 Å
HR1c
3.6 Å
L573
T576
Forming hydrogen bond
Without forming hydrogen bond
b
GP1
CA45 LC
GP2
CA45 HC
90º
c
HC variable domain of CA45 Fab
E545
Y32
3.0 Å
Y33
3.4 Å
H516
Hydrogen bond
Protomer 1
Protomer 3
Glycan cap
GP1
Protomer 2
GP2
612
Stalk
Foldon
EBOV Mayinga
GPΔmuc-WL2P4
Top view
HR1c: Cα-RMSD=0.40 Å
BDBV R4386L GPΔmuc
(PDB ID: 7KFE)
Top view
HR1c: Cα-RMSD=0.97 Å
LC variable domain of CA45 Fab
S56
N53
Y49
Q551
3.8 Å
3.3 Å
2.9 Å
N550
N514

Figure 3

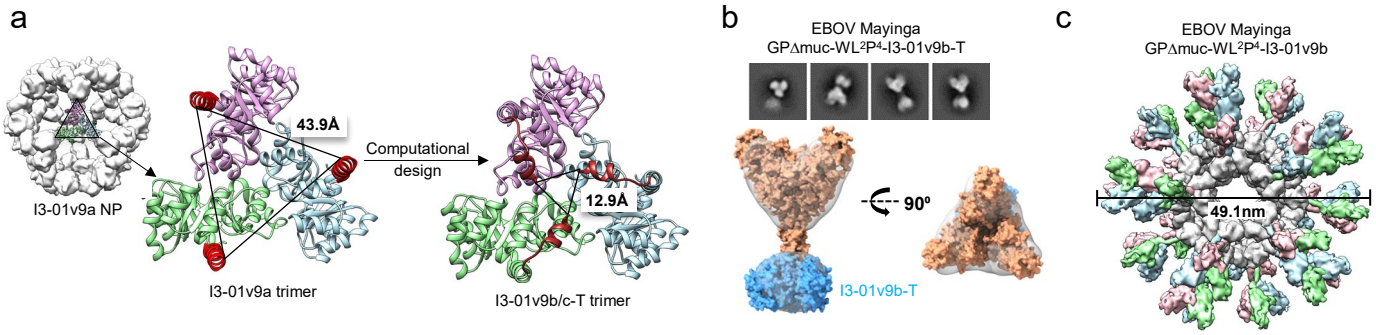

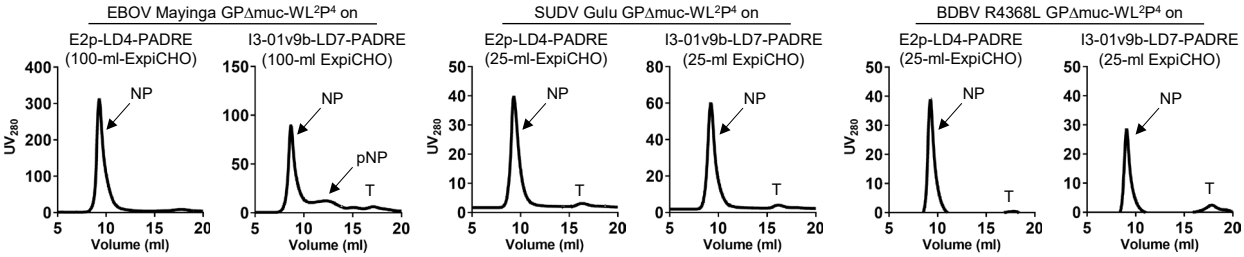

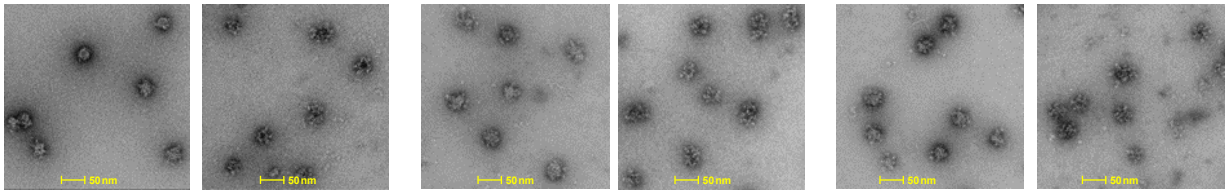

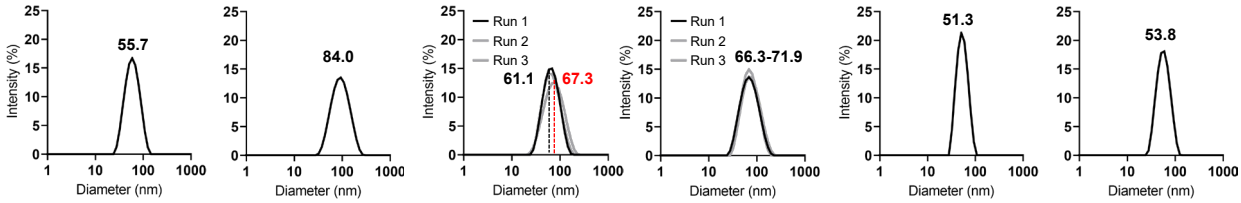

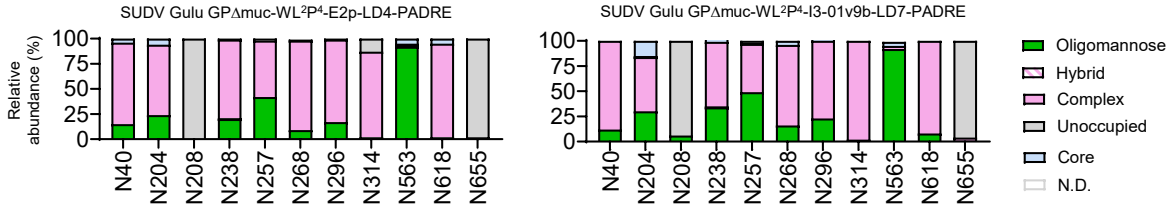

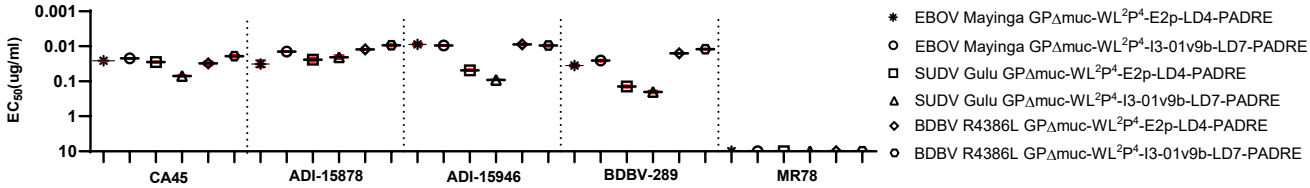

i

	CA45	ADI-15878	ADI-15946	BDBV-289	MR78
EBOV Mayinga GPΔmuc-WL^{2}P^4-E2p-LD4-PADRE	0.71	0.90	0.73	0.79	0.01
EBOV Mayinga GPΔmuc-WL^{2}P^4-I3-01v9b-LD7-PADRE	0.90	0.83	0.66	0.68	0.03
SUDV Gulu GPΔmuc-WL^{2}P^4-E2p-LD4-PADRE	1.37	1.60	1.37	0.51	0.00
SUDV Gulu GPΔmuc-WL^{2}P^4-I3-01v9b-LD7-PADRE	0.72	1.44	1.06	0.39	0.01
BDBV R4386L GPΔmuc-WL^{2}P^4-E2p-LD4-PADRE	0.95	1.68	1.24	2.03	0.01
BDBV R4386L GPΔmuc-WL^{2}P^4-I3-01v9b-LD7-PADRE	0.50	1.21	1.24	0.87	0.00

Figure 4

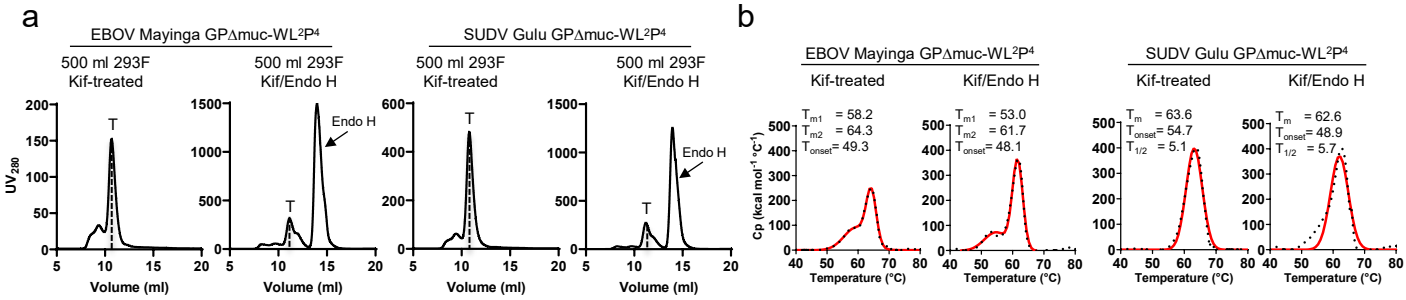

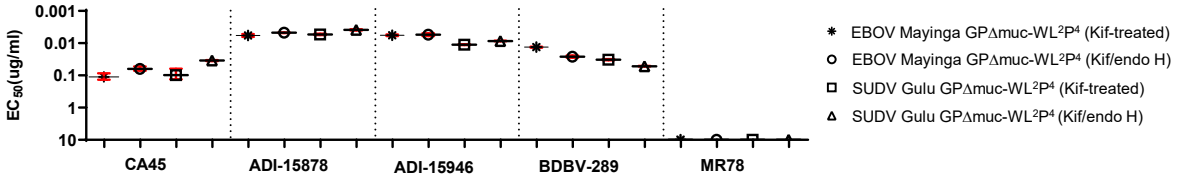

d

	CA45	ADI-15878	ADI-15946	BDBV-289	MR78
EBOV Mayinga GPΔmuc-WL^{2}P^4 (Kif-treated)	0.80	0.71	0.53	0.58	0.00
EBOV Mayinga GPΔmuc-WL^{2}P^4 (Kif/endo H)	0.74	0.62	0.45	0.51	0.00
SUDV Gulu GPΔmuc-WL^{2}P^4 (Kif-treated)	0.76	0.70	0.51	0.44	0.00
SUDV Gulu GPΔmuc-WL^{2}P^4 (Kif/endo H)	0.75	0.71	0.55	0.49	0.00

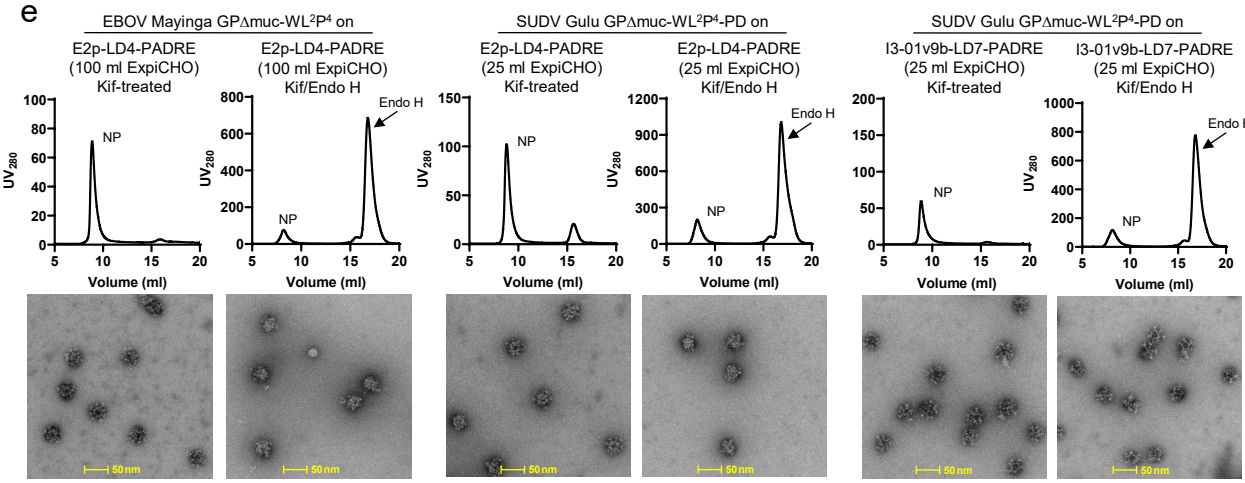

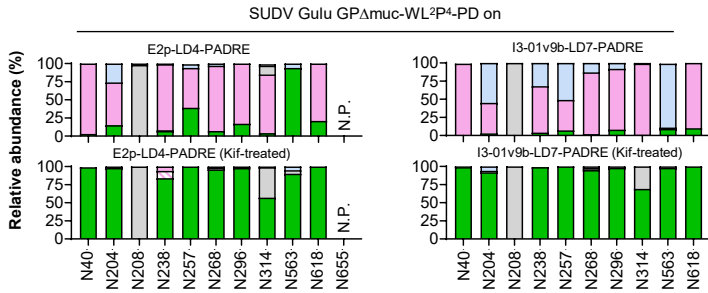

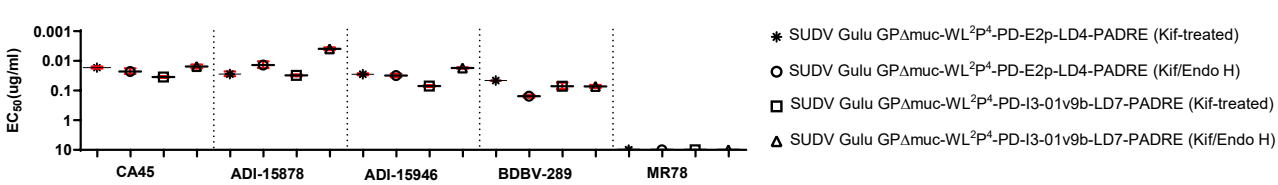

h

	CA45	ADI-15878	ADI-15946	BDBV-289	MR78
SUDV Gulu GPΔmuc-WL^{2}P^4-PD-E2p-LD4-PADRE (Kif-treated)	1.29	1.46	1.44	0.48	0.01
SUDV Gulu GPΔmuc-WL^{2}P^4-PD-E2p-LD4-PADRE (Kif/Endo H)	1.63	2.23	1.78	0.58	0.00
SUDV Gulu GPΔmuc-WL^{2}P^4-PD-I3-01v9b-LD7-PADRE (Kif-treated)	0.89	1.43	1.20	0.42	0.01
SUDV Gulu GPΔmuc-WL^{2}P^4-PD-I3-01v9b-LD7-PADRE (Kif/Endo H)	1.00	1.60	1.35	0.64	0.00

Figure 5

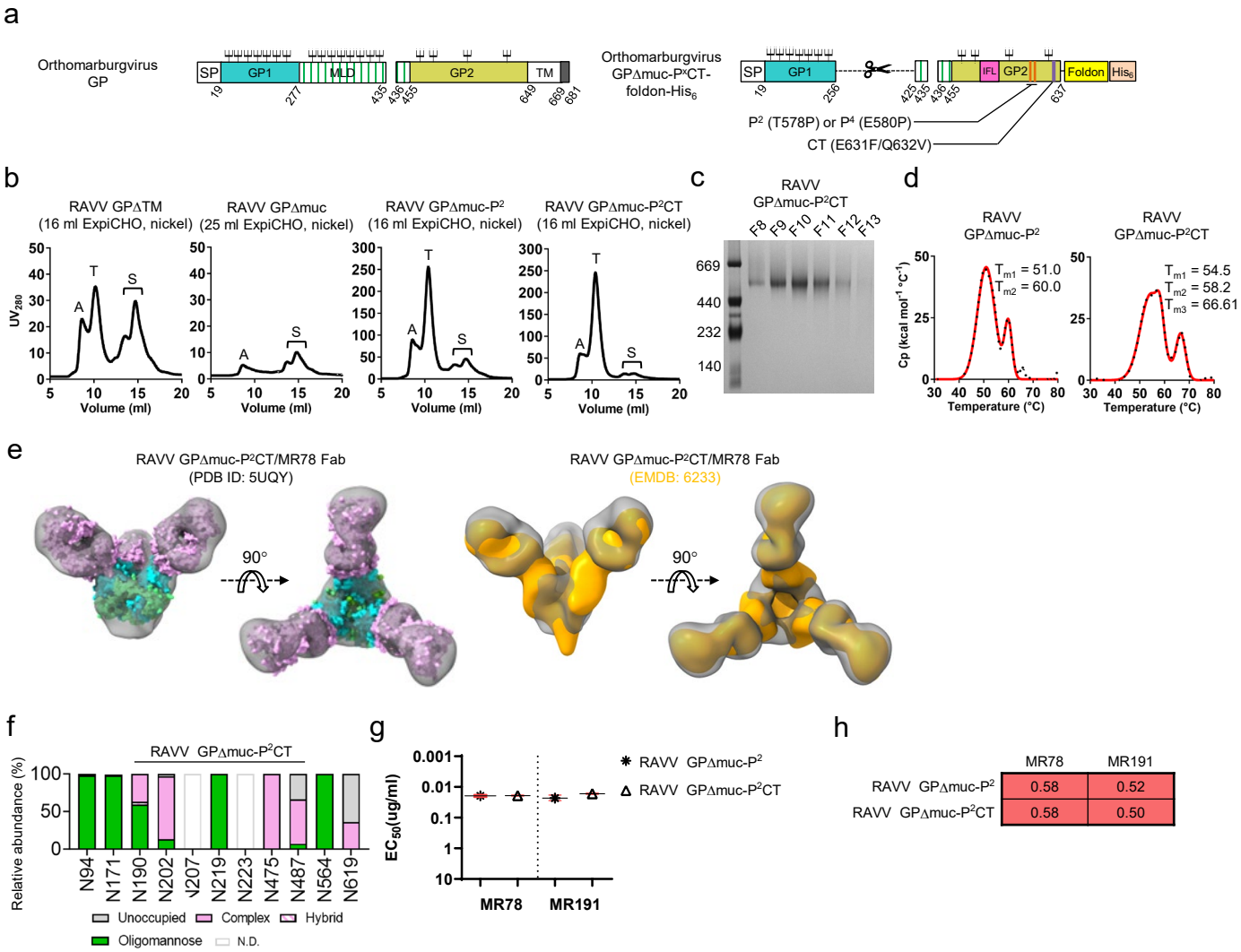
a
Orthomarburgvirus GP
SP
GP1
MLD
GP2
TM
19
277
435
436
455
649
669
681
Orthomarburgvirus GPΔmuc-P^X CT-foldon-His6
IFL
Foldon
His6
256
425
637
P2 (T578P) or P4 (E580P)
CT (E631F/Q632V)
b
RAVV GPΔTM (16 ml ExpiCHO, nickel)
RAVV GPΔmuc (25 ml ExpiCHO, nickel)
RAVV GPΔmuc-P2 (16 ml ExpiCHO, nickel)
RAVV GPΔmuc-P2CT (16 ml ExpiCHO, nickel)
UV280
Volume (ml)
A
T
S
c
RAVV GPΔmuc-P2CT
F8
F9
F10
F11
F12
F13
669
440
232
140
d
RAVV GPΔmuc-P2
RAVV GPΔmuc-P2CT
Cp (kcal mol-1 °C-1)
Temperature (°C)
Tm1 = 51.0
Tm2 = 60.0
Tm1 = 54.5
Tm2 = 58.2
Tm3 = 66.61
e
RAVV GPΔmuc-P2CT/MR78 Fab (PDB ID: 5UQY)
RAVV GPΔmuc-P2CT/MR78 Fab (EMDB: 6233)
90°
f
RAVV GPΔmuc-P2CT
Relative abundance (%)
N94
N171
N190
N202
N207
N219
N223
N475
N487
N564
N619
Unoccupied
Complex
Hybrid
Oligomannose
N.D.
g
EC50 (ug/ml)
RAVV GPΔmuc-P2
RAVV GPΔmuc-P2CT
MR78
MR191
h
MR78
MR191
RAVV GPΔmuc-P2
0.58
0.52
RAVV GPΔmuc-P2CT
0.58
0.50

Figure 6

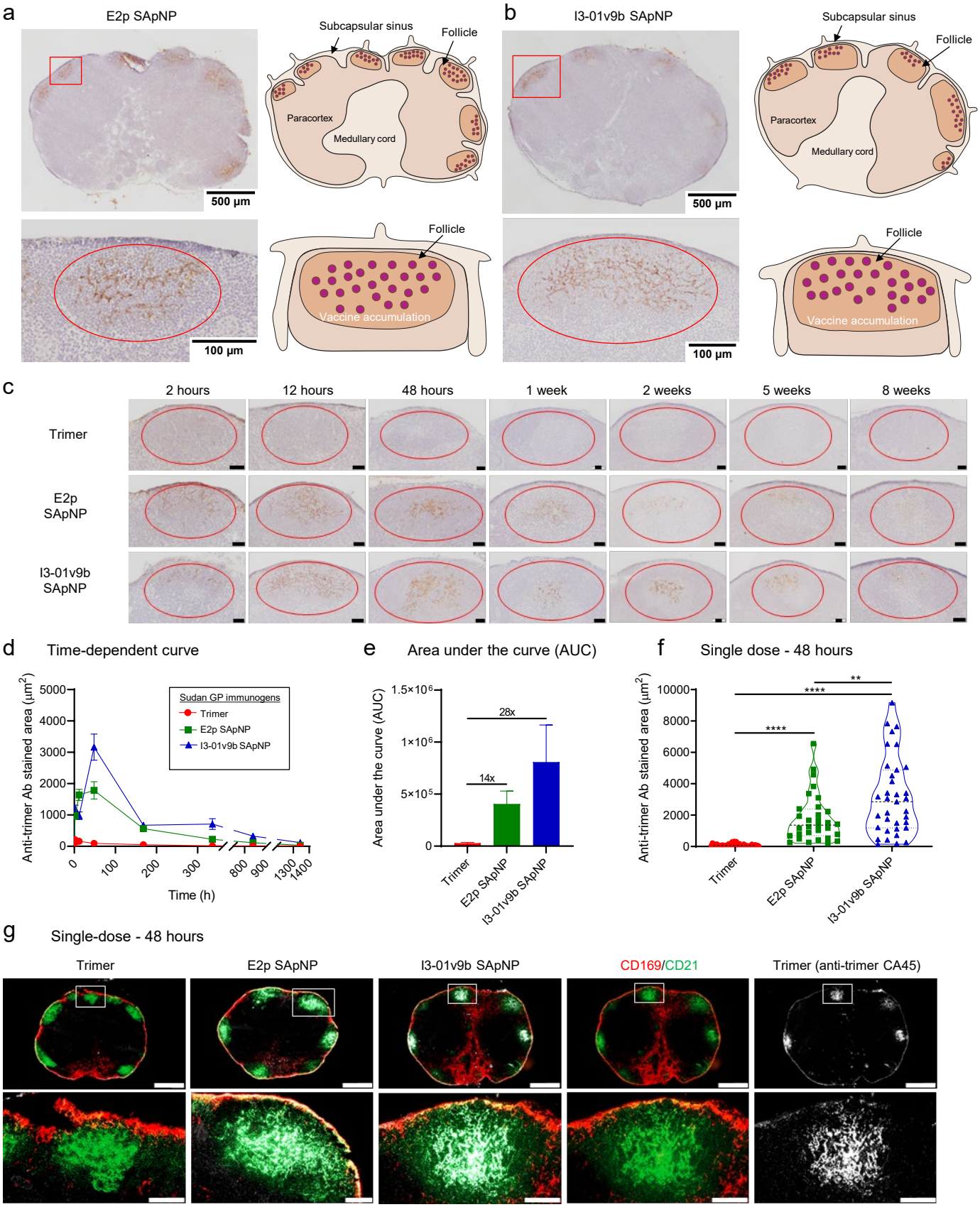
a
E2p SApNP
Subcapsular sinus
Follicle
Paracortex
Medullary cord
500 µm
Follicle
Vaccine accumulation
100 µm
b
I3-01v9b SApNP
Subcapsular sinus
Follicle
Paracortex
Medullary cord
500 µm
Follicle
Vaccine accumulation
100 µm
c
2 hours
12 hours
48 hours
1 week
2 weeks
5 weeks
8 weeks
Trimer
E2p SApNP
I3-01v9b SApNP
d
Time-dependent curve
Anti-trimer Ab stained area (µm²)
Sudan GP immunogens
Trimer
E2p SApNP
I3-01v9b SApNP
Time (h)
e
Area under the curve (AUC)
Area under the curve (AUC)
28x
14x
Trimer
E2p SApNP
I3-01v9b SApNP
f
Single dose - 48 hours
Anti-trimer Ab stained area (µm²)
****
****
**
Trimer
E2p SApNP
I3-01v9b SApNP
g
Single-dose - 48 hours
Trimer
E2p SApNP
I3-01v9b SApNP
CD169/CD21
Trimer (anti-trimer CA45)

Figure 7

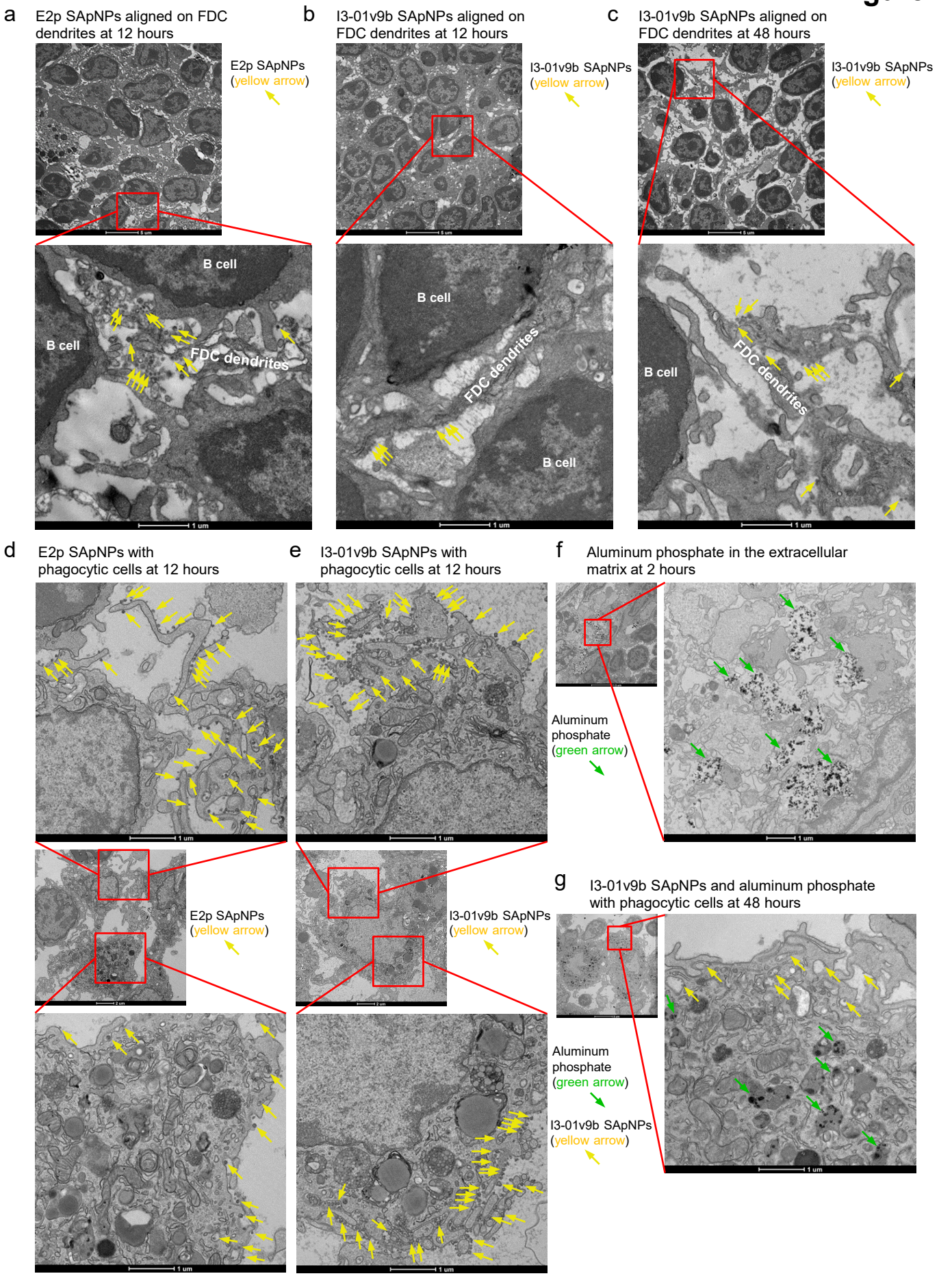
a
E2p SApNPs aligned on FDC dendrites at 12 hours
E2p SApNPs (yellow arrow)
B cell
B cell
FDC dendrites
b
I3-01v9b SApNPs aligned on FDC dendrites at 12 hours
I3-01v9b SApNPs (yellow arrow)
B cell
FDC dendrites
B cell
c
I3-01v9b SApNPs aligned on FDC dendrites at 48 hours
I3-01v9b SApNPs (yellow arrow)
B cell
FDC dendrites
d
E2p SApNPs with phagocytic cells at 12 hours
E2p SApNPs (yellow arrow)
e
I3-01v9b SApNPs with phagocytic cells at 12 hours
I3-01v9b SApNPs (yellow arrow)
f
Aluminum phosphate in the extracellular matrix at 2 hours
Aluminum phosphate (green arrow)
g
I3-01v9b SApNPs and aluminum phosphate with phagocytic cells at 48 hours
Aluminum phosphate (green arrow)
I3-01v9b SApNPs (yellow arrow)

Figure 8

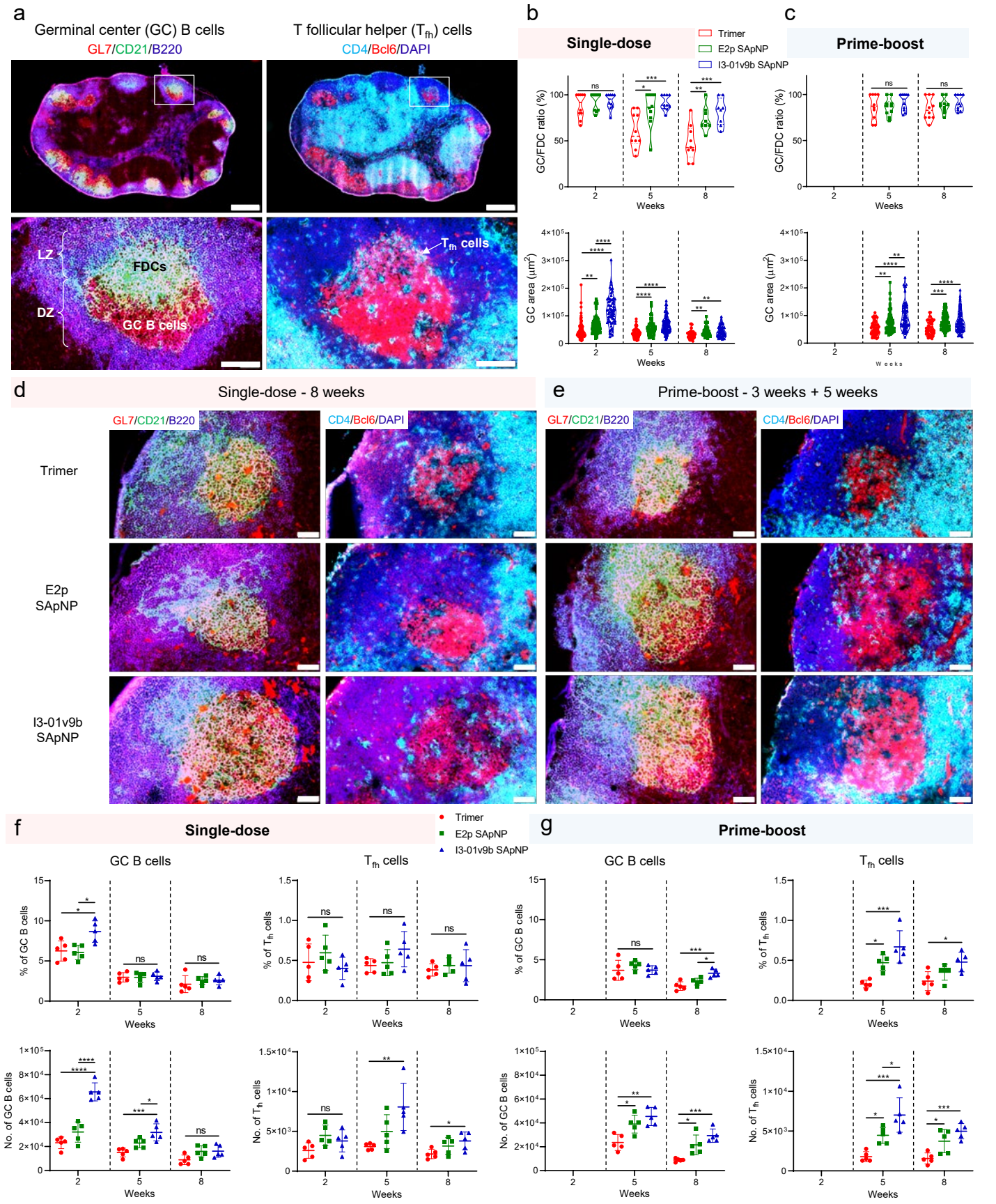
a
Germinal center (GC) B cells
GL7/CD21/B220
T follicular helper (Tfh) cells
CD4/Bcl6/DAPI
LZ
FDCs
DZ
GC B cells
Tfh cells
b
Single-dose
Trimer
E2p SApNP
I3-01v9b SApNP
c
Prime-boost
GC/FDC ratio (%)
GC area (μm2)
Weeks
d
Single-dose - 8 weeks
e
Prime-boost - 3 weeks + 5 weeks
GL7/CD21/B220
CD4/Bcl6/DAPI
Trimer
E2p SApNP
I3-01v9b SApNP
f
Single-dose
g
Prime-boost
GC B cells
Tfh cells
% of GC B cells
% of Tfh cells
No. of GC B cells
No. of Tfh cells
Weeks

Figure 9

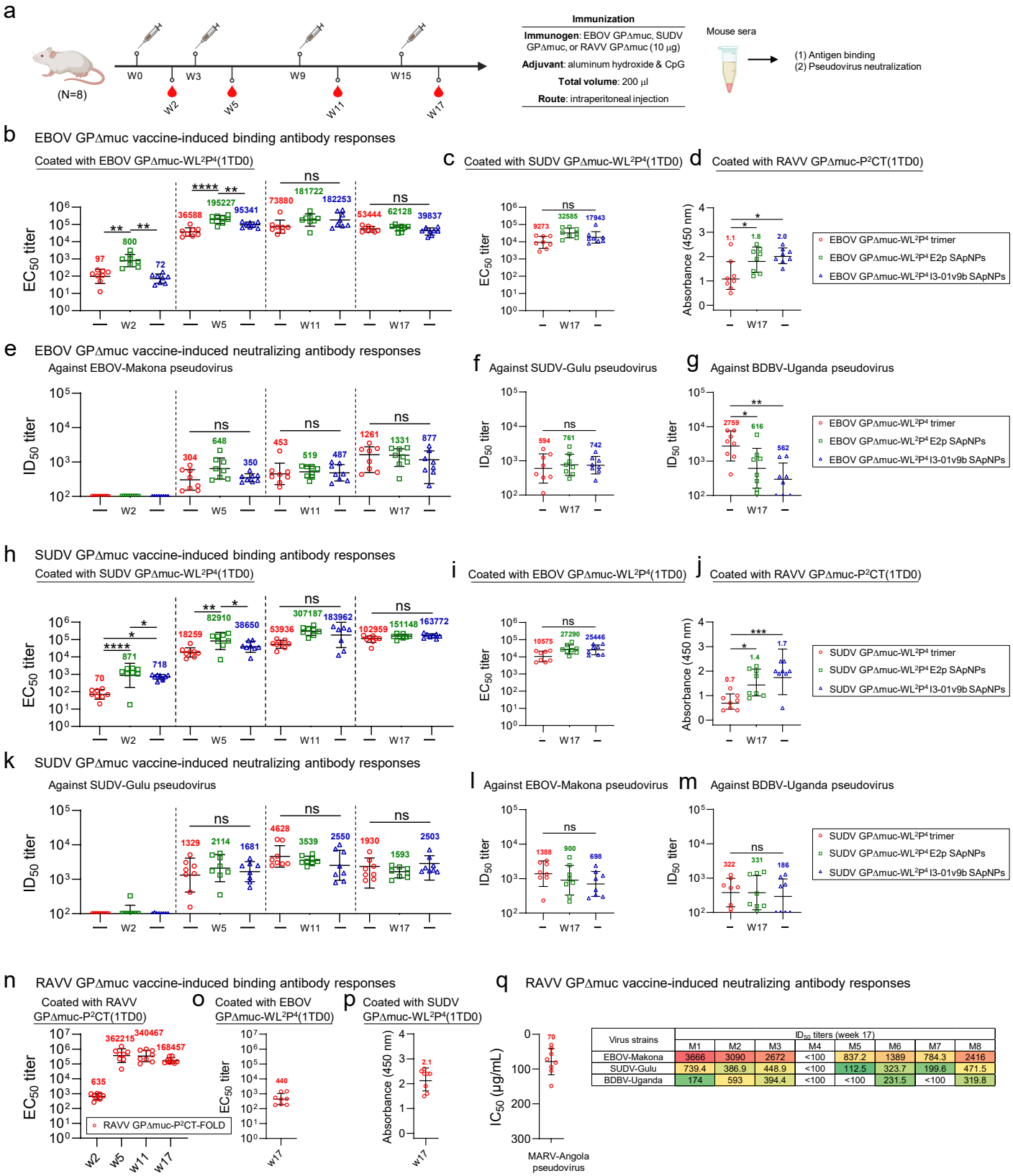

Virus strains	ID_{50} titers (week 17)							
	M1	M2	M3	M4	M5	M6	M7	M8
EBOV-Makona	3666	3090	2672	<100	837.2	1389	784.3	2416
SUDV-Gulu	739.4	386.9	448.9	<100	112.5	323.7	199.6	471.5
BDBV-Uganda	174	593	394.4	<100	<100	231.5	<100	319.8

Figure 10

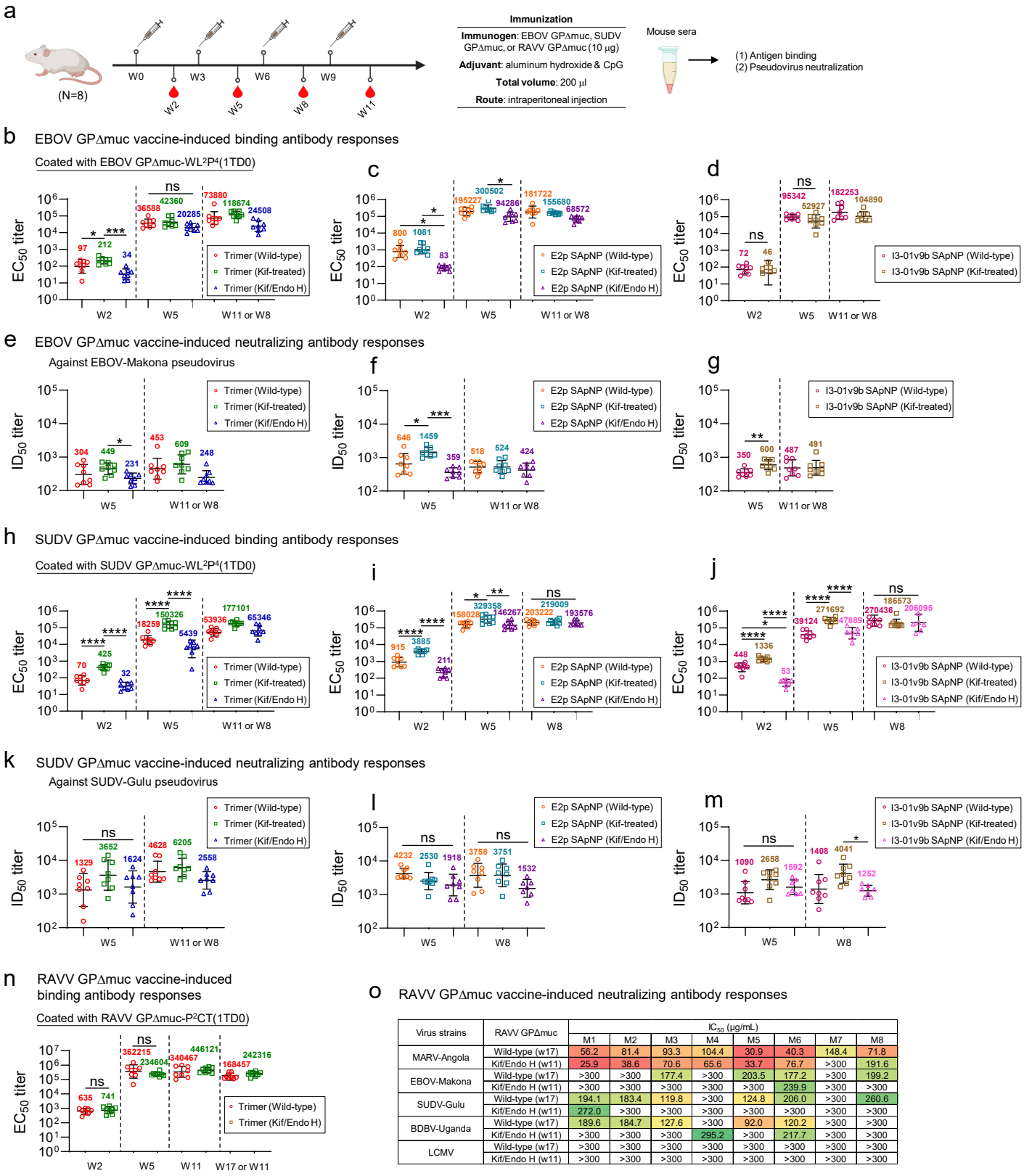

Virus strains	RAVV GPΔmuc	IC_{50} (μg/mL)							
		M1	M2	M3	M4	M5	M6	M7	M8
MARV-Angola	Wild-type (w17)	56.2	81.4	93.3	104.4	30.9	40.3	148.4	71.8
	Kif/Endo H (w11)	25.9	38.6	70.6	65.6	33.7	76.7	>300	191.6
EBOV-Makona	Wild-type (w17)	>300	>300	177.4	>300	203.5	177.2	>300	199.2
	Kif/Endo H (w11)	>300	>300	>300	>300	>300	239.9	>300	>300
SUDV-Gulu	Wild-type (w17)	194.1	183.4	119.8	>300	124.8	206.0	>300	260.6
	Kif/Endo H (w11)	272.0	>300	>300	>300	>300	>300	>300	>300
BDBV-Uganda	Wild-type (w17)	189.6	184.7	127.6	>300	92.0	120.2	>300	>300
	Kif/Endo H (w11)	>300	>300	>300	295.2	>300	217.7	>300	>300
LCMV	Wild-type (w17)	>300	>300	>300	>300	>300	>300	>300	>300
	Kif/Endo H (w11)	>300	>300	>300	>300	>300	>300	>300	>300